UNIVERSITÉ DE GENÈVE
Département de physique nucléaire et corpusculaire

FACULTÉ DES SCIENCES
Professeur Allan Clark

Measurement of the Inclusive Electron Cross-Section from Heavy Flavour Decays and of the Bottom Production Rate with the ATLAS Experiment

THÈSE

présentée à la Faculté des sciences de l'Université de Genève
pour obtenir le grade de Docteur ès sciences, mention physique

par

María Clemencia Rosario Mora Herrera

du Chili

Thèse N° 4495

GENÈVE
Atelier d'impression ReproMail
2012

UNIVERSITÉ DE GENÈVE

FACULTÉ DES SCIENCES

Doctorat ès sciences
Mention physique

Thèse de *Madame Maria Clemencia Rosario MORA HERRERA*

intitulée :

"Measurement of the Inclusive Electron Cross-Section from Heavy Flavour Decays and of the Bottom Production Rate with the ATLAS Experiment"

La Faculté des sciences, sur le préavis de Messieurs A. CLARK, professeur honoraire et directeur de thèse (Département de physique nucléaire et corpusculaire), X. WU, professeur associé et co-directeur de thèse (Département de physique nucléaire et corpusculaire), G. IACOBUCCI, professeur ordinaire (Département de physique nucléaire et corpusculaire), et M. CAMPANELLI. docteur (University College – Physics Department – London, United Kingdom), autorise l'impression de la présente thèse, sans exprimer d'opinion sur les propositions qui y sont énoncées.

Genève, le 3 décembre 2012

Thèse - 4495 -

Le Doyen, Jean-Marc TRISCONE

N.B.- La thèse doit porter la déclaration précédente et remplir les conditions énumérées dans les "Informations relatives aux thèses de doctorat à l'Université de Genève".

Acknowledgements

The road that lead to this thesis was long and difficult; I could not have travelled it without the support, encouragement and help of many people.

First of all, I am very grateful to my advisor, Allan Clark, for giving me the opportunity to work in ATLAS for my Ph.D. at the University of Geneva, coming from far away both physically and intellectually, for his will to motivate me and for helping me achieve my goals. Many thanks to Xin Wu, as well, for all the discussions, technical resourcefulness and for sharing the office with me, and to Peppe Iacobucci and Mario Campanelli for reading and examining this manuscript, giving me insightful questions that let me value my own work.

I am especially thankful to Gabriella Pásztor and Paul Bell for their hands-on guidance and fruitful comments on the analysis of the B-rate, on my contribution to the inclusive electron measurement, and on the manuscript of this thesis. I thank, as well, the rest of the inclusive electron analysis group for the very nice collaboration and a great paper published.

While I worked on the ATLAS Trigger, I knew I could always count on Joerg Stelzer and Tomasz Bold to solve any problem, I am thankful for their kindness and patience with my endless questions. Thanks to Sylvie Brunet for tutoring me for the Trigger@Tier0 job and to Simon George for introducing me to the world of Trigger Offline Monitoring shifts. It was a blessing to know and work with the all the amazing people I met while working on the Trigger.

Sharing the torment and the occasional joy of the doctorate-program hurdles with my dear colleagues in the ATLAS UniGe group made them easier to endure. I very much enjoyed their company, conversations, the Thursday trips to EPFL and the Friday morning rides to CERN. And thanks to Szymon and Yann for the very efficient work in the Geneva cluster.

Un grand merci à Catherine pour toute l'aide, surtout pour m'aider avec les démarches de la thèse alors que j'étais à l'étranger.

I acknowledge the financial support received during the first four years of the doctorate from the Chilean National Commission for Scientific and Technological Research (CONICYT) through the "Gestión Propia" scholarship for doctoral studies abroad.

The support of my parents, grand-parents, my two brothers, my sister-in-law and my god-daughter was indispensable for me in order to persevere and finish successfully; their prayers, thoughts and calls kept me going in the darkest hours. Finally, the greatest gratitude I have is to my husband, Antonio, who has been by my side incessantly (at least in spirit), helping me bear what I thought was unbearable, giving me enormous pride for his accomplishments, encouraging me to undertake new personal challenges and still reminding me of what is important in life. I dedicate this work to them.

Abstract

This thesis presents a measurement of the inclusive electron production cross-section from heavy-flavour decays with the ATLAS experiment at the LHC. A dataset of proton-proton collisions at a center-of-mass energy of 7 TeV with a total integrated luminosity of 1.28 ± 0.04 pb^{-1} is used for this measurement. Signal electrons, arising predominantly from semi-leptonic decays of charm and bottom hadrons, are extracted using a binned maximum likelihood method. A combination of particle identification techniques is used to discriminate against the dominant backgrounds of hadron fakes and photon conversions. Taking into account trigger, reconstruction and identification efficiencies, the extracted inclusive electron spectrum is unfolded into a differential cross-section as a function of the electron transverse momentum. A good agreement is found with theoretical predictions and with an ATLAS measurement using muons in the final state. The integrated cross-section for electrons originating from heavy-flavour decays, in the transverse momentum range $7 < p_{\mathrm{T}}^{e} < 26$ GeV and within the pseudorapidity range $|\eta^{e}| < 2$, excluding $1.37 < |\eta^{e}| < 1.52$, is

$$\sigma_{\mathrm{HF}}^{e} = 0.946 \pm 0.020_{(\mathrm{stat.})} \pm 0.146_{(\mathrm{syst.})} \pm 0.032_{(\mathrm{lumi.})}\ \mu\mathrm{b}.$$

A study of the production rate of bottom hadrons, based on the same dataset as the inclusive measurement, is also presented. The relative p_{T} of the electron with respect to a nearby track-jet, $p_{\mathrm{T}}^{\mathrm{rel}}$, is used in a binned maximum likelihood fit to differentiate the bottom hadron signal from charm, light hadron and photon conversion backgrounds. The spectrum of electrons from bottom decays as a function of the electron reconstructed E_{T} is compared to LO and NLO MC predictions.

Résumé

Cette thèse présente une mesure de la section efficace de production inclusive des électrons provenant de la désintégration des hadrons de saveur lourde ainsi qu'une étude sur le taux de production de hadrons B avec l'expérience ATLAS au LHC. L'étude de la production des saveurs lourdes, à savoir la production de hadrons contenant les quarks lourds *charm* ou *bottom*, constitue un test puissant de la chromodynamique quantique au LHC et est aussi intéressante parce que ces processus constituent un bruit de fond important à de nombreuses recherches de nouvelle physique au-delà du modèle standard. L'ensemble des données utilisées pour les mesures présentées dans cette thèse correspond à une luminosité intégrée de $1,28 \pm 0,04$ pb^{-1} de collisions proton-proton à une énergie dans le centre de masse de 7 TeV, enregistrées avec le détecteur ATLAS pendant l'année 2010.

Pour reconstruire les électrons, le détecteur ATLAS possède des trajectographes qui mesurent l'impulsion des particules chargées, aussi appelé détecteur interne (ID), et le calorimètre électromagnétique à argon liquide, divisé en trois couches radiales, permettant de mesurer l'énergie des électrons et des photons. Deux types de trajectographe sont utilisés: les trajectographes à silicium (les pixels et le trajectographe à micropistes de silicium, SCT), et un trajectographe gazeux à rayonnement de transition (TRT), qui permet aussi l'identication des électrons par rapport aux hadrons, en exploitant le rayonnement de transition. Les candidats à électron sont identifiés lorsqu'ils ont au moins une trace dans le détecteur interne et une gerbe étroite dans le calorimètre électromagnétique.

Pour la première mesure, les électrons du signal sont extraits à l'aide de la méthode du maximum de vraisemblance, en utilisant des techniques d'identification des particules. Ces techniques sont basées sur la présence d'un signal dans la première couche du trajectographe à pixels (B-layer), la fraction de coups au dessus du seuil le plus haut du trajectographe à radiation de transition (TRT), et le rapport entre l'énergie mesurée dans l'amas calorimétrique et l'impulsion de la trace. Ceci est nécessaire pour séparer le signal du bruit de fond dominant, constitu de hadrons

légers et de paires électron-positron provenant de conversion de photons. La section efficace différentielle est mesurée en fonction de l'impulsion transverse des électrons. La section efficace totale intégrée pour des électrons d'impulsion transverse comprise entre $7 < p_{\mathrm{T}} < 26$ GeV et de pseudorapidité $|\eta| < 2,0$ en excluant $1,37 < |\eta| < 1,52$ pour des électrons provenant de saveurs lourdes est de:

$$\sigma^{e}_{\mathrm{HF}} = 0,946 \pm 0,020_{(\mathrm{stat.})} \pm 0,146_{(\mathrm{syst.})} \pm 0,032_{(\mathrm{lumi.})}\,\mu\mathrm{b}.$$

Ce résultat est comparé avec des prédictions théoriques obtenues à partir de trois sources: avec un calcul fixé au deuxième ordre perturbatif (NLO) avec resommation des termes logarithmiques à l'ordre *next-to-leading log* (NLL), appelé `FONLL`; avec un générateur d'événements au premier ordre perturbatif (LO), `PYTHIA`; et avec un générateur d'événements au NLO, `POWHEG`. Pour la simulation de la cascade partonique dans les événements générés avec `POWHEG`, on peut associer soit `PYTHIA` soit `HERWIG`, ce qui produit des prédictions différentes pour la section efficace. Environ 50% de cette différence peut être attribué au traitement des désintégrations de hadrons de saveur lourde. Un bon accord est trouvé entre le résultat de la mesure obtenue avec des électrons et les prédictions théoriques générées par `FONLL` et `POWHEG`+`PYTHIA`, ainsi que par comparaison avec les résultats obtenus avec des muons.

L'étude sur le taux de production de hadrons B se désintégrant en électrons est basée sur le même ensemble de données que la mesure inclusive. L'impulsion transverse de l'électron par rapport à un jet de traces à proximité ($p_{\mathrm{T}}^{\mathrm{rel}}$) est utilisée pour différencier le signal du bruit de fond, composé de *charm*, de hadrons légers et de conversion de photons. Des coupures d'identification strictes sont appliquées pour obtenir un ensemble assez pur d'électrons dans le signal, avant d'extraire le taux de hadrons B en utilisant la méthode du maximum de vraisemblance sur la distribution de $p_{\mathrm{T}}^{\mathrm{rel}}$. Enfin, le spectre d'électrons provenant de hadrons B, en fonction de l'énergie transverse de l'électron reconstruit, E_{T}, est comparé avec des prédictions donées par des simulations Monte-Carlo aux ordres LO et NLO.

Contents

Introduction

Elementary particle physics is the study of the fundamental constituents of matter and their interactions, a subject of great interest ever since ancient Greek times, when Democritus postulated the existence of atoms, a fundamental unity of matter which could not be divided. In the XIX century, Dimitry Mendeleev classified all known elements into the periodic table, which hinted to the existence of some underlying structure. At the end of that century, the work of Marie and Pierre Curie investigating radioactivity allowed the indivisibility of the atom to be questioned for the first time. During the XX century, it was discovered that atoms are formed by a nucleus surrounded by orbiting electrons and that the atom could be split, as the atomic nucleus was formed by protons and neutrons, or even synthesised. Protons and neutrons were henceforth known as sub-atomic particles, which were bound together into nuclei by the strong nuclear force, postulated by Yukawa in the 1930s.

The theory of relativistic quantum mechanics, developed by Dirac, implied the existence of anti-particles, which have the same mass as the particle but opposite charge, and this was proved by the discovery of the positron. The muon was discovered through the study of cosmic rays, as was the pion, and during the mid-twentieth century various hadrons were discovered, which was known as the "particle zoo". It was not until the 1970s that a clearer picture of the model started emerging, where hadrons were explained as composite states made of quarks, held together by gluons, in a way that does not permit to observe quarks freely, but only bound in hadrons. The quantum field theories of electroweak interactions and quantum chromodynamics were developed almost in parallel. Observed particles were gradually accommodated into the model, and conversely sometimes predicted by the theory and subsequently observed, such as the W and Z bosons. A Lagrangian formalism was constructed, which gave an elegant set of rules via Feynman diagrams, but where singularities had to be carefully treated through renormalization techniques. The complete Standard Model (SM) of particle physics thus was born, proving to be extremely successful in describing the interactions of elementary particles.

In the present day, the experiments of the Large Hadron Collider (LHC) are at the forefront of research in particle physics, recording and analysing high-energy proton-proton (pp) collisions since December 2009. The ATLAS detector is one of the two general-purpose experiments of the LHC, designed to register and analyse the products of pp collisions in order to measure the outgoing particles created, looking for signatures of new physics and measuring established SM processes in an energy range never before attained in the laboratory. Chapter 1 gives a description of the ATLAS experiment at the LHC, including the main subdetectors.

Quantum chromodynamics (QCD), an important ingredient of the SM, is the theory of the strong interaction between quarks and gluons which make up hadrons (like the proton). Understanding QCD is thus essential for the analysis of any experimental data collected at the LHC, whether the aim is the discovery and study of a Higgs boson, a search for physics beyond the Standard Model such as supersymmetry or extra dimensions, or the precise measurement of well-known processes in a new energy regime. The study of heavy flavour production, i.e. the production of hadrons containing the heavy charm or bottom quarks, provides a powerful test of QCD at the LHC and is also of particular interest because these processes contribute an important background to many new physics searches. Inclusive lepton production can be used to constrain theoretical predictions for heavy-flavour (charm and bottom) production, which have large uncertainties [1, 2]. The decays of charm and bottom hadrons dominate the low transverse momentum (p_{T}) portion of inclusive electron and muon spectra. The charm and bottom production measurements in early LHC pp collision data at a centre-of-mass energy of 7 TeV give an interesting view of QCD in a region previously unexplored. Early experimental measurements of bottom production in $p\bar{p}$ collisions at the Tevatron appeared to be significantly larger than QCD calculations [3–6]; these discrepancies could be resolved only after improvements in the accuracy of both the experimental measurements [7, 8] and the theoretical predictions [1, 9–11] were made. Particularly for the theoretical predictions, the use of Next-to-Leading Order (NLO) calculations with Next-to-Leading Log (NLL) resummation theory applied consistently both to the matrix element calculation of the hard scattering process in $p\bar{p}$ collisions and to LEP data in order to extract the b-quark fragmentation function was a crucial step. The need to compare the theoretical predictions with experimental measurements of physical observables, as final state hadrons or lepton momenta, as opposed to unphysical quantities like the parent quark spectrum also emerged [1, 2, 10, 11]. On the experimental side, the extension to very low p_{T} b-quark production measurements by CDF [7] has shown good agreement with the fixed order QCD calculation in a region where the theoretical uncertainties related to fragmentation effects have very little relevance [11]. However, the Tevatron data were not sensitive to the p_{T} region where the deviation between the NLO and the NLO + NLL perturbative QCD (pQCD) calculations of the matrix elements becomes apparent. At the LHC, NLL resummation in the pQCD prediction for heavy-flavour production can be probed directly in hadron collisions for the first time.

Chapter 2 presents the theoretical framework of QCD, for which perturbative calculations are able to predict the production of heavy-flavour quarks. First, a summary of the SM of particle physics is given in Section 2.1, listing the known elementary particles of matter, fermions, and of interactions, gauge bosons. Quantum chromodynamics, the theory of strong interactions in the SM, and its features are described in Section 2.2. Section 2.3 gives a detailed account of the application of the perturbative QCD formalism in the predictions of heavy-flavour production in hadronic collisions, particularly for fixed-order NLO calculations with NLL resummation matching (the `FONLL` framework [9, 11]) and the fully exclusive event generators `POWHEG` (NLO) and `PYTHIA` (LO). To put these predictions in perspective, a summary of previous measurements for heavy-flavour production at hadron colliders is reported in Section 2.4.

The measurement of the inclusive electron cross-section with the ATLAS detector was published by the ATLAS Collaboration in 2011 [12], in a joint article with the inclusive muon measurement. The p_{T} spectrum of inclusive electrons is measured from a dataset of the first LHC *pp* collisions in 2010 recorded by the ATLAS experiment, with integrated luminosity $1.28 \pm 0.04\ \mathrm{pb}^{-1}$, in the kinematic acceptance region of $7 < p_{\mathrm{T}} < 26$ GeV and pseudorapidity $|\eta| < 2.0$, excluding the calorimeter transition region between barrel and end-cap, $1.37 < |\eta| < 1.52$. The spectrum of electrons from heavy-flavour decays is compared to the measured muon spectrum in the same kinematic region and to theoretical predictions of the lepton spectrum from heavy-flavour decays from LO and NLO Monte Carlo (MC) programmes, as well as a computation in fixed-order NLO with NLL resummation performed in the `FONLL` framework. The event selection, efficiency measurements, signal extraction, unfolding of the p_{T} spectrum and systematic uncertainties of this analysis are detailed in Chapter 3.

A natural extension of the inclusive electron study is the attempt to separate the contribution of B-hadrons to the signal, which is developed in full detail in Chapter 4. Using the transverse momentum of electrons relative to the axis of a nearby hadronic jet – $p_{\mathrm{T}}^{\mathrm{rel}}$– for non-isolated electron candidates, the $b \to B \to e$ component can be extracted via a binned maximum likelihood fit. This extraction is performed over the same collected dataset as the inclusive electron measurement. The result is presented as a distribution in transverse energy E_{T} and compared to MC simulations at LO and NLO, which include a full simulation of the detector response.

The personal contributions of the author to the analyses presented on this thesis are the following. In Chapter 2, the author produced the specialised MC samples and the studies of systematic effects such as the dependence on the decay tables, multiple-parton interactions and final state radiation in the signal heavy-flavour electrons.

The contributions to Chapter 3 were:

- Preparation of data and MC samples for the inclusive electron cross-section measurement and maintenance of the cutflow information webpage.
- Development of the algorithm that classifies the electrons in the MC history according to the primary hadron, used in order to assign the origin of true electrons in the simulation which allowed the evaluation of the efficiency for electrons from heavy-flavour decays and the predicted spectrum for these objects.
- Evaluation of the efficiencies and migration correction factors for electrons from heavy-flavour decays, needed for the unfolding of the electron spectrum, and the study of theoretical systematic uncertainties related to these quantities.
- Comparison of the predictions for efficiency and migration correction factors in different MC models; and between the primary hadron flavours in the main MC sample, particularly the difference in the response matrix of electrons from B or D hadrons due to nearby hadronic activity.
- The initial validation of different unfolding methods.

The work presented in Chapter 4 is mostly the personal contributions of the author for the development and execution of the measurement of electrons from B-hadron decays, including:

- Development of a tool to include the electron's impact parameter with respect to the primary vertex and their $p_{\mathrm{T}}^{\mathrm{rel}}$ with respect to nearby jets into the analysis files for data and simulated samples.
- Data preparation for the measurement of the production rate of electrons from B-hadron decays.

- The fitting code for the extraction of the electrons from B-hadron decays.
- Study of the systematic uncertainties of the production rate of electrons from B-hadrons.

The contributions to the ATLAS collaboration on the Trigger System were:

- As Trigger-Tier0 liaison from March 2009 to September 2010, responsible for the integration of the trigger software needed during offline reconstruction.
- As Trigger Offline Monitoring Expert from 2009 to 2011, assisting in the online reprocessing campaigns and overseeing the Trigger data-quality when on-call, and contributing with help and advice in issues concerning Trigger in offline software at any given time.

Chapter 1

The ATLAS Experiment

The ATLAS experiment (acronym of *A Toroidal Lhc ApparatuS*) at the LHC is one of the two general-purpose facilities that record LHC proton-proton collisions at CERN. The experiment's name originates from the toroidal magnets used in the muon spectrometer. One of the central goals of the ATLAS experiment is to study the SM of particle physics, in particular searching for the Higgs boson which is a missing cornerstone of the SM responsible for the spontaneous breaking of electroweak symmetry which give mass to gauge bosons W and Z. Through Yukawa interactions the Higgs boson also gives their masses to fermions [13–15]. Another goal of ATLAS is to search for new physics beyond the SM (BSM), such as Supersymmetry, extra-dimensions, or a fourth family of quarks or leptons [16].

This chapter presents the description of the ATLAS detector with its subsystems. First a brief explanation is given of the experimental setup of ATLAS in Section 1.1. The ATLAS coordinate system, its subdetectors and magnet systems are characterised in Section 1.2. A description of the ATLAS Trigger and Data Acquisition system follows in Section 1.3, including an account of the offline trigger monitoring and integration. Finally an overview of the reconstruction of events containing electrons is given in Section 1.4.

1.1 The Large Hadron Collider

The LHC is a two-ring-superconducting-hadron accelerator and collider installed in the tunnel that used to house the Large Electron Positron (LEP) collider. With 27 km of circumference and at a depth of approximately 100 m under the French-Swiss border near Geneva, it is designed to collide protons or lead ions [17]. The designed center-of-mass energy for proton-proton (pp) collisions is 14 TeV, i.e. 7 TeV per proton beam; however, for pp collisions during 2010 and 2011 the center-of-mass energy was 7 TeV and 8 TeV during 2012, as the LHC magnet system is being gradually commissioned for higher accelerating power. It is expected that the full design energy of 14 TeV for pp collisions will be attained after a long shut-down period, restarting in late 2014 when the energy per beam will begin at 6.5 TeV and then ramp-up to the goal of 7 TeV per beam [18]. The LHC has also successfully accelerated and collided lead ion beams in 2010 and 2011 at a center-of-mass energy of 2.76 TeV.

There are four interaction points in the LHC ring on which the four major experiments are centered: ATLAS, ALICE, LHCb and CMS, which are shown schematically in Figure 1.1. ATLAS and CMS are the two high-luminosity general-purpose experiments that study SM processes and search for the Higgs boson and for possible signals of BSM. At each interaction point the proton beams collide at a small crossing angle and the number of collisions per unit time per unit area is known as the instantaneous luminosity $\mathcal{L}$ which depends on the LHC running parameters [17]. The peak luminosity goal of the LHC machine for ATLAS and CMS is $\mathcal{L} = 10^{34}$ cm^{-2}s^{-1}, which has yet to be reached in 2012. The maximum instantaneous luminosity recorded by the ATLAS experiment was 2.1×10^{32} cm^{-2}s^{-1} in 2010 and 3.65×10^{33} cm^{-2}s^{-1} in 2011; which, integrated over time, gave a total $\int \mathcal{L}\mathrm{dt} = 45\,\mathrm{pb}^{-1}$ and $5.25\,\mathrm{fb}^{-1}$ of data collected by ATLAS in 2010 and 2011, respectively [19, 20]. Up to September 2012 collisions data-taking, the center-of-mass energy of proton-proton collisions is 8 TeV with a total integrated luminosity of $14\,\mathrm{fb}^{-1}$ and peak instantaneous luminosity of 7.7×10^{33} cm^{-2}s^{-1}.

1.2 The ATLAS subdetectors

The ATLAS experiment aims to measure all particles – except for neutrinos – emerging from the interaction point of the proton or heavy ion collisions over the maximum possible solid angle. For this purpose, it is equipped with a set of tracking detectors, calorimeters and muon detectors. Located closest to the beam axis are the tracking sub-detectors, called the Inner Detector (ID) as a group, comprising the Pixels, the Semiconductor Tracker (SCT) and the Transition Radiation Tracker (TRT). The ID is within a magnetic field generated by a superconducting solenoid and measures the momenta of charged particles originated in the event. Outside the solenoid, the next detector is the electromagnetic calorimeter, where electrons and photons are stopped

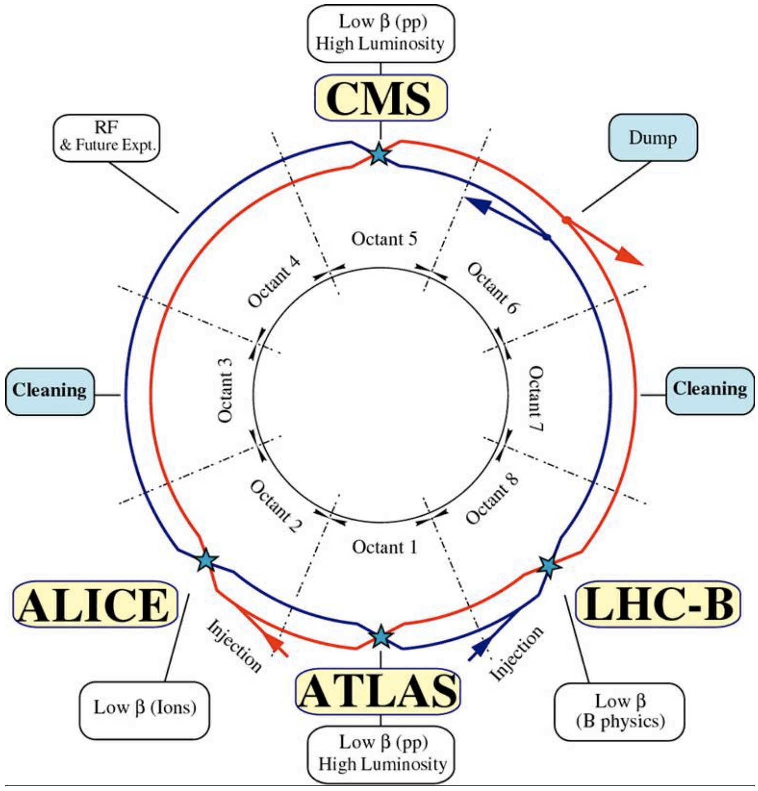

Figure 1.1: Diagram of the LHC, whose beams are shown in red and blue lines, and the four collision points for its main experiments: ATLAS, ALICE, LHCb and CMS, shown as the stars.

and their energies measured, using liquid Argon as active sampling material and copper as the absorber. The hadronic component of jets produced in the collisions will be stopped in the hadronic calorimeter, placed outside of the electromagnetic calorimeter and made of plastic scintillating tiles and steel in the central region of the detector and liquid argon in the forward region. The outermost of detectors are muon chambers that are placed within a toroidal magnetic field and form the muon spectrometer, where the momenta of the muons are measured before they escape the volume of the ATLAS detector. There are also a set of forward detectors placed close to the beam pipe and away from the interaction point, that attempt to cover most of the solid angle: LUCID, ALFA and the Zero-Degree Calorimeter (ZDC). The main function of the first two systems is to determine the luminosity delivered to ATLAS, while ZDC plays a key role in determining the centrality of heavy-ion collisions. Figure 1.2 shows the ATLAS detector in a cut-away view.

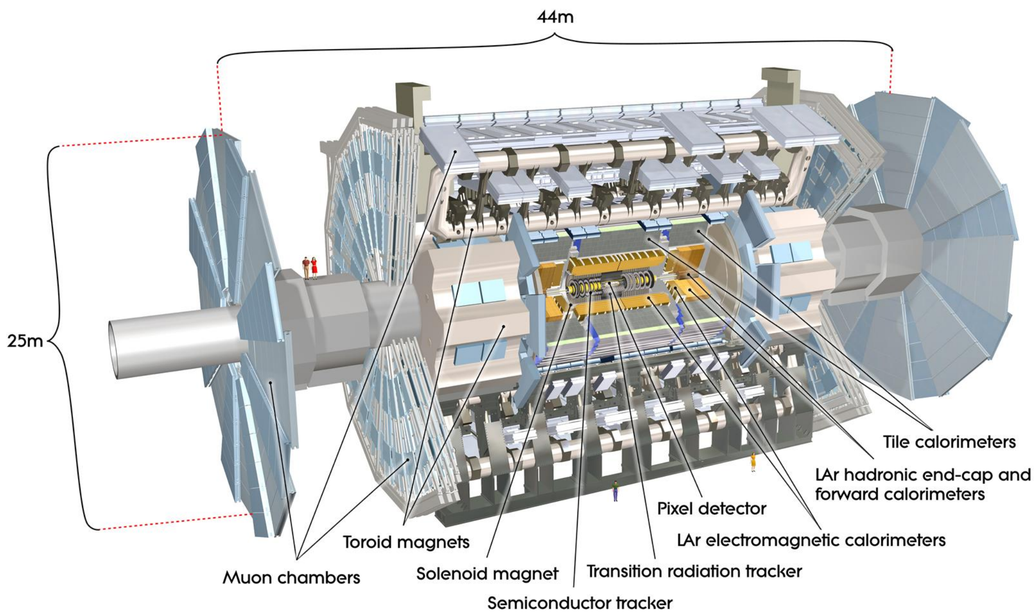

Figure 1.2: Cut-away view of the ATLAS detector with its components. The detector dimensions are 25 m in height and 44 m in length and it weights approximately 7000 tonnes.

1.2.1 Overview of the ATLAS Detector and Coordinate System

The nomenclature and system of coordinates used to describe the ATLAS detector and the particles coming from the hadron collisions are briefly summarised here. The nominal interaction point is defined as the origin of the coordinate system, while the direction of the beam defines the z-axis and the $x-y$ plane is transverse to the beam direction. The positive x-axis is defined as pointing from the origin to the centre of the LHC ring, and the positive y-axis is chosen to point upwards. The side-A of the detector is defined as that with positive z and side-C is that with negative z. The azimuthal angle ϕ is measured right-handedly around the beam axis, and the polar angle θ is the angle with respect to the beam axis. The pseudorapidity is defined as $\eta = -\ln\tan(\theta/2)$ The transverse momentum p_{T}, the transverse energy E_{T}, and the missing transverse energy $E_{\mathrm{T}}^{\mathrm{miss}}$ are defined in the $x-y$ plane. The distance ΔR in the pseudorapidity-azimuthal angle space is defined as $\Delta R = \sqrt{\Delta\eta^2 + \Delta\phi^2}$.

The ATLAS detector shown in Figure 1.2 has a cylindrical geometry which covers almost the entire solid angle around the nominal interaction point. Because of its cylindrical geometry, the detector components are described as being either part of the *barrel* when they are in the central region of pseudorapidity, or part of the *end-caps* when they are in the forward regions. The ATLAS detector is, by design, symmetric in the negative-positive z-axis.

The general requirements on LHC experiments are:

- The instrumentation electronics and sensor elements must be fast and withstand the high radiation in the experimental conditions of LHC collisions.
- High detector granularity is needed to handle the particle fluxes and to reduce the influence of overlapping events (pile-up).
- Large acceptance in pseudorapidity and full azimuthal coverage.
- Good charged-particle momentum resolution and track reconstruction efficiency.
- For offline identification of τ-leptons and b-jets, vertex detectors close to the interaction point are required to observe secondary vertices.
- Very good electromagnetic (EM) calorimetry for identification and measurements of electron and photon, complemented by full-coverage hadronic calorimetry to measure jet and missing transverse energy.
- Good muon identification and momentum resolution over a wide range of momenta and the ability to determine unambiguously the charge of high p_{T} muons.
- Highly efficient triggering on low p_{T} objects with sufficient background rejection, in order to achieve an acceptable trigger rate for most physics processes of interest, as well as good efficiency on high p_{T} triggers.

In order to meet these requirements, the performance of the components of ATLAS must match those listed in Table 1.1.

1.2.2 The Inner Detector

The ATLAS Inner Detector (ID) is designed to provide hermetic and robust pattern recognition, excellent momentum resolution and both primary and secondary vertex measurements for charged tracks above a 0.5 GeVand within the pseudorapidity range

Detector component	Required resolution	η coverage	
		Measurement	Trigger (L1)
Tracking	$\frac{\sigma_{p_T}}{p_T} = 0.05\%\, p_T \oplus 1\%$	± 2.5	–
Electromagnetic calorimetry	$\frac{\sigma_E}{E} = 10\%/\sqrt{E} \oplus 0.7\%$	± 3.2	± 2.5
Hadronic calorimetry:			
barrel and end-cap	$\frac{\sigma_E}{E} = 50\%/\sqrt{E} \oplus 3\%$	± 3.2	± 3.2
forward	$\frac{\sigma_E}{E} = 100\%/\sqrt{E} \oplus 10\%$	$3.1< \lvert\eta\rvert <4.9$	$3.1< \lvert\eta\rvert <4.9$
Muon spectrometer	$\frac{\sigma_{p_T}}{p_T} = 10\%$ at p_T=1TeV	± 2.7	± 2.4

Table 1.1: Requirements for the ATLAS detector components in order to reach the physics goals. The units for the energy and momenta are in GeV.

$|\eta| < 2.5$ [16]. It also provides electron identification over $|\eta| < 2.0$ and energies between 0.5 GeV and 150 GeV. This performance is required even at the highest luminosities expected from LHC collisions. The layout and dimensions of the main ID components are shown in Figure 1.3.

The ID is contained within the central solenoid, displayed in Figure 1.4(a). This solenoid is designed to provide a 2 T axial field at the center of the magnet at the nominal 7.730 kA operational current. In order to achieve the expected calorimeter performance the material thickness in front of the calorimeter was carefully optimised to be as low as possible, resulting in the solenoid assembly contributing a total of $\sim$0.66 radiation lengths at normal incidence [16]. The solenoid has an inner and outer diameter of 2.46 m and 2.56, respectively; and an axial length of 5.8 m. The flux is returned by the steel of the ATLAS hadronic calorimeter and its girder structure, shown in purple, green and light-blue in Figure 1.4(b). The magnetised steel on the tile calorimeter and solenoid flux-return girder, which surrounds the ID cavity, is predicted to modify the field by 4.1% at the geometrical centre of the coil. At nominal current, the total measured field is 1.998 T at the interaction point, and drops steeply from ~ 1.8 T at $z = 1.7$ m to ~ 0.9 T at the end of the ID cavity ($z = 2.9$ m).

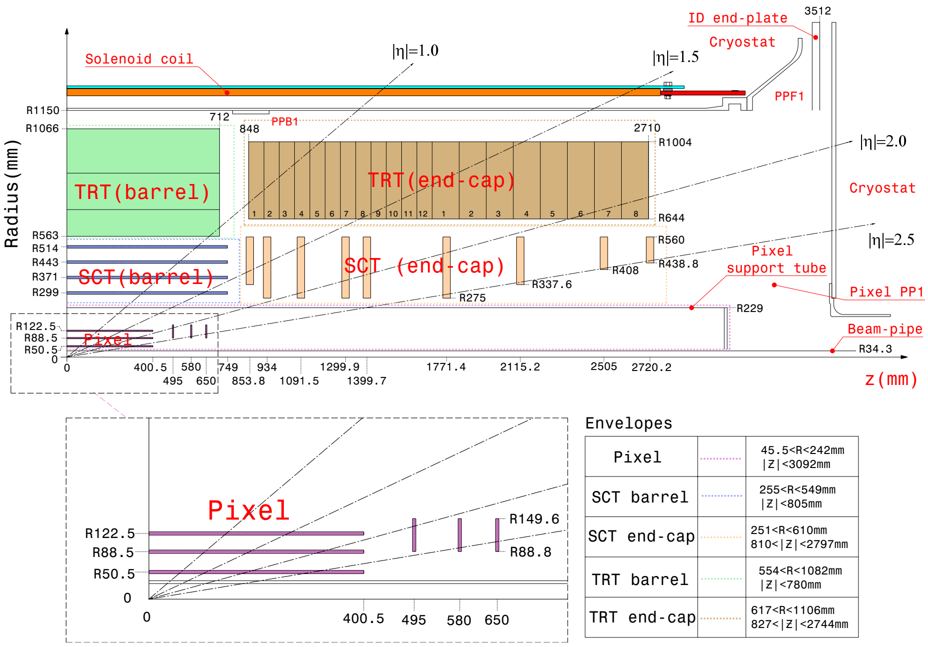

Figure 1.3: Plan view of a quarter-section of the ATLAS inner detector showing each of the major detector elements with its active dimensions and envelopes.

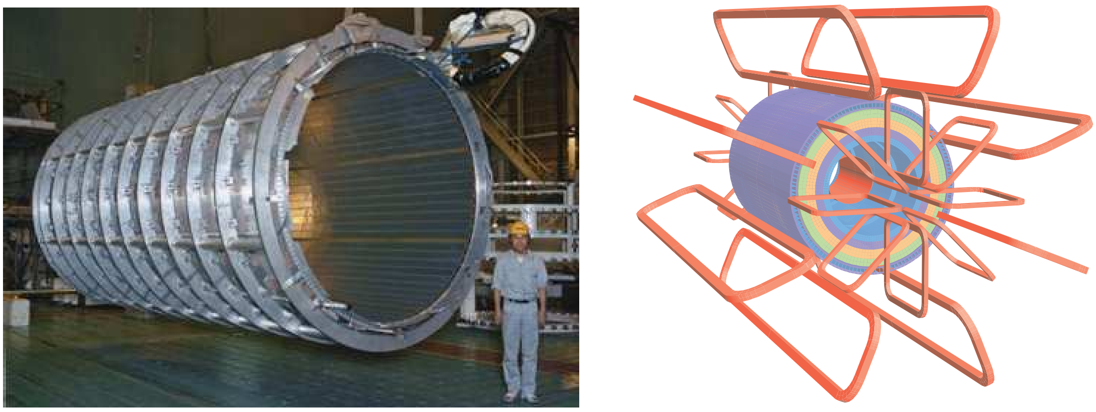

Figure 1.4: (b) Geometry of magnet windings and tile calorimeter steel. The eight barrel toroid coils with the end-cap coils interleaved are visible. The solenoid winding lies inside the calorimeter volume, here shown as the smallest red cylinder. (a) Bare central solenoid in the factory after completion of the coil winding.

The ID consists of three independent but complementary sub-detectors, the envelopes of each sub-detector are listed in Table 1.2. At inner radii, high-resolution pattern recognition capabilities are available using discrete space-points from silicon pixel layers and stereo pairs of silicon microstrip (SCT) layers. At larger radii, the transition radiation tracker (TRT) comprises many layers of gaseous straw tube elements interleaved with transition radiation material. With an average of 36 hits per track, it provides continuous tracking to enhance the pattern recognition and improve the momentum resolution over $|\eta| < 2.0$ and electron identification complementary to that of the calorimeter over a wide range of energies. Figure 1.5 shows a cut-away view of the inner detector.

Item		Radial extension (mm)	Length (mm)
Overall ID envelope		$0 < R < 1150$	$0 < \|z\| < 3512$
Beam-pipe		$29 < R < 36$	—
Pixel	Overall envelope	$45.5 < R < 242$	$0 < \|z\| < 3092$
3 cylindrical layers	Sensitive barrel	$50.5 < R < 122.5$	$0 < \|z\| < 400.5$
2×3 disks	Sensitive end-cap	$88.8 < R < 149.6$	$495 < \|z\| < 650$
SCT	Overall envelope	$255 < R < 549$ (barrel)	$0 < \|z\| < 805$
		$251 < R < 610$ (end-cap)	$810 < \|z\| < 2797$
4 cylindrical layers	Sensitive barrel	$299 < R < 514$	$0 < \|z\| < 749$
2×9 disks	Sensitive end-cap	$275 < R < 560$	$839 < \|z\| < 2735$
TRT	Overall envelope	$554 < R < 1082$ (barrel)	$0 < \|z\| < 780$
		$617 < R < 1106$ (end-cap)	$827 < \|z\| < 2744$
73 straw planes	Sensitive barrel	$563 < R < 1066$	$0 < \|z\| < 712$
160 straw planes	Sensitive end-cap	$644 < R < 1004$	$848 < \|z\| < 2710$

Table 1.2: Main parameters of the Inner Detector system.

1.2.2.1 Pixels

The precision tracking detectors (pixels and SCT) cover the region $|\eta| < 2.5$. In the barrel region, they are arranged on concentric cylinders around the beam axis while in the end-cap regions they are located on disks perpendicular to the beam axis. The highest granularity is achieved around the vertex region using silicon pixel detectors.

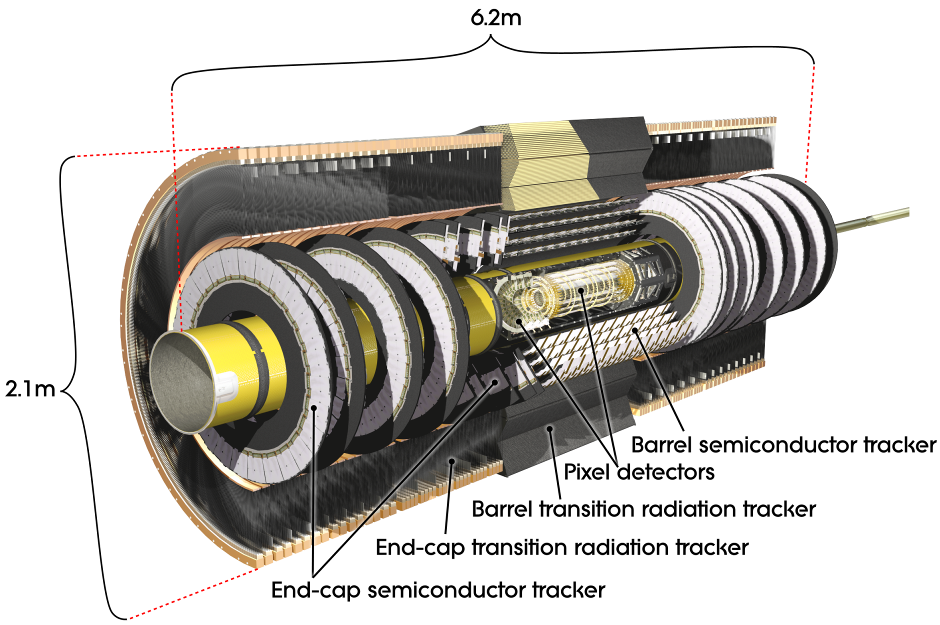

Figure 1.5: View of the Inner detector.

The pixel layers are segmented in R–ϕ and z with typically three pixel layers crossed by each track.

All pixel sensors are identical and have a minimum pixel size in R–ϕ $\times$ z of 50 $\times$ 400 μm^2 . The intrinsic spatial resolutions in the barrel are 10 μm (R–ϕ) and 115 μm (z) and in the disks are 10 μm (R–ϕ) and 115 μm (R). The pixel detector has approximately 80.4 million readout channels.

1.2.2.2 Semi-Conductor Tracker

For the SCT, eight strip layers, giving four space points, are crossed by each track. In the barrel region, this detector uses small-angle (40 mrad) stereo strips to measure both coordinates, with one set of strips in each layer parallel to the beam direction, measuring R–ϕ . They consist of two 6.4 cm long daisy-chained sensors with a strip pitch of 80μm. In the end-cap region, the detectors have a set of strips running radially and a set of stereo strips at an angle of 40 mrad. The mean pitch of the strips is also approximately 80μm. The intrinsic accuracies per module in the barrel are 17μm for R–ϕ and 580μm for z; and in the disks are 17μm for R–ϕ and 580μm R. The total number of readout channels in the SCT is approximately 6.3 million.

Figure 1.6 shows the photograph and a drawing of a barrel SCT module. The four sensors of a module, two each on the top and bottom side, are rotated with respect to their hybrid readout boards by ±20 mrad around the geometrical centre of the sensors.

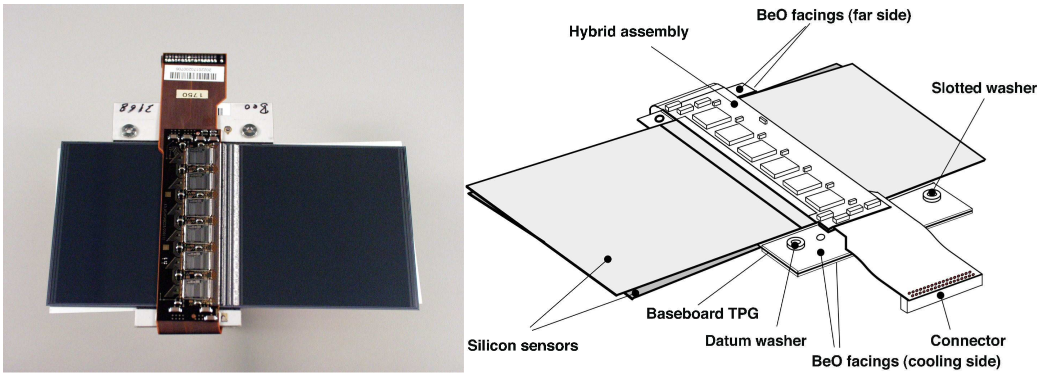

(a) (b)

Figure 1.6: (a)Photograph and (b) drawing of a barrel SCT module, showing its components. The thermal pyrolytic graphite (TPG) base-board provides a high thermal conductivity path between the coolant and the sensors.

1.2.2.3 Transition Radiation Tracker

The 4 mm diameter polyimide straw tubes of the TRT provide a high number of hits –typically 36 per track– which enables track-following up to $|\eta| = 2.0$. The TRT only provides R–ϕ information, for which it has an intrinsic accuracy of 130μm per straw. In the barrel region, the straws are parallel to the beam axis and are 144 cm long, with their wires divided into two halves, approximately at $\eta = 0$. In the end-cap region, the 37 cm long straws are arranged radially in wheels. The total number of TRT readout channels is approximately 351,000. In addition to contributing to the measurement of track momentum, the TRT enhances the electron identification capabilities by the detection of transition-radiation photons in the xenon-based gas mixture of the straw tubes.

The polyimide drift tubes –or straws– are the basic TRT detector elements. The straw tube wall, especially developed to have good electrical and mechanical properties with minimal wall thickness, is made of two 35μm thick multi-layer films bonded back-to-back. The bare material, a 25μm thick polyimide film, is coated on one side with a 0.2μm Al layer which is protected by a 5–6 μm thick graphite-polyimide layer. The other side of the film is coated by a 5μm polyurethane layer used to heat-seal the two films back-to-back.

Transition radiation (TR) is emitted when a highly relativistic charged particle with a Lorentz factor $\gamma \gtrsim 10^3$ traverses boundaries between materials of different dielectric constants [21]. Low-energy TR photons are absorbed in the Xe-based gas mixture, and yield much larger signal amplitudes than minimum-ionising charged particles. The distinction between TR and tracking signals is obtained on a straw-by-straw basis using separate low and high thresholds in the front-end electronics. The fraction of high-threshold hits in a track can be exploited for particle identification [22].

1.2.2.4 Tracking and Vertexing Performance

Figure 1.7 shows the sensors and structural elements traversed by a charged track of $p_{\mathrm{T}} = 10$ GeV in the barrel ID ($\eta = 0.3$). The track traverses successively the beryllium beam-pipe, the three cylindrical silicon-pixel layers with individual sensor elements of $50{\times}400$ μm^2, the four cylindrical double layers of barrel SCT sensors of pitch 80 μm –one axial and one with a stereo angle of 40 mrad– and approximately 36 axial straws of 4 mm diameter contained in the barrel transition-radiation tracker modules within their support structure.

Figure 1.8 shows the sensors and structural elements traversed by two charged tracks of $p_{\mathrm{T}} = 10$ GeV in the end-cap ID, at $\eta = 1.4$ and 2.2. The end-cap track at $\eta = 1.4$ traverses successively the beryllium beam-pipe, the three cylindrical silicon-pixel layers, four of the disks with double layers of end-cap SCT sensors, and approximately 40 straws in the end-cap transition radiation tracker wheels. In contrast, the end-cap track at $\eta = 2.2$ traverses only the first of the cylindrical silicon-pixel layers, two end-cap pixel disks and the last four disks of the end-cap SCT. The coverage of the end-cap TRT does not extend beyond $|\eta| = 2$.

The position of the individual detector elements of the ID after assembly is known with less precision than their intrinsic resolution. Therefore, in order to fully exploit their excellent spatial resolution, an alignment procedure has to be applied to accurately determine their position and orientation, with a precision better than $\sim 10\mu$m [23].

The quality of the alignment can be checked by the study of the residuals, which are defined as the measured hit position minus that expected from the track extrapolation [24]. The initial alignment used in the first months of 2010 data-taking was

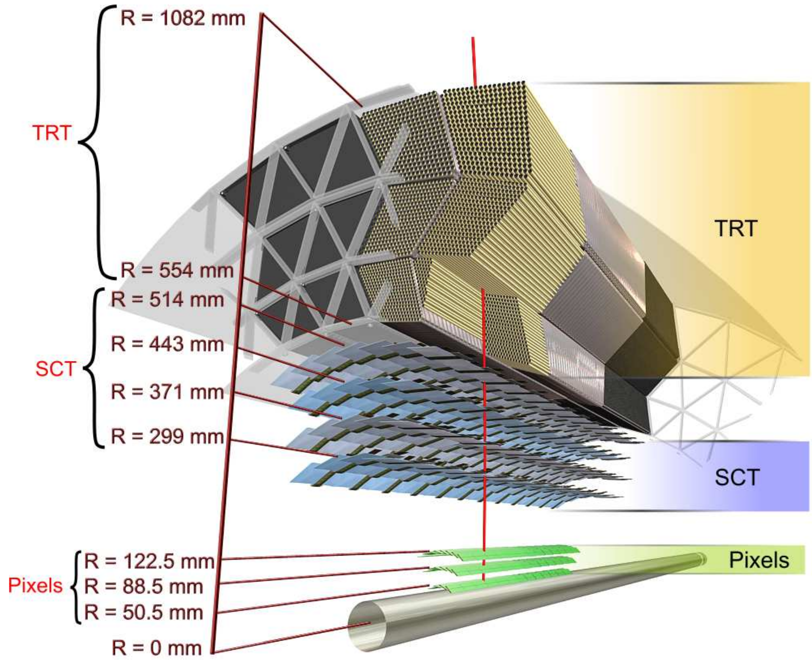

Figure 1.7: Schematic view of a charged track of η =0.3 and p_{T} of 10 GeV crossing the pixel, SCT and TRT layers in the barrel region.

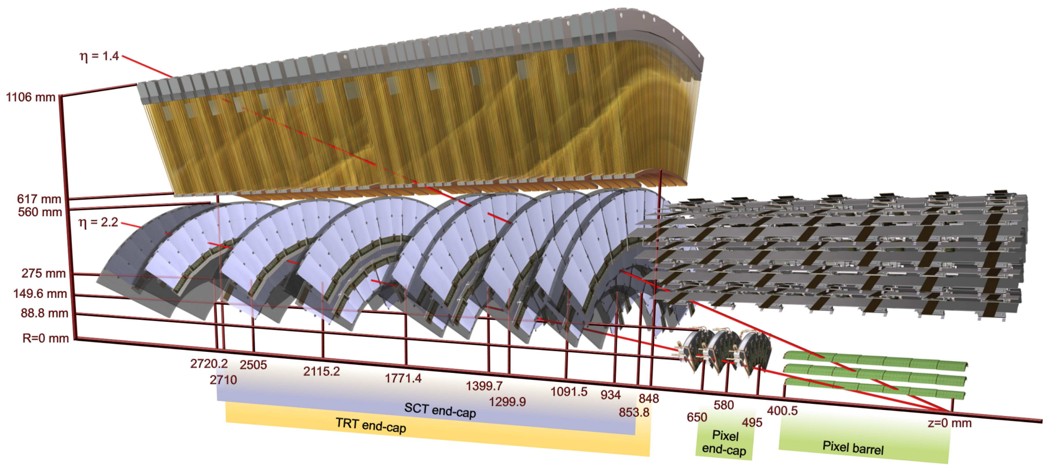

Figure 1.8: Schematic view of two charged tracks with $p_{\mathrm{T}}$of 10 GeVand η = 1.4 and 2.2, crossing different layers of the pixel, SCT and TRT (only up to $|\eta|$ =2.0) end-caps.

determined using a small sample of relatively low transverse momenta tracks from $\sqrt{s} = 900$ GeV proton-proton collisions collected in December 2009. The improved alignment was obtained using a larger sample of collision tracks at $\sqrt{s} = 7$ GeV with higher momenta ($p_{\mathrm{T}} > 9$GeV) and cosmic-ray tracks with $p_{\mathrm{T}} > 2$ GeV, applying an iterative procedure in three levels and with thousands of degrees of freedom [23]. Figure 1.9 shows, as an example, the comparison of the unbiased residual distributions in x for the pixel, SCT and TRT barrel with the initial 2010 alignment on the left column and with the improved alignment performed with 2010 data on the right column. The agreement with the perfect alignment MC improves greatly as the width of the gaussians are reduced for data, with better alignment precision [23].

Reconstructed charged-particle tracks in the ID are the basis of the interaction vertex reconstruction in ATLAS. The primary vertex (PV) reconstruction is pursued in two steps: first the primary vertex finding algorithm, dedicated to associate reconstructed tracks to the vertex candidates; second the vertex fitting algorithm, dedicated to reconstruct the vertex position and its error matrix, which also refits the tracks associated to the PV, constraining them to originate from the reconstructed interaction point [25]. Reconstructed tracks selected for the primary vertex reconstruction must fulfill the following quality requirements: $p_{\mathrm{T}} > 150$ MeV; transverse impact parameter $|d_0| < 4$ mm with respect to the centre of the luminous region (beam-spot), with an associated error $\sigma(d_0) < 5$ mm; the uncertainty on the longitudinal impact parameter $\sigma(z_0) < 10$ mm; and at least 6 hits in the pixel and SCT detectors, with at least 4 hist in the SCT. Using these preselected tracks, an *Iterative Vertex Finding* algorithm is applied [25], starting from a vertex seed found by looking for the global maximum in the distribution of z coordinates of the tracks at the point of closest approach to the beam-spot center. The parameters of the beam-spot [26] are used both during the finding to preselect compatible tracks and during the fitting step to constrain the vertex fit. Figure 1.10(a) shows the distribution in the transverse plane $(x - y)$ of the reconstructed primary vertices in data, where it can be seen that the center of the distribution is pulled towards the position of the beam-spot, which can vary from fill to fill. Figure 1.10(b) shows the dependence of the vertex position resolution in the x-coordinate on the number of fitted tracks. The resolution can be evaluated as well as a function of the sum of the square of the transverse momenta of the tracks belonging to the primary vertex ($\sum_{trk} p_{\mathrm{T}}^2$). For events with 70 tracks or $\sum_{trk} p_{\mathrm{T}}^2$ over 8 GeV the resolution has been measured to be about 30 μm in the transverse plane and about 50 μm in the longitudinal direction, as evaluated with about 6 nb^{-1} of collisions recorded during 2010 data-taking [25].

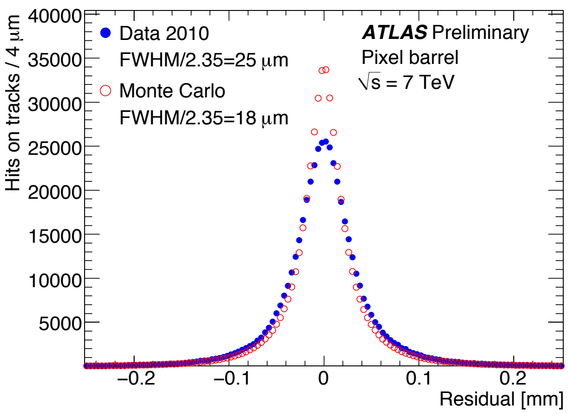

(a)

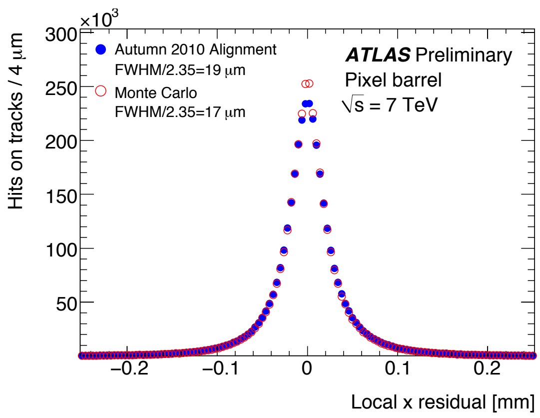

(b)

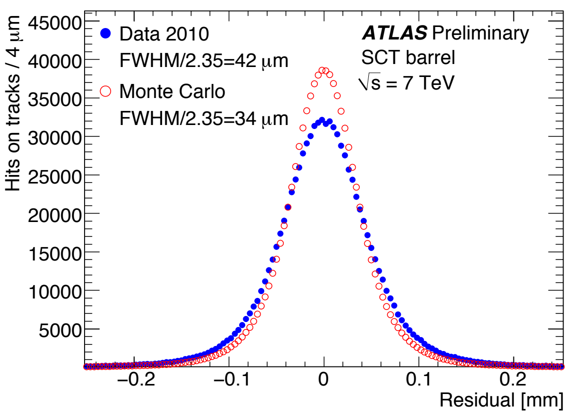

(c)

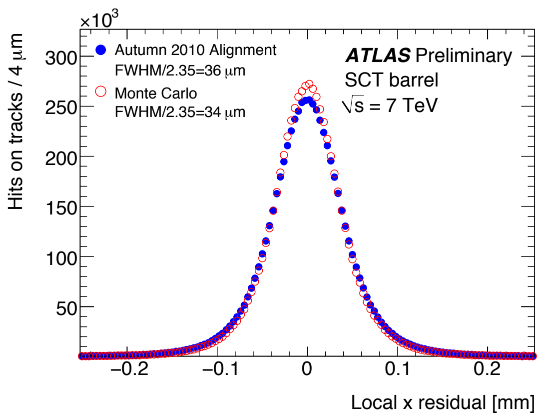

(d)

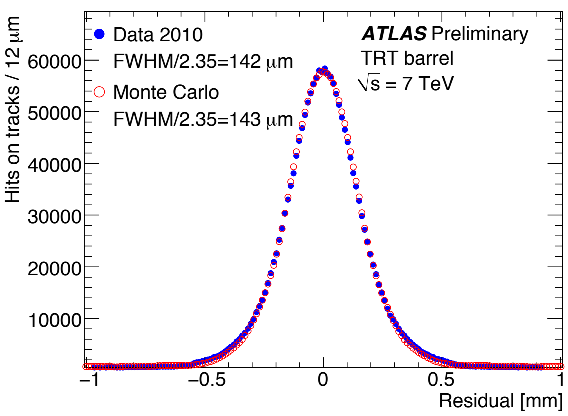

(e)

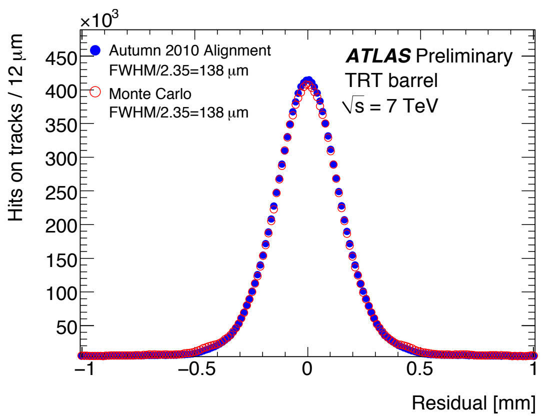

(f)

Figure 1.9: Unbiased residual distributions in x, integrated over all hits-on-tracks in in the pixel (top), the SCT (middle) and the TRT (bottom) barrel for the MC with perfect alignment (red) and for $\sqrt{s} = 7$ TeV collision data taken in 2010 (blue), on the left column with initial ID alignment and on the right with improved conditions, derived from a large sample of collisions and cosmic tracks. The MC distributions are normalised to the number of entries in the data.

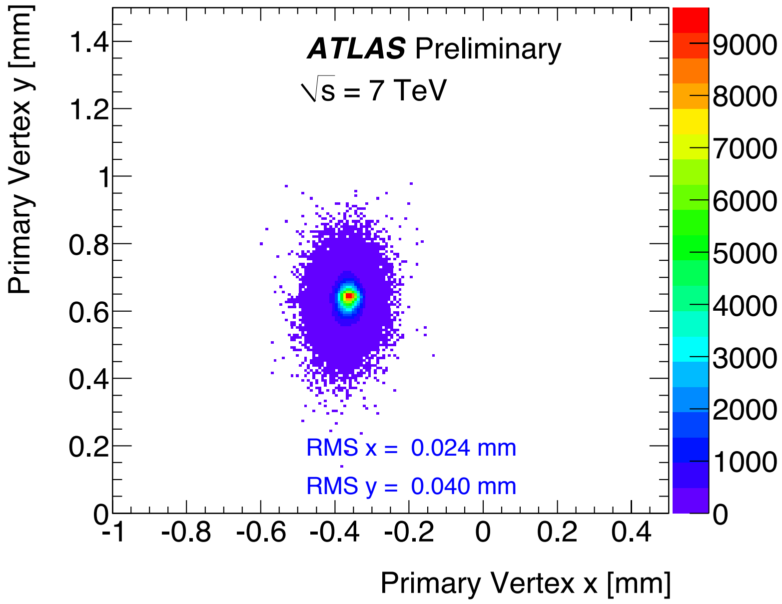

(a)

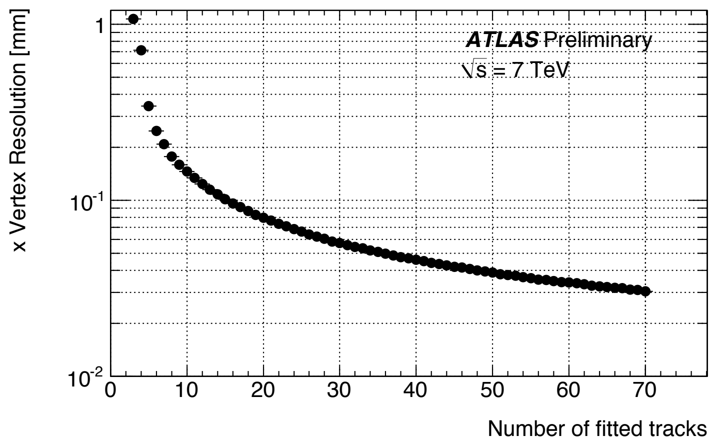

(b)

Figure 1.10: (a) Two-dimensional distribution of reconstructed primary vertices in $\sqrt{s} = 7$ TeV data, in the $x - y$ plane. (b) Estimated vertex resolution in the x coordinate from data as a function of the number of tracks.

1.2.3 The Calorimeters

The ATLAS calorimeters consist of a number of sampling detectors with full ϕ-symmetry and coverage around the beam axis. The calorimeters closest to the beam-line are housed in three cryostats, one barrel and two end-caps. The barrel cryostat contains the electromagnetic barrel calorimeter, whereas the two end-cap cryostats each contain an electromagnetic end-cap calorimeter (EMEC), a hadronic end-cap calorimeter (HEC), located behind the EMEC, and a forward calorimeter (FCal) to cover the region closest to the beam. All these calorimeters use liquid argon as the active detector medium; liquid argon has been chosen for its intrinsic linear behaviour, its stability of response over time and its intrinsic radiation-hardness.

The precision electromagnetic calorimeters are lead-liquid argon detectors with accordion shape absorbers and electrodes. This geometry allows the calorimeters to have several active layers in depth, three in the precision-measurement region ($0< |\eta| <2.5$) and two in the higher-η region ($2.5< |\eta| <3.2$) and in the overlap region between the barrel and the EMEC. An accurate position measurement in the precision-measurement region is obtained by finely segmenting the first layer in η. The direction of photons in η is determined by the position of the photon cluster in the first and the second layers. The FCal provides additional electromagnetic coverage at higher η, in the range $3.1< |\eta| <4.9$. Furthermore in the central region, $0< |\eta| <1.8$, the electromagnetic calorimeters are complemented by presamplers, an instrumented argon layer, which provides a measurement of the energy lost in front of the electromagnetic calorimeters.

For the outer hadronic calorimeter, the sampling medium consists of scintillator tiles and the absorber medium is steel. The tile calorimeter is composed of three parts, one central barrel and two extended barrels, which together cover the range $0< |\eta| <1.7$. The hadronic calorimetry is extended to larger pseudorapidities by the HEC, a copper/liquid-argon detector, and the FCal, a copper-tungsten/liquid-argon detector. The hadronic calorimetry thus reaches one of its main design goals, namely coverage over $|\eta| < 4.9$. A cut-away view of the calorimeters of ATLAS is shown in Figure 1.11.

1.2.3.1 Liquid-Argon Electromagnetic Calorimeter

An accordion geometry has been chosen for the absorbers and the electrodes of the barrel and end-cap electromagnetic calorimeters. Such a geometry provides naturally a full coverage in ϕ without any cracks, and a fast extraction of the signal at the rear

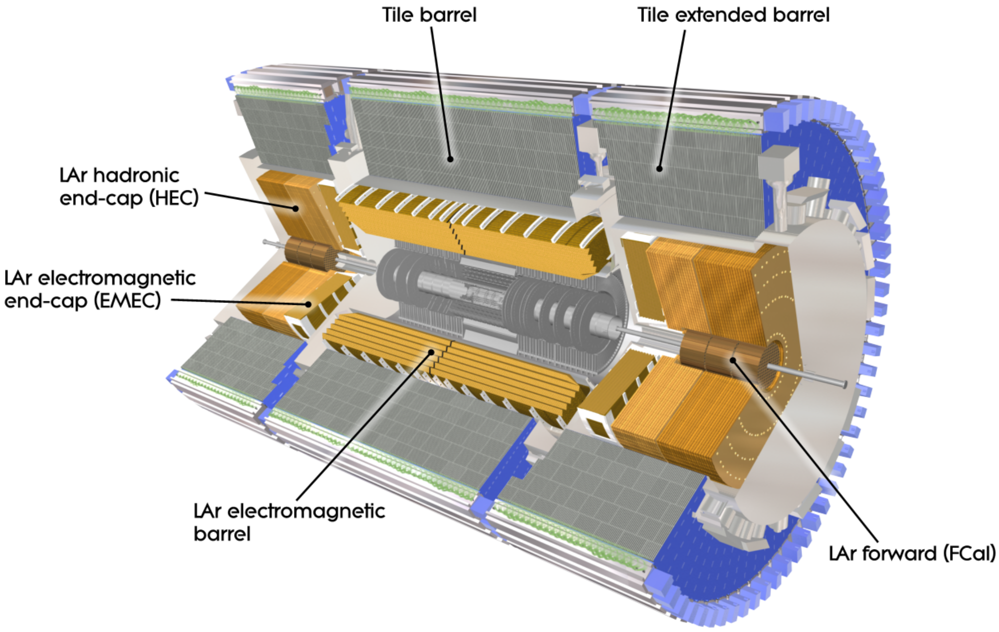

Figure 1.11: View of the calorimeters.

or at the front of the electrodes. In the barrel, the accordion waves are radial and run in ϕ , and the folding angles of the waves vary with radius to keep the liquid-argon gap constant. In the end-caps, the waves are parallel to the z-axis and run with the azimuthal angle. Since the liquid-argon gap increases with radius in the end-caps, the wave amplitude and the folding angle of the absorbers and electrodes vary with radius. All these features of the accordion geometry lead to a very uniform performance in terms of linearity and resolution as a function of ϕ. The first layer is finely segmented along η, as for example in the barrel where there are eight strips in front of a middle cell. One can note however the coarser granularity of the first layer in the edge zones of the barrel and end-caps, as explicitly given in Table 1.3. The second layer collects the largest fraction of the energy of the electromagnetic shower, and the third layer collects only the tail of the electromagnetic shower and is therefore less segmented in η.

The absorbers are made of lead plates with a thickness of 1.53mm for $|\eta| < 0.8$ and 1.13mm for $|\eta| > 0.8$. The change in lead thickness at $|\eta| = 0.8$ limits the decrease of the sampling fraction as $|\eta|$ increases. In the end-cap calorimeters, the plates have a thickness of 1.7mm for $|\eta| < 2.5$ and 2.2mm for $|\eta| >2.5$.

EM calorimeter				
	Barrel		End-cap	
Number of layers and $\lvert\eta\rvert$ coverage				
Presampler	1	$\lvert\eta\rvert < 1.52$	1	$1.5 < \lvert\eta\rvert < 1.8$
Calorimeter	3	$\lvert\eta\rvert < 1.35$	2	$1.35 < \lvert\eta\rvert < 1.475$
	2	$1.375 < \lvert\eta\rvert < 1.50$	3	$1.5 < \lvert\eta\rvert < 2.5$
			2	$2.5 < \lvert\eta\rvert < 3.2$
Granularity $\Delta\eta \times \Delta\phi$ versus $\lvert\eta\rvert$				
Presampler	0.025×0.1	$\lvert\eta\rvert < 1.52$	0.025×0.1	$1.5 < \lvert\eta\rvert < 1.8$
Calorimeter 1^{st} layer	$0.025/8 \times 0.1$	$\lvert\eta\rvert < 1.40$	0.050×0.1	$1.375 < \lvert\eta\rvert < 1.425$
	0.025×0.025	$1.40 < \lvert\eta\rvert < 1.475$	0.025×0.1	$1.425 < \lvert\eta\rvert < 1.5$
			$0.025/8 \times 0.1$	$1.5 < \lvert\eta\rvert < 1.8$
			$0.025/6 \times 0.1$	$1.8 < \lvert\eta\rvert < 2.0$
			$0.025/4 \times 0.1$	$2.0 < \lvert\eta\rvert < 2.4$
			0.025×0.1	$2.4 < \lvert\eta\rvert < 2.5$
			0.1×0.1	$2.5 < \lvert\eta\rvert < 3.2$
Calorimeter 2^{nd} layer	0.025×0.025	$\lvert\eta\rvert < 1.40$	0.050×0.025	$1.375 < \lvert\eta\rvert < 1.425$
	0.075×0.025	$1.40 < \lvert\eta\rvert < 1.475$	0.025×0.025	$1.425 < \lvert\eta\rvert < 2.5$
			0.1×0.1	$2.5 < \lvert\eta\rvert < 3.2$
Calorimeter 3^{rd} layer	0.050×0.025	$\lvert\eta\rvert < 1.35$	0.050×0.025	$1.5 < \lvert\eta\rvert < 2.5$
Number of readout channels				
Presampler	7808		1536 (both sides)	
Calorimeter	101760		62208 (both sides)	

Table 1.3: Main parameters of the Liquid-Argon Electromagnetic calorimeter.

The readout electrodes are located in the gaps between the absorbers and consist of three conductive copper layers separated by insulating polyimide sheets. The two outer layers are at the high-voltage potential and the inner one is used for reading out the signal via capacitive coupling. The segmentation of the calorimeter in η and in depth is obtained by etched patterns on the different layers, as shown in Figure 1.12. The ϕ-segmentation is obtained by ganging together the appropriate number of electrodes. Each barrel gap between two absorbers is equipped with two electrodes, one type for $|\eta| < 0.8$ and another for $|\eta| > 0.8$. Similarly, each end-cap gap between two absorbers is equipped with one type of electrode for $|\eta| < 2.5$ and with another for $|\eta| > 2.5$.

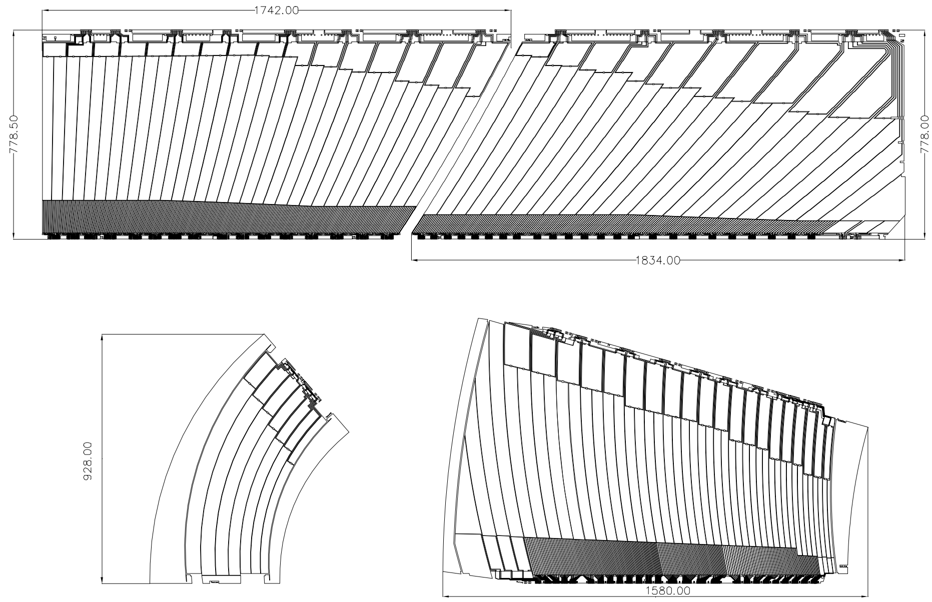

Figure 1.12: Layout of the four different types of electrodes –in the signal layer– before folding into the accordion shape between the absorbers. The two top electrodes are for the barrel and the two bottom electrodes are for the end-cap inner (left) and outer (right) wheels. The drawings are all at the same scale, with the dimensions in mm, and the two or three different layers in depth with different granularity are clearly visible.

The barrel electromagnetic calorimeter is made of two half-barrels, centred around the z- axis. One half-barrel covers the region of positive z ($0 < \eta < 1.475$) and the other one the region of negative z ($-1.475 < \eta < 0$). The length of each half-barrel is 3.2 m, their inner and outer diameters are 2.8 m and 4 m respectively, and each half-barrel weighs 57 tonnes. Each half-barrel is made of 1024 accordion-shaped absorbers, interleaved with readout electrodes. The size of the drift gap on each side of the electrode is 2.1 mm, which corresponds to a total drift time of about 450 ns for an operating voltage of 2000 V. Once assembled, a half-barrel presents no discontinuity along the azimuthal angle ϕ; however, in order to facilitate construction, each half-barrel has been divided into 16 modules, each covering a $\Delta\phi = 22.5°$. The total thickness of a module is at least 22 radiation lengths (X_0) at $|\eta| = 0$, increasing to 30 X_0 at $|\eta| = 0.8$, and ranging from 24 X_0 at $|\eta| = 0.8$ to 33 X_0 at $|\eta| = 1.3$. The design of a barrel module of the LAr electromagnetic calorimeter is shown in Figure 1.13.

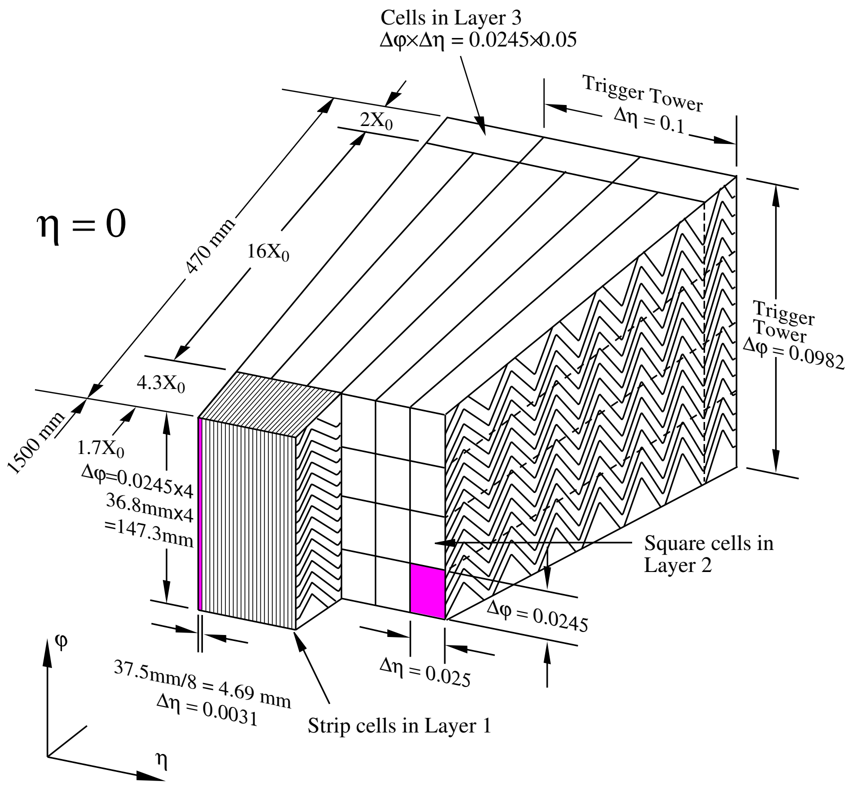

Figure 1.13: Sketch of a barrel module where the different layers are clearly visible with the ganging of electrodes in phi. The granularity in eta and phi of the cells of each of the three layers and of the trigger towers is also shown.

A module, as depicted in Figures 1.13 and 1.14(a), has three layers in depth: front, middle and back –as viewed from the interaction point. The front layer is read out at the low-radius side of the electrode, whereas the middle and back layers are read out at the high-radius side of the electrode. The readout granularity of the different layers is detailed in Table 1.3 and can be seen in in the electrode layout in Figure 1.12. In total, including the presampler cells, there are 3424 readout cells per module.

The presampler is a separate thin liquid-argon layer, 11 mm in depth, which provides shower sampling in front of the active electromagnetic calorimeter and inside the barrel cryostat. This presampler layer is made of 64 identical azimuthal sectors –32 per half-barrel. Each sector is 3.1 m long and 0.28 m wide, thus covering the half-barrel length and providing a coverage in $\Delta\eta \times \Delta\phi$ of 1.52 × 0.2. It is composed of eight modules of different size, whose length increases with $|\eta|$ to obtain a constant η-granularity of $\Delta\eta = 0.2$ for each module, except for the module at the end of the barrel, for which the η-coverage is reduced to 0.12. The presampler modules are made of interleaved cathode and anode electrodes glued between glass-fibre composite plates. The electrode spacing varies slightly, from 1.9 to 2.0 mm according to the presampler module type. The cathodes are double-sided printed-circuit boards while the anodes have three conductive layers separated by glass-fibre composite layers. The required segmentation, $\Delta\eta \sim 0.025$ and $\Delta\phi = 0.1$, for each module is obtained by ganging the appropriate number of anodes in the η direction and by etching each anode into two halves in the ϕ-direction. A high voltage potential of +2 kV is applied to the outer layers of the anodes and the signal is read out through capacitive coupling to the central layer at ground potential.

The electromagnetic end-cap (EMEC) calorimeters consist of two wheels, one on each side of the electromagnetic barrel. Each wheel is 63 cm thick and weighs 27 tonnes, with external and internal radii at ambient temperature of 2098 mm and 330 mm, respectively. It covers the region $1.375 < |\eta| < 3.2$. In the transition region between the barrel and the end-cap calorimeters, the material in front of the calorimeter amounts to several radiation lengths.In order to improve the energy measurement in this region, a liquid-argon presampler is implemented in front of the end-cap calorimeter, covering the range $1.5 < |\eta| < 1.8$. Each end-cap calorimeter consists itself of two co-axial wheels. The boundary between the inner and the outer wheel, which is 3 mm wide and located at $|\eta| = 2.5$, is mostly filled with low-density material. This boundary is approximately projective and matches the acceptance of the inner detector. Each end-cap wheel is further divided into eight wedge-shaped modules without introducing any discontinuity along the azimuthal angle owing to the accordion geometry. A view of a module is shown in Figure 1.14(b). Each end-cap contains 768 absorbers interleaved with readout electrodes in the outer wheel and 256 absorbers in the inner wheel. The thickness increases from 24 to 38 X_0 as $|\eta|$ increases from 1.475 to 2.5 for the outer wheel; and from 26 to 36 X_0 as $|\eta|$ increases from 2.5 to 3.2 for the inner wheel.

In the outer wheel, signals from the different pads are read out from both sides of the electrode, as in the case of the barrel electromagnetic calorimeter. In the inner wheel, because of the higher radiation levels, the signals are all read out from the back side. Similarly to the barrel electromagnetic calorimeter, the precision region in the end-cap electromagnetic calorimeters ($1.5 < |\eta| < 2.5$) is divided in depth into three longitudinal layers. The front layer, about 4.4 X_0 thick, is segmented

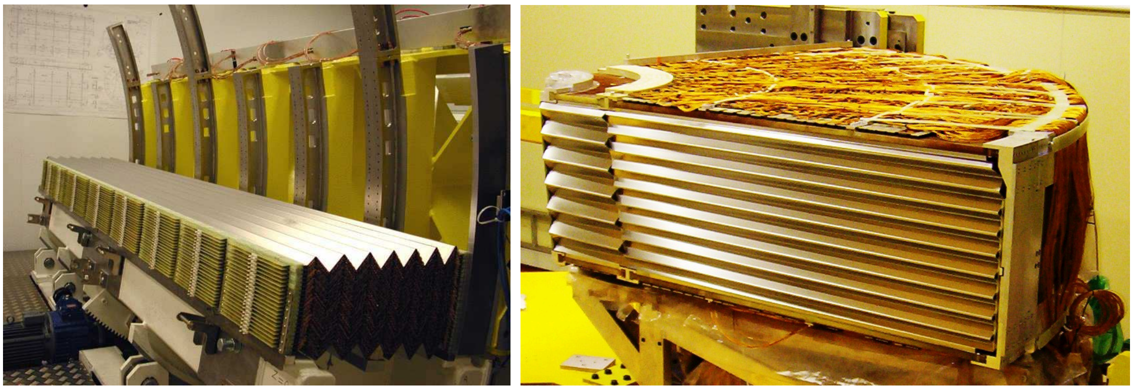

(a) (b)

Figure 1.14: Photograph of (a) a partly stacked barrel electromagnetic LAr module and (b) a side view of an electromagnetic end-cap LAr module.

with strips along the η direction. The transverse size of the projective cell in the middle layer is the same as defined in the barrel electromagnetic calorimeter, $\Delta\eta \times \Delta\phi = 0.025 \times 0.025$. The back layer has a twice coarser granularity in η . The outermost region $|\eta| < 1.5$ of the outer wheel and the inner wheel ($2.5 < |\eta| < 3.2$) are segmented in only two longitudinal layers and have a coarser transverse granularity. Table 1.3 summarises the longitudinal and transverse readout granularities of the electromagnetic end-cap calorimeter as a function of $|\eta|$. The η-granularity in the front layer varies with pseudorapidity in order to keep the copper strip width larger than a few mm as specified in Table 1.3. The ϕ-granularity is obtained by ganging the signals from adjacent electrodes. Each module contains 3984 readout channels, including the 96 channels in the presampler. Each end-cap presampler consists of 32 identical azimuthal sectors or modules. These are placed in a 5 mm deep cavity in the back of the cryostat cold wall. The granularity of the presampler is $\Delta\eta \times \Delta\phi = 0.025\times0.1$. One end-cap presampler module consists of two, 2 mm thick, active liquid argon layers, formed by three electrodes parallel to the front face of the EMEC calorimeter. A negative high voltage is applied to the external electrodes and the signals are read out from the central electrode which is segmented into pads. The same signal, calibration and high-voltage cables as for the end-cap calorimeter are used.

1.2.3.2 Scintillating Tiles Hadronic Calorimeter

The tile calorimeter is a sampling calorimeter using steel as the absorber and scintillator as the active medium. It is located in the region, $|\eta| < 1.7$, behind the liquid argon electromagnetic calorimeter and is subdivided into a central barrel, 5.8 m in length, and two extended barrels, 2.6 m in length and each having an inner radius of 2.28 m and an outer radius of 4.25 m. The parameters of the tile calorimeter are listed in Table 1.4.

Scintillator tile calorimeter		
	Barrel	Extended barrel
$\|\eta\|$ coverage	$\|\eta\| < 1.0$	$0.8 < \|\eta\| < 1.7$
Number of layers	3	3
Granularity $\Delta\eta \times \Delta\phi$	0.1×0.1	0.1×0.1
Last layer	0.2×0.1	0.2×0.1
Readout channels	5760	4092 (both sides)

Table 1.4: Main parameters of the Tile Hadronic calorimeter.

The radial depth of the tile calorimeter is approximately 7.4λ (interaction lengths). Each barrel consists of 64 modules or wedges of size $\Delta\phi = 5.625°$, made of steel plates and scintillating tiles. The assembled module forms an almost-periodic steel-scintillator structure, as shown in Figure 1.15(a). The orientation of the scintillator tiles radially and normal to the beam line, in combination with wavelength-shifting fibre readout on the tile edges – as shown in Figure 1.15(b) – allows for almost seamless azimuthal calorimeter coverage. The grouping of the readout fibres into the readout photomultiplier tubes (PMTs) provides an approximately projective geometry in pseudorapidity. The gap region between the barrel and the extended barrel is instrumented with special modules, made of steel-scintillator sandwiches with the same sampling fraction as the rest of the tile calorimeter and with thin scintillator counters in the sectors where the available space in the gaps is even more limited, which allow to partially recover the energy lost in the crack regions.

The scintillating tiles constitute the active medium of the tile calorimeter. Ionising particles crossing the tiles induce the production of ultraviolet scintillation light in the base material –polystyrene– and this light is subsequently converted to visible light by wavelength-shifting fluors[1].

[1]the polystyrene is doped with 1.5% PTP as the primary fluor and with 0.044% POPOP as the secondary fluor

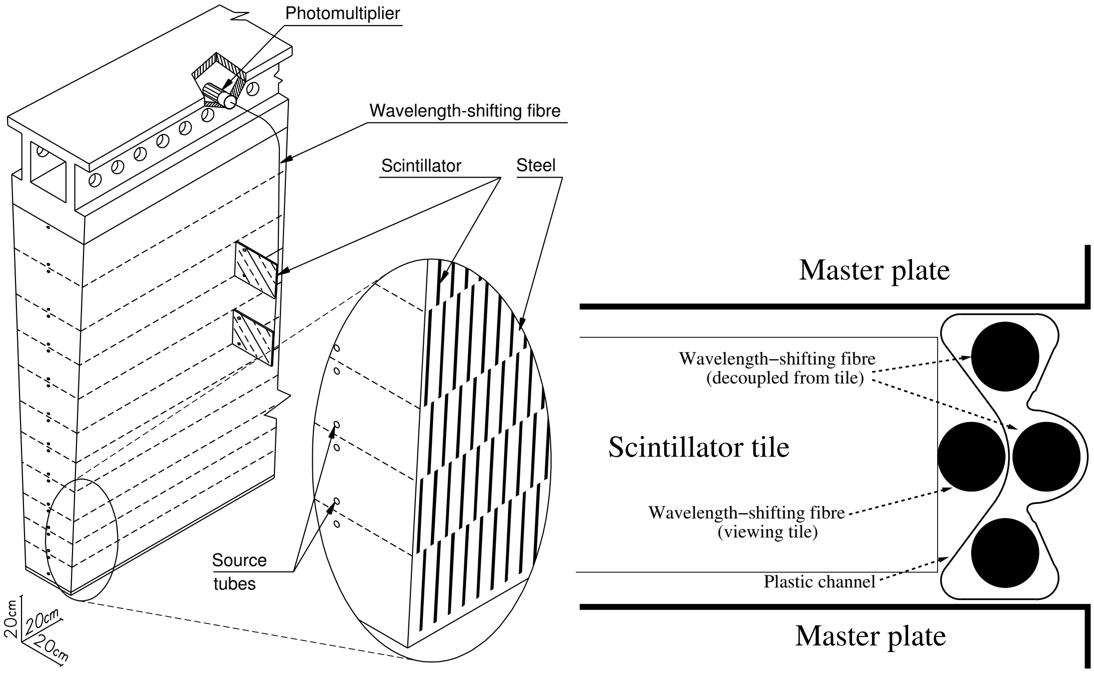

Figure 1.15: The schematic view of (a) the geometry of a Tile module and (b) the position of wavelength-shifting fibers for signal readout.

Wavelength-shifting fibres placed in contact with the tile edges collect the scintillation light produced in the scintillators and convert it to a longer wavelength. Each fibre collects light from tiles located at one or two radial depths in the calorimeter and transmits it to the PMTs located inside the girder. The wavelength shifting fibres are grouped together and coupled to the PMTs which are housed at the outer edge of each module. The fibre grouping is used to define a three-dimensional cell structure in such a way as to form three radial sampling depths, approximately 1.5, 4.1 and 1.8 λ thick at $\eta = 0$. These cells have dimensions $\Delta\eta \times \Delta\phi = 0.1 \times 0.1$ in the first two layers and $0.2{\times}0.1$ in the last layer.

1.2.3.3 Hadronic End-cap and Forward Calorimeters

The hadronic end-cap calorimeter (HEC) is a copper/liquid-argon sampling calorimeter with a flat-plate design, which covers the range $1.5 < |\eta| < 3.2$. The HEC shares each of the two liquid-argon end-cap cryostats with the electromagnetic end-cap

(EMEC) and forward (FCal) calorimeters. It consists of two wheels in each end-cap cryostat: a front wheel (HEC1) and a rear wheel (HEC2), each wheel containing two longitudinal sections. The wheels are cylindrical with an outer radius of 2030 mm. Each of the four HEC wheels is constructed of 32 identical wedge-shaped modules, as illustrated in Figure 1.16(a). Two sliding rails support the wheels inside the cryostat. The final vertical deformation of the wheel structure has been measured for the four wheels to represent a sag of 0.3 mm on average. The wheels remain perpendicular to their axis within ± 1.0 mm. The main parameters of the hadronic end-cap are listed in Table 1.5.

LAr hadronic end-cap		
$\|\eta\|$ coverage		$1.5 < \|\eta\| < 3.2$
Number of layers		4
Granularity $\Delta\eta \times \Delta\phi$	0.1×0.1	$1.5 < \|\eta\| < 2.5$
	0.2×0.2	$2.5 < \|\eta\| < 3.2$
Readout channels		5632 (both sides)

Table 1.5: Main parameters of the Liquid-Argon hadronic end-cap calorimeter.

The modules of the front wheels are made of 24 copper plates, each 25 mm thick, plus a 12.5 mm thick front plate. In the rear wheels, the sampling fraction is coarser with modules made of 16 copper plates, each 50 mm thick, plus a 25 mm thick front plate. The gaps in between the plates all have a thickness of 8.5 mm. The resulting sampling fractions for HEC1 and for HEC2 are 4.4% and 2.2% respectively. The wheels have an inner radius of 372 mm for the first nine plates of HEC1 and of 475 mm for the remaining plates of HEC1 and for all 17 plates of HEC2, as shown in Figure 1.16(b). Three electrodes divide the 8.5 mm gaps into four separate LAr drift zones of 1.8 mm width each. Each drift zone is individually supplied with high voltage of +1800 V. The middle electrode carries a pad structure covered by a high-resistivity layer, serving as the readout electrode and defining the lateral segmentation of the calorimeter. The two other electrodes carry surfaces of high resistivity to which high voltage is applied. For the nominal high voltage of 1800 V, the typical drift time for electrons in the drift zone is 430 ns.

The readout cells are defined by pads etched on the central foil in each gap. The arrangement of these pads provides a semi-pointing geometry as shown by the dashed diagonal lines in Figure 1.16(b). The size of the readout cells is $\Delta\eta \times \Delta\phi = 0.1 \times 0.1$ in the region $|\eta| < 2.5$ and 0.2×0.2 for larger values of $|\eta|$. Another important aspect of the HEC is its ability to detect muons and to measure any radiative energy loss.

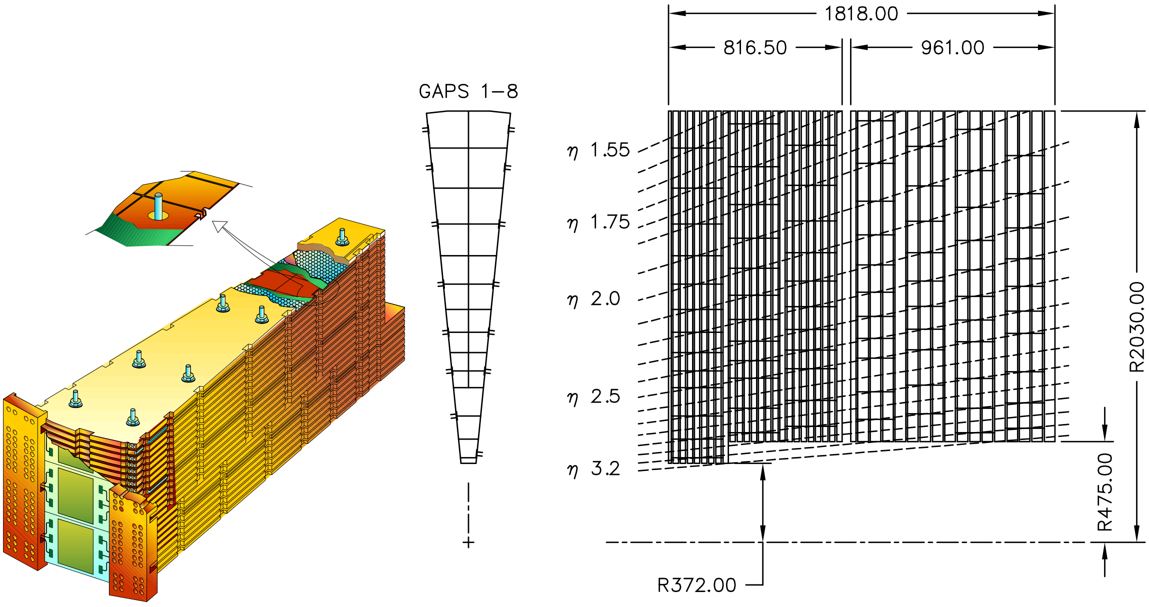

(a) (b)

Figure 1.16: Schematic view of (a) a HEC module with a cut-away showing the readout structure and the active-pad electronics, and (b) the $R-\phi$ and $R-z$ planes of the HEC calorimeter, where the dashed lines show the semi-pointing layout of the readout electrodes. Dimensions are in mm.

The forward calorimeters (FCal) are located in the same cryostats as the end-cap calorimeters and provide coverage over $3.1 < |\eta| < 4.9$. The close vicinity and coupling between these systems result in a quite hermetic design, which minimises energy losses in cracks between the calorimeter systems and also limits the backgrounds which reach the muon system. As the FCal modules are located at high η, at a distance of approximately 4.7 m from the interaction point, they are exposed to high particle fluxes. Thus a design with very small liquid-argon gaps has been obtained by using an electrode structure of small-diameter rods, centred in tubes which are oriented parallel to the beam direction. The liquid-argon gaps are smaller than the usual 2 mm gap of the electromagnetic barrel calorimeter to avoid ion build-up problems and to provide at the same time the highest possible density. In the electromagnetic layer (FCal1), the triangular current pulse at the electrode has a full drift time of 60 ns. For FCal2 and FCal3, the full drift time scales with the gap size since the field in the gaps is similar for all three modules. The main parameters of the forward calorimeters are detailed in Table 1.6.

LAr forward calorimeter		
$\lvert\eta\rvert$ coverage		$3.1 < \lvert\eta\rvert < 4.9$
Number of layers		3
Granularity $\Delta x \times \Delta y$ (cm^2)	FCal1: 3.0×2.6	$3.15 < \lvert\eta\rvert < 4.30$
	FCal1: $\sim$ four times finer	$3.10 < \lvert\eta\rvert < 3.15$ $4.30 < \lvert\eta\rvert < 4.83$
	FCal2: 3.3×4.2	$3.24 < \lvert\eta\rvert < 4.50$
	FCal2: $\sim$ four times finer	$3.20 < \lvert\eta\rvert < 3.24$ $4.50 < \lvert\eta\rvert < 4.81$
	FCal3: 5.4×4.7	$3.32 < \lvert\eta\rvert < 4.60$
	FCal3: $\sim$ four times finer	$3.29 < \lvert\eta\rvert < 3.32$ $4.60 < \lvert\eta\rvert < 4.75$
Readout channels		3524 (both sides)

Table 1.6: Main parameters of the Liquid-Argon forward calorimeter.

Each FCal is split into three 45 cm deep modules: one electromagnetic module (FCal1) and two hadronic modules (FCal2 and FCal3), as illustrated in Figure 1.17. To optimise the resolution and the heat removal, copper was chosen as the absorber for FCal1, while mainly tungsten was used in FCal2 and FCal3, to provide containment and minimise the lateral spread of hadronic showers. A shielding plug made of a copper alloy has been mounted behind FCal3 to reduce backgrounds in the end-cap muon system.

The FCal1 layer is made of stacked copper plates with 12,260 holes drilled in them through which the electrode structures –a co-axial copper rod and copper tube separated by a plastic fibre– are inserted. The hadronic modules FCal2 and FCal3 are optimised for a high absorption length. This is achieved by maximising the amount of tungsten in the modules.

Signals are read out from the side of FCal1 nearer to the interaction point and from the sides of FCal2 and FCal3 farther from the interaction point; keeping the cables and connectors away from the region of maximum radiation damage, near the back of FCal1. High voltage of 250, 375 and 500 V –for FCal1, FCal2 and FCal3, respectively– is distributed on the summing boards, mounted on the back of the HEC calorimeter, through current-limiting resistors.

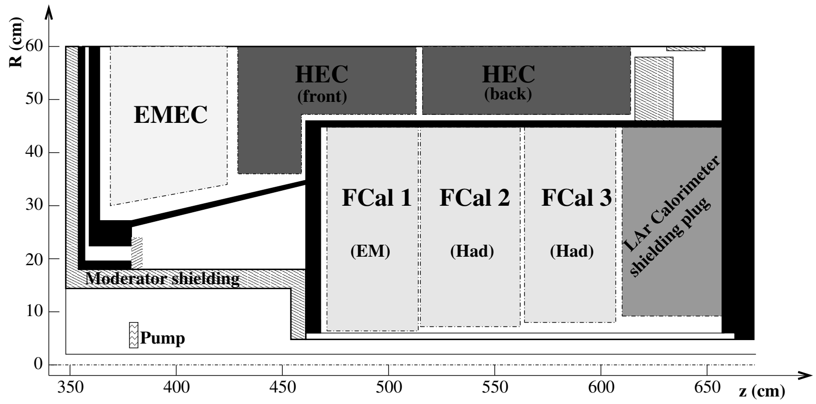

Figure 1.17: Schematic diagram showing the three FCal modules located in the end-cap cryostat. The material in front of the FCal and the shielding plug behind it are also shown. The black regions are structural parts of the cryostat.

1.2.4 The Muon Spectrometer

The muon spectrometer forms the outer part of the ATLAS detector and is designed to detect charged particles exiting the barrel and end-cap calorimeters and to measure their momentum in the pseudorapidity range $|\eta| < 2.7$. It is also designed to trigger on these particles in the region $|\eta| < 2.4$. The driving performance goal is a stand-alone transverse momentum resolution of approximately 10% for 1 TeV tracks, which translates into a sagitta along the beam axis (z) of about 500 μm, to be measured with a resolution of $\leq 50\mu$m. Muon momenta down to 3 GeV may be measured by the spectrometer alone. Even at the high end of the accessible range ($\sim$ 3 TeV), the standalone measurements still provide adequate momentum resolution and excellent charge identification. The main parameters of the components of the muon spectrometer are listed in Table 1.7. A cutaway view of the components of the muon spectrometer are shown in Figure 1.18.

The measurement of the muon momentum is based on the magnetic deflection of muon tracks in the large superconducting air-core toroid magnets, instrumented with separate trigger and high-precision tracking chambers. Over the range $|\eta| < 1.4$, magnetic bending is provided by the large barrel toroid. For $1.6 < |\eta| < 2.7$, muon tracks are bent by two smaller end-cap magnets inserted into both ends of the barrel toroid. Over $1.4 < |\eta| < 1.6$, usually referred to as the transition region, magnetic deflection is provided by a combination of barrel and end-cap fields. This magnet configuration provides a field which is mostly orthogonal to the muon trajectories, while minimising the degradation of resolution due to multiple scattering.

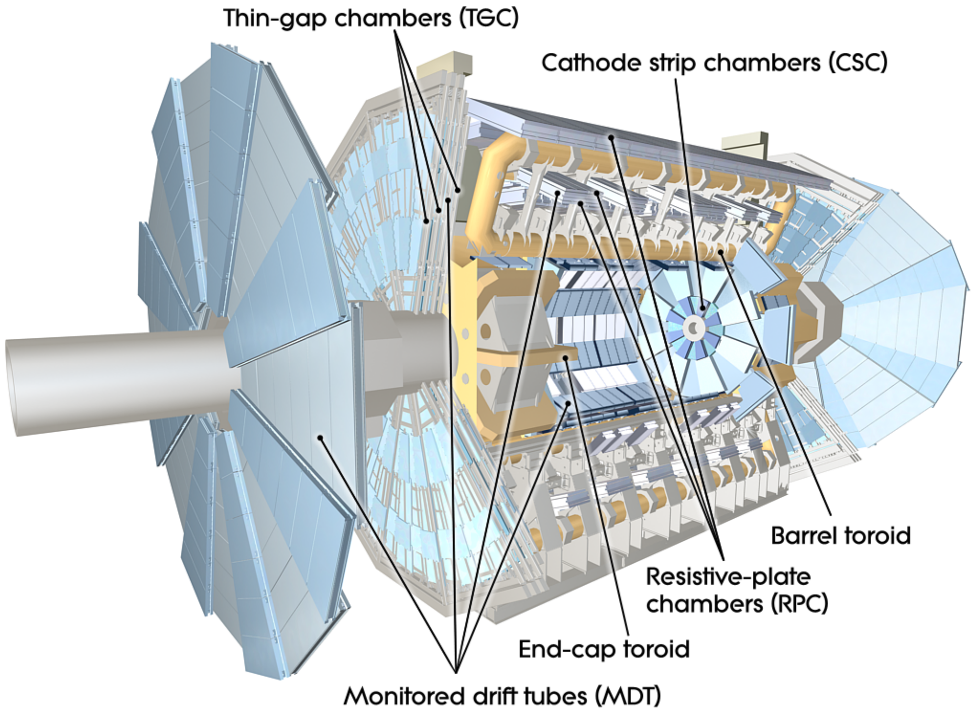

Figure 1.18: View of the muon spectrometer.

Type	$\|\eta\|$ coverage	Chamber resolution RMS			Measmt./track		Number of		Function
		z/R	ϕ	time	barrel	endcap	chambers	channels	
MDT	$\|\eta\| < 2.7$ (2.0 at 1^{st} layer)	35 μm (z)	—	—	20	20	1150	354k	Tracking
CSC	$2.0 < \|\eta\| < 2.7$	40 μm (R)	5 mm	7 ns	—	4	32	31k	Tracking
RPC	$\|\eta\| < 1.05$	10 mm (z)	10 mm	1.5 ns	6	—	606	373k	Trigger, 2^{nd} coord.
TGC	$1.05 < \|\eta\| < 2.7$ (2.4 for trigger)	2-6 mm (R)	3-7 mm	4 ns	—	9	3588	318k	Trigger, 2^{nd} coord.

Table 1.7: Main parameters of the muon spectrometer.

The magnetic field that fills the cylindrical volume of the barrel muon system has an average value of 0.5 T and is generated by the eight coils of the barrel toroid, shown in Figure 1.19 and in Figure 1.18. The overall size of the barrel toroid system as installed is 25.3 m in length, with inner and outer diameters of 9.4 m and 20.1 m, respectively.

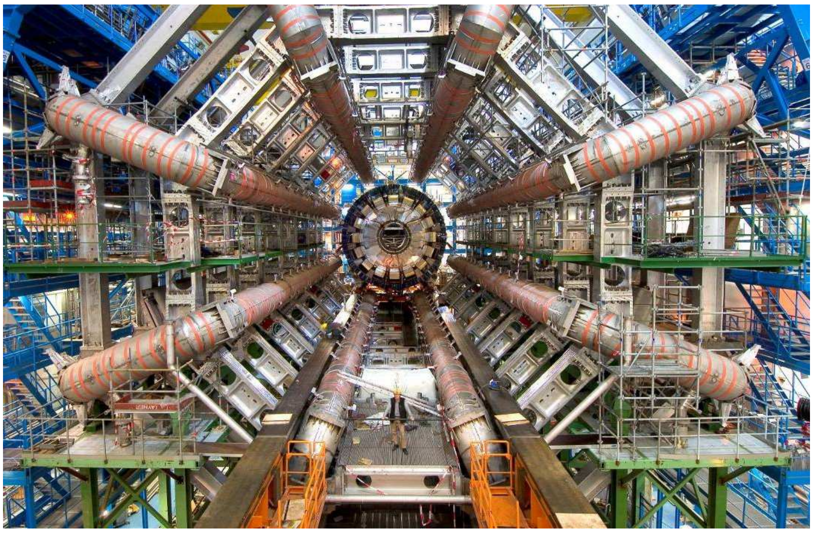

Figure 1.19: Barrel toroid as installed in the underground cavern.

The end-cap toroids generate the magnetic field required for optimising the bending power in the end-cap regions of the muon spectrometer. They are supported from and can slide along the central rails, facilitating the opening of the detector for access and maintenance. Figure 1.20 shows the interior of one of the end-cap toroids just before the closing of the vacuum vessel. The average magnetic field generated by each end-cap toroid is 1T [24].

1.2.4.1 High-precision Muon Chambers

Precision-tracking chambers in the barrel region are located between and on the eight coils of the superconducting barrel toroid magnet, while the end-cap chambers are in front and behind the two end-cap toroid magnets. The ϕ symmetry of the toroids is reflected in the symmetric structure of the muon chamber system, consisting of eight octants. Each octant is subdivided in the azimuthal direction in two sectors with slightly different lateral extensions, a large and a small sector, leading to a region of overlap in ϕ. This overlap of the chamber boundaries minimises gaps in detector coverage and also allows for the relative alignment of adjacent sectors using tracks recorded by both a large and a small chamber. The chambers in the barrel are arranged in three concentric cylindrical shells around the beam axis at radii of approximately 5 m, 7.5 m, and 10 m. In the two end-cap regions, muon chambers form large wheels, perpendicular to the z-axis and located at distances of $|z| \approx 7.4$ m, 10.8 m, 14 m, and 21.5 m from the interaction point.

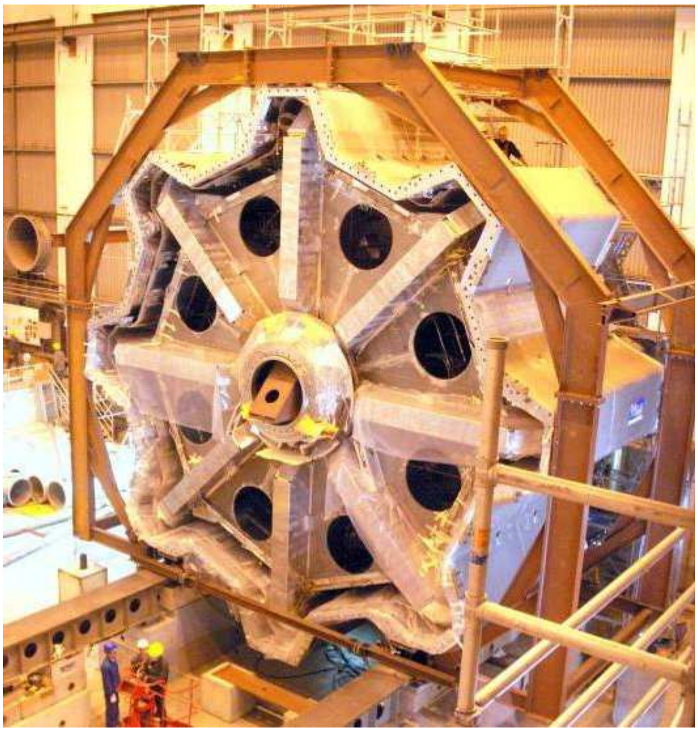

Figure 1.20: End-cap toroid cold mass inserted into the cryostat. The eight flat, square coil units and eight keystone wedges (with the circular holes) are visible.

Figure 1.21 shows the cross-section of the muon detectors in the bending ($R-z$) plane. In the centre of the detector ($|\eta| \approx 0$), a gap in chamber coverage has been left open to allow for services to the solenoid magnet, the calorimeters and the inner detector. The size of the gap varies from sector to sector depending on the service necessities, the biggest gaps of 1-2 m being located in the large sectors. The angular range, seen from the interaction point, where a high momentum (straight) track is not recorded in all three muon layers due to the gaps is about $\pm 4.8°$ ($|\eta| \leq 0.08$) in the large and $\pm 2.3°$ ($|\eta| \leq 0.04$) in the small sectors. Additional gaps in the acceptance occur in sectors 12 and 14 due to the detector support structure (feet).

The precision momentum measurement is performed by the Monitored Drift Tube chambers (MDTs), which combine high measurement accuracy, predictability of mechanical deformations and simplicity of construction. They cover the pseudorapidity range $|\eta| < 2.7$, except in the innermost end-cap layer where their coverage is limited to $|\eta| < 2.0$. These chambers consist of three to eight layers of drift tubes, operated at an absolute pressure of 3 bar, which achieve an average resolution of 80 μm per tube, or about 35 μm per chamber. The air-core magnet concept for the muon

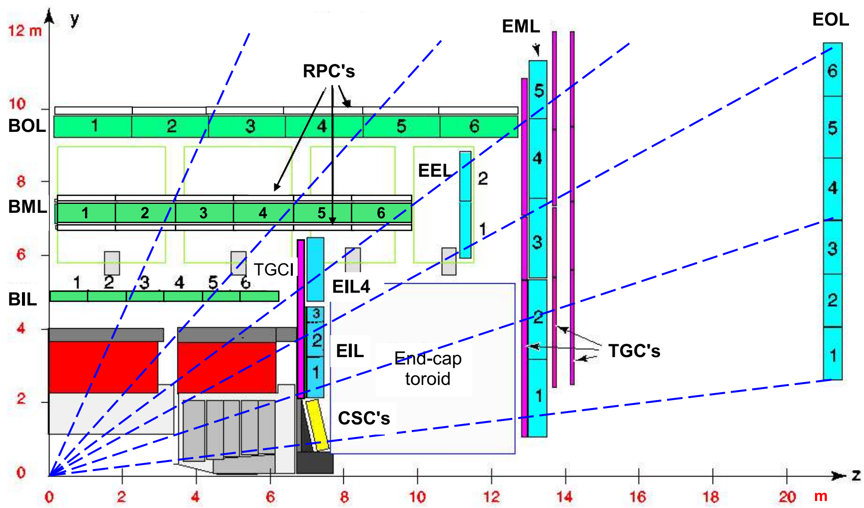

Figure 1.21: Cross-section of the muon system in the bending plane ($R - z$).

spectrometer minimises the amount of material traversed by the muons after exiting the calorimeters. However, the muons also encounter the muon chambers themselves and their supports, as well as other passive materials such as the toroid coils, vacuum vessels and magnet support structures.

In the forward region, $2 < |\eta| < 2.7$, Cathode-Strip Chambers (CSCs) are used in the inner-most tracking layer –just downstream of the end-cap calorimeter, where the limit for safe operation of the MDTs of 150 Hz/cm^2 is exceeded– due to their higher rate capability and time resolution. The CSCs are multiwire proportional chambers which combine high spatial, time and double track resolution with high-rate capability and low neutron sensitivity. The CSC cathode planes are segmented into strips in orthogonal directions, which allows both coordinates to be measured from the induced-charge distribution. The resolution of a chamber is 40 μm in the bending plane and about 5 mm in the transverse plane. The difference in resolution between the bending and non-bending planes is due to the different readout pitch, and to the fact that the azimuthal readout runs parallel to the anode wires. To achieve the sagitta resolution quoted above, the locations of MDT wires and CSC strips along a muon trajectory must be known to better than 30 μm. To this effect, a high-precision optical alignment system monitors the positions and internal deformations of the MDT chambers, complemented by track-based alignment algorithms.

1.2.4.2 Trigger Muon Chambers

The muon trigger system covers the pseudorapidity range $|\eta| < 2.4$. Resistive Plate Chambers (RPC) are used in the barrel and Thin Gap Chambers (TGC) in the end-cap regions. In the barrel, the trigger system consists of three concentric cylindrical layers around the beam axis, referred to as the three trigger stations. The RPCs are located at the inner and outer planes of the middle layer of the MDTs. On the outer layer of MDTs, the RPCs are located in the outer plane (largest radius) for the large sectors and the inner plane (smallest radius) for the small sectors.

The large lever arm between inner and outer RPCs permits the trigger to select high momentum tracks in the range $9 < p_{\mathrm{T}} < 35$ GeV (high-p_{T} trigger), while the two inner chambers provide the low-p_{T} trigger in the range $6 < p_{\mathrm{T}} < 9$ GeV. Each RPC station consists of two independent detector layers, each measuring η and ϕ. A track going through all three stations thus delivers six measurements in η and ϕ. Figure 1.22 shows a view of the location of the RPCs in red (for large sectors) in the $R - z$ plane.

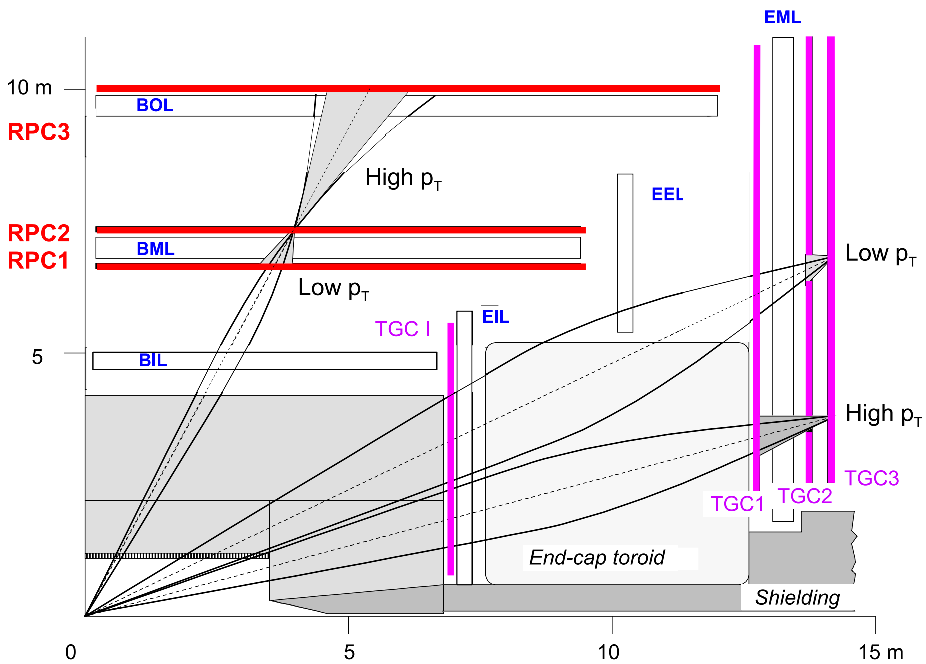

Figure 1.22: Schematics of the muon trigger system. The reference (pivot) plane for the barrel is RPC2 and for the end-cap is TGC3.

The RPC is a gaseous parallel electrode-plate detector. Two resistive plates are kept parallel to each other at a distance of 2 mm by insulating spacers. The electric field between the plates of about 4.9 kV/mm allows avalanches to form along the ionising tracks towards the anode. The signal is read out via capacitive coupling to metallic strips, which are mounted on the outer faces of the resistive plates.

Thin Gap Chambers (TGCs), used for the muon trigger in the end-caps, are multi-wire proportional chambers with the characteristic that the wire-to-cathode distance of 1.4mm is smaller than the wire-to-wire distance of 1.8 mm. They provide two functions in the end-cap muon spectrometer: the muon trigger capability and the determination of the second, azimuthal coordinate to complement the measurement of the MDTs in the bending (radial) direction. Anode wires of TGCs are arranged in the azimuthal direction and provide signals for R information, while readout strips orthogonal to these wires provide signals for ϕ information. Both wire and strip signals are used for the muon trigger.

The TGCs need good time resolution to tag the beam-crossing with high efficiency ($\geq 99\%$) and fine granularity to provide a sufficiently sharp cut-off in the momentum of the triggering muon. To match the granularity to the required momentum resolution, the size of the wire groups varies from 6 to 31 as a function of η, corresponding to a variation in width from 10.8 mm to 55.8 mm. Figure 1.22 shows in magenta the location of the TGCs in the muon end-caps.

The high electric field around the TGC wires and the small wire-to-wire distance lead to very good time resolution for the large majority of the tracks. Only tracks at normal incidence passing midway between two wires have much longer drift times due to the vanishing drift field in this region. In the TGC wheels the angle of incidence for tracks emerging from the interaction point will always be greater than 10°, thus a part of the track will be outside of the low field region. Including the variation of the propagation time on wires and strips, signals arrive with 99% probability inside a time window of 25 ns.

1.3 The ATLAS Trigger System

The ATLAS trigger system selects interesting events from LHC proton-proton or lead ion collisions. The LHC is designed with a maximum bunch crossing rate of 40 MHz and the ATLAS trigger system is designed to record approximately 200-400 per second. This limit, corresponding to an average data rate of ~300-500 MB/s, is determined by the computing resources for offline storage and data processing [27–29]. The trigger system selects events by rapidly identifying signatures of muon, electron, photon, tau lepton, jet, and B meson candidates, as well as using global event signatures, such as missing transverse energy.

This section contains the general description of the ATLAS Trigger system, a brief summary of the commissioning phase and an overview of the performance on collisions during 2010 first LHC runs.

1.3.1 General Description of the ATLAS Trigger System

At the LHC design luminosity of 10^{34} cm^{-2}s^{-1} with 25 ns bunch spacing, the bunch crossing rate is around 40 MHz, whereas the design data recording rate is limited to $\sim$ 300 Hz, constrained by technology and available resources. However in 2012 the whole system, including the data storage, was able to tolerate rates of up to 500 Hz leading to a typical rate in ATLAS of 275-350 Hz and a data transfer rate of about 500 MB/s. Thus only one out of $O(10^5)$ events will be recorded by ATLAS for analysis; the rest will be rejected by the trigger system. The ATLAS trigger system is divided into three levels: the hardware-based first level trigger (L1), and the software based second-level (L2) and Event Filter triggers (EF) jointly called the High Level Trigger (HLT). Each trigger level refines the decision made at the previous level and applies additional selection criteria when needed. For each bunch crossing, the trigger system verifies if at least one of hundreds of conditions (triggers) – configured via the *trigger menu* – is satisfied. The triggers are based on identifying combinations of candidate physics objects (signatures) such as electrons, photons, muons, jets, jets with b-flavour tagging (b-jets) or specific B-physics decay modes. In addition, there are triggers for inelastic pp collisions (*Minimum Bias*) and triggers based on global event properties like missing transverse energy ($E_{\mathrm{T}}^{\mathrm{miss}}$) and summed transverse energy ($\sum E_{\mathrm{T}}$). A schematic diagram of the ATLAS trigger system is shown in Figure 1.23.

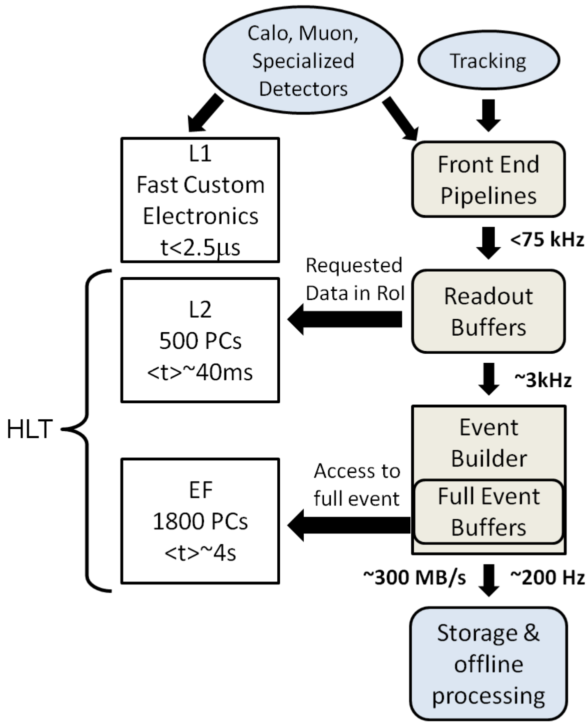

Figure 1.23: Schematic of the ATLAS trigger system.

1.3.1.1 Level 1

Detector signals are stored in front-end pipelines awaiting a decision from the L1 trigger system. In order to achieve a latency of less than 2.5 μs, the L1 trigger system is implemented in fast custom electronics. The L1 trigger system is designed to reduce the rate to a maximum of 75 kHz –in 2010 running the maximum L1 rate did not surpass 30 kHz. In addition to performing the first selection step, the L1 triggers identify *Regions of Interest* (RoIs), geometrical regions within the detector in $\Delta\eta \times \Delta\phi$ where potential signatures are located, to be further investigated by the HLT.

The L1 trigger decision is formed by the Central Trigger Processor (CTP) based on information from the calorimeter trigger towers and dedicated triggering layers in the muon system [16, 30]. The CTP applies the multiplicity requirements and prescale factors configured through the *trigger menu* to the inputs from the L1 trigger systems, thus producing the L1 trigger decision. The CTP also provides random triggers and can apply specific LHC bunch crossing requirements. The L1 trigger decision is distributed, together with timing and control signals, to all ATLAS sub-detector readout systems.

The L1 calorimeter trigger [31] is based on inputs from the electromagnetic and hadronic calorimeters covering the region $|\eta| < 4.9$. It supplies triggers for localized objects –electrons, photons, tau and jets– and for global transverse energy. A series of custom built hardware modules with a latency of less than 1 μs is used to carry out the pipelined processing and logic. Section 1.3.1.4 gives the details on the configured L1Calo trigger thresholds for electrons or photons, tauons and jets, as well as $E_{\mathrm{T}}^{\mathrm{miss}}$. Section 1.3.4 includes the description of the L1Calo architecture for electron and photon triggers.

The L1 muon trigger system [16, 22] is a hardware-based system to process input data from fast muon trigger detectors, the RPCs and TGCs described in Section 1.2.4.2, that cover the pseudorapidity range $|\eta| < 2.4$. The main task of this system is to select muon candidates and identify the bunch crossing in which they were produced. The efficient triggering for muons with $p_{\mathrm{T}} > 6$ GeV is the primary performance requirement [27].

The L1 trigger system also takes input from LUCID and ZDC forward detectors and a set of specialized detectors that include:

BPTX: electrostatic beam pick-up devices which are located at $z = \pm 175$ m.

BCM: the *Beam Conditions Monitor* which consists of two stations containing diamond sensors located at $z = \pm 1.84$ m, corresponding to $|\eta| \simeq 4.2$.

MBTS: the *Minimum Bias Trigger Scintillators*, consisting of two scintillator wheels with 32 counters mounted in front of the calorimeter end-caps, which cover the region $2.1 < |\eta| < 3.8$.

1.3.1.2 High Level Trigger

The HLT consists of farms of commercially available processors connected by fast dedicated networks of Gigabit and 10 Gigabit Ethernet. During 2010 running, the HLT processing farm was composed of about 800 nodes configurable as either L2 or EF plus 300 nodes dedicated exclusively to EF. Eight processor cores –most of them with a 2.4 GHz clock speed– comprise each node. The system is designed to expand to about 500 L2 nodes and 1800 EF nodes for running at the LHC design luminosity.

When an event is accepted by the L1 trigger (known as an *L1 accept*), data from each detector are transferred to the detector-specific *Readout Buffers* (ROB), which store the event in fragments pending the L2 decision. One or more ROBs are grouped into Readout Systems (ROS) that are connected to the HLT networks. Fast custom algorithms that process partial event data within the RoIs identified by L1 are the basis for the L2 selection. The L2 processors request data from the ROS corresponding to detector elements inside each RoI, reducing the amount of data to be transferred and processed in L2 to a mere 2–6% of the total data volume. The L2 triggers reduce the rate to ∼3 kHz with an average processing time of ∼40 ms/event. Any event with a L2 processing time exceeding 5 s is recorded as a *timeout* event and is written to a dedicated data *stream* –called the *debug stream*– in order to be analysed and possibly recovered. During runs with instantaneous luminosity $\sim 10^{32}\,\mathrm{cm}^{-2}\mathrm{s}^{-1}$, the average processing time of L2 was ∼50 ms/event.

For events accepted by L2, the Event Builder assembles all event fragments from the ROBs, providing full event information to the EF. The EF is most often based on offline algorithms, which are invoked from custom *online* interfaces for running in the trigger system. The EF is designed to decrease the rate to ∼200 Hz with an average processing time of ∼4 s/event. Any event with an EF processing time above 180 s is recorded as a *timeout* event and written to the debug stream to be analysed and hopefully recovered. During runs with instantaneous luminosity $\sim 10^{32}\,\mathrm{cm}^{-2}\mathrm{s}^{-1}$, the average processing time of EF was ∼0.4 s/event due to the low pile-up conditions of that year.

1.3.1.3 Data Streams

Data for events selected by the trigger system are written to inclusive data *streams* based on the trigger type. There are four primary physics streams: *Egamma*, *Muons*, *JetTauEtmiss* and *MinBias*, plus several additional calibration streams. About 10% of events are written to an *express* stream where prompt offline reconstruction provides calibration and Data Quality (DQ) information prior to the reconstruction of the physics streams.

Events for which a trigger decision could not be made are written to the debug stream, mentioned above, in order to be analysed and reprocessed by the HLT. A dedicated framework for the analysis and reprocessing the debug stream exists, where these events are inspected to understand the cause of the lack of decision. Additionally, in this framework the HLT algorithms are run offline (called reprocessing), benefiting from longer offline timeout limits. At this stage an event that ended up in the debug stream is expected to be recovered –a trigger decision is made to either accept or reject it– and can be considered for physics analyses.

In addition to writing complete events to a stream, it is also possible to write partial information from one or more sub-detectors into a stream. Such events, used for detector calibration, are written to the calibration streams.

1.3.1.4 Configuration of the Trigger

The trigger system is configured through a trigger *menu* which defines trigger *chains*. Trigger chains start from a L1 trigger and specify a sequence of reconstruction and selection steps for the particular trigger signatures required. A trigger chain is often referred to simply as a trigger.

Figure 1.24 illustrates an example of a trigger chain to select electrons. Each chain is composed of *Feature Extraction (FEX)* algorithms which create the objects –e.g. calorimeter clusters– and *Hypothesis (HYPO)* algorithms that apply selection criteria to the objects, for example a cut on transverse momentum greater than a certain threshold. The trigger system allows features extracted from one chain to be re-used in another chain for the same event using *caching*, reducing the data access and processing time.

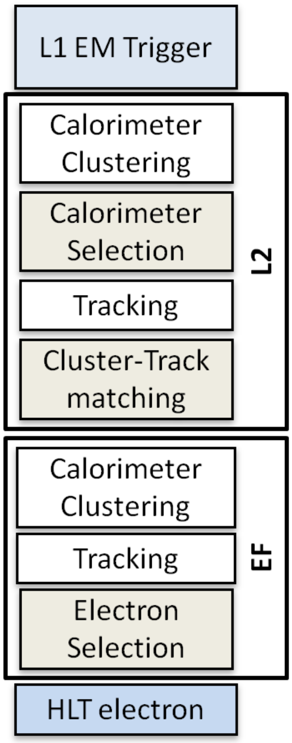

Figure 1.24: Electron trigger chain. The *FEX* algorithms for L2 and EF are shown in the white rectangles while the *HYPO* algorithms correspond to the grey rectangles.

Trigger Signature	Representation		L1 Thresholds (GeV)							
	L1	HLT								
electron	EM	e	2	3	5	10	10i	14	14i	85
photon	EM	g	2	3	5	10	10i	14	14i	85
muon	MU	mu	0	6	10	15	20			
jet	J	j	5	10	15	30	55	75	95	115
tau	TAU	tau	5	6	6i	11	11i	20	30	50
$E_{\mathrm{T}}^{\mathrm{miss}}$	XE	xe	10	15	20	25	30	35	40	50
$\sum E_{\mathrm{T}}$	TE	te	20	50	100	180				
MBTS	MBTS	mbts								

Table 1.8: A selected subset of some of the key trigger objects present in the menu at $\mathcal{L}$=$10^{32}\,\mathrm{cm}^{-2}\mathrm{s}^{-1}$, used during 2010 data-taking, with the shortened names used to represent them in the trigger menu at L1 and the HLT, and the L1 thresholds used for each trigger signature. Thresholds are applied to E_{T} for calorimeter triggers and p_{T} for muon triggers.

The trigger menus used during data-taking define many hundreds of trigger chains. Table 1.8 shows an example of some of the most essential physics objects identified by the trigger system with their abbreviated representation as used in the trigger menus during 2010 data-taking. The L1 thresholds applied to *transverse energy* (E_{T}) for calorimeter triggers (electron, photon, tau, jet and $E_{\mathrm{T}}^{\mathrm{miss}}$) and to *transverse momentum* (p_{T}) for muon triggers are also displayed.

The menu is composed of a number of different classes of trigger:

Single object triggers: used for final states with at least one characteristic object. For example, a single muon trigger with a nominal 6 GeV threshold is referred to in the trigger menu as `mu6`.

Multiple object triggers: used for final states with two or more characteristic objects of the same type (for example, di-muon triggers for selecting $J/\psi \to \mu\mu$ decays). Triggers requiring a multiplicity of two or more are indicated in the trigger menu by prepending the multiplicity to the trigger name, as in `2mu6`.

Combined triggers: used for final states with two or more characteristic objects of different types. For example, a $p_{\mathrm{T}} > 13$ GeV muon plus $E_{\mathrm{T}}^{\mathrm{miss}} > 20$ GeV trigger for selecting $W \to \mu\nu$ decays would be denoted `mu13_xe20`.

Topological triggers: used for final states that require selections based on information from two or more RoIs. For example the $J/\psi \to \mu\mu$ trigger combines tracks from two muon RoIs.

A particular level of a trigger (L1, L2 or EF) appears as a prefix in the label, so `L1_MU6` refers to the L1 trigger item with a 6 GeV threshold and `L2_mu6` refers to the L2 trigger item with a 6 GeV threshold. A name without a level prefix refers to the whole trigger chain.

Trigger rates can be controlled by modifying the thresholds at any level or applying different sets of selection cuts at the HLT. The severity of a set of cuts applied to a given trigger object in the menu is represented by the terms *loose*, *medium*, and *tight*, which are suffixed to the trigger name, for example `e10_medium`. Additional requirements, such as *isolation*, can also be imposed to reduce the rate of some triggers. Isolation is a measure of the amount of energy or number of particles near a signature, and is indicated in the trigger menu by an `i` appended to the trigger name (capital `I` for L1), for example `L1_EM20I` or `e20i_tight`. Isolation was not used in any primary triggers during 2010.

Prescale factors can be applied to each L1 trigger or HLT chain, such that for a prescale factor of N only 1 in N events, selected at random among those which would normally pass the trigger, causes the event to be accepted at that trigger level. Prescales can also be set so as to disable specific chains, if set to negative numbers or 0. Prescale factors are also used to control the rate and composition of the express stream. A series of L1 and HLT prescale sets, covering a range of luminosities, are defined to accompany each menu. These prescales are auto-generated based on a set of rules that take into account the priority for each trigger within the following categories:

Primary triggers: main physics triggers, which should not be prescaled.

Supporting triggers: triggers meant to support the primary triggers, for example orthogonal triggers for efficiency measurements or prescaled versions of primary triggers with lower E_{T} threshold.

Monitoring and Calibration triggers: used to collect data to ensure the correct operation of the trigger and detector, including detector calibrations.

As the luminosity drops during an LHC fill, the prescales are adjusted in order to maximize the bandwidth for physics while ensuring a constant rate for monitoring and calibration triggers. These changes can be applied at any point during a run at the beginning of a new *luminosity block* (*LB*). A luminosity block is the fundamental unit of time for the luminosity measurement and during 2010 data-taking it was approximately 120 s.

Further flexibility is obtained by defining *bunch groups*, which allow triggers to include specific requirements on the LHC bunches colliding in ATLAS. These requirements include paired (colliding) bunches for physics triggers and empty bunches for cosmic-ray, random noise and pedestal triggers.

1.3.2 Commissioning and Performance of the ATLAS Trigger System in 2010

The commissioning of the ATLAS trigger system started before the first LHC beam using cosmic-ray events. The L1 trigger system was exercised for the first time with beam during 2008, with single beam commissioning runs. Some of these runs included so-called *splash events* for which the proton beam was intentionally brought into collision with the collimators upstream from the experiment in order to generate very large particle multiplicities that were used for detector commissioning. Following the single beam data-taking in 2008, there was a period of cosmic ray data-taking, during which the HLT algorithms ran online, in preparation for operations with the first *pp* collisions in December 2009.

1.3.2.1 Commissioning with *pp* Collisions

For the early collision running in 2009 and 2010, a set of specialized commissioning trigger menus were developed. The initial low interaction rate of the order of a few Hz allowed all events passing L1 to be recorded, hence the commissioning menus consisted mainly of L1-based triggers. Initially, the L1 MBTS trigger was the primary physics trigger, recording all interactions without a prescale factor. As soon as the luminosity exceeded $\sim 2 \cdot 10^{27}\,\text{cm}^{-2}\text{s}^{-1}$, the L1 MBTS trigger was prescaled and the lowest threshold muon and calorimeter triggers became the primary physics triggers. With further luminosity increase, these triggers were also prescaled and higher threshold triggers, which were already included in the commissioning menus, became the primary physics triggers. A coincidence with a paired bunch crossing was required for physics triggers. In addition, for most of the lowest threshold physics triggers a corresponding non-collision trigger – which required a coincidence with an empty or unpaired bunch crossing – was included in the menus to be used for background studies. Several supporting triggers needed for commissioning the L1 trigger system were also incorporated in the commissioning menus.

The event streaming in the commissioning menus was based on the L1 trigger categories. Three main inclusive physics streams were recorded: *L1Calo* for calorimeter-based triggers, *L1Muon* for triggers coming from the muon system and *L1MinBias* for events triggered by minimum bias and forward detectors such as MBTS, LUCID and ZDC. In addition to these L1-based physics streams, the express stream was also recorded. During the first weeks of data-taking the content of the express stream varied significantly. In the early data-taking, it comprised a random 10-20% of all triggered events in order to exercise the offline express stream processing system. Afterward, the content was changed to enhance the proportion of electron, muon, and jet triggers. Finally, a small set of triggers of each trigger type was sent to the express stream. The fraction of each individual trigger contributing to the express stream was adjustable by using dedicated prescale values. During this period, the use of the express stream for data quality assessment and for calibration prior to offline reconstruction of the physics streams was commissioned.

For the HLT commissioning during the very first collision data-taking at $\sqrt{s}$ = 900 GeV in 2009, no HLT algorithms were run online; instead they were exercised offline on collision events recorded in the express stream. Careful checks of the HLT results were performed to confirm that the trigger algorithms were functioning correctly and the algorithm execution times were evaluated to verify that timeouts would not occur during online running.

The HLT algorithms were deployed online in *monitoring mode* after a few days of running offline, following the positive assessment of their performance from offline results. In monitoring mode, the HLT algorithms ran online producing trigger objects, like calorimeter clusters and tracks, and a trigger decision at the HLT; however events were selected based solely on their L1 decision.

Operating first in monitoring mode allowed each trigger to be validated before the trigger was put into *active rejection mode*. Additionally, the efficiency of each trigger chain could be measured with respect to offline reconstruction, since the HLT objects and decision were recorded in each event. Furthermore, a *rejection factor*, defined as input rate over output rate, could be evaluated for each trigger chain at L2 and EF. Finally, running the HLT algorithms online also permitted the online trigger monitoring system to be exercised and commissioned under real conditions.

An important feature of the trigger system is the possibility of setting each trigger chain in monitoring or active rejection mode. As a result, individual triggers could to be put into active rejection mode gradually as luminosity increased and trigger rates exceeded allocated maximum values. During the first months of 2010 data-taking, the LHC peak luminosity increased from $10^{27}\,\mathrm{cm}^{-2}\mathrm{s}^{-1}$ to $10^{29}\,\mathrm{cm}^{-2}\mathrm{s}^{-1}$, which was sufficiently low to allow the HLT to continue running in monitoring mode while controlling the trigger rates by applying prescale factors at L1. The HLT rejection for the highest rate L1 triggers needed to be enabled once the peak luminosity delivered by the LHC reached $1.2\times10^{29}\,\mathrm{cm}^{-2}\mathrm{s}^{-1}$. As luminosity progressively increased, more triggers were put into active rejection mode. Figure 1.25 shows the maximum instantaneous luminosity as a function of time during 2010; the commissioning menus were used until the end of May 2010.

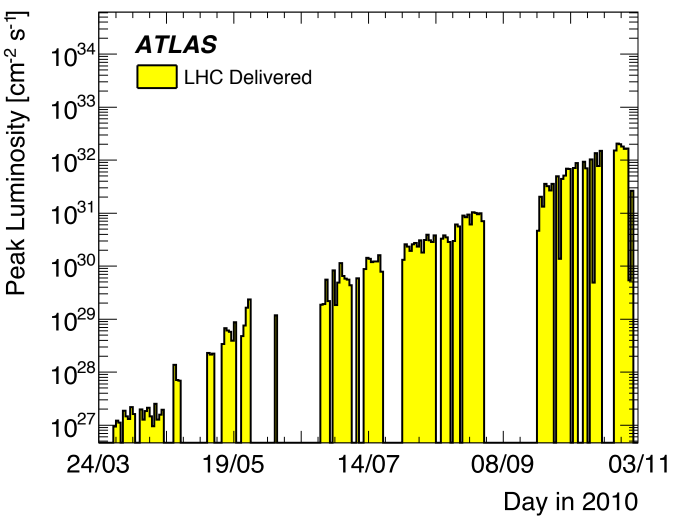

Figure 1.25: Profile with respect to time of the maximum instantaneous luminosity per day recorded by ATLAS during stable beams in $\sqrt{s} = 7$ TeV pp collisions.

1.3.2.2 Physics Trigger Menu

The physics trigger menu – designed for luminosities from $10^{30}\,\mathrm{cm}^{-2}\mathrm{s}^{-1}$ to $10^{32}\,\mathrm{cm}^{-2}\mathrm{s}^{-1}$ – was deployed for the first time at the end of July 2010, when LHC luminosity approached $10^{30}\,\mathrm{cm}^{-2}\mathrm{s}^{-1}$, as seen in Figure 1.25. In order to adapt to the LHC conditions, the physics trigger menu continued to evolve during 2010. In its final form, it consisted of more than 470 triggers, and comprised mostly primary and supporting physics triggers.

The L1 commissioning items were removed from the physics menu, allowing for the addition of higher threshold physics triggers in preparation for increased luminosity.

Another incorporation of the physics menu were the combined triggers, based on a logical "and" between two L1 items. The L1-based streaming was disabled and replaced by streaming based on the HLT decision, which meant that in addition to calibration and express streams, data were recorded in the physics streams. At the same time, preliminary bandwidth allocations were defined as guidelines for all trigger groups, as listed in Table 1.9. As luminosity increased and the trigger rates approached the limits imposed by offline processing, primary and supporting triggers continued to evolve by progressively tightening the HLT selection cuts and by prescaling the lower E_{T} threshold triggers.

	Luminosity [cm^{-2}s^{-1}]		
	10^{30}	10^{31}	10^{32}
Trigger Signature	Rate [Hz]	Rate [Hz]	Rate [Hz]
Minimum bias	20	10	10
Electron/Photon	30	45	50
Muon	30	30	50
Tau	20	20	15
Jet and forward jet	25	25	20
b-jet	10	15	10
B-physics	15	15	10
$E_{\mathrm{T}}^{\mathrm{miss}}$ and $\sum E_{\mathrm{T}}$	15	15	10
Calibration triggers	30	13	13

Table 1.9: Preliminary bandwidth allocations defined as guidelines to the various trigger groups, at three luminosity points, for an EF trigger rate of ~200 Hz.

Figure 1.26 shows a comparison between online measured rates at $10^{32}\,\mathrm{cm}^{-2}\mathrm{s}^{-1}$ and predictions based on extrapolation from *enhanced bias* data (data recorded with a very loose L1 trigger selection and no HLT selection, collected at lower luminosity) for the three levels of the trigger and three physics streams. Usually, online rates agreed with predictions within 10%. The biggest discrepancy was seen in rates from the *JetTauEtmiss* stream, as a result of the non-linear scaling of $E_{\mathrm{T}}^{\mathrm{miss}}$ and $\sum E_{\mathrm{T}}$ trigger rates with luminosity. This non-linearity is caused by *in-time pile-up*, defined as the effect of multiple *pp* interactions in a bunch crossing. The maximum mean number of interactions per bunch crossing reached 3.5 in 2010. The most significant effects of in-time pile-up have been seen on the $E_{\mathrm{T}}^{\mathrm{miss}}$, $\sum E_{\mathrm{T}}$, and minimum bias signatures [27]. *Out-of-time pile-up*, defined as the effect of an earlier bunch crossing on the detector signals (especially in the LAr calorimeter) for the current bunch crossing, did not have a significant effect in the 2010 *pp* data-taking because the bunch spacing was at least 150 ns.

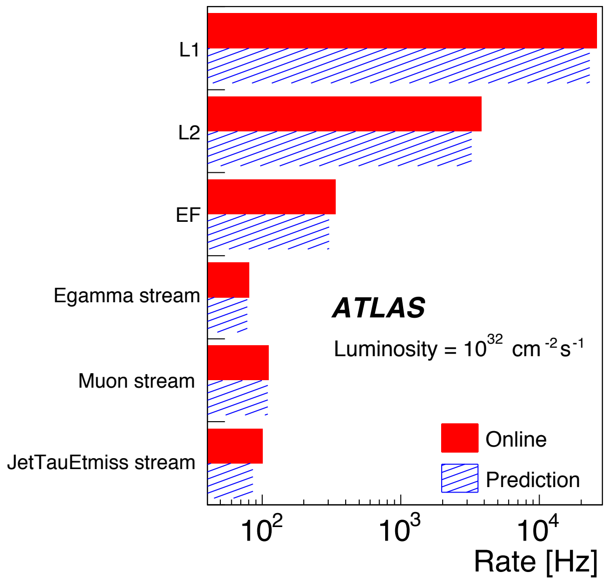

Figure 1.26: Comparison of measured online rates (solid) with offline rate predictions from enhanced bias data (hashed) at luminosity $10^{32}\,\mathrm{cm}^{-2}\mathrm{s}^{-1}$ for L1, L2, EF and main physics streams.

1.3.3 Integration of the Trigger Information in Offline Reconstruction

The offline monitoring of the ATLAS trigger system and the evaluation of trigger efficiencies are important steps for the validation of the trigger algorithms and for physics analyses. In order to access the objects constructed online by the HLT in the offline environment, a tool for unpacking the bytestream raw data is integrated into the offline reconstruction software (ATHENA). The correct identification of the version of trigger menu and prescale sets used online is also integrated in offline reprocessing, by accessing the metadata for each run and luminosity block. The primary event processing occurs at CERN in a Tier-0 facility, which is responsible for the archiving and distribution of the primary RAW data received from the Event Filter. It provides the prompt reconstruction of the calibration and express streams, and the somewhat slower first-pass processing of the primary event stream [32, 33]. Coordination between the versions of the trigger objects (the *Event Data Model*) used in the online software and in the Tier-0 prompt reconstruction software is imperative.

Another part of the trigger software that is executed during offline reconstruction is the trigger offline monitoring. The efficiency of HLT selection is evaluated with respect to offline objects, usually from the express stream. This monitoring has to be robust enough so as to allow for seamless Tier-0 running even in the case of errors, in order not to disrupt the prompt reconstruction of data. Finally, in order to have a faster response to issues found in the early stages of trigger commissioning, the prompt reconstruction processing produced *Trigger Commissioning Ntuples*, which also had to obey the Tier-0 rule of being extremely robust in the face of errors and keep up with the content of online data. These trigger commissioning ntuples proved to be extremely useful for the first months of collisions to validate the performance of the HLT algorithms. The trigger monitoring has continued to operate during the current high-luminosity data-taking.

1.3.4 Triggering on Electrons with the ATLAS Detector

Electrons and photons leave most of their energy in the electromagnetic calorimeter, and electrons also have a track in the inner detector. These characteristics are exploited by the trigger in order to identify electrons and photons.

1.3.4.1 Level 1 Electron and Photon selection

The L1 calorimeter (L1Calo) trigger decision is based on dedicated analogue trigger signals supplied by the ATLAS calorimeters separately from those read out and utilised by the HLT and offline. Instead of using the full granularity of the calorimeter, the L1 decision is based on the information from *trigger towers* (TT) – analogue sums of calorimeter elements within projective regions. The dimensions of the trigger towers are approximately $\Delta\eta \times \Delta\phi = 0.1 \times 0.1$ in the central region of the calorimeter with $|\eta| < 2.5$; whereas in the more forward region they become larger and less regular. Separate trigger towers exist for the electromagnetic and hadronic calorimeters.

The 7168 analogue sums are first digitized and they are then associated to a particular LHC bunch crossing. Two separate processor systems, working in parallel, run the trigger algorithms taking as input the digital transverse energies per LHC bunch crossing. One of these systems, the *cluster processor*, employs the full L1 trigger granularity information in the central region to look for small localized clusters, typically produced by electrons, photons or τ leptons. The other system, the *jet and energy-sum processor*, uses so-called jet elements – which are 2×2 sums of trigger towers – in order to identify jet candidates and form global transverse energy sums: missing transverse energy, total transverse energy and jet-sum transverse energy. The results are sent to the CTP which forms the L1 trigger decision by comparing the magnitude of the objects and sums produced to programmable thresholds. The thresholds used during 2010 are shown in Table 1.8. Figure 1.27 shows the architecture of the L1 calorimeter trigger.

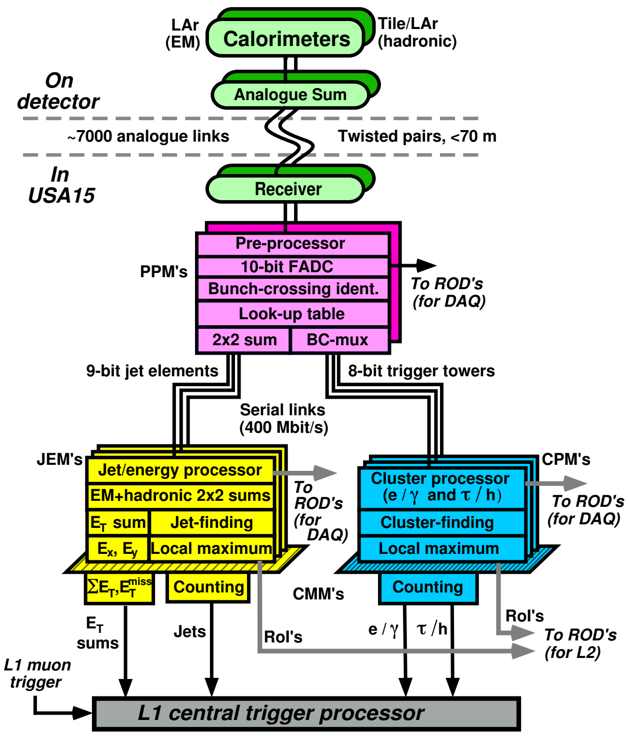

Figure 1.27: Architecture of the L1Calo trigger. Analogue data from the calorimeters are digitised and matched to the correct bunch crossing in the pre-processor and then sent to the jet/energy-sum and the cluster processors. The results are sent to the central trigger processor.

For the L1 selection of electrons and photons, the candidates are found by a sliding window algorithm of 4×4 trigger towers, as illustrated in Figure 1.28. The cluster candidate must satisfy the following conditions:

- The central 2 × 2 trigger tower transverse energy (E_T) sum (RoI core) must be a local maximum.

- The cluster energy is defined as the highest 2 × 1 or 1 × 2 sum of EM trigger towers within the central 2 × 2 window. This energy sum, which is expressed as an integer number in units of GeV, has to be above a configured threshold. For a threshold of 2 GeV the cluster satisfies $E_T \geq 3$ GeV.

Figure 1.28 shows diagrammatically the definition of the L1 clustering algorithm for electrons and photons. The central RoI core is shown in green with the vertical and horizontal pair sums for the assessment of the electromagnetic cluster energy displayed as the yellow bars.

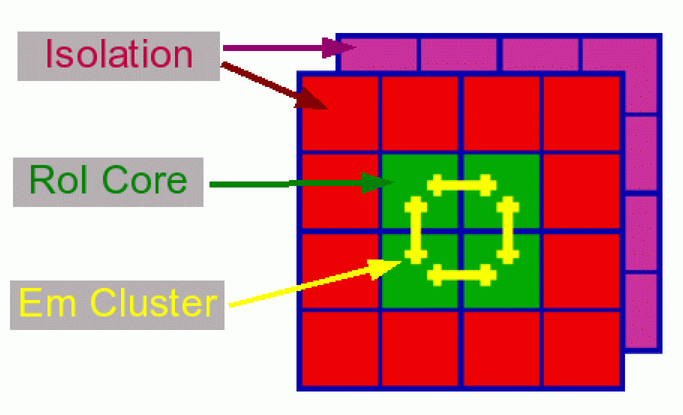

Figure 1.28: Diagrammatic representation of the sliding window algorithm used for Level 1 electromagnetic calorimeter triggers. The basic objects are shown in different colors as described in the text.

1.3.4.2 HLT Electron and Photon selection

Each electromagnetic object identified at L1 has an associated RoI containing the direction in η and ϕ and the transverse energy thresholds that have been fulfilled, as specified by the L1 trigger menu of Table 1.8. The L2 photon and electron selections employ a fast calorimeter reconstruction algorithm which resembles the offline clustering algorithms, with the exception that they are seeded by the cell with the highest E_T in the middle layer of the EM calorimeter, within the RoI indicated by the L1. The L2 track reconstruction algorithm, used for electrons, was developed independently to fulfill the more stringent timing requirements. The EF also performs calorimeter cluster and track reconstruction using the offline reconstruction algorithms (described in Section 1.4), applying similar – though somewhat looser – cuts in order to remain nearly 100% efficient for offline-identified objects [22, 34].

The cluster E_{T} and cluster shape parameters are the basis of the L2 and EF selections; they provide a calorimeter-based requirements for both electrons and photons. Distributions of two important parameters are shown in Figure 1.29. The hadronic leakage parameter, defined as $R_{had} = E_{\mathrm{T}}^{had}/E_{\mathrm{T}}^{EM}$, is the ratio of the cluster transverse energy in the hadronic calorimeter to that in the electromagnetic calorimeter. The distribution of R_{had} at L2 for offline reconstructed electrons is shown in Figure 1.29(a). Another important parameter is $E_{ratio} = (E_T^{(1)} - E_T^{(2)})/(E_T^{(1)} + E_T^{(2)})$, where $E_T^{(1)}$ and $E_T^{(2)}$ are the transverse energies of the two most energetic cells in the first layer of the electromagnetic calorimeter in a region of $\Delta\eta\times\Delta\phi = 0.125\times0.2$. Figure 1.29(b) shows the distribution of this parameter at the EF. The E_{ratio} distribution peaks at one for showers with no substructure, and thus distinguishes clusters due to single electrons and photons from those originated from hadrons and $\pi^0 \rightarrow \gamma\gamma$ decays. Additionally, the electron selection requires a track to be paired to the calorimeter cluster.

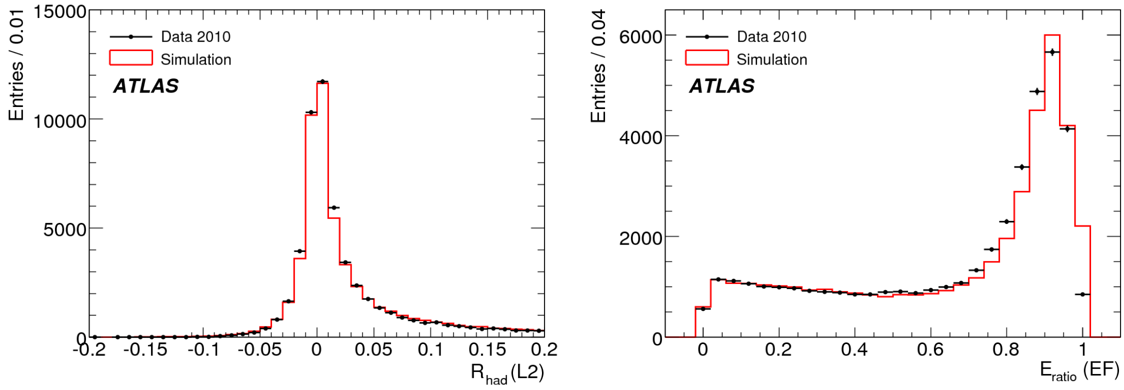

(a) (b)

Figure 1.29: Distributions of the e/γ cluster shape variables (a) R_{had} at L2 and (b) E_{ratio} at the EF for offline electrons passing the L1 EM trigger with a nominal 3 GeV threshold.

For electrons, three sets of reference cuts are defined with increasing power to reject background: *loose*, *medium*, and *tight*. All selections include the same cuts on the shower shape parameter, R_η, and hadronic leakage parameter, R_{had}, and a track broadly-matched to the cluster. The medium selection adds cuts on the shower shape in the first calorimeter layer, E_{ratio}, track quality requirements – number of hits in the pixel detector ≥ 1, number of silicon hits ≥ 7 – and stricter cluster-track matching using the strip layer of the calorimeter $\Delta\eta_1 < 0.01$. The tight selection introduces, in addition to the medium selection, requirements on the ratio of calorimeter cluster E_T to inner detector track p_T, a requirement for a hit on the innermost tracking layer, and particle identification by the TRT – an $|\eta|$ dependent cut on the number of hits in the TRT and the fraction that correspond to high-threshold hits (TR) [35].

1.4 Reconstruction of Electrons and Photons

The reconstruction of electrons [34,36] in the *central region* of $|\eta| < 2.47$ starts from clusters of energy depositions in the EM calorimeter which are subsequently paired to reconstructed tracks of charged particles in the inner detector.

To reconstruct the EM clusters, a *sliding-window* algorithm seeks seed clusters of longitudinal towers with total transverse energy above 2.5 GeV. The size of the window is 3×5 cells, each cell having dimensions 0.025×0.025 in $\eta \times \phi$, corresponding to the granularity of the calorimeter middle layer. For true electrons, the cluster reconstruction is expected to be very efficient. In MC simulations, the efficiency is about 95% at $E_{\mathrm{T}} = 5$ GeV and 100% for electrons with $E_{\mathrm{T}} > 15$ GeV from W and Z decays.

In the Inner Detector volume of $|\eta| < 2.5$, reconstructed tracks, extrapolated from their last measurement point to the middle layer of the calorimeter, are very loosely matched to the seed clusters. The distance between the impact point of the track and the position of the cluster is required to satisfy $\Delta\eta < 0.05$. The $\Delta\phi$ window is asymmetric in order to account for bremsstrahlung losses [34,36]. On the side where the extrapolated track bends as it traverses the solenoidal magnetic field the $\Delta\phi$ size is 0.1 and is 0.05 on the other side. An electron is reconstructed if at least one track is matched to the seed cluster. If several tracks are matched to the same cluster, those with silicon hits are preferred, and the track with the smallest $\Delta R = \sqrt{\Delta\eta^2 + \Delta\phi^2}$ distance to the seed cluster is selected.

The $\Delta\eta$ track-cluster matching variable used in electron reconstruction and identification is shown in Figure 1.30. Here, a sample of electron candidates collected at the end of the 2010 data taking period with $p_{\mathrm{T}} > 20$ GeV, passing the medium identification cuts to select W and Z boson decay candidates, is used. The two-peak structure for $-2.47 < \eta < -1.52$ visible on the left is due to the transverse displacement of the LAr end-cap by about 5 mm, which vanishes after the application of the ID-LAr alignment procedure – where the positions of the four independent parts of the EM calorimeter were measured with respect to the inner detector position [34] – shown by in the black data points.

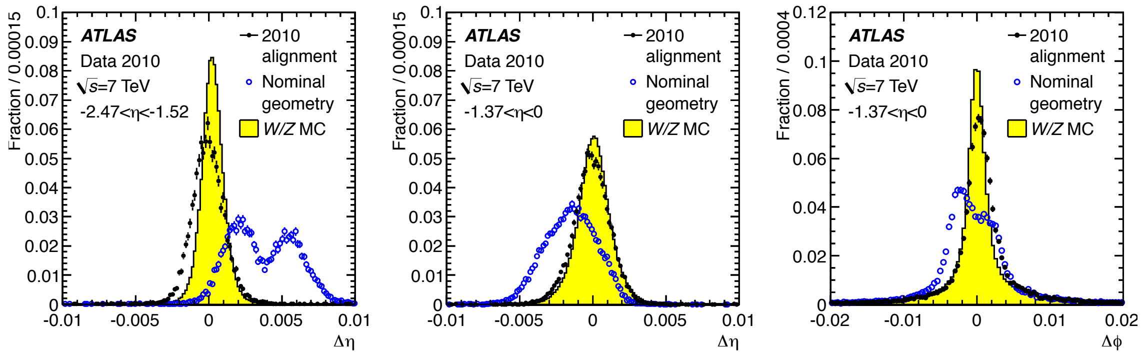

Figure 1.30: Track-cluster matching variables of electron candidates from W and Z boson decays for reconstruction with nominal geometry and after the 2010 alignment corrections have been applied: (left) $\Delta\eta$ distributions for $-2.47 < \eta < -1.52$ and (middle) $-1.37 < \eta < 0$; (right) $\Delta\phi$ distributions for $-1.37 < \eta < 0$. The MC prediction with perfect alignment is also shown

After finding a track associated to the electron, the cluster is rebuilt using 3×7 longitudinal towers of cells in the barrel or 5×5 cells in the end-caps. These lateral cluster sizes were optimized to take into account the different overall energy distributions in the barrel and end-cap calorimeters [36]. The cluster energy is then determined [22] by summing four different contributions:

1. the estimated energy deposit in the material in front of the EM calorimeter,
2. the measured energy deposit in the cluster,
3. the estimated external energy deposit outside the cluster (lateral leakage),
4. the estimated energy deposit beyond the EM calorimeter (longitudinal leakage).

The four terms are parametrised as a function of the measured cluster energies in the presampler detector –where it is present– and in the three longitudinal layers of the EM calorimeter based on detailed simulation of energy deposition in both active and inactive material in the relevant detector systems. Therefore, in order to correctly reconstruct the electron energy, it is essential to have a good description of the detector in the MC simulation.

The information from both the final cluster and the best track matched to the original seed cluster are used to calculate the four-momentum of central electrons. The energy is given by the cluster energy, while the ϕ and η directions are taken from the corresponding track parameters at the vertex.

1.4.1 Electron Identification

In the central region of pseudorapidity $|\eta| < 2.47$, the standard electron identification uses a cut-based selection that takes calorimeter, tracking and combined variables which provide good separation between isolated or non-isolated signal electrons, background electrons from photon conversions or Dalitz decays, and jets faking electrons. Identification cuts can be applied independently.

Similarly to what happens in the trigger, there are three reference sets of electron identification cuts called *loose*, *medium* and *tight* [34] according to their increasing background rejection power. The expected jet rejection based on MC simulation is about 500 for the *loose* selection, 5000 for *medium* and 50000 for *tight*. In the *loose* selection, only the shower shape variables of the EM calorimeter middle layer and the hadronic leakage variables are used. The *medium* selection includes, in addition to the loose selection, variables from the first layer of the EM calorimeter (called the strip layer because of its fine segmentation in η), track quality requirements and more stringent track-cluster matching $|\Delta\eta| < 0.01$ than the basic reconstruction match. At the *tight* selection more variables are considered: the ratio of the measured energy to the momentum, E/p; particle identification using the TRT, and discrimination against photon conversions via a B-layer hit requirement and information about reconstructed conversion vertices. The tight track-cluster matching cuts ($|\Delta\eta| < 0.005$ and $|\Delta\phi| < 0.02$) can be applied with high efficiency for data after the ID-LAr inter-alignment corrections have been implemented. Table 1.10 lists all variables used in the *loose*, *medium* and *tight* selections. The cuts have been optimised in 10 bins of cluster η, defined by calorimeter geometry, detector acceptances and regions of increasing material in the inner detector; and 11 bins of cluster E_{T} from 5 GeV to above 80 GeV.

Type	Description	Name
Loose selection		
Acceptance	$\|\eta\| < 2.47$	
Hadronic leakage	Ratio of E_T in the first layer of the hadronic calorimeter to E_T of the EM cluster (used over the range $\|\eta\| < 0.8$ and $\|\eta\| > 1.37$)	R_{had1}
	Ratio of E_T in the hadronic calorimeter to E_T of the EM cluster (used over the range $\|\eta\| > 0.8$ and $\|\eta\| < 1.37$)	R_{had}
Middle layer of EM calorimeter	Ratio of the energy in 3×7 cells over the energy in 7×7 cells centred at the electron cluster position	R_η
	Lateral width of the shower	$w_{\eta 2}$
Medium selection (includes loose)		
Strip layer of EM calorimeter	Total shower width	w_{stot}
	Ratio of the energy difference between the largest and second largest energy deposits in the cluster over the sum of these energies	E_{ratio}
Track quality	Number of hits in the pixel detector (≥ 1)	n_{pixel}
	Number of total hits in the pixel and SCT detectors (≥ 7)	n_{Si}
	Transverse impact parameter ($\|d_0\| <5$ mm)	d_0
Track–cluster matching	$\Delta\eta$ between the cluster position in the strip layer and the extrapolated track ($\|\Delta\eta\| < 0.01$)	$\Delta\eta$
Tight selection (includes medium)		
Track–cluster matching	$\Delta\phi$ between the cluster position in the middle layer and the extrapolated track ($\|\Delta\phi\| < 0.02$)	$\Delta\phi$
	Ratio of the cluster energy to the track momentum	E/p
	Tighter $\Delta\eta$ requirement ($\|\Delta\eta\| < 0.005$)	$\Delta\eta$
Track quality	Tighter transverse impact parameter requirement ($\|d_0\| <1$ mm)	d_0
TRT	Total number of hits in the TRT	n_{TRT}
	Fraction of the number of hits in the TRT with high-threshold	f_{TR}
Conversions	Number of hits in the b-layer (≥ 1)	n_{BL}
	Veto electron candidates matched to reconstructed photon conversions	

Table 1.10: Definition of variables used for *loose*, *medium* and *tight* electron identification cuts for the central region of the detector with $|\eta| < 2.47$.

1.4.2 Performance of the Tracking for Electron Reconstruction

The TRT particle identification capabilities can be used in electron identification, exploiting the emission of TR photons from electrons. Figure 1.31 shows the high-threshold probability for pions and electrons from photon conversions or Z bosons in the barrel and in the end-cap [21].

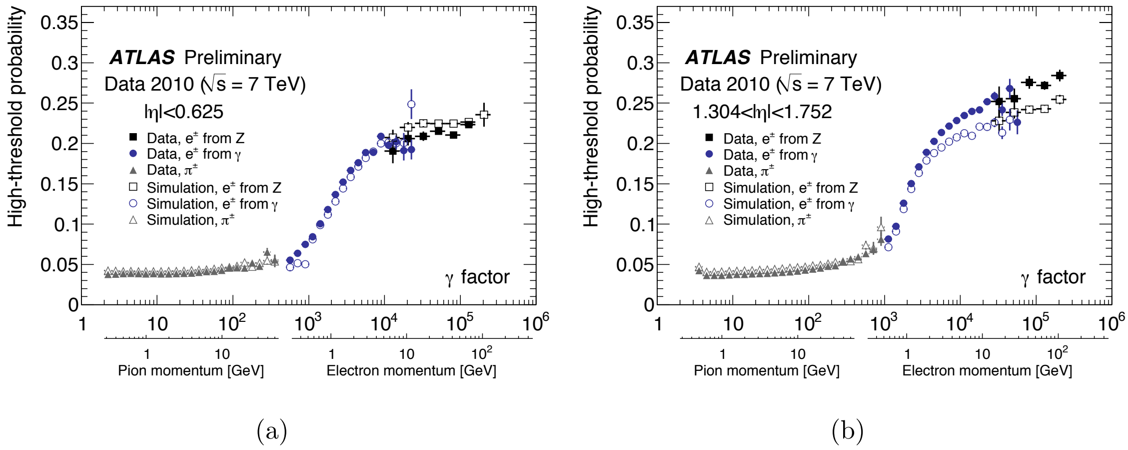

Figure 1.31: The probability per straw to measure a high-threshold hit for samples of hadrons and of electrons from reconstructed photon conversion vertices or reconstructed Z bosons where indicated (b) in the central-barrel region of the TRT ($|\eta| < 0.625$) (b) in a portion of the end-cap TRT ($1.304 < |\eta| < 1.752$) as a function of the Lorentz γ-factor of the particle.

Figure 1.32 shows the distributions of the transverse impact parameter of the electron candidate with respect to the reconstructed primary vertex of the event for candidates passing the custom identification cuts of Table 3.2 in Figure 1.32(a) and for electrons passing custom *tight* identification cuts in Figure 1.32(b), corresponding closely to Table 1.10 – which include $d_0 < 1$mm – but exceptionally require neither tight $\Delta\eta$ and $\Delta\phi$ cuts nor the conversions veto [37].

1.4.3 Performance of the LAr Electromagnetic Calorimeter for Electron Reconstruction

The fractional energy resolution in the calorimeter is parametrised as

$$\frac{\sigma(E)}{E} = \frac{a}{\sqrt{E[\text{ GeV}]}} \oplus \frac{b}{E[\text{ GeV}]} \oplus c \tag{1.1}$$

where a is the sampling term which describes the statistical fluctuations of the electromagnetic shower, b is the noise term due to the electronic noise and c is the constant term which takes into account the non uniformity of the calorimeter and of its response. The coefficients a, b and c are η dependent. The construction tolerances

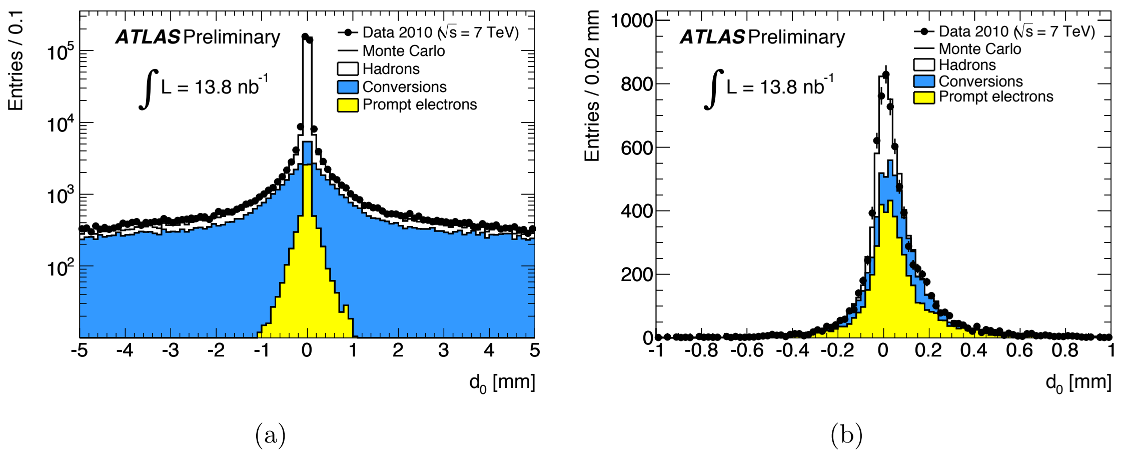

Figure 1.32: Distributions of the transverse impact parameter, d_0, with respect to the reconstructed primary vertex, for *medium* (a) and *tight* electron candidates (b).

and the calibration system ensure that the LAr calorimeter response is locally uniform within 0.5% [38], over regions of typical size $\Delta\eta \times \Delta\phi = 0.2 \times 0.4$. This uniformity is expected to be intercalibrated in situ to 0.5%, achieving a global constant term [2] of about 0.7%.

At high energies the resolution is dominated by the constant term. A significant fraction of the particle energy is lost in the inactive material in front of the calorimeter thus degrading the energy resolution because of the fluctuating loss in the energy measurement. The effective constant term, which includes both the calorimeter constant term and the effect of inhomogeneities due to possible additional material in front of the calorimeter, has been measured from the 2010 data using the invariant mass of $Z \to e^+e^-$ decays.

Two examples of the di-electron mass distribution are shown in Figure 1.33: for electrons reconstructed in the LAr electromagnetic barrel in Figure 1.33(a), and in Figure 1.33(b) for electrons reconstructed in the EM end-caps outer wheel (OW). The resolution is derived from fits to the invariant mass distributions using a Breit-Wigner convolved with a Crystal Ball function [39–41]. The Breit-Wigner width is fixed to the measured Z width, and the experimental resolution is described by the Crystal Ball function (σ). The obtained resolution for pairs with $|\eta| < 1.37$ in data corresponds to 1.62 ± 0.01 GeV and in Monte Carlo 1.45 ± 0.02 GeV, and for pairs in the end-caps

[2] The long-range constant term is the residual miscalibration between the different calorimeter regions, and the global constant term is the quadratic sum of the local and long-range constant terms

OW ($1.52 < |\eta| < 2.47$) the resolution in data is found to be 1.99 ± 0.22 GeV and in MC 1.63 ± 0.06 GeV. Figure 1.34 shows the measured di-electron mass distribution of electrons coming from $J/\psi \to e^+e^-$ decays is in good agreement with the MC prediction (both for the mean and the width). Since the electron energy resolution at these low energies is dominated by the contribution from the sampling term a, it is assumed that the term a is well described, within a 10% uncertainty, as a function of η by the MC simulation. The noise term has a significant contribution only at low energies and its effect on the measurement of the constant term cancels out to first order, since the noise description in the MC simulation is derived from calibration data runs. This implies that, for the two $|\eta|$ ranges taken as example, the effective constant term measured –which includes both the calorimeter constant term and the effect of inhomogeneities due to possible additional material– is $1.2\% \pm 0.1\%(\text{stat})^{+0.5\%}_{-0.6\%}(\text{syst})$ in the barrel and $1.8\% \pm 0.4\%(\text{stat}) \pm 0.4\%(\text{syst})$ in the end-caps OW [34].

The longitudinal development of the shower in the layers of the EM calorimeter is illustrated in Figure 1.35, based on the measured layer energies before cluster corrections are applied. For the selected sample of electron candidates passing the identification cuts of Table 3.2, most of which have $p_{\mathrm{T}} < 15$ GeV and correspond predominantly to hadrons, more than half of the total energy is deposited on average in the middle layer (f_2), a third in the strip layer (f_1), and less than 10% in the presampler(f_0). A small amount is also deposited in the back layer (f_3) [37]. Some correlated discrepancies are seen between data and simulation at large values of f_0 and small values of f_2, where MC simulations present an excess of misidentified hadrons. The fraction of the energy deposited in the first layer of the calorimeter, f_1, shows better agreement between data and MC and is the quantity used for electron identification.

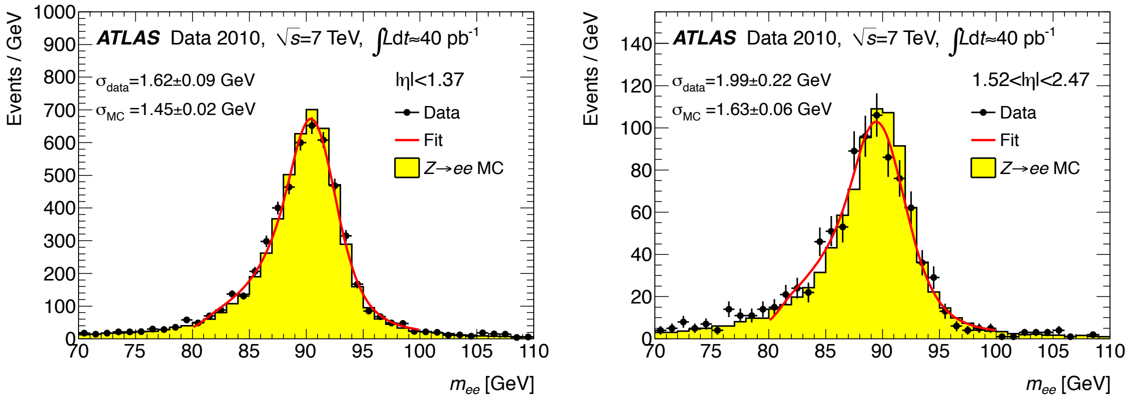

(a) (b)

Figure 1.33: Reconstructed di-electron mass distributions for $Z \rightarrow e^+e^-$ decays, for electrons in the barrel (a) and in the endcap (b) of the LAr EM calorimeter. The data points (circles) are compared to the signal MC expectation (filled histograms). The fit of a Breit-Wigner convolved with a Crystal Ball function is shown (red lines). The Gaussian width (σ) of the Crystal Ball function is given both for data and MC simulation.

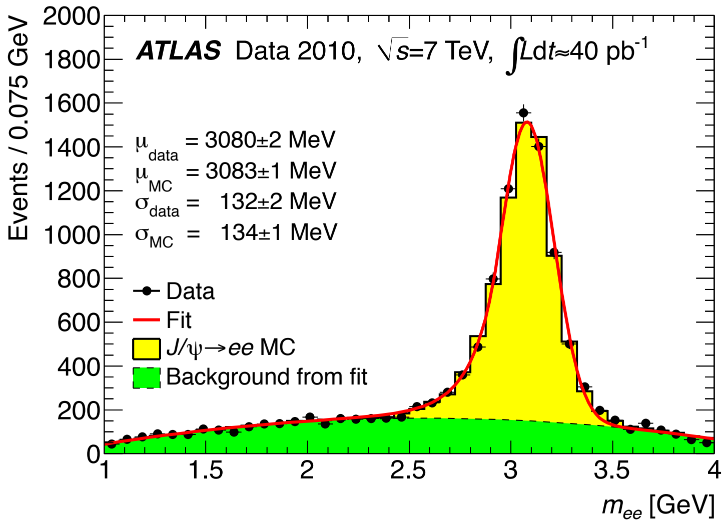

Figure 1.34: Reconstructed di-electron mass distribution for $J/\psi \rightarrow e^+e^-$ decays. The data (circles) are compared to the sum of the MC signal (light filled histogram) and the background contribution (darker filled histogram) modelled by a Chebyshev polynomial. The mean (μ) and the Gaussian width (σ) of the fitted Crystal Ball function are given both for data and MC.

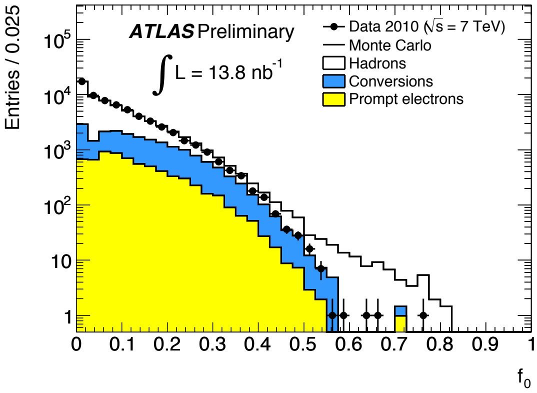

(a)

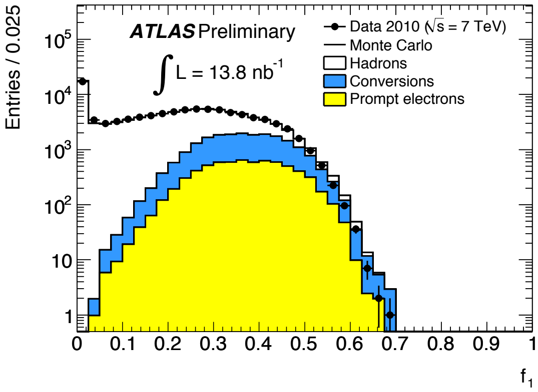

(b)

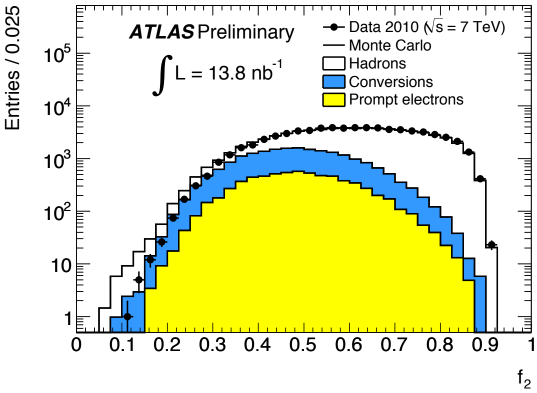

(c)

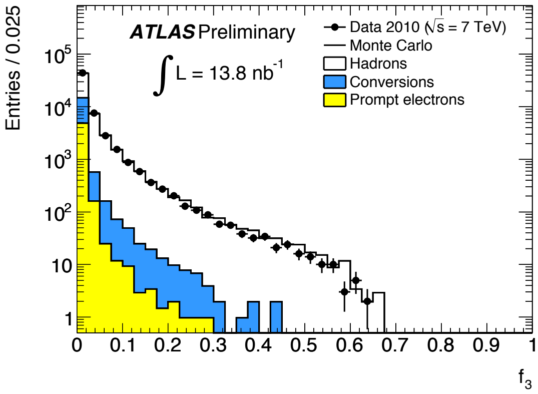

(d)

Figure 1.35: Fraction of cluster energy observed in each layer of the electromagnetic calorimeter for data and simulation. These fractions are labelled as f_0 for the presampler layer (a), f_1 for the first (strip) layer (b), f_2 for the middle layer (c) and f_3 for the back layer (d).

Chapter 2

Theoretical Motivation and Previous Measurements

The theoretical advances and experimental discoveries of thousands of physicists over the past century have resulted in a remarkable insight into the fundamental structure of matter: everything in the Universe is thought to be made from twelve basic building blocks called fermions (leptons and quarks), governed by four fundamental forces carried by vector bosons, all of which are fundamental particles. Our best understanding of how these twelve particles and three of the forces are related to each other is encapsulated in the Standard Model (SM) of particles and forces. Developed from the late 1960s, it has successfully explained a host of experimental results and precisely predicted a wide variety of phenomena. Over time and through many experiments by many physicists, this theory has become well-established and, as a consequence, is now known as "standard".

In this chapter the formalism of gauge theories, in particular quantum chromodynamics (QCD), is reviewed. The properties of QCD and the application of perturbation theory and Monte Carlo (MC) models to predict heavy-flavour production in hadronic collisions are described. Finally a synopsis of previous measurements of heavy-flavour production in hadronic collisions is given.

2.1 Standard Model

The SM of particle physics is one of the most successful theories in physics. Almost all of the particles predicted by this model have been found, with the exception of the Higgs boson, although an observation by the ATLAS and CMS experiments at the

LHC of a new particle that seems to be consistent with the Higgs boson definition was recently announced (July 2012) [42, 43]. Nearly every observation in particle physics can be explained by this model with the exception of neutrino oscillations, which implies that neutrinos are massive, and the anomalous magnetic moment of the muon where theory and experiment differ by 3.6σ with the biggest uncertainty coming from the theoretical calculation of the hadronic loop contributions to the vacuum polarization [44].

The SM is a gauge theory with $SU(3)_C \otimes SU(2)_L \otimes U(1)_Y$ as its symmetry group. The first factor $SU(3)_C$ is the symmetry group of Quantum Chromodynamics (QCD) which governs the strong interactions observable in atomic nuclei and its component nucleons. The combination of the other two factors $SU(2)_L \otimes U(1)_Y$ corresponds to the symmetry group of the electroweak (EW) theory, where L represents the fact that only the fields with *left chirality* are $SU(2)$ doublets, while right handed fields are singlets. The EW symmetry is spontaneously broken through the Higgs-Englert-Brout mechanism [13, 14] into the weak and electromagnetic interactions leaving the electromagnetic $U(1)_{e.m.}$ gauge group as a valid symmetry of the theory, giving mass to the weak gauge bosons $W^{\pm}$ and Z and predicting the existence of a fundamental scalar particle, the Higgs boson [15].

2.1.1 Fermions

In the SM, all ordinary matter is composed of fermions, particles with spin $\frac{1}{2}$ in units of the Planck constant $\hbar$ that obey the Pauli principle: no two identical fermions can be in the same quantum state. There are two types of fermions in the SM: leptons, which have integral electric charge in units of the elementary charge e of the electron; and quarks, which have fractional electric charge and participate in strong interactions. The current knowledge of the particle landscape is that there are three generations – or families – of fermions, shown in Table 2.1 for the leptons and in Table 2.2 for quarks, in addition to their anti-particles [45].

Each lepton generation is composed of a charged particle – electron, muon or tauon – and its neutral partner, the neutrino, which participates only in weak interactions. The electron is the lightest charged lepton and is stable, whereas the muon and the tauon have larger masses and can decay through weak interactions into electrons, neutrinos or other particles with a lifetime of $2.2\,\mu$s for muons and $2.91 \times 10^{-13}\,$s for tauons. Neutrinos, on the other hand, are massless in the SM; however, recent experiments on solar [46–52], atmospheric [53, 54] , reactor [55–58] and accelerator neutrinos [59–61] have demonstrated that they oscillate (i.e. they change their flavour

name	symbol	spin	charge [$\|e\|$]	mass [MeV]
electron	e^-	1/2	-1	$0.511 \pm O(10^{-8})$
electron neutrino	ν_e	1/2	0	$< 2 \times 10^{-6}$
muon	μ^-	1/2	-1	$105.66 \pm O(10^{-6})$
muon neutrino	ν_μ	1/2	0	—
tauon	τ^-	1/2	-1	1776.82 ± 0.16
tau neutrino	ν_τ	1/2	0	—

Table 2.1: The leptons of the SM, electrons, muon and tauon and the three accompanying neutrinos. Source [44].

as they travel in space-time) which implies that the flavour eigenstates of neutrinos ν_e, ν_ν and ν_τ are linear combinations of mass eigenstates ν_1, ν_2 and ν_3. Cosmological principles limit the sum of the neutrino masses to be smaller than 11 eV and direct tritium decay measurements put an upper limit on the mass of the electron neutrino at 2 eV, while the measurements of their oscillations give information on the mass differences: $\Delta m^2_{21} = (7.50 \pm 0.20) \times 10^{-5}$ eV^2 and $|\Delta m^2_{32}| = (2.32^{+0.12}_{-0.08}) \times 10^{-3}$ eV^2, and on their mixing angles[1]. The SM also includes the anti-leptons, which have the same mass and lifetime as the leptons but have the opposite charge. These anti-particles are the positron e^+, anti-muon μ^+, anti-tauon τ^+ and the anti-neutrinos $\overline{\nu}_e$, $\overline{\nu}_\mu$ and $\overline{\nu}_\tau$. Every lepton has lepton number $L = +1$ and all anti-leptons have $L = -1$, an additive quantum number which is conserved in the SM. Furthermore, the lepton family numbers L_e, L_μ and L_τ, defined in a similar way for each lepton generation, are also conserved.

Quarks are the fundamental fermions that compose nucleons. Table 2.2 shows the properties of the three generations of quarks known in the SM, each one consisting of one quark with charge $-\frac{1}{3}$ and one quark with charge $+\frac{2}{3}$ in units of the elementary charge. Every quark has baryon number $\mathcal{B} = \frac{1}{3}$ and has an internal quantum number (QN) relating to its *flavour*: for up (u) and down (d) quarks this QN is the isospin I_z equal to $\frac{1}{2}$ or $-\frac{1}{2}$, respectively. For the other quarks it is almost equivalent with their name: S – strangeness – for the s quark, C – charm – for the c quark, T – top – for the t quark and B – bottom (or beauty) – for the b quark; all of which, by convention , have the same sign as the charge of the quark. The SM also includes the anti-particles of quarks, the antiquarks $\overline{q}$, which have opposite charge, baryon number and flavour QN, but the same mass, as the quark. The relation between the charge of the quark and its quantum numbers is given by the Gell-Mann-Nishijima formula shown in equation 2.1, where $\mathcal{B}$ is the baryon number [44, 45].

[1] $\Delta m^2_{ij} \equiv m^2_{\nu_i} - m^2_{\nu_j}$, where m_{ν_i} with $i = 1, 2, 3$ are the neutrino mass eigenvalues.

$$Q = I_z + \frac{1}{2}(\mathcal{B} + S + C + B + T) \tag{2.1}$$

name	symbol	spin	charge [$\|e\|$]	$\mathcal{B}$	mass [GeV]	flavour QN
up	u	1/2	$+\frac{2}{3}$	1/3	$2.3^{+0.7}_{-0.5} \times 10^{-3}$	$I_z = +\frac{1}{2}$
down	d	1/2	$-\frac{1}{3}$	1/3	$4.8^{+0.7}_{-0.3} \times 10^{-3}$	$I_z = -\frac{1}{2}$
charm	c	1/2	$+\frac{2}{3}$	1/3	1.275 ± 0.025	$C = +1$
strange	s	1/2	$-\frac{1}{3}$	1/3	$(95 \pm 5) \times 10^{-3}$	$S = -1$
top	t	1/2	$+\frac{2}{3}$	1/3	$173.5 \pm 0.6 \pm 0.8$	$T = +1$
bottom	b	1/2	$-\frac{1}{3}$	1/3	4.18 ± 0.03	$B = -1$

Table 2.2: The quarks of the Standard Model. The u, d, and s-quark masses are estimations of so-called "current quark masses", in the MS renormalization scheme at a scale $\mu \sim 2$ GeV. The value for the top quark mass is the measured one and the value for the bottom quark mass corresponds to the $\overline{MS}$ renormalization scheme. Source [44].

Theoretically, quarks cannot be found free; they are restricted to exist only grouped together in *hadrons*, bundles of two or three quarks. The only exception is the top quark, which decays too quickly to form hadrons; however, the top quark is only indirectly detected via its decay products and as a result it has not been observed as a free particle. Hadrons made of a quark and an anti-quark are called *mesons* and have integer spin, therefore correspond to composite bosons. When three quarks are grouped together they form a *baryon* which has half-integer spin; hence baryons are fermions. Protons, for example, are baryons made mainly of *uud*; since the two up quarks are, in principle, indistinguishable, there must be an additional internal quantum number preventing them to occupy the same quantum state, and that is called the *colour charge* of QCD. More details on the dynamics of quarks and colour are discussed in Section 2.2.

2.1.2 Bosons

Elementary gauge bosons in the SM act as force carriers: the photon is the carrier of electromagnetic interactions, the massive vector bosons $W^{\pm}$ and Z mediate the weak interactions, and the gluons – of which there are 8 *color* combinations – carry the strong force. The underlying $SU(2)_L \otimes U(1)_Y$ electroweak symmetry of the SM is in reality broken, but gauge invariance of the electromagnetic $U(1)_{e.m.}$ symmetry is maintained. This is indicated by the fact that the photon is massless, but the weak bosons are heavy. A theoretical mechanism to break EW symmetry maintaining gauge invariance was provided by the Higgs-Englert-Brout mechanism for *spontaneous symmetry breaking*, introducing a scalar field with a non-zero vacuum expectation value in the Glashow-Salam-Weinberg model [62–64]. In this way the masses of the heavy vector bosons were predicted, leading to their discovery in 1983 by the UA1 and UA2 experiments at the Sp$\overline{\text{p}}$S collider [65–69]. A consequence of the Higgs-Englert-Brout mechanism is the existence of a fundamental scalar particle, the Higgs boson, but the theory does not predict its mass. The existence of a new boson with a mass ~ 126 GeV has been shown by the ATLAS and CMS collaborations during this year, however the collaborations need to measure its properties in greater detail in order to conclude with reasonable precision whether it is compatible with the definition of the SM Higgs particle [42, 43]. Table 2.3 shows the charge, spin and mass of the gauge bosons of the SM, and the allowed mass range for the Higgs boson, derived from the observations of ATLAS and CMS. Gluons, shown as g_a, are electrically neutral but carry color charge in the form of 8 colour-anticolour combinations, called the color octet, more details of which are given in the following section.

name	symbol	spin	charge [$\|e\|$]	mass [GeV]
photon	γ	1	0	0
W-boson	$W^{\pm}$	1	± 1	80.385 ± 0.015
Z-boson	Z	1	0	91.1876 ± 0.0021
gluons	g_a	1	0	0
Higgs boson	H	0	0	$124.7 < m_H < 126.6$

Table 2.3: The gauge bosons of the Standard Model and the Higgs boson. For the latter, the allowed mass range as determined by the observations of the LHC experiments is shown. The index a in the gluons indicates the existence of 8 bi-chromatic states. Source [44] for gauge bosons and [42, 43] for the Higgs mass range.

2.2 QCD

Quantum Chromodynamics is the gauge theory that describes the strong interactions. It is based on the non-abelian symmetry group $SU(3)_C$, where the charge involved is called *colour* and the gauge bosons that mediate colour-exchange are called *gluons*. The colour charge of a quark can have three values that can be arbitrarily named red (R), blue (B) and green (G); while antiquarks carry anti-colour: $\overline{\text{R}}$, $\overline{\text{B}}$ and $\overline{\text{G}}$ in the notation above.

The Lagrangian of QCD is given by:

$$\mathcal{L}_0^{QCD} = \sum_j \overline{q}_{j,a} \left(i\gamma^\mu \partial_\mu \delta_{ab} - g_s \gamma^\mu \left(\frac{\lambda}{2}\right)^C_{ab} \mathcal{A}_\mu^C - m_{q_j} \delta_{ab} \right) q_{j,b} - \frac{1}{4} G^A_{\mu\nu} G^{\mu\nu}_A, \tag{2.2}$$

where a sum over repeated indices is implied. The $q_{j,a}$ are the spinor fields for a quark of flavour j and mass m_{q_j}, with colour index a running from 1 to $N_C = 3$. The γ^μ are the Dirac γ-matrices. The gluon field is represented by the term $\mathcal{A}_\mu^C$, where the index C runs from 1 to $N_C^2 - 1 = 8$, i.e. there are eight kinds of gluon. In this term g_s is the strong coupling constant of QCD. The $\frac{\lambda}{2}^C$ are the generators of the $SU(3)$ group in the fundamental representation: eight 3×3 matrices, that verify the commutation relation

$$\left[\frac{\lambda}{2}^A, \frac{\lambda}{2}^B \right] = i f_{ABC} \frac{\lambda}{2}^C, \tag{2.3}$$

where f^{ABC} are the structure constant of SU(3). In this case the matrices λ are chosen as the Gell-Man matrices [70]. Finally the field tensor $G^A_{\mu\nu}$ is given by:

$$G^A_{\mu\nu} = \partial_\mu \mathcal{A}^A_\nu - \partial_\nu \mathcal{A}^A_\mu - g_s f_{ABC} \mathcal{A}^B_\mu \mathcal{A}^C_\nu. \tag{2.4}$$

The Feynman rules derived from the Lagrangian of equation 2.2 include a quark-antiquark-gluon ($q\overline{q}g$) vertex with strength g_s, from the second term; and, from the last term, a triple gluon vertex with strength g_s and a quartic gluon vertex with strength g_s^2.

In analogy to the fine structure constant of quantum electrodynamics, sometimes the coupling is substituted by [71]:

$$\alpha_s \equiv \frac{g_s^2}{4\pi}. \tag{2.5}$$

In order to quantize the QCD Lagrangian properly, two terms need to be added: one to fix the gauge and the so-called *Fadeev-Popov* term that introduces non-physical fields called *ghosts*:

$$\mathcal{L}_{QCD} = \mathcal{L}_0^{QCD} + \mathcal{L}_{GF} + \mathcal{L}_{ghost}. \tag{2.6}$$

The following section explains how the formalism of QCD can be used in perturbation theory to make predictions for physical observables.

2.2.1 Perturbative QCD and Renormalization

When calculating physical observables using perturbation series expansion in the coupling α_s, divergences appear as a result of one or more quantum-loop corrections, as in Figure 2.3(b), which integrate over infinite momenta inside the loop. In order to obtain a physical result, it is necessary to introduce *renormalization* in order to remove the divergences.

The renormalization procedure introduces a mass scale, called the *renormalization scale* μ_R, the point at which the divergences are subtracted. QCD is said to be a renormalizable theory because all *ultraviolet divergences* can be reabsorbed by redefining the fields and the couplings. Therefore the parameters of the QCD Lagrangian – the strong coupling constant and the quark masses – are redefined into a running coupling and running masses that depend on the renormalization scale and on the chosen *renormalization scheme*. Measurable physical quantities calculated in perturbative QCD (pQCD) are expressed as a function of the renormalized coupling $\alpha_s(\mu_R^2)$.

2.2.2 Running Coupling and Asymptotic Freedom

As a consequence of renormalization, the coupling $\alpha_s(\mu_R)$ can be calculated as a function of the renormalization scale μ_R through the *Renormalization Group Equation* (RGE):

$$\mu_R^2 \frac{d\alpha_s}{d\mu_R^2} = \beta(\alpha_s) = -(b_0\alpha_s^2 + b_1\alpha_s^3 + b_2\alpha_s^4 + ...), \tag{2.7}$$

where b_0 is the 1-loop beta-function coefficient given by

$$b_0 = \frac{33 - 2n_f}{12\pi}, \tag{2.8}$$

for QCD (as a consequence of $SU(3)$ symmetry), where n_f is the number of active quark flavours (in the case of pQCD this is 5, i.e. all quarks except the top, whose mass is too large and is considered decoupled). The subsequent beta-function coefficients for two and three loops are b_1 and b_2, and so on and so forth in the perturbative expansion, which can be found in the literature [72].

Equation 2.7 can be solved at 1-loop, taking only the b_0 term and neglecting the rest, to obtain

$$\alpha_s(Q^2) = \frac{\alpha_S(\mu^2)}{1 + \alpha_s(\mu^2) b_0 \ln\left(\frac{Q^2}{\mu^2}\right)} \tag{2.9}$$

where Q is the scale of the momentum transfer in a process, μ is an arbitrary scale and $\alpha_s(Q^2)$ gains the physical meaning of the running coupling: the effective coupling strength which varies according to the energy of a process. This does not completely fix the equation, but once α_s is measured at a certain scale, the value at different scales can be predicted. In order to illustrate the divergence as Q^2 decreases, it is convenient to define a new scale Λ:

$$\Lambda = \frac{\mu^2}{\mathrm{e}^{1/b_0 \alpha_s(\mu^2)}}, \tag{2.10}$$

thus transforming equation 2.9 to

$$\alpha_s(Q^2) = \frac{1}{b_0 \ln\left(\frac{Q^2}{\Lambda^2}\right)}. \tag{2.11}$$

From equation 2.9 one can conclude that the fact that b_0 is positive for $n_f < 16$ implies that as Q^2 increases the coupling $\alpha_s(Q^2)$ decreases, which is called the *asymptotic freedom* and is a feature of non-abelian gauge theories. In practice this means that the strong coupling becomes weak for processes involving large momentum transfers, therefore allowing the use of perturbation theory for so-called “hard processes”. On the other hand, it can be seen from equation 2.11 that when Q^2 approaches Λ, the coupling constant goes to infinity, as a result this is an energy scale at which perturbation theory is no longer valid. This is identified as the non-perturbative QCD region where *quark confinement* sets in, and the equations above are no longer valid to make accurate predictions.

Figure 2.1 shows the measurements of the strong coupling constant in different processes as a function of the energy scale, Q, of each measurement. The label specifies the order of QCD perturbation theory used in the extraction of α_s for each measurement, indicated in brackets. LO or leading-order corresponds to the first non-zero contribution in an expansion in powers of α_s. NLO means next-to-leading order, for example for an observable with LO $\propto \alpha_s$, this would be up to the term $\propto \alpha_s^2$. NNLO corresponds to a calculation at next-to-next-to leading order, whereas the label "res. NNLO" means NNLO matched with resummed next-to-leading logs and N^{3}LO is next-to-NNLO. The figure shows how as the scale of the process becomes smaller the value of α_s gets larger, and at $Q < 1$ GeV the approximation $\alpha_s \ll 1$ does not hold.

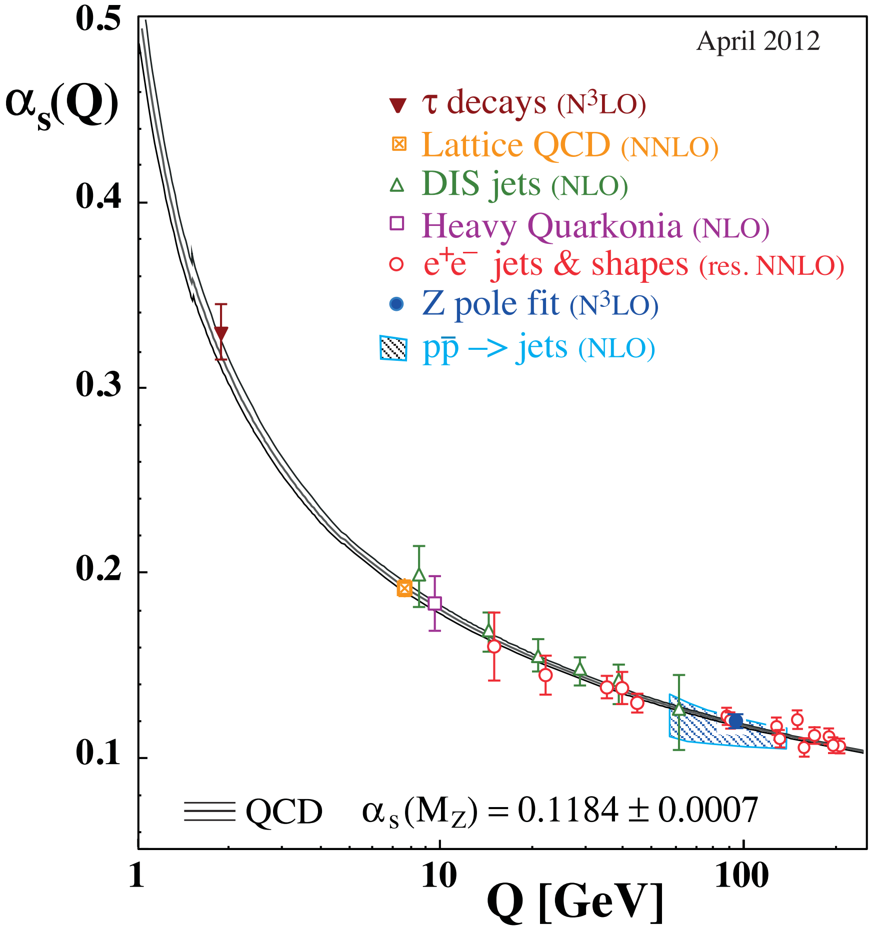

Figure 2.1: Summary of measurements of α_s as a function of the respective energy scale of the measurement Q. Source: Particle Data Group [44].

2.3 Heavy-Flavour Hadroproduction

Theoretical calculations of processes involving the charm, bottom and top quarks (jointly called heavy-flavour) can fully exploit the tools of perturbative QCD. Since the strong coupling constant α_s is small at the scale of the heavy quark masses, observables like cross-sections can be estimated in powers of α_s. Thus the study of heavy-flavour processes can probe the validity of perturbative QCD predictions when contrasting the theoretical predictions with heavy-flavour measurements. The main leading-order (LO, also known as Born-level) Feynman diagrams for heavy-flavour pair production ($Q\overline{Q}$) in pp collisions are displayed in Figure 2.2. Next-to-leading order (NLO) processes can provide large corrections which must be included in order to have an accurate description of the process.

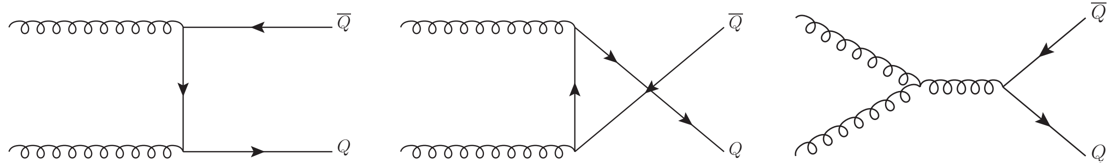

(a)

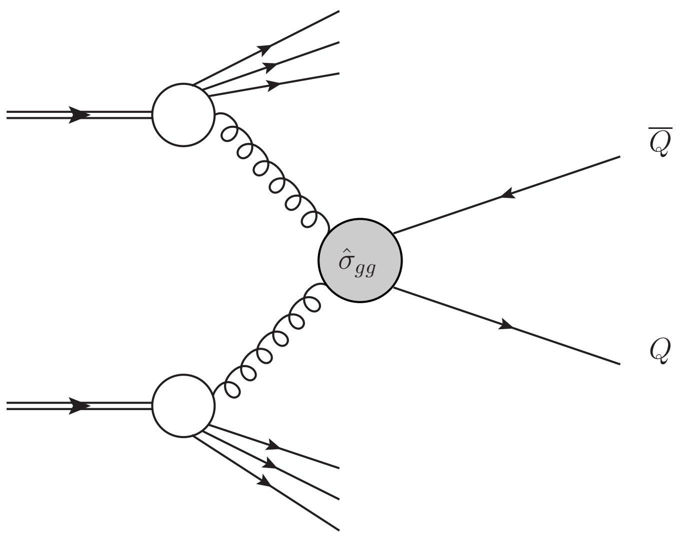

(b)

Figure 2.2: (a) Leading-order Feynman diagrams for the production of $Q\overline{Q}$ pairs via $gg \to Q\overline{Q}$ in pp collisions. The shaded circle in (b) corresponds to the three processes in (a) as a part of hadron collisions.

The state-of-the art calculations at NLO can produce inclusive observables (for example, the cross-section as a function of p_{T} of a final state particle) or they can produce fully exclusive observables by matching perturbative NLO calculations at parton level to Parton Shower Monte Carlos (PSMCs). In the first category are the `FONLL` framework [2, 9, 11] and the general-mass variable-flavour-number scheme (`GM-VFN`) [73,74], for example. In the second class are found NLO MC generators such as `POWHEG` [75, 76], which can be interfaced with `PYTHIA` [77] or `HERWIG` [78] for the parton shower, or `MC@NLO` [79, 80] which is interfaced with `HERWIG`. When using MC simulations, current tools allow to include detector-level simulation using `GEANT4` [81] to compare directly to the observed data. In the following, the two approaches will be outlined for the implementation of `FONLL` for the inclusive prediction and `POWHEG` for the generation of exclusive observables at NLO, which are used later on in the comparison with ATLAS results.

Figure 2.3 shows two examples of NLO contributions to the $Q\overline{Q}$ production cross-section: 2.3(a) for the case of real gluon emission, which are corrections of order $\mathcal{O}(\alpha_s^3)$; and 2.3(b) for virtual gluon emission, giving terms of order $\mathcal{O}(\alpha_s^4)$ that must be included together with the Born-level amplitude diagrams to account for interference. Including these higher order corrections improves predictions and reduces theoretical uncertainties.

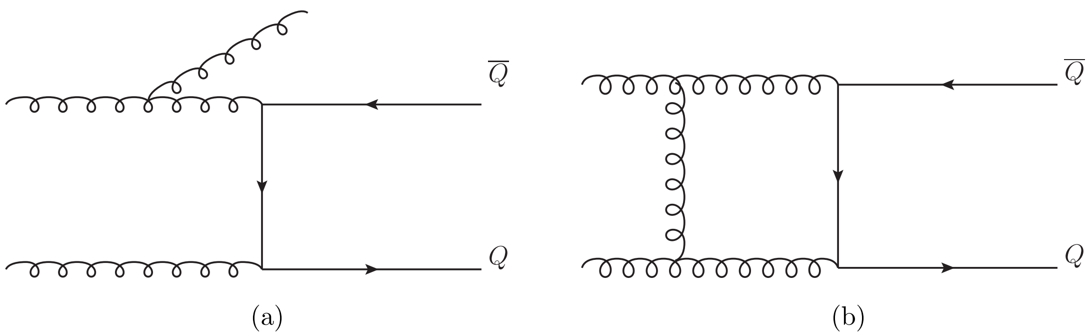

Figure 2.3: Examples of next-to-leading order Feynman diagrams for the production of $Q\overline{Q}$ with (a) a real gluon and (b) a virtual gluon emission.

2.3.1 FONLL

The "Fixed-Order + Next to Leading Log" (FONLL) framework for the calculation of heavy-flavour production is based on three main components:

The heavy-quark production cross-section $\mathrm{d}\sigma_{\mathbf{Q}}^{\mathbf{FONLL}}$ is calculated in pQCD by matching the Fixed Order NLO terms with NLL high-p_{T} resummation. The fixed-order NLO component, that uses a power expansion in α_s evaluated at $\mu_R \sim m_Q$ [82, 83] is appropriate when the mass scale is close to the heavy-quark mass, but fails when $p_{\mathrm{T}} \gg m_Q$, since large logarithms of the ratio p_{T}/m_Q appear [9].

On the other hand, in the limit where $p_{\mathrm{T}} \gg m_Q$ a *resummation formalism* can be used to compute the pQCD cross-section, where so-called *perturbative fragmentation functions* (PFF) can be derived from QCD first principles. Normally, one understands a fragmentation function $D_i^h(z, \mu_F^2)$ as the probability that a parton i *fragments* into a hadron h with a fraction z of its momentum, at a factorization or fragmentation scale μ_F; the fragmentation function usually depend on the *factorization scheme*. In this formalism, however, the cross-section is factorized into a partonic cross-section calculated to NLO, where all partons are produced as "massless" (i.e. contributions of order m_Q/p_{T} are not included), and a fragmentation function for the produced parton to fragment into a massive heavy quark, i.e.

$$\mathrm{d}\sigma_Q^{FONLL} \approx \int \mathrm{d}\hat{\sigma}_i^{NLO} \times D_i^Q(z, \mu_F^2). \tag{2.12}$$

The fragmentation functions that describe the $i \to Q$ step are calculable from QCD at an initial state with scale $\mu_0 \sim m_Q$, and then evolved through DGLAP evolution equations to the desired factorization scale μ_F [84]. The cross-section is then numerically evaluated and has been shown to be reliable in the large p_{T} region [9, 84].

In order to merge the fixed-order NLO (FO) approach, which is valid when the energy scale $\sim m_Q$, and the resummation formalism (RF), that suits better when $p_{\mathrm{T}} \gg m_Q$, a matching is devised. First the FO calculation is brought to the same renormalization scheme as was used in the RF (minimal subtraction $\overline{MS}$), and the number of flavours considered in the evolution of α_s is increased, since in the RF the heavy-flavour quark is considered an active light flavour. Then the FO computation is evaluated at the "massless limit" (FOM0), in order to subtract from the RF result the contributions which are already included in the full FO calculation, and avoid double counting of the logarithmic terms up to order α_s^3 [9]. The result of the resummation approach can be expressed in powers of α_s and $\log p_{\mathrm{T}}/m_Q$ by solving the DGLAP evolution equations iteratively. At this point the terms up to order α_s^3 can be identified to cancel exactly those in the FOM0 limit, while the remaining terms of the RF calculations are added to the FO calculation, resulting in the FONLL prediction. The logarithms resummed up to next-to-leading accuracy are of the form $\alpha_s^n \log^n(p_{\mathrm{T}}/m_Q)$ and $\alpha_s^n \log^{n-1}(p_{\mathrm{T}}/m_Q)$. Thus the accuracy of the FONLL calculation is labelled as being NLO+NLL.

In the FONLL framework, one-particle inclusive distributions of a heavy quark can be calculated while integrating over the degrees of freedom of the other particles in the event. This has the drawback that heavy quark-antiquark correlations cannot be studied in this approach.

The non-perturbative heavy-flavour fragmentation functions $\mathbf{D^{NP}_{Q\rightarrow H_Q}}$, which describe the fragmentation of the heavy-flavour quark Q in to the heavy-flavour hadron H_Q, are determined from e^+e^- collisions and extracted in the same framework. This is done by using a calculation with accuracy at NLO+NLL, in this framework, of heavy-flavour production in e^+e^- collisions, convoluted with a parametrization of the non-perturbative fragmentation functions $D^{NP}_{Q\rightarrow H_Q}(v)$ and using a fit procedure to extract the parameters from LEP and SLC data [85]. The chosen functional form for the parametrization of the non perturbative fragmentation function for bottom production is a Kartvelishvili et al. distribution [86]

$$D^{NP}_{b\rightarrow H_b} = (\alpha+1)(\alpha+2)x^{\alpha}(1-x). \tag{2.13}$$

The central value of $m_b = 4.75$ GeV is chosen, for which the value obtained in the e^+e^- data fits performed in [85] is $\alpha = 24.2$. For charm production the picture is more complex. Three fragmentation functions are used $D^{NP}_{c\rightarrow D^*}$, $D^{NP}_{c\rightarrow D^+}$ and $D^{NP}_{c\rightarrow D^0}$, which are theoretically related. In this manner, a single parameter was extracted from $c \rightarrow D^*$ fragmentation from ALEPH data and used for the construction of the three non-perturbative fragmentation functions through their theoretical relations [87], using branching ratios extracted from data when necessary. The value of the parameter in question, r, obtained in the fit is 0.1 for a charm quark with mass $m_c = 1.5$ GeV [2] for Mellin moment with $N = 5$. Then, in order to obtain the FONLL prediction for the H_Q hadron spectrum, the FONLL quark spectra is convoluted with the appropriate non-perturbative fragmentation function for $Q \rightarrow H_Q$.

The weak decays of the heavy hadrons to leptons $g^{weak}_{H_Q \to l}$ can be included using decay tables and form factors from B-factories, in such a way to have a prediction for the p_{T} spectrum of leptons from heavy-flavour production.

The `FONLL` prediction for a single inclusive distribution of a lepton l can be written as the numerical convolution of the three contributions listed above, i.e.

$$d\sigma^{FONLL} = d\sigma^{FONLL}_{Q} \otimes D^{NP}_{Q \to H_Q} \otimes g^{weak}_{H_Q \to l}. \tag{2.14}$$

2.3.1.1 Systematic Uncertainties of the `FONLL` Prediction

The central value of the `FONLL` prediction is calculated using the renormalization (μ_R) and factorization (μ_F) scales fixed to $\mu_0 = \sqrt{p_{\mathrm{T}}^2 + m_Q^2}$, where p_{T} is the heavy-quark transverse momentum and m_Q its mass; the bottom and charm masses are chosen as $m_b = 4.75$ GeV and $m_c = 1.5$ GeV and the proton Parton Distribution Function (PDF) used is `CTEQ6.6`, with a value for the strong coupling constant $\alpha_s = 0.118$. The following systematic uncertainties are evaluated by varying the choices of scales, quark masses and PDFs:

- The dominant theoretical uncertainty comes from the renormalization (μ_R) and factorization (μ_F) scales and amounts to less than 35% for a lepton with $p^l_{\mathrm{T}} > 7$ GeV, as shown in Figure 2.4. The scale uncertainty is determined by changing the scales independently within $0.5 < \xi_{R,F} < 2.0$ – with $\xi_{R,F} \equiv \mu_{R,F}/\mu_0$ – while keeping the relation $0.5 < \xi_R/\xi_F < 2.0$. More specifically, the seven points

$$(\xi_R, \xi_F) \in \{(1,1), (0.5,0.5), (2,2), (0.5,1), (1,0.5), (2,1), (1,2)\}, \tag{2.15}$$

  are evaluated while leaving the other variables fixed at their central values. The envelope of all variations in σ,

$$\Delta\sigma^{+,scales}_{-,scales}, \tag{2.16}$$

  is taken as the uncertainty.

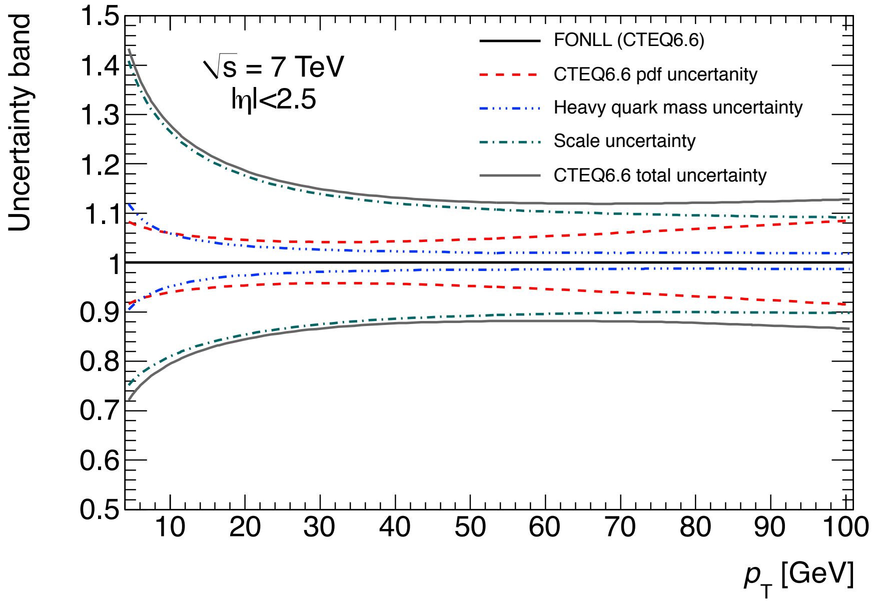

Figure 2.4: Uncertainties on the FONLL theoretical prediction of the charged lepton p_{T} distribution from heavy-flavour decays for leptons with $|\eta| < 2$, excluding the $1.37 < |\eta| < 1.52$ region. The uncertainty bands from different sources are normalized to the central prediction. The total uncertainty is indicated by the full red curve.

- The heavy quark masses are set to $m_b = 4.75 \pm 0.25$ GeV and $m_c = 1.5 \pm 0.2$ GeV, whereupon the parameters of the non-perturbative fragmentation functions for B and D hadrons are adjusted [2, 85]. For a bottom-quark mass of $m_b =$ 4.5 GeV, the NP parameter is $\alpha = 26.7$ and for $m_b = 5$ GeV, $\alpha = 22.2$. For the charm-quark variation, the value obtained at $m_c = 1.3$ GeV is $r = 0.06$ and for $m_c = 1.7$ GeV the parameter is $r = 0.135$ [2]. The sensitivity of the cross-section to the heavy quark mass value reduces at large p_{T} as a consequence of this adjustment, arising from the fact that neither the heavy quark mass nor the non-perturbative fragmentation are physical observables and therefore their variations must compensate each other in their interplay [2]. The envelope of the variations,

$$\Delta\sigma^{+,masses}_{-,masses}, \tag{2.17}$$

is taken as the associated uncertainty. The largest effect of the heavy-quark mass variation is seen at low p_{T}, giving 7% uncertainty at 7 GeV, which decreases to 3% at 25 GeV, as seen in Figure 2.4.

- The PDF related uncertainty of the predictions of three different NLO sets, `CTEQ6.6` [88], `MSTW2008` [89] and `HERAPDF1.0` [90] with their corresponding 1σ error eigenvectors are compared in Figure 2.5, and found to be below 6% in the p_{T} range $7 < p_{\mathrm{T}} < 26$ GeV. The variation in the cross-section prediction from the `CTEQ6.6` PDF uncertainty is taken as the associated uncertainty,

$$\Delta\sigma^{+,PDF}_{-,PDF}. \tag{2.18}$$

- The systematic uncertainties due to the value of α_s are estimated with the `CTEQ6.6AS` [91] set, which covers α_s values in the range $0.116 < \alpha_s < 1.120$, and are found to be negligible – about 1% – as shown in Figure 2.5.

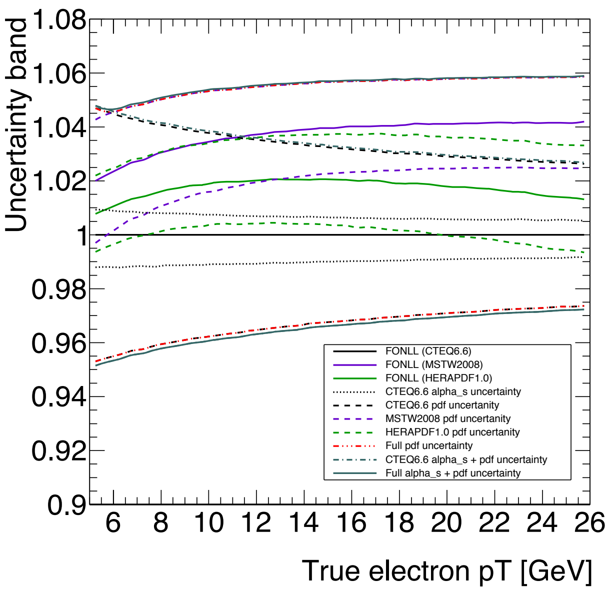

Figure 2.5: Uncertainties on the `FONLL` theoretical prediction of the charged lepton p_{T} distribution arising from α_{s} and PDF uncertainties.

The total uncertainty is calculated as the quadratic sum of the scale, quark mass and PDF uncertainties,

$$\Delta_{\pm} = \sqrt{\Delta^2_{\pm,PDFs} + \Delta^2_{\pm,masses} + \Delta^2_{\pm,scales}}, \tag{2.19}$$

where $\Delta_{\pm,X} = \dfrac{\Delta\sigma_{\pm,X}}{\sigma}$ is the fractional uncertainty from source X. The typical uncertainty is 20%, rising above 30% at low p_{T}, as shown in Figure 2.4 [2, 12].

2.3.2 Monte-Carlo Event Generators

2.3.2.1 Parton Shower Monte Carlo Generators

PSMC event generators – like `PYTHIA` [77], `HERWIG` [78], and `SHERPA` [92] – provide fully exclusive simulations of QCD events, such as hadron collisions. They are a crucial tool for all applications that involve simulating the response of detectors to QCD events, because they provide access to an event at the "hadron-level".

The MC generation of an event starts with the random generation of the kinematics and partonic channels of a hard scattering process requested at some high scale Q_0. This is followed by a parton shower, usually based on the successive random generation of gluon emissions or $g \to q\bar{q}$ splittings. Each emission is generated at a scale lower than the previous emission, following a perturbative QCD distribution that depends on the momenta of all previous emissions. Common choices of scale for the ordering of emissions are virtuality, transverse momentum or angle. Parton showering stops at a scale of ~ 1 GeV, at which point a hadronisation model is used to convert the resulting partons into hadrons.

Additional modeling is needed to treat the collision between the two hadron remnants in pp collisions, which generates an underlying event (UE), usually implemented via "multiple parton interactions" (further $2 \to 2$ scatterings) at a scale of a few GeV [44].

PYTHIA Parton Shower Monte Carlo

`PYTHIA` is a PSMC programme widely used by particle physicists [77]. It can give a complete exclusive description of the events generated: the hard scattering, parton showering and hadronisation, and can even handle the underlying event as multiple parton interactions. `PYTHIA` implements both an ordering in virtuality (Q^2) and a p_{T}-ordering for the parton shower evolution [77, 93]. The hadronisation model used in `PYTHIA` involves stretching a color "string" across quarks and gluons, and breaking it up into hadrons [77]. Figure 2.6 shows a diagram of an event simulation with a PSMC programme, where the hard scattering is represented by the red globes, the parton shower in dark-red lines and curls, the multiple parton interactions in purple, and the hadronisation in green.

In `PYTHIA` three mechanisms are provided to produce b-quark: flavour creation $gg \to b\bar{b}$, corresponding to the diagrams shown in Figure 2.2(a), and $q\bar{q} \to b\bar{b}$; flavour excitation $gb \to gb$, where the initial b-quark comes from a branching $g \to b\bar{b}$; and

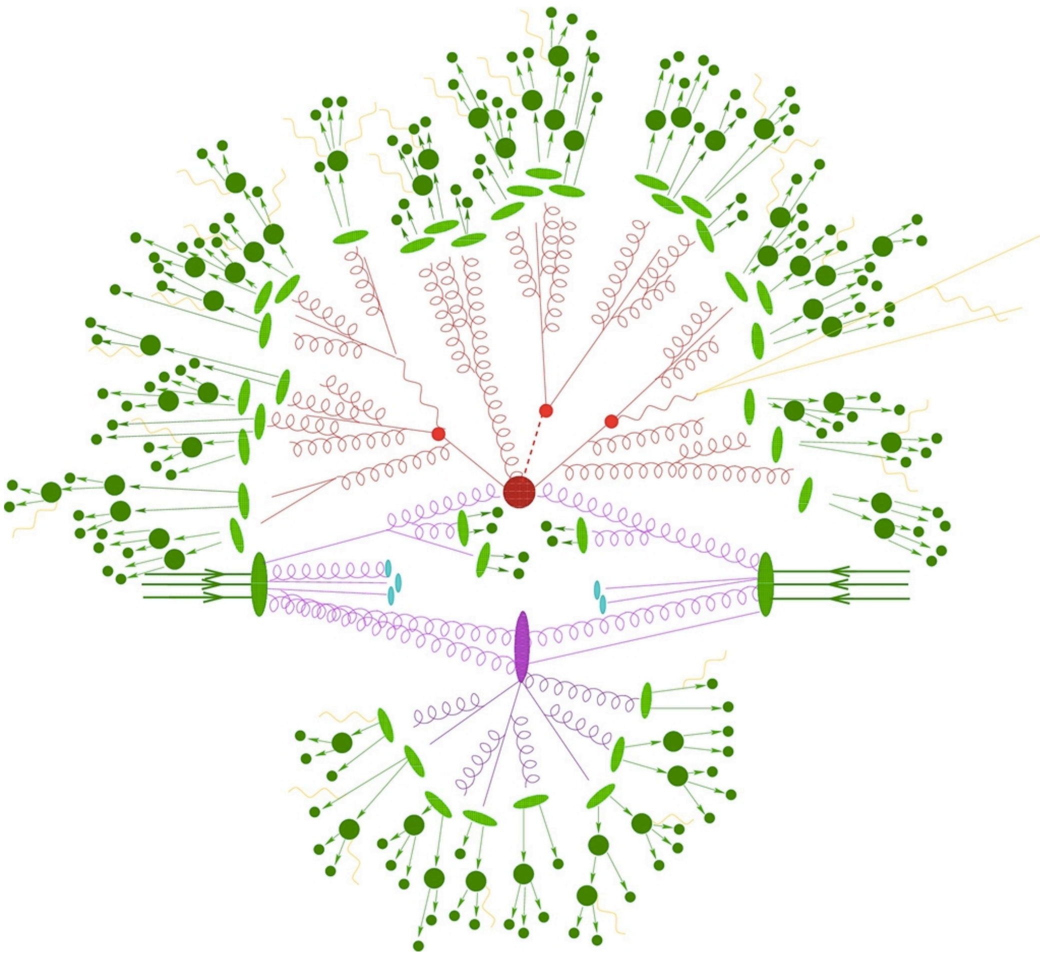

Figure 2.6: A diagram of a PSMC event, including the hard scattering in the red globes, the parton shower in dark-red lines and spirals, the multiple parton interactions in purple and the hadronisation in green. Source: S. Schumann [94].

gluon splitting $g \to b\bar{b}$. The last two are NLO processes [95] and their Feynman diagrams are shown in Figure 2.7. All of these mechanisms are activated if the parameter `msel=1`. In this regime bottom quark is produced approximately in 1% of events [96, 97]. In order to speed up the simulation in `msel=1` mode, a specialized module used by ATLAS – called `PythiaB` – interrupts a simulation after the parton development, just before the hadronisation, to check for the presence of $b\bar{b}$ quarks satisfying previously defined limits in p_{T} and η [98]. Direct b-quark production in `PYTHIA` can be activated with `msel=5`, but its use is discouraged since it does not describe well b-quark production at the Tevatron [96, 98].

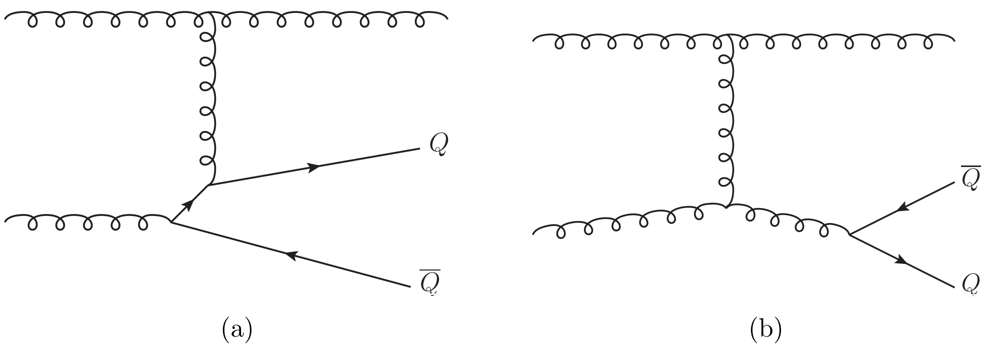

Figure 2.7: Feynman diagrams for heavy flavour production through flavour excitation (a) and gluon splitting (b).

HERWIG Parton Shower Monte Carlo

HERWIG is another extensively applied PSMC programme, that is able to generate the hard scattering, parton showering and hadronisation, and can deal with multiple parton interactions. In contrast to PYTHIA, this programme implements angular-ordering for the parton shower evolution, i.e. subsequent emissions are characterized by smaller and smaller angles. The hadronisation model of HERWIG breaks each gluon into a $q\bar{q}$ pair and then groups quarks and anti-quarks into colorless clusters, which then give rise to the hadrons [78].

2.3.2.2 NLO Monte Carlo: POWHEG

The POWHEG method can be used to generate MC simulations of many high-energy physics processes, e.g. Higgs or heavy vector boson production, using exact NLO matrix elements [75]. In particular, the POWHEG heavy-flavour generation method is based upon the heavy flavour production next-to-leading order calculation, up to order α_s^3, provided by Mangano, Nason et. al. [82, 83, 99]. This implementation of heavy flavour production can be used to generate events with either $t\bar{t}$, $b\bar{b}$ or $c\bar{c}$ pairs [76]. The output is an event file in the Les Houches Interface for User Processes (LHIUP) format [100], that in turn can be given as input to any PSMC programme that complies with the requirements of the LHIUP, like PYTHIA and HERWIG, in order to generate complete events by performing the parton showers and the non-perturbative hadronisation. In contrast with the FONLL computation, where the non-perturbative fragmentation function used is obtained by fitting to e^+e^- data with a theoretical calculation based on the very same underlying FONLL approach, when POWHEG is used the non-perturbative part of the shower that leads to the formation of the heavy-flavour hadrons is handled by the PSMC programme. The corresponding parameters are tuned using final-state observables reconstructed with particles emerging from the parton shower, but with the hard production cross-section of the PSMC, not that of the next-to-leading order observables used in the NLO+PS methods.

In the POWHEG approach, the generation of the hardest event is performed with NLO accuracy, in a framework that does not depend upon the shower algorithm of the PSMC, with a technique that yields only positive-weighted events. This is why it is fully independent from the PSMC chosen and the same POWHEG output can be used with a variety of PSMCs to generate events. The subsequent showers generated by the PSMC take place at softer transverse momenta, and thus affect infrared-safe observables [2] only at the next-to-next-to-leading order (NNLO). If the PSMC is ordered in p_{T}, it is required that the shower is started with an upper limit on the scale equal to k_T, the transverse momentum of the radiation of the POWHEG NLO event. In case the PSMC uses a different ordering variable (like angular ordering in HERWIG), the hardest emission may not be the first, so a veto on emissions with transverse momentum larger than k_T has to be put in place in order to comply with the requirement of POWHEG of suppressing these emissions in the PSMC. It has been discussed [76, 101] that standard showers need be supplemented by so-called *vetoed-truncated showers* – soft showers that can restore colour coherence, which is lost because of the requirement that the hardest radiation be always the first – but these are not available in most PSMC programmes[3]. However, there is no evidence that the effect of these truncated showers may have any practical importance [102]. When POWHEG is interfaced to shower programmes that use transverse-momentum ordering, the double logarithmic (soft and collinear) accuracy should be correctly retained if the PSMC programme is already double-log accurate. PYTHIA adopts transverse-momentum ordering when used with the new showering formalism, available from version 6.4 [77], and aims to have an accurate soft resummation approach, at least in the limit of large number of colors [102].

In ATLAS samples, POWHEG has been interfaced to PYTHIA version 6.4.21, and HERWIG 6.510. Table 2.4 lists the MC samples of heavy-flavour production used in the analysis presented in Chapter 3 with the generator filter settings, the precision of the calculation and the value of the cross-section returned by the MC programme.

[2]Infrared-safe observables are defined as those invariant to soft emissions or collinear splitting.
[3]The newest implementation of HERWIG, called HERWIG++, can handle these truncated showers.

name	generator	filter comments	precision	cross-section [nb]
PythiaB_bbe3X	PYTHIA	gen-level b-quark, $p_T^e > 3$ GeV	LO	17167
PythiaB_cce3X	PYTHIA	gen-level c-quark, $p_T^e > 3$ GeV	LO	19797
PythiaB_bbe7X	PYTHIA	gen-level b-quark, $p_T^e > 7$ GeV	LO	1790
PythiaB_cce7X	PYTHIA	gen-level c-quark, $p_T^e > 7$ GeV	LO	960
BBbar_Powheg_Jimmy	POWHEG	PS in HERWIG, $p_T^e > 5$ GeV	NLO	1258
CCbar_Powheg_Jimmy	POWHEG	PS in HERWIG, $p_T^e > 5$ GeV	NLO	1449
BBbar_Powheg_Pythia	POWHEG	PS in PYTHIA, $p_T^e > 5$ GeV	NLO	2021
CCbar_Powheg_Pythia	POWHEG	PS in PYTHIA, $p_T^e > 5$ GeV	NLO	1599

Table 2.4: Monte Carlo samples used for the simulation of $b\bar{b}$ and $c\bar{c}$ signal.

2.3.2.3 Cross-checks on Monte Carlo predictions for Heavy-Flavour production

The FONLL prediction computed for charged leptons (muons or electrons) within the fiducial cuts of the analysis presented in Chapter 3 (i.e. $|\eta| < 2$ and excluding the region $1.37 < |\eta| < 1.52$) is presented in Figure 2.8 and compared to a NLO prediction from the FONLL framework but without the logarithm resummation in the matrix element. At the transverse momentum range studied here, the NLO prediction stays within the FONLL band. The uncertainty on the FONLL computation was evaluated as detailed in Section 2.3.1.1. The effect of the quasi-collinear resummation, the softening of the p_{T} spectrum, can be tested at larger p_{T} only [2, 12].

The inclusive lepton cross-section from heavy-flavour decays predicted by PYTHIA and by POWHEG (interfaced with PYTHIA and HERWIG), for charged leptons within the fiducial cuts specified above, are also compared to the FONLL prediction in Figure 2.8. As expected, POWHEG+PYTHIA, based on the same NLO calculation as FONLL, agrees well with the FONLL predictions; however POWHEG+HERWIG predicts a significantly lower cross-section. The disagreement between these MC samples might originate from differences in the parton shower, hadronisation model, ATLAS MC tunes, and the B and D hadron decay models. Standalone PYTHIA predicts of about a factor two higher cross-section and a somewhat steeper p_{T} spectrum.

To understand the differences and study the systematic effects due to various ingredients of the MC generators the following cross-checks were made using specialized generator level MC simulations:

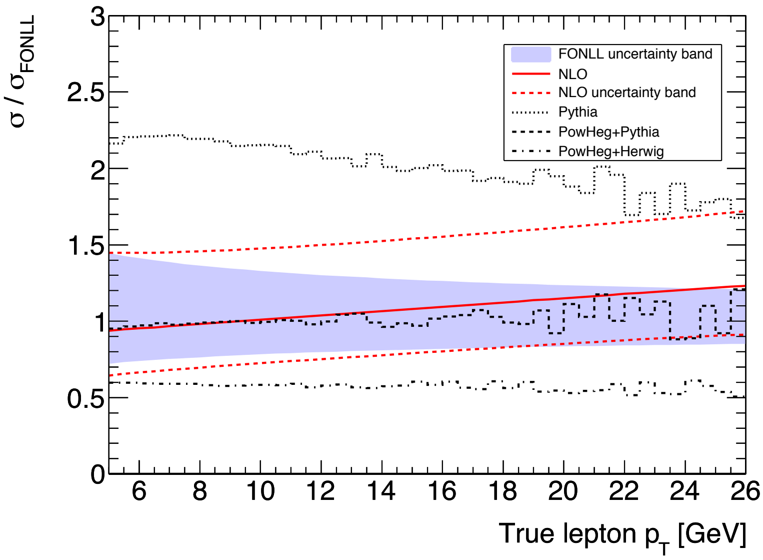

Figure 2.8: Predictions of different MC generators (black lines; dotted: `PYTHIA`, dashed: `POWHEG+PYTHIA` and dot-dashed: `POWHEG+HERWIG`) normalized to the `FONLL` inclusive electron cross-section from heavy-flavour production as a function of the lepton p_{T}. The `FONLL` uncertainty band is indicated by the light blue shaded area and the NLO prediction by the red lines (solid: central value, dashed: uncertainty band).

- The dependence on the **B and D hadron decay model** was checked by comparing the cross-section predictions using the standard `PYTHIA` and `HERWIG` decay tables to the predictions using `EVTGEN` [103]. The results are shown in Figure 2.9. While the difference is typically 10% between `PYTHIA` and `EVTGEN` decay tables, the `HERWIG` prediction is significantly (30−40)% lower than `EVTGEN`. The effect of the decay tables in `PYTHIA` is most apparent in the charm hadron component, which can be observed in Figure 2.9(b).

- In order to check whether the large difference between the `POWHEG` predictions when interfaced to different parton shower MC generators are related to the underlying event simulation, the effect of the ATLAS **MC tunes** was inspected by switching off the simulation of **multiparton interactions** (MPI). The results are presented in Figure 2.10. Note that this is a rather radical variation, so significant changes are expected at low p_{T}. However the changes between MPI on and off simulations with `POWHEG+PYTHIA` and with `POWHEG+HERWIG` are similar, typically at the 10% level. This suggests that the modeling of MPIs does not contribute significantly to the difference in the predicted cross-sections.

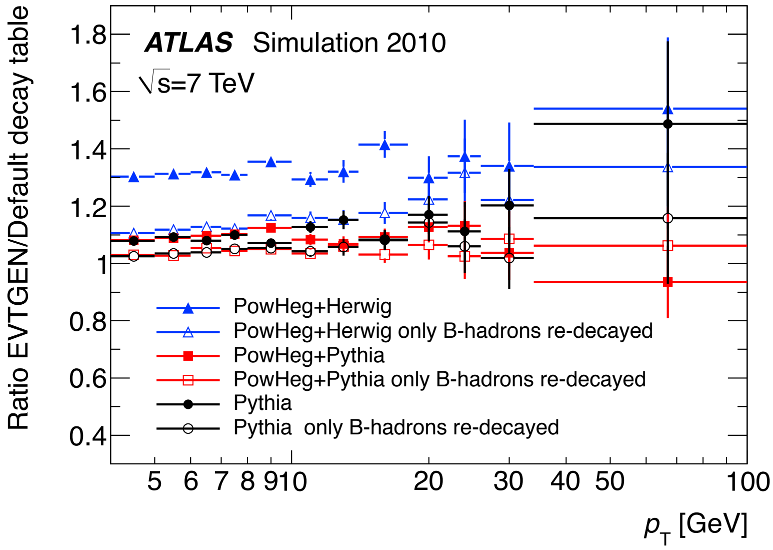

(a)

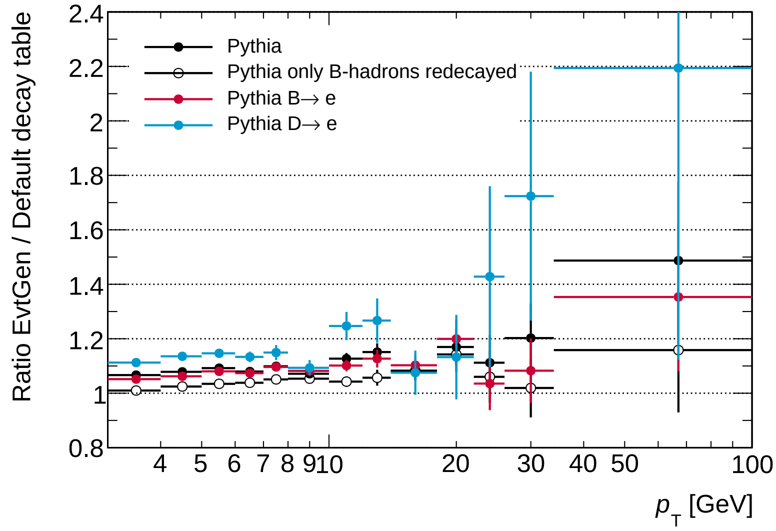

(b)

Figure 2.9: Uncertainties due to the B and D hadron decay model as a function of the lepton p_T. (a) The ratios of the cross-section using EVTGEN to the default decay table are shown for PYTHIA (circles), POWHEG+PYTHIA (squares) and POWHEG+HERWIG (triangles) considering two cases: when only B hadrons are redecayed by EVTGEN (open symbols) and when both B and D hadrons are redecayed (full symbols). (b) Cross-section ratios for PYTHIA separating the $B \to e$ (red) and the $D \to e$ (cyan) components.

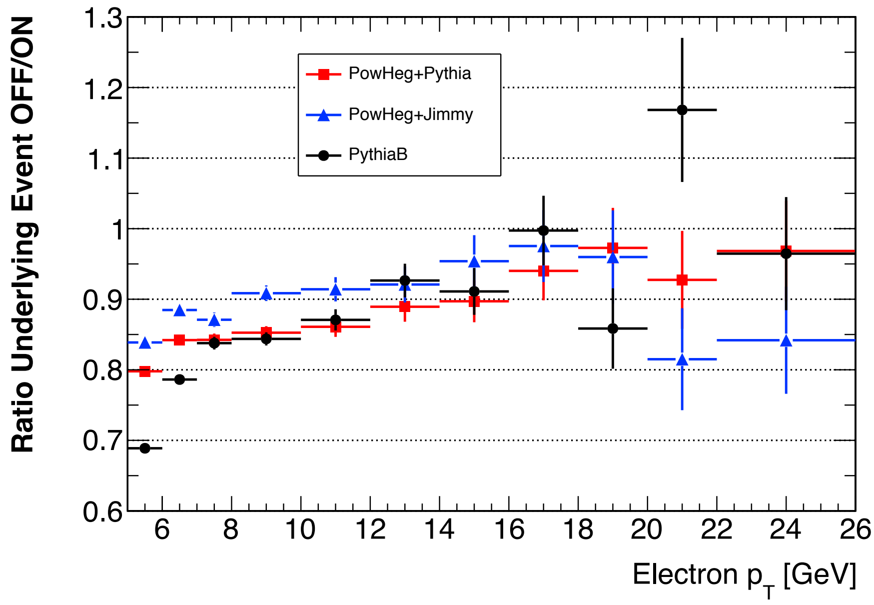

Figure 2.10: Effect of the multiparton interaction simulation (MC tune) as a function of the lepton p_T. Cross-section ratios with multiparton interactions OFF and ON are shown for `PYTHIA` (circles), `POWHEG+PYTHIA` (squares) and `POWHEG+HERWIG` (triangles) are shown.

- The systematic effect of **final state QED radiation** on the cross-section was also studied. In the range of interest above 7 GeV the effect is $3-5\%$. The ratio going below 3% at low p_T is related to the generator level lepton filter of $p_\mathrm{T} > 3$ GeV of the `POWHEG+PYTHIA` sample. On Figure 2.11, three distinct methods are used to account for FSR:

  (GenVtx ΔR $<$ 0.1) the electrons 4-momentum is corrected ("dressed") by summing up the 4-momenta of photons coming from the same vertex and being within $\Delta R < 0.1$

  (GenVtx closest) electrons are dressed by photons coming from the same vertex and being closest to the electron, which solves some ambiguities when the vertex contains two or more electrons.

  (ΔR $<$ 0.1) electrons are dressed by photons within $\Delta R < 0.1$ coming from any vertex of the generated event.

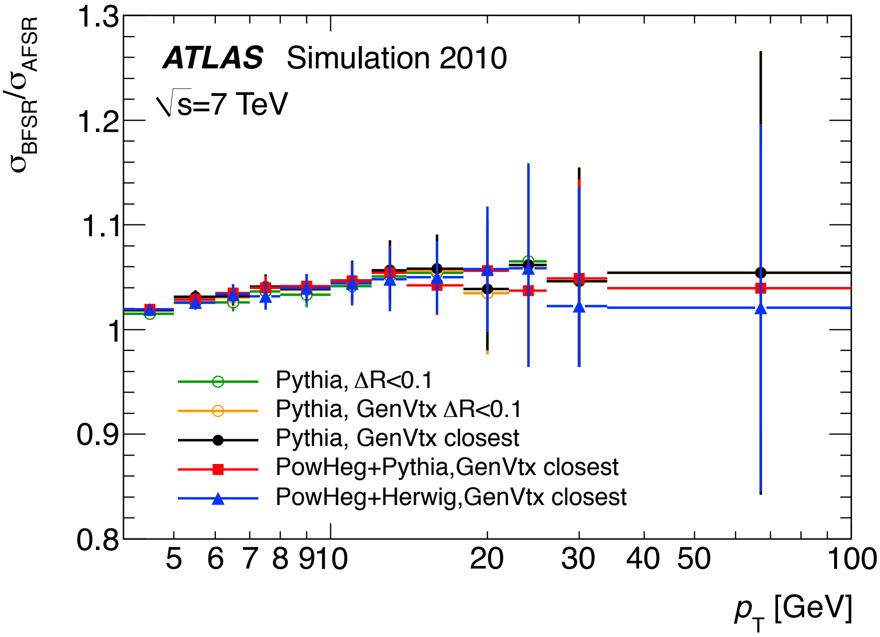

Figure 2.11: Effect of QED final state radiation as a function of the electron p_{T}. Cross-section ratios before and after QED FSR are displayed for `PYTHIA` (circles), `POWHEG+PYTHIA` (squares) and `POWHEG+HERWIG` (triangles) interfaced to `PHOTOS`.

> Since the impact of FSR on the spectrum is small ($\sim 4\%$) and constant above 7 GeV, no additional systematic uncertainty is considered from this source. As expected, no difference is seen in the effect of FSR for the two `POWHEG` samples, since both use `PHOTOS` to model photon radiation.

The conclusion is that approximately 50% of the difference between the `POWHEG` predictions with `PYTHIA` and `HERWIG` can be attributed to the different decay models, while the different MC tunes do not seem to contribute significantly. Other potentially important effects, like the influence of the choice of heavy-flavour fragmentation parameters on the predicted cross-section, have not been included in this MC study. It should be noted that different fragmentation methods are, in fact, used by `PYTHIA` and `HERWIG`, as mentioned in Section 2.3.2.1.

2.4 Previous Heavy-Flavour Measurements at Hadron Colliders

The production of heavy-flavour can be studied through the measurement of the contribution of semi-leptonic heavy-flavour decays to the inclusive lepton spectra, among other channels. Both charm and bottom hadrons have considerably large branching ratios, of the order of $\sim 10\%$, to electrons or muons [44], leading to a large ratio of signal leptons from heavy-flavour hadron decays to background from other lepton sources. Figure 2.12 [104] shows the production cross-section for different processes in proton-proton collisions at the collision energies of the LHC ($\sqrt{s} \in [7\text{ TeV}, 14\text{ TeV}]$) and or proton-antiproton collisions at the Tevatron with $\sqrt{s} = 1.96$ TeV, where the production of bottom quarks with large cross-sections, of the order of several μb in hadronic collisions, is displayed in red.

Single electrons from heavy-flavour decays were first observed in the range $1.6 < p_{\mathrm{T}} < 4.7$ GeV in pp collisions at the CERN ISR at $\sqrt{s} = 52.7$ GeV [105], not long before the charm-quark was actual discovered [106, 107]. The signal of high transverse momentum electrons directly produced in proton-proton collisions was found at the time (1974) to occur at a level of approximately 10^{-4} of the inclusive pion cross-section.

Since then, there has been continuous interest in the analysis of hadron collisions for heavy-flavour signatures. A review of the measurements of semi-leptonic heavy-flavour measurements in $p\bar{p}$ and pp collisions during the past 25 years and their comparison with QCD calculation is given in the following.

2.4.1 Semi-leptonic Heavy-flavour Measurements in $\mathbf{p\bar{p}}$ Collisions

The production of heavy-flavour quarks was studied in proton-antiproton collisions with the UA1 and UA2 detectors at the CERN Super Proton-Antiproton Synchrotron (Sp$\bar{\mathrm{p}}$S), which provided $p\bar{p}$ collisions at $\sqrt{s} = 546$ GeV and 630 GeV [108–112]. Later on, at the Tevatron accelerator and collider at Fermilab, the CDF and D0 collaborations analysed heavy-flavour production in $p\bar{p}$ collisions at $\sqrt{s} = 1.8$ TeV and $\sqrt{s} = 1.96$ TeV, studying final states with both electrons and muons [3–8].

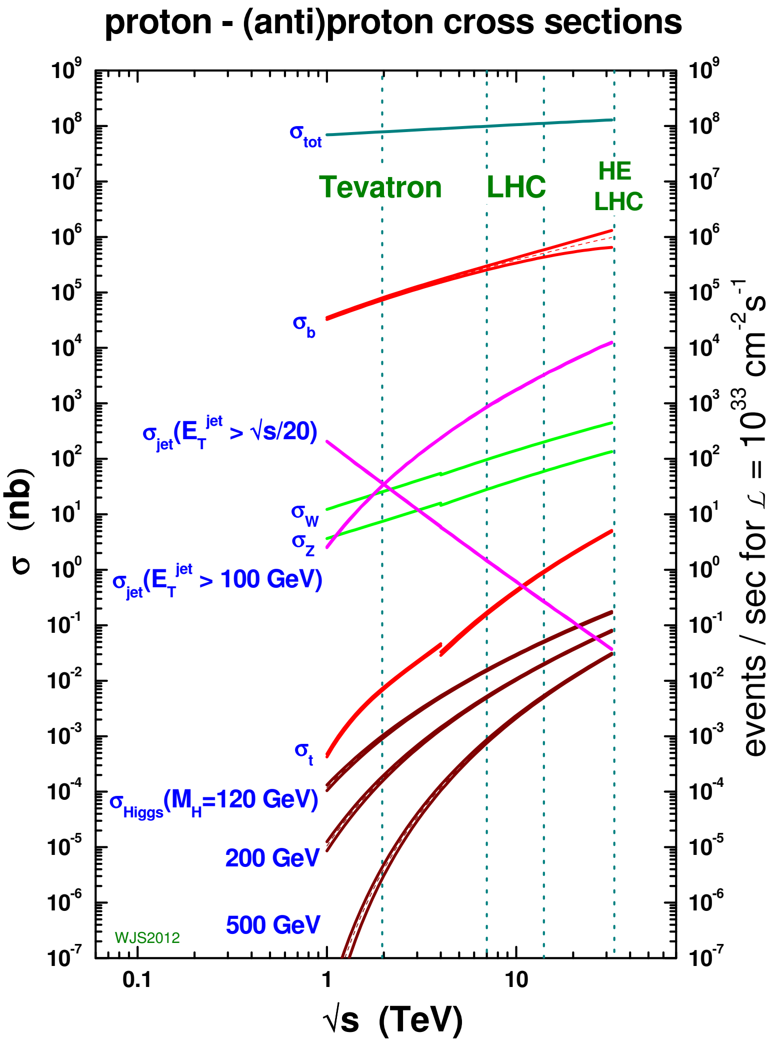

Figure 2.12: Cross-section predictions for SM processes at the Tevatron and at the LHC. W.J. Stirling [104].

2.4.1.1 Heavy-flavour Production in p$\bar{\text{p}}$ Collisions at the Sp$\bar{\text{p}}$S

A measurement of b-quark production was performed by the UA1 experiment using single and di-muon final states in the rage $10 < p_{\mathrm{T}} < 40$ GeV [108]. This study used the relative p_{T} of the muon with respect to the accompanyingjet – $p_{\mathrm{T}}^{\mathrm{rel}}$ – for non-isolated muons, to distinguish among muons from bottom decays, from charm decays, and from other background sources. For isolated di-muons, a fit in the di-muon mass for Υ, Drell-Yan and heavy flavour pairs components was performed after removing $Z \to \mu^+\mu^-$ events and subtracting the background. This analysis used data for pp collisions at energies of $\sqrt{s} = 546$ GeV and 630 GeV. The result for the $b\bar{b}$ production cross-section was:

$$\sigma(\bar{p}p \to \bar{b}b + X \; ; \; p_{\mathrm{T}}^{b} > 5 \text{ GeV} \wedge |\eta| < 2) = 1.1 \pm 0.1_{(\mathrm{stat.})} \pm 0.4_{(\mathrm{syst.})} \; \mu\mathrm{b}. \tag{2.20}$$

Additionally, the cross section for Υ production, times the branching ratio for its decay into muon pairs was measured to be

$$\sigma \cdot B(\bar{p}p \to \Upsilon, \Upsilon', \Upsilon'' \to \mu^+\mu^-) = 0.98 \pm 0.21_{(\mathrm{stat.})} \pm 0.19_{(\mathrm{syst.})} \text{ nb}, \tag{2.21}$$

after acceptance corrections, which matched well the QCD calculations at the time [108]. This analysis led to the observation of $B^0 - \bar{B}^0$ oscillations from an excess of like-sign di-muons [109]. The UA1 collaboration repeated this analysis with many improvements [111], requiring non-isolated muons in the range $10 < p_{\mathrm{T}} < 40$ GeV in order to use the $p_{\mathrm{T}}^{\mathrm{rel}}$ discrimination technique, including the chain decay of $\bar{p}p \to b \to J/\psi$ and extrapolating the measured cross-section to $p_{\mathrm{T}}^{min} = 0$ of the b-quark and from rapidity $|y| < 1.5$ [4] to all rapidities, which gives

$$\sigma(p\bar{p} \to b\bar{b} + X) = 19.3 \pm 7_{(\mathrm{exp.})} \pm 9_{(\mathrm{theo.})} \; \mu\mathrm{b}. \tag{2.22}$$

This result, together with the differential cross section provided as a function of b-quark and B-hadron p_{T} threshold, compared well to the fresh QCD calculations of Nason et al. [82, 83] at $\mathcal{O}(\alpha_s^3)$ [112].

Another experiment in the Sp$\bar{\mathrm{p}}S$, the UA2 experiment, measured electrons from charm decays in the range $0.5 < p_{\mathrm{T}} < 2$ GeV, from $p\bar{p}$ collisions at $\sqrt{s} = 630$ GeV, using a RICH counter to distinguish electrons from pions with a rejection rate of 10^5 [110]. By evaluating the ratio of electron/hadron (minimum bias) events, and normalizing by the measured cross-section of the miminum bias sample, a total charm cross-section was measured in the region $0.9 < p_{\mathrm{T}} < 1.5$ GeV of

$$\sigma_{tot}(p\bar{p} \to c\bar{c} + X) = 0.68 \pm 0.56_{(\mathrm{stat.})} \pm 0.25_{(\mathrm{syst.\,exp.})} \pm 0.21_{(\mathrm{syst.\,theo.})} \text{ mb}. \tag{2.23}$$

[4] Rapidity is defined as $y = \frac{1}{2} \ln(\frac{E+p_z}{E-p_z})$

Assuming that all prompt electrons come from charm decays, this translates into an upper limit for the $c\bar{c}$ cross section of $\sigma_{tot}(p\bar{p} \to c\bar{c} + X) < 1.9\,\text{mb}$. Both results compared well with the theory at that moment [110].

2.4.1.2 Tevatron Run I: Heavy-flavour Production in $\mathbf{p\bar{p}}$ Collisions at $\mathbf{\sqrt{s} = 1.8\,TeV}$

At the Tevatron, the CDF and D0 experiments measured bottom production via semi-leptonic decays into electrons ($7 < p_{\mathrm{T}}^{e} < 60$ GeV) [3] and muons ($3.5 < p_{\mathrm{T}}^{\mu} < 60$ GeV) [4, 5]. These analyses use $p_{\mathrm{T}}^{\mathrm{rel}}$, the relative p_{T} of the lepton with respect to a nearby jet, to determine the fraction of charm in data, similarly to the UA1 method. In the electron analysis of CDF, an independent technique is also used to obtain the charm fraction: the chain $\bar{K}^{*}(892)^{0} \to K^{-}\pi^{+}$ is reconstructed using charged tracks in association with electrons, finding a peak for this charge combination signaling the b-quark decay chain and no significant peak in the opposite combination $K^{+}\pi^{-}$. This gives an upper limit for the fraction of electrons from c-quark decays of 30%, which matched the $p_{\mathrm{T}}^{\mathrm{rel}}$ result. The muon measurement uses the fraction of charm from simulation, and assigns a systematic uncertainty of 10% from this assumption. Another signature for bottom production exploited in the electron measurement is the associated production of a charmed particle from the decay $B \to e\bar{\nu}D^{0}X$, with the D^{0} meson identified through its decay to $K^{-}\pi^{+}$, requiring the K and the electron to have the same charge sign, which provides another point in the measurement.

The comparison of the b-quark production cross-section measured by CDF [3, 4] and D0 [6] was found to be between two and three times larger than the $\mathcal{O}(\alpha_s^3)$ prediction, which in terms of the errors in the measurement was between 1.0 and 2.2 σ discrepancy. The D0 measurements of that time were found to be at the edge of the theoretical uncertainty band [5]. This conclusion prompted better fits and calculations on the theory side, and better experimental handling on the other to reach a better agreement [11]. One of the practices questioned was the fact that the experiments deconvoluted the spectra to the quark p_{T} level, an exercise that relied heavily on theory inputs for the parametrisation of the fragmentation functions in addition to be deemed an unphysical quantity, since free quarks are not observed [10, 113]. Just from a more appropriate fit to the b-quark to B-meson fragmentation functions, the discrepancy decreased the ratio Data/Theory from 2.9 to 1.7 [10].

The heaviest quark, the top, was detected for the first time by the Tevatron experiments. CDF saw the first evidence for a top quark of mass 174 GeV in 1994 [114], and later in 1995 both experiments announced the observation of $t\bar{t}$ pairs [115, 116].

2.4.1.3 Tevatron Run II: Heavy-flavour Production in $\mathbf{p\bar{p}}$ Collisions at $\sqrt{\mathbf{s}} = \mathbf{1.96\,TeV}$

A measurement of the b-quark cross section by CDF [7] used exclusively muon pairs from J/ψ decays to infer a B-hadron production cross section. The fraction of J/ψ from B-hadrons is taken from a fit of its pseudoproper time, and Monte Carlo simulations are used to deconvolute to the parent B-hadron spectrum. Although from the increase in collision energy an increase in the measured cross-section was expected, the measure bottom cross-section for 1.96 TeV was reduced to 0.864 times the value at 1.8 TeV, and found to be in good agreement with the newly available `FONLL` prediction [7].

The D0 experiment did not perform inclusive b measurements in Run II, however a measurement the differential cross-section for $\Upsilon(1S)$ using their decays into isolated muon pairs is available [8], with good agreement with theoretical predictions on bottomium production [117, 118].

2.4.2 Heavy-flavour Measurements at the LHC

Heavy-flavour production at LHC proton-proton collisions at center-of-mass energy $\sqrt{s} = 7$ TeV have been studied by the four main experiments, many of which exploit the semi-leptonic decays of charm and bottom, as summarized in the following.

2.4.2.1 J/ψ and Bottom Production in CMS

The CMS experiment measured the inclusive b-quark cross section using muons in association with jets, and exploiting the $p_{\mathrm{T}}^{\mathrm{rel}}$ distributions to distinguish bottom from charm and light hadrons. In the range $6 < p_{\mathrm{T}}^{\mu} < 30$ GeV and $|\eta^{\mu}| < 2.1$, the bottom production cross section is found to be

$$\sigma(pp \to b + X \to \mu + X') = 1.32 \pm 0.01_{(\mathrm{stat.})} \pm 0.3_{(\mathrm{syst.})} \pm 0.15_{(\mathrm{lumi.})}\,\mu\mathrm{b}, \tag{2.24}$$

which, as well as the differential cross section as a function of p_{T}^{μ}, is found to agree well with `MC@NLO` predictions [119]. A more recent comparison with `FONLL` found the total bottom cross-section to be 1.5 larger than the prediction, but compatible within the theoretical and experimental uncertainties [2].

Using oppositely charged muons, the CMS collaboration has measured the prompt and non-prompt J/ψ production cross-section as a function of the J/ψ transverse momentum in the range $6.5 < p_{\mathrm{T}} < 30$ GeV and over rapidity $|y| < 2.4$. The non-prompt fraction was estimated with a 2-dimensional fit to the decay length versus invariant di-muon mass distribution. The result for the $b \to J/\psi \to \mu^+\mu^-$ matches the predictions of FONLL and other generators [120]. An updated measurement, using the same technique, added an estimation for the $\psi(2S)$ meson to the fit. The ratio of the cross-section of $\psi(2S)$ over J/ψ, with the advantage that many systematics cancel out, is compared to theoretical predictions with good agreement [121].

The CMS collaboration has also used $J/\psi \to \mu^+\mu^-$ signatures in association with ϕ, K_s^0 and K^+ mesons to measure the production cross-sections of B_s, B^0 and B^+, respectively [122–124]. In addition, measurements of the production of $\Upsilon \to \mu^+\mu^-$ have been published [125].

Finally, CMS has recently published a measurement of the production cross-section of b-quark pairs decaying to muons with transverse momentum $p_{\mathrm{T}} > 4$ GeV or $p_{\mathrm{T}} > 6$ GeV and with $|\eta| < 2.1$, where the fraction of muon pairs from $b\bar{b}$ is estimated using a 2-dimensional fit in the muon pair impact parameters [126]. The results are compatible with the MC@NLO prediction for the two ranges within the errors.

2.4.2.2 Electrons and Muons from Heavy-Flavour in ALICE

Electrons from heavy-flavour hadron decays were measured by the ALICE experiment in the range $0.5 < p_{\mathrm{T}} < 8$ GeV at mid-rapidity $|y| < 0.5$ using two electron identification techniques, based on the particle specific energy loss $\mathrm{d}E/\mathrm{d}x$ in the Time Projection Chamber (TPC) [127]. The first approach uses information from the Time-OF-Flight (TOF) detector and the Transition Radiation Detector (TRD) to remove kaons, protons and other hadrons. The second approach uses the electromagnetic calorimeter (EMCal) to evaluate the ratio E/p, using it to suppress hadronic backgrounds [127]. The result is found to be in good agreement with FONLL predictions and, in one shared p_{T} bin, with the ATLAS inclusive electron measurement [12] described in Chapter 3.

The ALICE experiment also produced a measurement of muons from heavy-flavour decay in the forward region $2.5 < y < 4$ and in the range $2 < p_{\mathrm{T}} < 12$ GeV [128]. The differential cross-sections are found to be about 1.3 times the central theoretical prediction over the whole p_{T} and y range, nevertheless the data points lie within the theoretical uncertainty band [128].

2.4.2.3 Bottom and J/ψ Production in LHCb

The LHCb experiment, which was built as a forward spectrometer, measured the inclusive bottom hadron (H_b) cross section through the decay $b \to D^0\mu^-\bar{\nu}$ with $D^0 \to K^-\pi^+$, as in the CDF electron measurement [3], in the interval $2 < \eta < 6$ [129]. The D^0 mesons coming from b-hadron decays are identified by means of the impact parameter and by forming a common vertex with the muon track. The total cross-section is

$$\sigma(pp \to H_b + X) = 75.3 \pm 5.4_{(\text{stat.})} \pm 13.0_{(\text{syst.})}\,\mu\text{b}, \qquad (2.25)$$

which is in good agreement with FONLL calculations [2]. The differential cross-section as a function of η is also evaluated, and is well inside the theoretical uncertainty band [129].

Other measurements by the LHCb collaboration identify the decay $J/\psi \to \mu^+\mu^-$ to measure the prompt J/ψ production rate [130], as well as the B-hadron production rate by either looking for the decay chain $B^\pm \to K^\pm J/\psi$ [131] or using the pseudo-proper time [130]. The bottom production results agree well with FONLL computations [2], and the prompt J/ψ production compared to a variety of charmonium production models is in good accord with most predictions [130].

2.4.2.4 Heavy-flavour Measurements in ATLAS

The ATLAS collaboration measured the inclusive electron and muon cross-sections, subtracting the $W/Z/\gamma^*$ contribution in order to compare with predictions of heavy-flavour production with FONLL [12]. The analysis on electrons is the main topic of this thesis and is detailed in Chapter 3. The muon measurement is performed in the range $4 < p_\text{T} < 100$ GeV and $|\eta| < 2.5$. Signal muons from heavy-flavour and vector boson decays, as well as from Drell-Yan, are disentangled from background – comprised of pion and kaon decays in flight and fake muons from hadronic showers that reach the muon spectrometer – using $\Delta p_\text{T} = p_\text{T}^{MS} - p_\text{T}^{ID}$, where p_T^{MS} is the transverse momentum of the muon as measured in the muon spectrometer and p_T^{ID} is the p_T evaluation from Inner Detector tracks. After subtracting the vector boson and Drell-Yan contributions, the measured cross-section for muons from heavy-flavour decays is

$$\sigma^\mu_{HF} = 0.818 \pm 0.003_{(\text{stat.})} \pm 0.036_{(\text{syst.})} \pm 0.028_{(\text{lumi.})}\,\mu\text{b}. \qquad (2.26)$$

This measurement includes leptons from prompt charm hadrons $H_c \to l + X$, prompt bottom hadrons $H_b \to l + X$ and from cascade decays $H_b \to H_c + X \to l + X'$. The differential cross-section as a function of the muon p_T is compared to FONLL predictions as well as with POWHEG NLO MC – interfaced with PYTHIA and HERWIG for parton showering and hadronisation. Figure 2.13 shows the agreement of the muon data with the FONLL computation in the whole p_{T} range, as well as with the POWHEG+PYTHIA expectation [12]. The results show sensitivity to the resummation of large logarithms at large p_{T} in the FONLL approach. This result was subsequently compared to a calculation without the large logarithm resummation, but where the non-perturbative fragmentation function is extracted from LEP data with an input at fixed-order NLO ("NLO NP fit"). This modified NLO approach behaves similarly to FONLL at large p_{T}, matching well with the measurement, but deteriorates below ~ 20 GeV, as shown in Figure 2.14. This corroborates that FONLL gives a better description in the entire momentum region studied [2].

Additional heavy-flavour production cross-sections have been measured in ATLAS with muons in the final states. In particular, the J/ψ production cross-section measurement in the range $1 < p_{\mathrm{T}}^{J/\psi} < 70$ GeV and with $|y^{J/\psi}| < 2.4$ used a 2-dimensional fit in the di-muon invariant mass and the J/ψ pseudo-proper time to separate the prompt and non-prompt components of the inclusive J/ψ signal [132], which are compared to theoretical predictions and to the CMS result in similar kinematic regions [120] with good accord. The differential production cross-section of $\Upsilon(1S)$ has also been measured by ATLAS as a function of $p_{\mathrm{T}}^{\Upsilon(1S)}$ and $y^{\Upsilon(1S)}$ for muons with $p_{\mathrm{T}}^{\mu} > 4$ GeV and $|\eta| < 2.5$ [133]. The result is found to disagree with NLO predictions in color-singlet model, but show a better agreement with NRQCD model [134] implemented in PYTHIA8 [135].

Finally, the ATLAS collaboration has also used the decays $H_b \to D^{*+}\mu^- X$ to measure the production cross-section of B-hadrons with $p_{\mathrm{T}}^{H_b} > 9$ GeV and $|\eta^{H_b}| < 2.5$. The result is found to be approximately 1.5 times larger than the theoretical predictions of POWHEG and MC@NLO, but within the uncertainties [136].

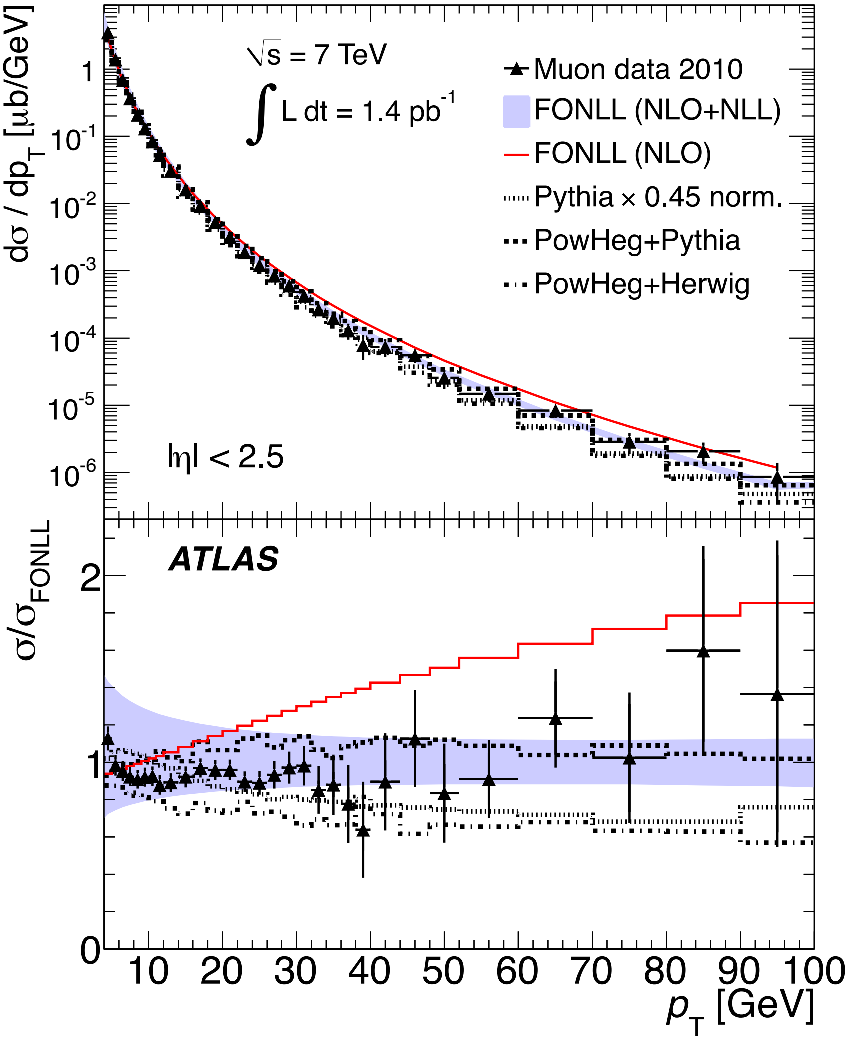

Figure 2.13: Muon differential cross-section as a function of the muon transverse momentum for $|\eta| < 2.5$, where the data points include statistical and systematic uncertainties. The ratio of the measured cross-section and the other predicted cross-sections to the `FONLL` calculation is given in the bottom. The PYTHIA (LO) cross-section is normalised to the data in order to compare the shape of the spectrum. Source: The ATLAS collaboration [12].

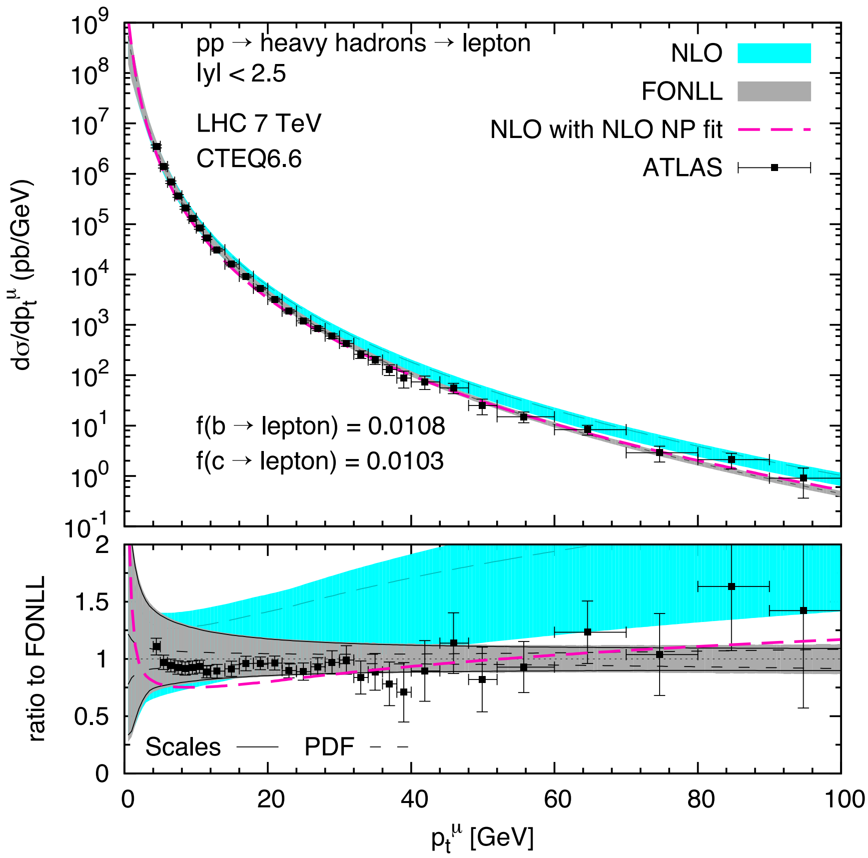

Figure 2.14: Muon differential cross-section as a function of the muon transverse momentum for $|\eta| < 2.5$, compared to the default `FONLL` prediction and to two instances where logarithm resummation has been turned off: one where the non-perturbative fragmentation function extracted in the default `FONLL` framework is used (NLO) and the second where a new non-perturbative fragmentation function is extracted from NLO without resummation input ("NLO NP fit"). Source: Cacciari et al. [2].

Chapter 3

Measurement of the Inclusive Electrons Cross-Section

This chapter details the measurement of the inclusive electron cross-section[1] using the ATLAS detector with 1.3pb^{-1} of data taken during 2010. At a centre-of-mass energy of 7 TeV, the electron candidates with transverse energy above 7 GeV consist of a mixture of electrons from vector bosons and decays of bottom and charm hadrons – from now on denoted as signal – plus electrons from photon conversions and hadron fakes [137].

In Section 3.1 the selection of useful events and electron candidates from a sample of data obtained with stable beams and very loose electromagnetic trigger requirements is described. Section 3.2 presents the extraction of the heavy-flavour electron signal from these electron candidates. The extraction uses a binned maximum likelihood method in order to extract the signal component. The variables used for the extraction are: the fraction of High Threshold hits in the TRT along the electron track, described in Section 1.2.2.3;the information on the hit in the innermost layer of the Pixel, which is also termed B-layer; and the ratio of the electron cluster energy over the track momentum E/p.

In order to obtain the heavy-flavour differential cross-section, measurements of the efficiency of the event trigger and the reconstruction and identification efficiency of electrons are needed. These measurements, derived using MC based methods and cross-checked with data, are detailed in Section 3.3.2. The final result of the cross-section is presented in Section 3.3.4.2 and compared to the expectation from NLO MC simulations from `POWHEG` [102] and to the theoretical predictions from the `FONLL` [9,11] programme, both described in Chapter 2.

[1]The inclusive muon and electron measurement has been published by the ATLAS Collaboration in 2011 [12]

3.1 Event Selection

3.1.1 Samples and Trigger Selection

The data sample used for this analysis was collected with the ATLAS detector from LHC collisions at $\sqrt{s} = 7$ TeV during 2010 data-taking and was recorded under four different trigger conditions that depended on the instantaneous luminosity delivered by the LHC. As the instantaneous luminosity increased the trigger requirements became tighter, rejecting the lower energy events or accepting them only under prescale. This is why, in order to maintain a high trigger efficiency, each period necessitates a different reconstructed electron E_{T} threshold that increases with the trigger threshold. The value of this threshold for each period is listed in Table 3.1. For periods A, B and C the lowest available electromagnetic trigger threshold at Level 1 of 3 GeV was adopted; this accounts for a total integrated luminosity of $14.1\,\mathrm{nb}^{-1}$, approximately 1% of the total dataset. Period D was separated in two categories according to run and luminosity block. Those luminosity blocks where the lowest unprescaled Level 1 electromagnetic threshold was 6 GeV and no bias from any further HLT selection was present fit into the first category and correspond to approximately 9% of the total dataset. In the second category are those luminosity blocks where the 11 GeV threshold trigger was preferred as it was the lowest unprescaled selection, amounting to $\sim 14\%$ of the full sample. In period E the trigger threshold at 15 GeV was used, making up 76% of the dataset. The uncertainty on the luminosity measured by the ATLAS detector is 3.4% [19].

In addition to passing the trigger selection, each event is required to have at least one reconstructed primary vertex, which should be reconstructed with three tracks or more. Finally the event must also pass the ATLAS data quality conditions defined by the electron-photon combined performance group [34]. This ensures that the selected events have the appropriate detector status, this is that the solenoidal field is at its nominal value and that the ID and the electromagnetic calorimeter are in high quality recording mode with nominal voltage [34].

3.1.2 Electron Reconstruction and Identification

Inclusive electron candidates are selected following a set of optimised cuts, shown in Table 3.2. The acceptance cuts include the condition on minimum transverse cluster energy defined by the period as shown in Table 3.1, along with the requirement that

L1 Threshold (GeV)	Period	Minimum E_{T} (GeV)	Integrated luminosity (nb^{-1})
3	ABC	7	14.1 ± 0.5
6	D	10	111.6 ± 3.8
11	D	14	176.4 ± 6.0
15	E	18	975.0 ± 33.2
Total Integrated Luminosity(nb^{-1})			1277 ± 43

Table 3.1: Breakdown of the full dataset by the trigger type and the data-taking period, showing the minimum cluster transverse energy requirement and the corresponding integrated luminosity.

the electron candidates must lie within the TRT coverage of $|\eta| < 2.0$ and must not be in the transition region between the barrel and the end-cap electromagnetic calorimeters, $1.37 < |\eta| < 1.52$.

The electrons that pass the basic acceptance criteria are subject to the preselection cuts. The tracks associated to the electron candidates must contain at least ten TRT hits and a minimum of four silicon hits. In order to avoid ambiguities, the candidates whose cluster's barycentre is near a specific problematic region of the electromagnetic calorimeter are rejected, as are those whose tracks pass through dead B-layer modules. The location of the problematic regions in the calorimeter and of the dead B-layer modules are run-dependent. At last, the preselected electron candidates must fulfill a requirement on the fraction of the raw energy deposited in the strip layer (f_1).

Furthermore, the candidates must comply with custom identification criteria, which grant a high efficiency for the heavy-flavour signal electrons and reduce significantly the fake signatures coming from QCD jets. These criteria differ from the standard *medium* selection described in Section 1.4 in that the cuts on the shower shape variable R_η and on the hadronic leakage parameters are not applied, since they degrade the efficiency for electrons from heavy-flavour decays [37]. The specific cut value for the variables listed varies according to the η position of the candidate and its transverse energy. These identification cuts comprise requirements on the energy deposits in the strip and middle layers of the EM calorimeter and on the track quality and track-cluster matching.

In the first layer of the EM calorimeter, which is finely segmented in η as described in Section 1.2.3.1, the total lateral width of the shower w_{stot} in a window of $\Delta\eta \times \Delta\phi \approx 0.0625 \times 0.2$, corresponding to 20 strips, is required to be below a certain value, typically from 2 to 4, in order to keep narrow showers; and the quantity $E_{\mathrm{ratio}} = (E_T^{(1)} - E_T^{(2)})/(E_T^{(1)} + E_T^{(2)})$, where $E_T^{(1)}$ and $E_T^{(2)}$ are the transverse energies

Type	Description	Name
Acceptance		
Fiducial cuts	$\|\eta\| < 2.0$ ($1.37 < \|\eta\| < 1.52$ excluded) $E_T > 7$, 10, 14 or 18 GeV depending on period	- -
Preselection cuts		
Fiducial cuts	Remove candidates with clusters near problematic regions in EM calorimeter Remove candidates with tracks passing through dead B-layer modules	- -
Tracking cuts	At least 10 TRT and 4 silicon hits	-
Strip layer of the EM calorimeter	Fraction of the raw energy deposited in the strip layer (> 0.1)	f_1
Identification cuts (in addition to the preselection cuts)		
Strip layer of the EM calorimeter	Total lateral shower width (20 strips) Ratio of the energy difference between the largest and second largest energy deposits over the sum of these energies	w_{stot} E_{ratio}
Middle layer of the EM calorimeter	Lateral width of the shower	w_2
Track quality	Number of hits in the pixel detector (at least one) Number of hits in the pixels and SCT (at least seven) Transverse impact parameter (< 1 mm)	- - d_0
Track matching	$\Delta\eta$ between the cluster and the track (< 0.01)	$\Delta\eta_1$

Table 3.2: Definition of variables used for all electron candidate acceptance, preselection and identification cuts. Cut values are given only in the cases where a fixed cut is used, independent of E_T and $|\eta|$.

of the two most energetic cells in this layer, has to be close to 1 in order to reject jets containing π^0 decays. In the second layer of the EM calorimeter, the lateral width of the shower in η, w_2, is constrained to be below a value, normally between 0.01 and 0.03. Finally, besides asking for a minimum amount of hits in the pixel detector and in the pixel plus SCT, requirements are set on the transverse impact parameter, i.e. the distance at the point of closest approach, of the electron track with respect to the primary vertex $d_0 < 1$ mm and on the distance in η between the electron track and its cluster $|\Delta\eta| < 0.01$.

Figure 3.1 shows the E_T and η distributions for electron candidates passing the preselection and identification criteria, where data with $E_T < 18$ GeV has been scaled up to a luminosity of 1.28 pb^{-1} in Figure 3.1(a) and the distribution of pseudorapidity in Figure 3.1(b) has an upper limit of 26 GeV imposed on E_T. The cuts were chosen this way in order to optimise the efficiency for non-isolated electrons from bottom and charm decays rather than isolated electrons from decays of gauge bosons W/Z.

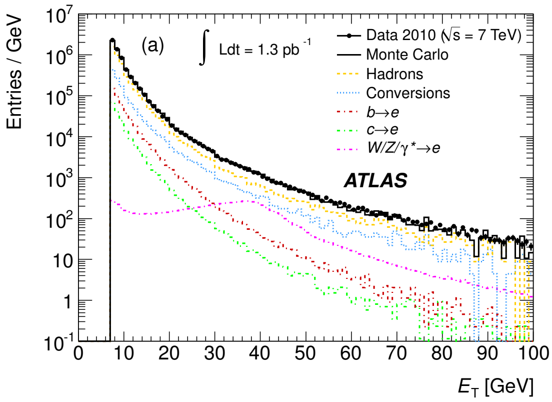

(a)

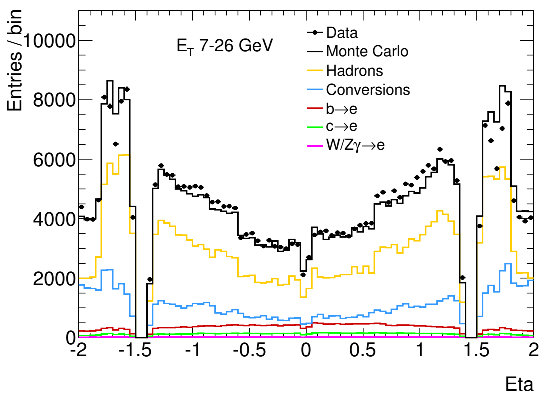

(b)

Figure 3.1: Distributions of cluster transverse energy E_{T} (a) and pseudorapidity η (b) for electron candidates passing the preselection and identification cuts.

3.1.3 Sample Composition from Simulations

A study of the origin of the electron candidates from MC simulations indicates that the heavy-flavour signal fraction increases from 2.0% after the preselection cuts to around 10% when identification cuts are also applied, as shown in Table 3.3. Of the two background components hadron fakes dominate at both stages of selection, while the secondary electrons from photon conversions and Dalitz decays are at $\sim$ 20% which is nevertheless a larger fraction than that of the signal.

Component	Preselection	Preselection + Identification
Hadron fakes (%)	75.6 ± 0.1	69.6 ± 0.4
Conversions (%)	22.4 ± 0.2	20.3 ± 0.6
Signal electrons (%)	2.0 ± 0.7	10.1 ± 0.7

Table 3.3: Breakdown of electron candidates with $7 < E_{\mathrm{T}} < 26$ GeV in the MC simulation according to their origin, after preselection and identification cuts. Signal electrons comprise mostly non-isolated electrons from charm and bottom hadron decays and only a very small fraction of them are expected to be isolated electrons from W/Z-boson decay. The errors indicated are purely statistical.

When dealing with isolated electrons from W/Z decays the usual approach to suppress these backgrounds is to require more stringent identification criteria to be satisfied by the electron candidates [34]. Specifically, conditions are applied on the fraction of high-threshold TRT hits out of all hits in the TRT, f_{TR}, in order to reject charged hadrons; on the presence of a hit in the B-layer of the pixel detector, which distinguishes the signal electrons from photon conversions; and on the measured energy in the electromagnetic cluster divided by the track momentum E/p. These cuts – which correspond to the *tight* selection described in Section 1.4, except the R_η and R_{had} cuts are not reintroduced – improve the heavy flavour electron signal purity only to $\sim 50\%$, therefore a more complex extraction procedure is needed in order to obtain the number of heavy-flavour signal electrons in each E_{T} bin.

3.2 Signal Extraction

The method employed for the heavy-flavour signal extraction takes advantage of the different distributions for various components of the discriminating variables mentioned above: the fraction of high-threshold TRT hits, f_{TR}, the number of hits in the B-layer, n_{BL}, and the ratio of the electromagnetic cluster energy to the track momentum, E/p. The distributions are shown in Figure 3.2.

In this section the method and the evaluation of the associated systematic uncertainties are described.

3.2.1 The "Tiles" Method

A binned maximum likelihood method, based on the distributions of f_{TR}, n_{BL} and E/p, is used to extract the heavy-flavour plus Drell-Yan signal electrons from the selected candidates. The expression for the number of electrons $N(i)$ in some bin i of the three-dimensional distribution in $(f_{\mathrm{TR}}, n_{\mathrm{BL}}, E/p)$ is

$$N(i) = N^{Q\to e}p^{Q\to e}(i) + N^{\gamma\to e}p^{\gamma\to e}(i) + N^{h\to e}p^{h\to e}(i), \tag{3.1}$$

where the three N^k are the fitted total number of electrons in each component k: $N^{Q\to e}$ for the signal from heavy flavour and Drell-Yan, $N^{\gamma\to e}$ for the secondary electrons from photon conversions and $N^{h\to e}$ for the hadron fakes; and $p^k(i)$ is the three dimensional probability density function (pdf) for component k, i.e. the probability for an electron candidate of the k species to belong in bin i in the $(f_{\mathrm{TR}},\ n_{\mathrm{BL}},\ E/p)$ 3-dimensional space.

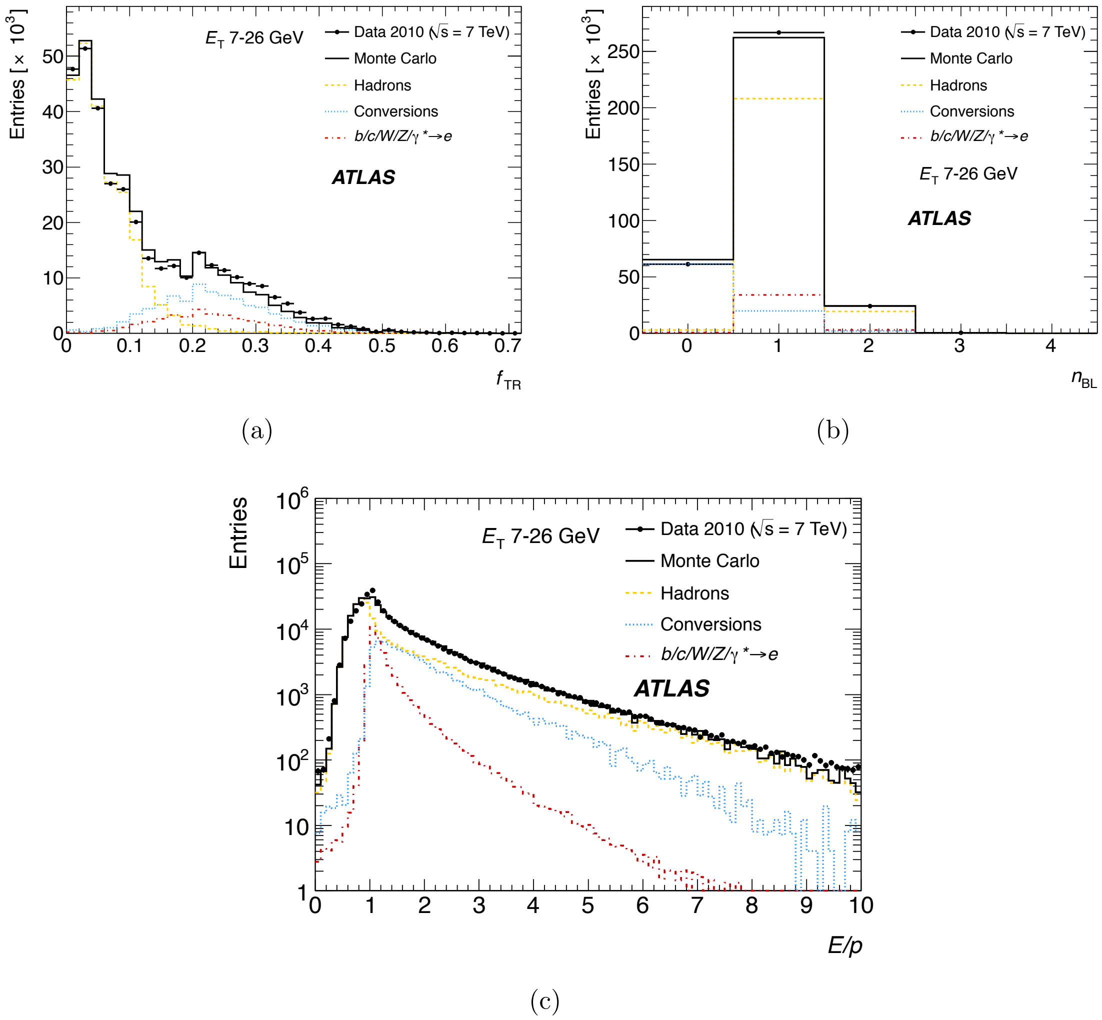

Figure 3.2: Discriminating variables for the heavy-flavour electrons signal against the hadron fakes and conversion backgrounds.

The extended log-likelihood expression is given by

$$-\ln L(N^{Q\to e}, N^{\gamma\to e}, N^{h\to e}) \;=\; \sum_i N(i) - N_{obs}(i)\ln N(i), \qquad (3.2)$$

where $N_{obs}(i)$ is the number of electron candidates from data observed in bin i of E_{T} and $N(i)$ is the fitted total number of candidates, defined in Equation 3.1.

If the three dimensional hadronic pdf is unknown, but the assumption is made that it can be factorised as the product of the three one-dimensional f_{TR}, n_{BL} and E/p templates, then the expression for the number of hadronic background candidates becomes

$$N^{h\to e}(i) = N^{h\to e}p^{h\to e}(i) = N^{h\to e}\ p^{h\to e}_{f_{\mathrm{TR}}}(i)p^{h\to e}_{n_{\mathrm{BL}}}(i)p^{h\to e}_{E/p}(i) \tag{3.3}$$

where the $p_j^{h\to e}(i)$ $(j = f_{\mathrm{TR}},\ n_{\mathrm{BL}},\ E/p)$ are now the one-dimensional pdfs and are additional unknowns in the fit. Through the normalisation of the pdfs, this introduces $\sum_j (b_j - 1)$ additional free parameters, where b_j is the number of bins in the one-dimensional $h \to e$ pdf for template j.

With the intention of providing the final number of signal, conversion and hadronic fake candidates in each E_{T} bin, the pdfs for the signal and conversion components are binned in E_{T} in the range 7-26 GeV and in η, on which there is some dependency. In this particular implementation twelve bins $(2 \times 2 \times 3)$ are used: two in f_{TR} (typically $f_{\mathrm{TR}} > 0.1$ and $f_{\mathrm{TR}} < 0.1$, however this bin boundary is finely adjusted in an E_{T} and η dependent way in order to optimise the sensitivity), two in n_{BL} ($n_{\mathrm{BL}} \geq 1$ and $n_{\mathrm{BL}} = 0$) and three in E/p ($E/p < 0.8$, $0.8 < E/p < 2.0$ and $E/p > 2.0$). This is performed in each E_{T} and η bin. The difficulty in obtaining background templates for this extraction below 7 GeV is the main reason to choose this value for the lower limit of the measurement.

Given these twelve observations, seven unknown quantities are left for the fitting procedure to estimate: the number of each candidate type, $N^{Q\to e}$, $N^{\gamma\to e}$ and $N^{h\to e}$ plus four more parameters to describe the three hadronic pdfs with the above binning.

The outcome of this fitting procedure yields the number of electron candidates that belong to each component, with the statistical uncertainties given by the MINOS computation in MINUIT [138]. The results are shown in Table 3.4 and in Figures 3.3 and 3.4.

3.2.2 Systematic Uncertainties on Signal Extraction

The systematic uncertainties for the extractions were estimated from the various sources listed in Table 3.5. The most important uncertainties evaluated and the method for their assessment are the following:

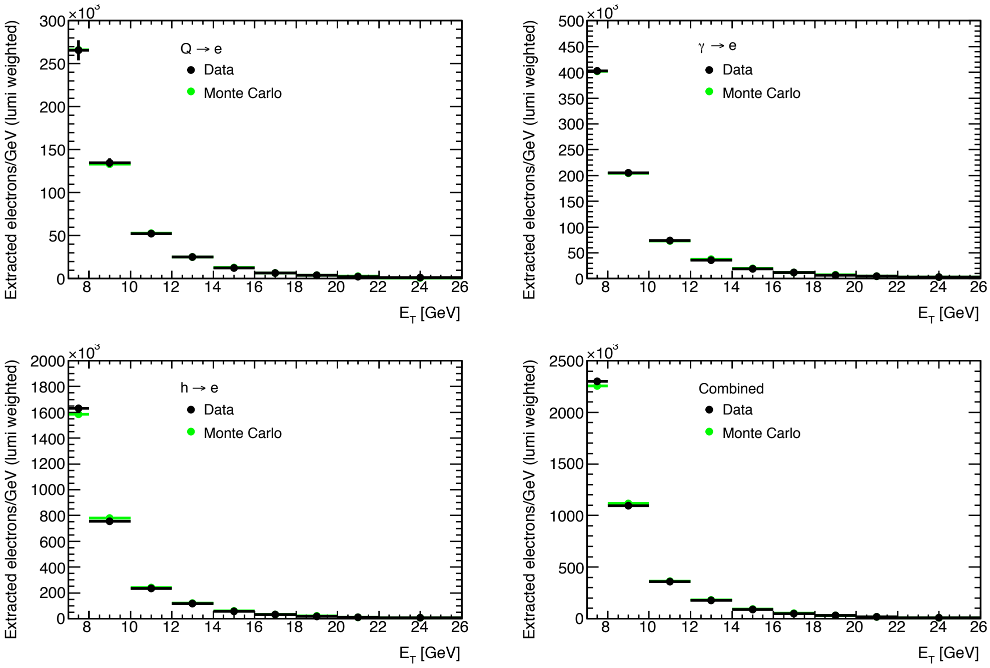

Figure 3.3: Distributions of the cluster transverse energy of the extracted $Q \to e$, $\gamma \to e$ and $h \to e$ components, after reweighting to 1.28 pb^{-1}, compared to MC truth expectation. In each plot the simulation has been normalised to the number of extracted electrons in data and the error bars are purely statistical.

1. **Data-MC discrepancies of templates** A discrepancy between templates from data and simulation for the $Q \to e$ or $\gamma \to e$ components could result in a systematic bias of the final extraction results. In order to assess this potential effect in the three discriminating distributions, different evaluation procedures were used :

   - For the $\boldsymbol{f_{\mathrm{TR}}}$ **distribution**, a high purity (95.1%) sample of conversions was selected as a subset of the data candidates by imposing the additional requirements of $n_{\mathrm{BL}} = 0$ and $E/p > 0.8$. The clear discrepancy observed in Figure 3.5 between the data and MC distributions may be modelled as a shift in the simulated value of f_{TR}. This shift has been evaluated for every E_{T} and η bin and assumed to be the same for the signal electrons and for the conversions. The E_{T} and η binned simulation-based templates

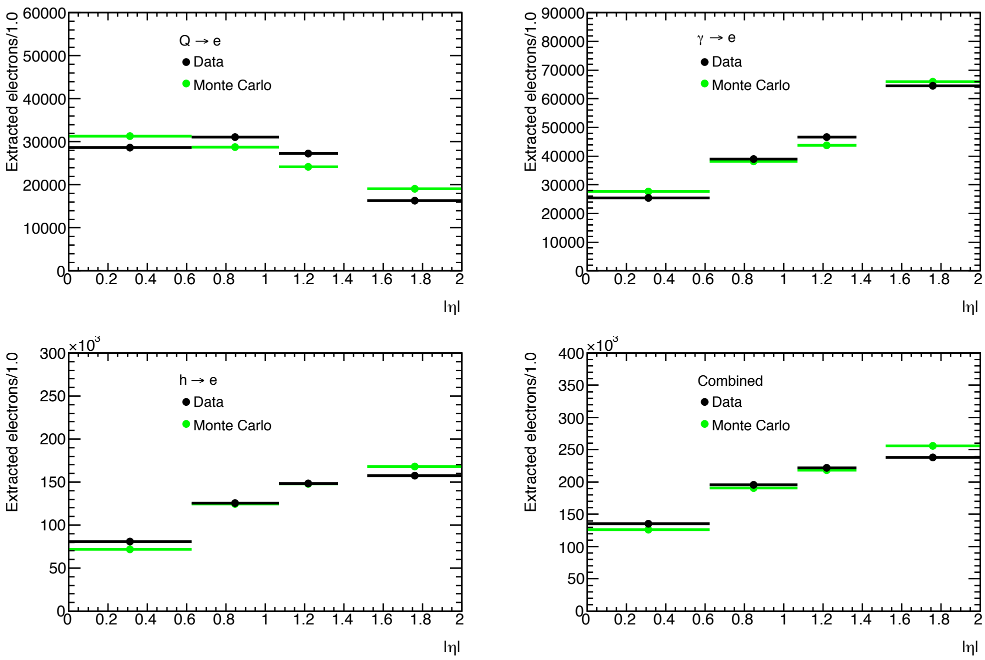

Figure 3.4: Distributions of the track pseudorapidity of the extracted $Q \to e$, $\gamma \to e$ and $h \to e$ components compared to MC truth expectation. In each plot the simulation has been normalised to the number of extracted electrons in data and the error bars are purely statistical.

for these two components were consequently adjusted by the appropriate shift, the modified pdfs created and the signal extraction repeated, with the resulting change in $N^{Q\to e}$ taken as the magnitude of the systematic uncertainty.

- In the case of the ***E*/*p* distribution**, a high purity (97.8%) sample of conversions was selected as a subset of the data candidates by imposing the additional requirements of $n_{\mathrm{BL}} = 0$ and $f_{\mathrm{TR}} > 0.1$. Some data-MC difference is also visible in Figure 3.6, notably a shift in the location of the rising edge at $E/p = 1$. It should be noted that the location of the bin boundary at $E/p = 0.8$, away from the rising edge, will reduce the impact of this discrepancy. The effect on $N^{Q\to e}$ was evaluated by applying a shift of 0.1 (conservatively evaluated from the $E_{\mathrm{T}} - \eta$ bin with the worst data-MC discrepancy) to both the $Q \to e$ and $\gamma \to e$ MC templates, recreating the pdf and repeating the extraction. The full difference found with the result after the shift in the templates is taken as the systematic uncertainty.

E_{T} bin (GeV)	7-8	8-10	10-12	12-14	14-16	16-18
$N^{Q\to e}$	2934±127	2982±108	10337±313	4912±180	6000±163	3174±116
$N^{\gamma\to e}$	4449±81	4533±82	14580±148	6984±101	9007±114	5453±89
$N^{h\to e}$	18004±173	16690±156	46087±362	22846±223	27170±219	14766±159

E_{T} bin (GeV)	18-20	20-22	22-26
$N^{Q\to e}$	7490±236	4757±154	5203±186
$N^{\gamma\to e}$	13628±141	9015±116	10630±124
$N^{h\to e}$	36533±294	19793±201	24650±236

Table 3.4: Summary of results obtained from the signal extraction method from the data detailing the $h \to e$ (hadrons) and $\gamma \to e$ (conversions) background components and the $Q \to e$ electron signal component in bins of E_{T}. The errors are purely statistical.

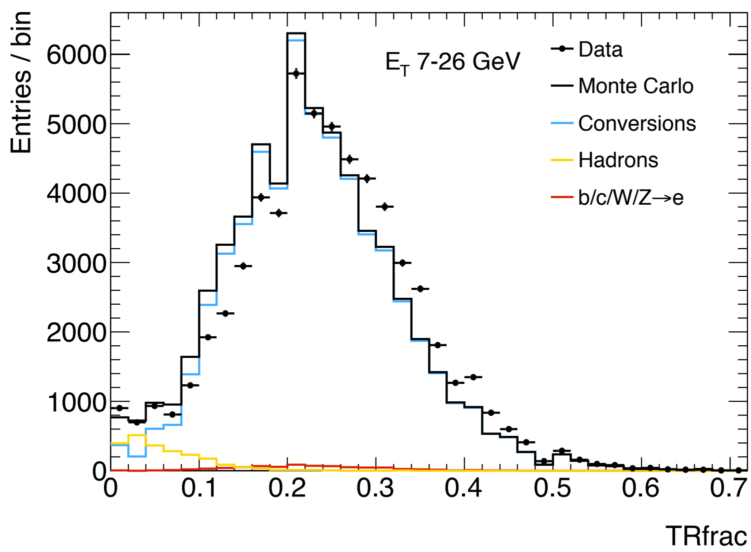

Figure 3.5: Comparison between data and MC for f_{TR} for a pure sample of conversions, selected from the data using the criteria of Section 3.1 but with the additional requirements of $n_{\mathrm{BL}} = 0$ together with $E/p > 0.8$.

Source	Uncertainty on $N^{Q\to e}$ (%)
MC-data discrepancies in $Q \to e$ and $\gamma \to e$ templates:	
-f_{TR} distribution	2.3
-E/p distribution	3.0
-n_{BL} distribution	1.3
Correlation bias from hadron pdf	7.3
Energy scale uncertainty	3.5
MC statistical uncertainty	0.8 - 2.5
Total uncertainty	9.1 - 9.4

Table 3.5: Summary of the systematic uncertainties on the extracted electron signal. For each source the resulting systematic uncertainty on $N^{Q\to e}$, averaged over all E_{T} bins, is given.

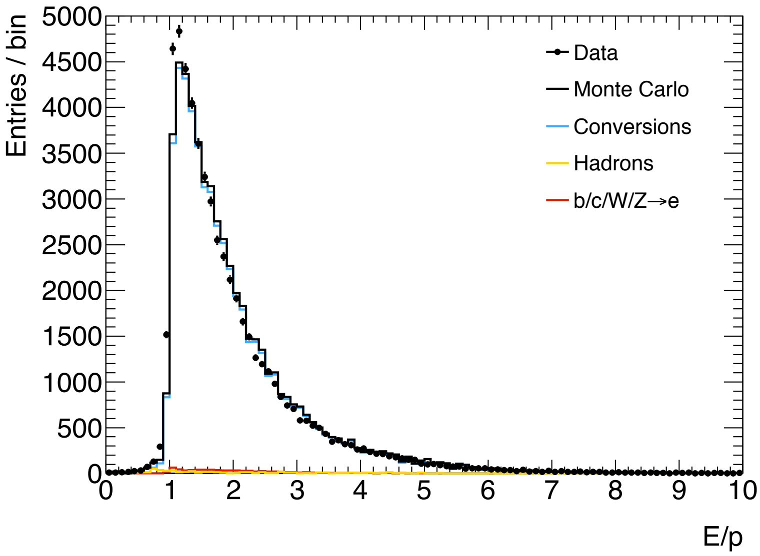

Figure 3.6: Comparison between data and MC for E/p for a pure sample of conversions, selected from the data using the criteria of Section 3.1 with the additional requirements of $n_{\mathrm{BL}} = 0$ together with $f_{\mathrm{TR}} > 0.1$.

- The effect of the discrepancy between data and simulation for the $\boldsymbol{n_{\mathrm{BL}}}$ **distribution** on conversions was estimated by varying the simulated distribution coherently by $\pm 5\%$ for the $n_{\mathrm{BL}} = 0$ bin and by $\mp 1\%$ for the $n_{\mathrm{BL}} > 0$ bin. This is a sensible variation given the excellent understanding of the material in the ID based on the analysis of charged tracks and of K_s^0 decays in minimum-bias events [139], combined with the accurate knowledge of the beam-pipe material which dominates the uncertainty on the number of conversions that do not present a hit in the B-layer. For the signal electrons the effect is negligible, at the current precision of the analysis, since tracks going through non-functional B-layer modules are not considered. Possible bremsstrahlung effects occurring in the beam-pipe for signal electrons are also estimated to be negligible.

Each uncertainty is calculated separately for each bin in η and E_{T} with the summation over η taking into account correlations between bins. A weighted average over E_{T} is then calculated using the statistical error on $N^{Q\to e}$ in each bin to give the figure shown in Table 3.5.

2. **Correlations in hadron pdf** As mentioned in the description of the procedure, the Tiles Method assumes that there are no correlations between the discriminating variables in the dominant hadronic background component. The systematic bias associated with this assumption is evaluated in simulations by running pseudo-experiments in which the 3-dimensional (f_{TR}, n_{BL}, E/p) pdf of the $h \to e$ pseudo-data is replaced by the product of the three 1-dimensional templates, thus removing any correlations.

3. **Energy scale uncertainty** The energy scale is corrected according to the recommendation provided by the ATLAS electron-photon combined performance group for the 2010 data [140]. An energy scale correction was applied to the measured candidate electron energy in data, using factors determined from $Z \to e^+e^-$ events. The scale uncertainty for electrons in the barrel is 1% and for those in the end-cap it corresponds to 3%. The systematic uncertainty on the extraction arising from the energy scale error is then obtained by scaling the electron cluster E_{T} in the data up and down by 1% in the barrel and 3% in the end-cap, and repeating the signal extraction. An uncertainty of 3.5% on $N^{Q\to e}$ is assigned [141].

4. **Statistical uncertainty on MC templates** Uncertainties arising from the finite MC statistics behind the pdfs for the signal and conversion components were estimated by rerunning the data extraction with 250 resampled pdfs, obtained from the original MC samples by varying the templates themselves within the

Poisson uncertainty of their statistics (the so-called *bootstrap* technique [142]). The width of the resulting distribution of extracted $N^{Q\to e}$ values in each E_{T} and η bin was taken as the uncertainty on $N^{Q\to e}$ in that bin.

In summary, for the signal extraction the greatest source of systematic uncertainty is the correlation between the distributions in the 3-dimensional pdf for the hadron component, followed by the mismodelling of the signal and conversion templates and the energy scale uncertainty. The total systematic uncertainty on the extracted signal ranges between 9.1 and 9.4%.

3.2.3 Final Signal Extraction Results

The number of signal events with statistical and systematic uncertainty in each E_{T} bin, which corresponds to the sum over the separate η bins of the fit, is shown in Table 3.6 and graphically in the left hand plot of Figure 3.7. The graph on the right shows the distribution of the number of signal electrons extracted for bins of $E_{\mathrm{T}} > 18$ GeV, and the result scaled to $1.28\,\mathrm{pb}^{-1}$ for bins with $E_{\mathrm{T}} < 18$ GeV.

E_{T} bin (GeV)	7-8	8-10	10-12	12-14	14-16	16-18	18-20	20-22	22-26
Final $N^{Q\to e}$ result	2934	2982	10337	4912	6000	3174	7490	4757	5203
Statistical uncertainty	± 127	± 108	± 313	± 180	± 163	± 116	± 236	± 154	± 186
Systematic uncertainty	± 267	± 271	± 940	± 452	± 564	± 289	± 689	± 447	± 489

Table 3.6: The final result obtained from the Tiles Method for the extraction of the electron signal component from the data, with statistical and systematic uncertainties.

3.3 Cross-Section Measurement

The measured differential cross-section within the kinematic acceptance of the detector is defined by

$$\frac{\Delta\sigma_i}{\Delta p_{\mathrm{T}_i}} = \left(\frac{N_{\mathrm{sig}\,i}}{\epsilon_{\mathrm{trigger}_i}\cdot\int\mathcal{L}dt} - \sigma^{\mathrm{W/Z/}\gamma^*}_{\mathrm{accepted}_i}\right)\cdot\frac{C_{\mathrm{migration}_i}}{\epsilon_{(\mathrm{reco+ID})_i}}\cdot\frac{1}{\Gamma_{\mathrm{bin}\,i}}, \tag{3.4}$$

where $N_{\mathrm{sig}\,i}$ is the number of signal electrons with reconstructed p_{T} in bin i of width $\Gamma_{\mathrm{bin}\,i}$, corresponding to the result of the extraction described in Section 3.2; $\int\mathcal{L}dt$ is the integrated luminosity as listed in Table 3.1; $\epsilon_{\mathrm{trigger}_i}$ is the trigger efficiency, measured in Section 3.3.1; $\epsilon_{(\mathrm{reco+ID})_i}$ is the combined reconstruction plus identification efficiency and $C_{\mathrm{migration}_i}$ is the bin migration correction factor, which are both

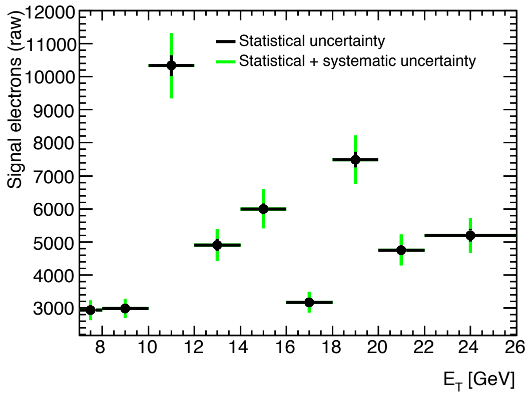

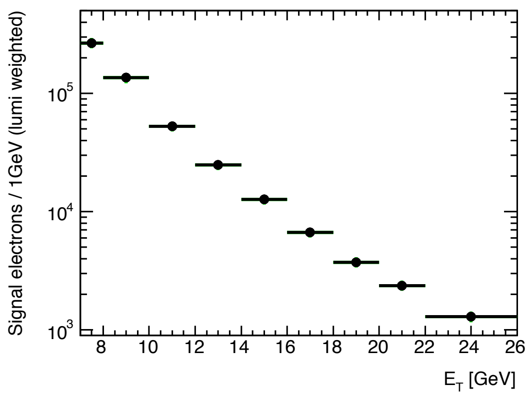

Figure 3.7: Distributions of the E_{T} of the extracted $Q \to e$ electron signal component before (left) and after (right) reweighting to 1.28 pb^{-1}. Statistical and systematic uncertainties are shown.

discussed in in Section 3.3.2. $\sigma^{\mathrm{W/Z}/\gamma^*}_{\mathrm{accepted}_i}$ is the expected value of the accepted W, Z and low-mass Drell-Yan cross-section in bin i, where the W and Z contribution is normalised to the NNLO theoretical prediction; while the low-mass Drell-Yan is only normalised to the Pythia prediction, since no higher order estimate was available.

3.3.1 Trigger Efficiency Measurement

The efficiency with which the signal electrons pass the L1 EM trigger is measured from the data in bins of cluster E_{T}. For the 3 and 6 GeV threshold triggers the efficiencies are measured using events selected by an alternative, very inclusive minimum bias trigger, based on hit information in the Minimum Bias Trigger Scintillator [143]. The efficiencies of the 11 and 15 GeV threshold triggers are measured using events recorded by the 6 GeV trigger, which is fully efficient in the E_{T} region for which the higher threshold triggers are used. Since these data-derived measurements are performed on the selected electron candidates, dominated by the hadronic background, a systematic uncertainty is estimated by comparing the measured trigger efficiencies to those expected in the simulation for heavy-flavour electrons. The trigger efficiencies are measured to be between 92.1% and 100.0% with a maximum uncertainty of 1.8%, where a luminosity weighted average of the different periods has been computed and is summarized in Table 3.7. Figure 3.8 shows the measurement of the trigger efficiency for each L1 trigger used, in the E_{T} bins implemented for the measurements, for both data and MC simulations.

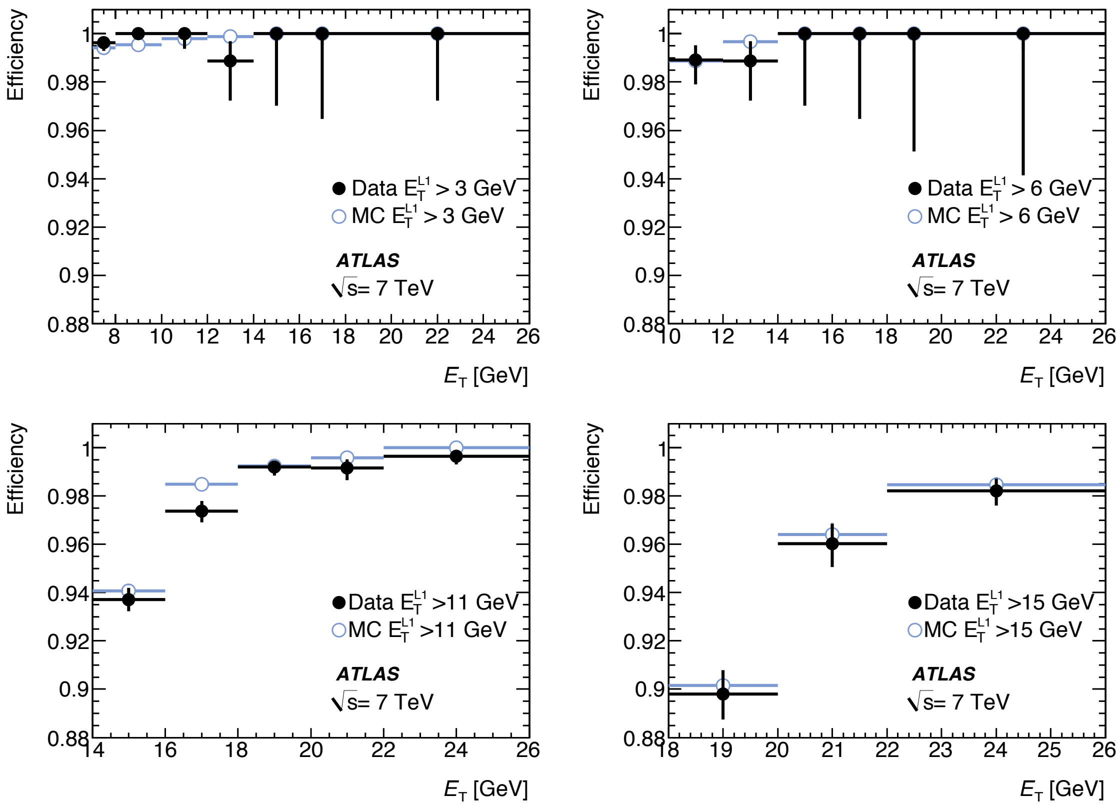

Figure 3.8: Measured efficiencies for the four triggers used in this analysis (for thresholds of 3, 6, 11 and 15 GeV respectively) as a function of E_T for electrons passing all selection criteria. The lower limit in the X-axis corresponds to the cut applied in the electron selection in each period.

3.3.2 Reconstruction and Identification Efficiencies and Migration Correction Factors

Apart from the trigger efficiency, all selection and identification efficiencies used to unfold detector effects are taken from MC simulations using a high statistics sample generated with `PYTHIA 6.4` [77] passed through a full simulation of the detector response based on `GEANT4` [81].

The correction of Equation 3.4 to the measured data may be defined using two quantities: the combined electron reconstruction plus identification efficiency, $\epsilon_{\mathrm{reco+ID}}$, and a term $C_{\mathrm{migration}}$ – defined as the ratio of the number of electrons in bin i of true p_T over the number of electrons in the same bin of reconstructed E_T after the full

L1 Threshold (GeV)	E_T bin (GeV)				
	7-8	8-10	10-12	12-14	14-16
3	$99.6^{+0.2}_{-0.3} \pm 0.2$	$100.0^{+0.0}_{-0.2} \pm 0.5$	$100.0^{+0.0}_{-0.6} \pm 0.2$	$98.9^{+0.8}_{-1.6} \pm 1.0$	$100.0^{+0.0}_{-3.0} \pm 0.0$
6	–	–	$98.9^{+0.6}_{-1.0} \pm 0.0$	$98.9^{+0.8}_{-1.6} \pm 0.8$	$100.0^{+0.0}_{-3.0} \pm 0.0$
11	–	–	–	–	$93.8^{+0.5}_{-0.5} \pm 0.3$
Overall	$99.6^{+0.2}_{-0.3} \pm 0.2$	$100.0^{+0.0}_{-0.2} \pm 0.5$	$99.0^{+0.5}_{-1.0} \pm 0.0$	$98.9^{+0.8}_{-1.6} \pm 0.9$	$96.4^{+0.3}_{-1.5} \pm 0.2$

L1 Threshold (GeV)	E_T bin (GeV)			
	16-18	18-20	20-22	22-26
3	$100.0^{+0.0}_{-3.5} \pm 0.0$	$100.0^{+0.0}_{-2.8} \pm 0.0$	$100.0^{+0.0}_{-2.8} \pm 0.0$	$100.0^{+0.0}_{-2.8} \pm 0.0$
6	$100.0^{+0.0}_{-3.5} \pm 0.0$	$100.0^{+0.0}_{-4.9} \pm 0.0$	$100.0^{+0.0}_{-5.9} \pm 0.0$	$100.0^{+0.0}_{-5.9} \pm 0.0$
11	$97.4^{+0.4}_{-0.5} \pm 1.1$	$99.2^{+0.3}_{-0.3} \pm 0.0$	$99.2^{+0.4}_{-0.5} \pm 0.4$	$99.6^{+0.2}_{-0.3} \pm 0.4$
15	–	$89.8^{+1.0}_{-1.1} \pm 0.4$	$96.0^{+0.8}_{-1.0} \pm 0.4$	$98.2^{+0.5}_{-0.6} \pm 0.3$
Overall	$98.5^{+0.2}_{-1.7} \pm 0.6$	$92.1^{+0.8}_{-1.3} \pm 0.3$	$96.8^{+0.7}_{-1.4} \pm 0.4$	$98.6^{+0.4}_{-1.0} \pm 0.3$

Table 3.7: Trigger efficiency in % by E_T bin with luminosity weighted average. Errors are statistical and systematic, respectively.

identification selection – to account for migration between the different p_T bins. These quantities are calculated using simulated electrons classified as originating from a B or D primary hadron (i.e. the first hadron, after the hard scattering, found in the MC history, from which the electron eventually stemmed), according to the algorithm described in Appendix A.

The individual cut efficiencies for the acceptance, preselection and identification requirements listed in Table 3.2 with respect to the previous cut are shown in Figure 3.9(a) in true p_T bins, and the values may be found in Table 3.8. The identification cuts are applied in one single step in this evaluation. In Figure 3.9 the distribution labelled as "η fiducial" corresponds to the efficiency of matching the simulated electron from heavy-flavour to a reconstructed electron within the acceptance volume, i.e. $|\eta| < 2.0$ and excluding $1.37 < |\eta| < 1.52$. For electrons with $p_T > 7$ GeV, this efficiency ranges between 83 and 90%, and at least 5% of the loss is due to a failure to match the simulated electron to a reconstructed electron's track in an environment with many tracks (non-isolated). The cumulative effect of successive cuts, or cutflow, for $\epsilon_{\text{reco+ID}} = \epsilon_{\text{reco}} \times \epsilon_{\text{ID}}$ is shown in Figure 3.9(b). The full tables can be found in Appendix B. Figure 3.10 shows the single cut efficiencies as a function of the reconstructed E_T, for simulated electrons that have a reconstructed match; the identification efficiency shown here was also measured in data, as discussed in Section 3.3.2.4.

Cut	p_T bin (GeV)				
	7-8	8-10	10-12	12-14	14-16
Vertexing	99.99 ± 0.00	99.99 ± 0.00	100.00 ± 0.00	100.00 ± 0.00	99.99 ± 0.01
η fiducial	83.25 ± 0.10	85.14 ± 0.09	86.87 ± 0.14	87.56 ± 0.21	88.49 ± 0.28
E_T	63.10 ± 0.13	89.00 ± 0.09	97.22 ± 0.07	99.04 ± 0.06	99.40 ± 0.07
Calorimeter fiducial	96.30 ± 0.07	95.38 ± 0.06	93.60 ± 0.11	92.63 ± 0.18	91.99 ± 0.26
N_{Si}	99.91 ± 0.01	99.88 ± 0.01	99.86 ± 0.02	99.87 ± 0.02	99.85 ± 0.04
N_{TRT}	97.19 ± 0.06	97.01 ± 0.05	97.49 ± 0.07	97.95 ± 0.10	98.32 ± 0.13
B-Layer fiducial	95.72 ± 0.07	95.88 ± 0.06	96.00 ± 0.09	96.20 ± 0.13	95.96 ± 0.19
f_1	99.69 ± 0.02	99.67 ± 0.02	99.69 ± 0.03	99.60 ± 0.04	99.62 ± 0.06
Identification	89.69 ± 0.11	90.06 ± 0.10	87.95 ± 0.16	86.96 ± 0.24	85.13 ± 0.36
Total	42.03 ± 0.13	60.27 ± 0.13	64.78 ± 0.20	65.47 ± 0.30	64.65 ± 0.42

Cut	p_T bin (GeV)			
	16-18	18-20	20-22	22-26
Vertexing	100.00 ± 0.00	99.93 ± 0.04	100.00 ± 0.00	100.00 ± 0.00
η fiducial	88.52 ± 0.39	89.19 ± 0.50	89.67 ± 0.63	90.26 ± 0.62
E_T	99.59 ± 0.08	99.50 ± 0.12	99.81 ± 0.09	99.55 ± 0.15
Calorimeter fiducial	92.23 ± 0.35	91.97 ± 0.46	92.15 ± 0.59	91.66 ± 0.61
N_{Si}	99.84 ± 0.05	99.76 ± 0.08	99.89 ± 0.08	99.79 ± 0.11
N_{TRT}	98.44 ± 0.17	98.82 ± 0.19	98.88 ± 0.24	98.74 ± 0.26
B-Layer fiducial	95.48 ± 0.28	95.75 ± 0.36	96.49 ± 0.42	95.96 ± 0.46
f_1	99.65 ± 0.08	99.40 ± 0.14	99.63 ± 0.14	99.54 ± 0.16
Identification	83.10 ± 0.52	81.42 ± 0.72	79.50 ± 0.95	77.56 ± 1.00
Total	63.19 ± 0.58	62.31 ± 0.77	62.26 ± 1.00	60.12 ± 1.03

Table 3.8: Efficiencies of event, acceptance, preselection and identification cuts in true p_T bins with respect to the previous cut, determined from `PYTHIA` MC simulations for electrons from heavy-flavour decays.

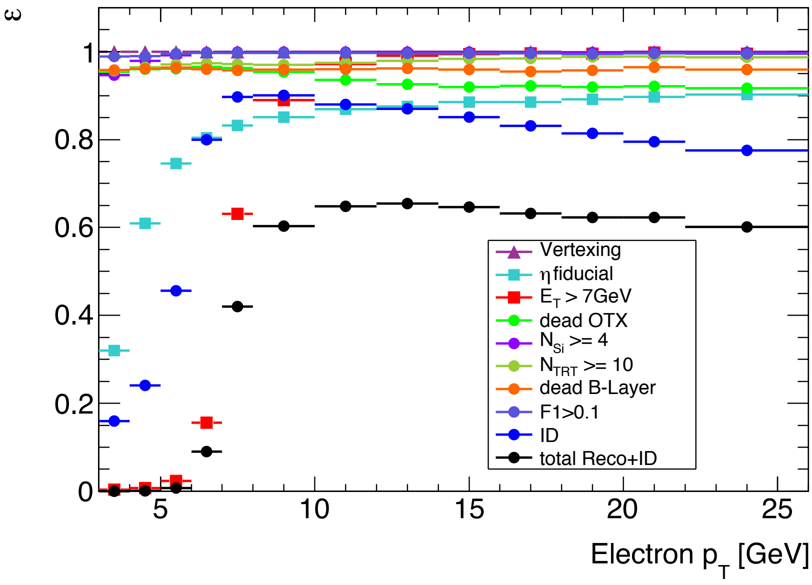

(a)

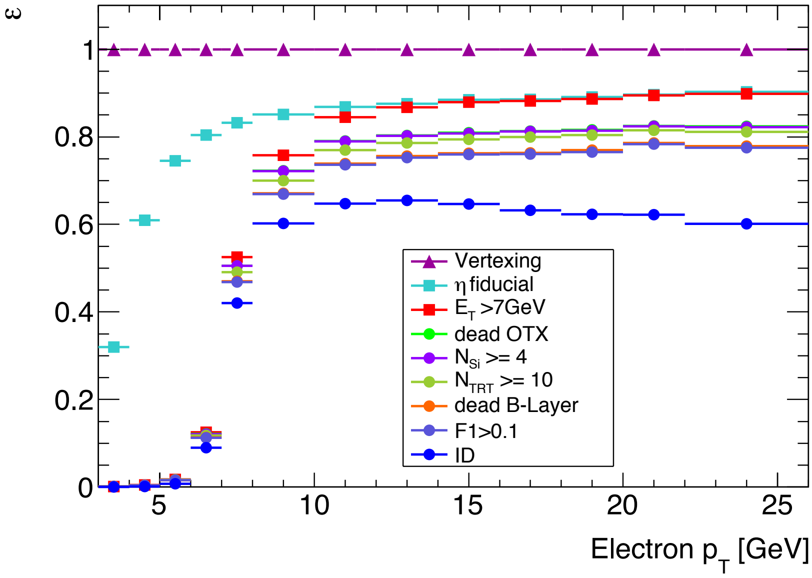

(b)

Figure 3.9: Efficiencies for all selection cuts with respect to the previous cut (a) and cumulative (b) in true p_{T} bins.

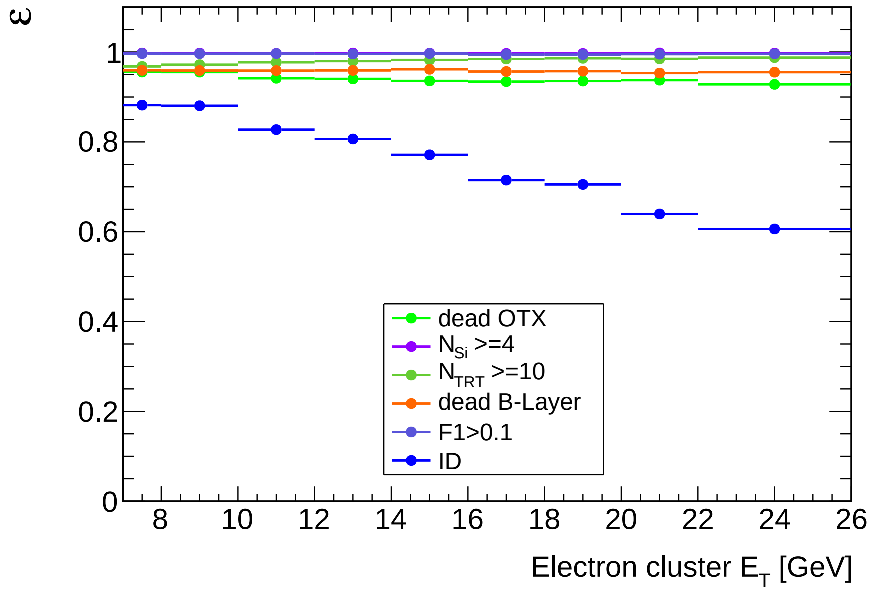

Figure 3.10: Efficiencies for all selection cuts with respect to the previous cut, in reconstructed E_{T} bins.

3.3.2.1 Monte Carlo Model Comparisons of Efficiencies and Migration Correction Factors

The highest statistics MC sample used for the central result is generated by `PYTHIA v6.4.21` [77]. As NLO MC generators are expected to better describe the data, additional samples of `POWHEG-hvq v1.0 patch 4` [75, 76] interfaced to both `PYTHIA v6.421` and `JIMMY v4.31` (for multi-parton interactions [144]) plus `HERWIG v6.510` [78] are used. A description of `PYTHIA`, `HERWIG` and `POWHEG` is given in Section 2.3.2.1. The `POWHEG` samples use `TAUOLA v2.7` to describe τ-lepton decays [145, 146] and `PHOTOS v2.15` to model QED FSR [147].

The comparison of the predictions of different MC generators for efficiencies and correction factors are shown in Figure 3.11. The efficiencies calculated with the LO and NLO samples agree within statistical errors, i.e. within a few percent, as illustrated by the ratio of `POWHEG` to `PYTHIA` predictions for $\epsilon_{\mathrm{reco+ID}}/C_{\mathrm{migration}}$ in Figure 3.12. Therefore, for the evaluation of efficiencies and migration correction factors, the high statistics sample of `PYTHIA` is used.

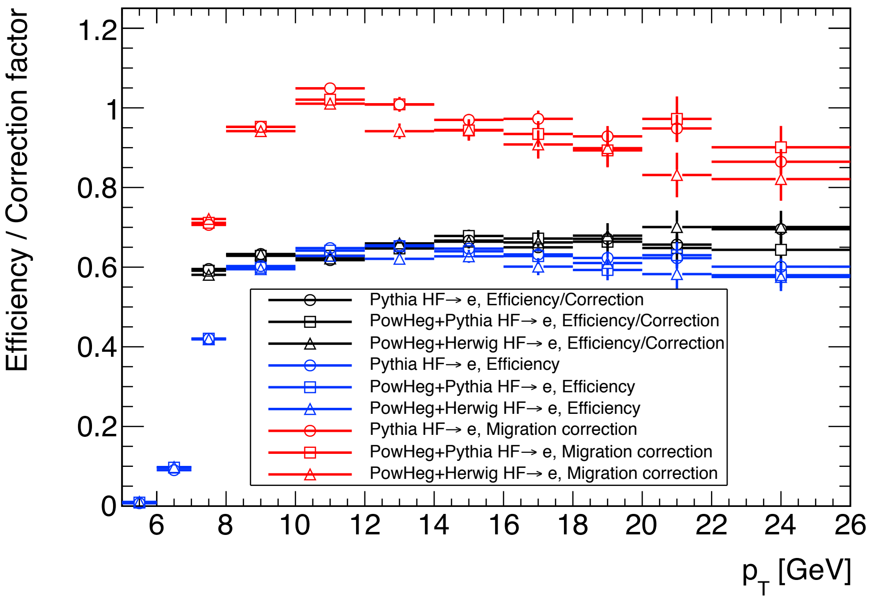

Figure 3.11: Electron reconstruction and identification efficiencies (blue), migration correction factors (red) and the total correction factor $\epsilon_{\text{reco+ID}}/C_{\text{migration}}$ (black) as a function of the true electron p_{T} for heavy-flavour signal candidates, comparing three different MC models: `PYTHIA` (circles), `POWHEG+PYTHIA` (squares) and `POWHEG+HERWIG` (triangles).

The impact of pile-up on the efficiency and migration corrections was checked to be negligible by comparing $\epsilon_{\text{reco+ID}}/C_{\text{migration}}$ obtained from a `PYTHIA` MC sample without pile-up to a `PYTHIA` sample simulated with an average number of interactions per bunch-crossing $\langle n \rangle = 2$. The events simulated with pile-up are reweighted according to the number of reconstructed vertices in order to match the distribution of the number of interactions per bunch-crossing to what is observed in data [148]. The ratio of the total correction factor for the sample with pile-up to the prediction without pile-up with and without event weights is shown in Figure 3.13. This ratio is compatible with unity in the whole range, therefore MC samples without pile-up are used to unfold the data distribution.

As the efficiency and its uncertainty are estimated from data using the tag-and-probe technique and show a good agreement with the predictions, as described in Section 3.3.2.4, the cross-checks detailed in this section do not introduce additional systematic errors.

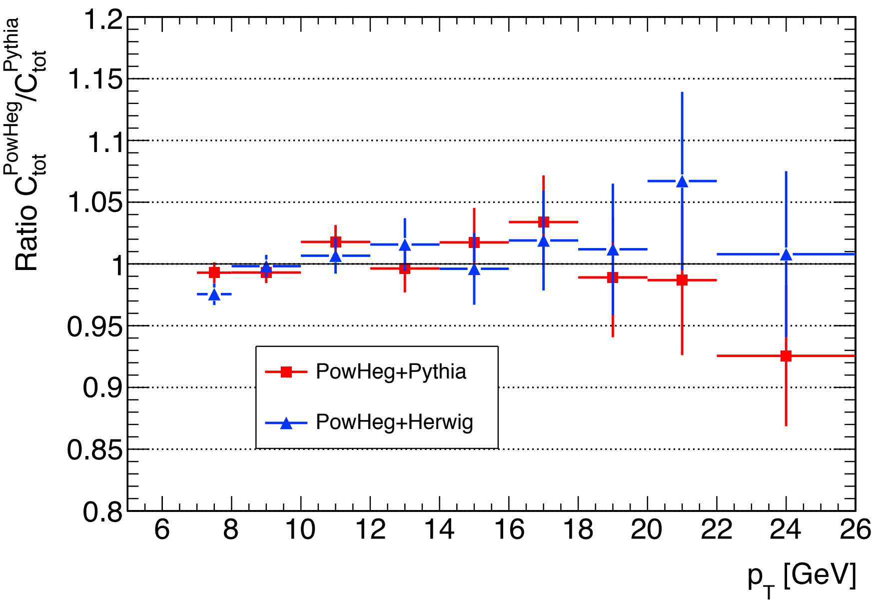

Figure 3.12: The ratio of the total correction factor $\epsilon_{\text{reco+ID}}/C_{\text{migration}}$ for POWHEG+PYTHIA and POWHEG+HERWIG to that of PYTHIA.

3.3.2.2 Comparison of Efficiencies and Migration Correction Factors for Electrons from B or D-hadrons

The predictions of FONLL, PYTHIA, POWHEG+PYTHIA and POWHEG+HERWIG for the B-hadron fraction are shown in Figure 3.14. The uncertainty bands on the FONLL prediction are calculated assuming D and B rates are either fully correlated, anti-correlated or independent. The latter is used to estimate the systematic uncertainty on the heavy-flavour composition, found to be less than 12% (relative) in the p_{T} range of interest. Because of the large uncertainty in the relative amount B and D hadrons produced, studying the efficiency for electrons from B and D hadrons separately is essential.

The efficiencies $\epsilon_{\text{reco+ID}}$ and correction factors $C_{\text{migration}}$ are calculated using the heavy-flavour composition predicted by PYTHIA, shown by the black dots in Figure 3.14. While the efficiencies and migration correction factors are different for B and D-hadron decays, as shown in Figure 3.15, the total correction factor $\epsilon_{\text{reco+ID}}/C_{\text{migration}}$ coincides for both sources, typically within 5% (relative). The effect of the B-hadron fraction uncertainty on the total correction factor is thus estimated to be only of the order of 1%.

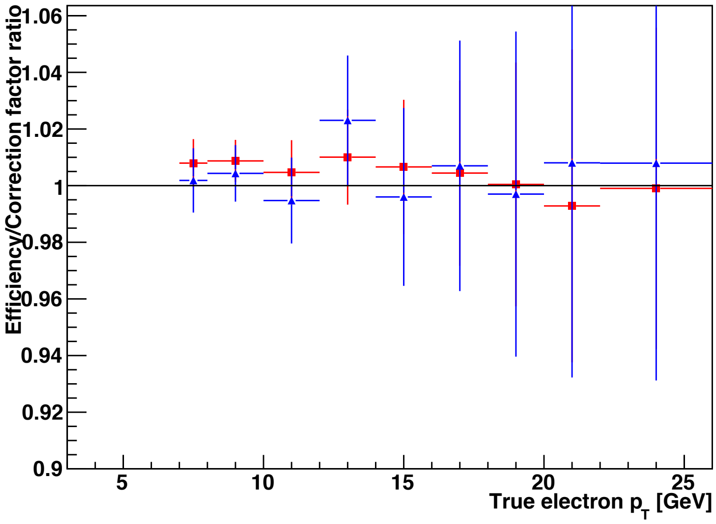

Figure 3.13: The ratio of $\epsilon_{\text{reco+ID}}/C_{\text{migration}}$ obtained with different pile-up conditions to the the prediction in the simulation without pile-up. The red squares correspond to a simulation with $\langle n\rangle = 2$ interactions per bunch crossing and the blue triangles correspond to the case when event weights are applied to the simulation in order to reproduce the distribution of the number of vertices seen in data.

To illustrate the sources of lower efficiency for electrons from D-hadron decays, Figure 3.16 shows the distribution of the calorimeter shower shapes E_{ratio} and w_{stot}, on which cuts are applied at the identification level, versus the true electron p_{T} for preselected electrons from B-hadrons and D-hadrons. The latter display a behaviour more background-like, with a slightly wider shower and more disperse distribution of E_{ratio}, which explains the lower identification efficiency for electrons from $D \to e$ than from $B \to e$ observed in Figure 3.15. This can also be observed from Figure 3.17, where the distributions of E_{ratio} and w_{stot} are shown for both heavy-flavour sources for preselected electrons in p_{T} bins $10 - 12$ GeV and $22 - 26$ GeV.

The kinematics of B-hadron decays, where large mass differences with its decay products exist, allow the decay products to have high momentum. Therefore, the electron from $B \to e$ can often have a higher angular separation from the rest of the hadronic remnants – i.e. high $p_{\text{T}}^{\text{rel}}$. In contrast, in the case of D-hadron decays the mass differences are smaller, and the electron tends to be closer to the hadrons from the decay. It is this nearby hadronic activity that can be detected in the LAr calorimeter and which affects the estimation of the electron's shower shape parameters.

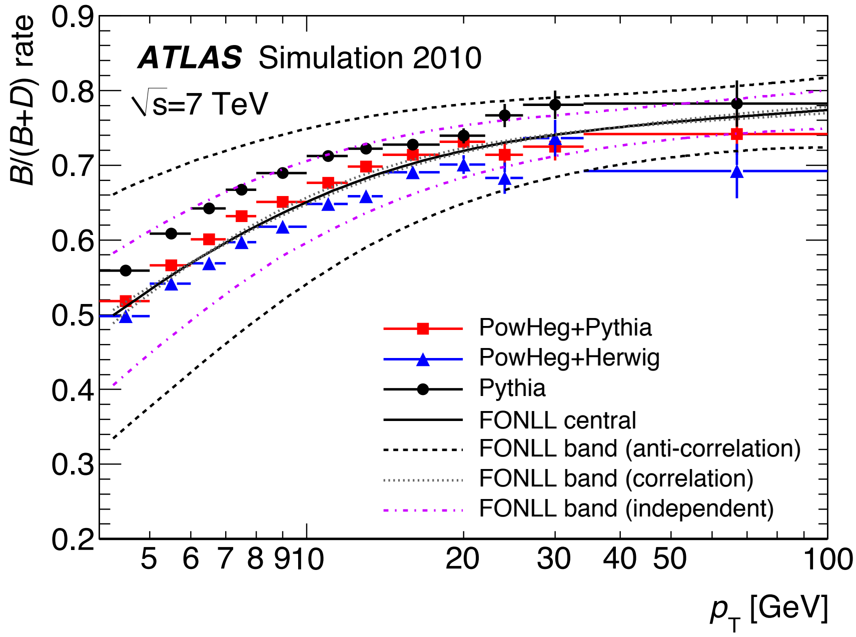

Figure 3.14: The B-hadron fraction as a function of the true electron p_T for three MC models: `PYTHIA` (dots), `POWHEG+PYTHIA` (squares) and `POWHEG+HERWIG` (triangles); together with the `FONLL` prediction (solid line) with fully correlated (dotted), anti-correlated (dashed) and independent (dot-dashed) D and B rates in the uncertainty bands. The latter is used to estimate the dependence of the total correction factor on this fraction.

It was also studied how the fraction of electrons from prompt J/ψ production might affect the efficiency. The comparison of the electron reconstruction and identification efficiencies, migration correction factors and their combination $\epsilon_{\rm reco+ID}/C_{\rm migration}$ is shown on Figure 3.18 for electrons from prompt J/ψ production compared to electrons produced in all heavy-flavour decays. The former are more isolated and exhibit a higher efficiency and lower migration between bins. For the total correction $\epsilon_{\rm reco+ID}/C_{\rm migration}$ the largest difference, of about 10% relative, is observed at high p_T. This translates to less than 1% change in $\epsilon_{\rm reco+ID}/C_{\rm migration}$ for the proper mixture of electrons (i.e. $\sim 15\%$ of electrons from prompt J/ψ in the $D \to e$ component) and is neglected in the following.

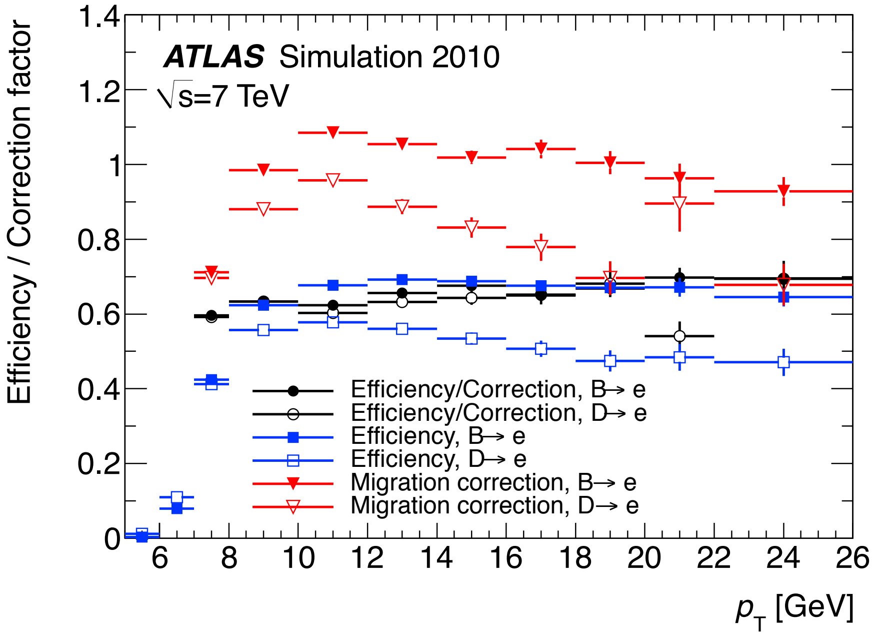

Figure 3.15: Reconstruction and identification efficiencies (blue), migration correction factors (red) and the total correction factor $\epsilon_{\text{reco+ID}}/C_{\text{migration}}$ (black) as a function of electron p_{T} evaluated from `PYTHIA` MC for $B \to e$ (full symbols) and $D \to e$ (open symbols) Errors are statistical only.

The electron p_{T} is measured with good precision as shown in Figure 3.19. The top row of Figure 3.19 shows the distribution of the relative difference between true p_{T} and the reconstructed E_{T} in linear and logarithmic scales, and the correlation of these two quantities for electrons from all heavy-flavour decays. The middle and bottom rows of the figure show the resolution and correlation for electrons from B and D-hadron decays, respectively. The energy scale and resolution are slightly better for electrons from B hadrons than from D hadrons, with smaller mean and root mean square between the true and the reconstructed p_{T} and a more diagonal correlation. The combined result for electrons from all heavy-flavour decays translates in a resolution of $\sim 14\%$ and leads to a quasi-diagonal response matrix.

The shape of the residuals in Figure 3.19 can be explained by energy loss by bremsstrahlung for electrons with E_{T} reconstructed below the true value, which populate the small tail with negative residuals; and by the contributions to the cluster energy from nearby hadrons for non-isolated electrons whose reconstructed E_{T} is above the true value, present in the large tail of positive residuals, that affects

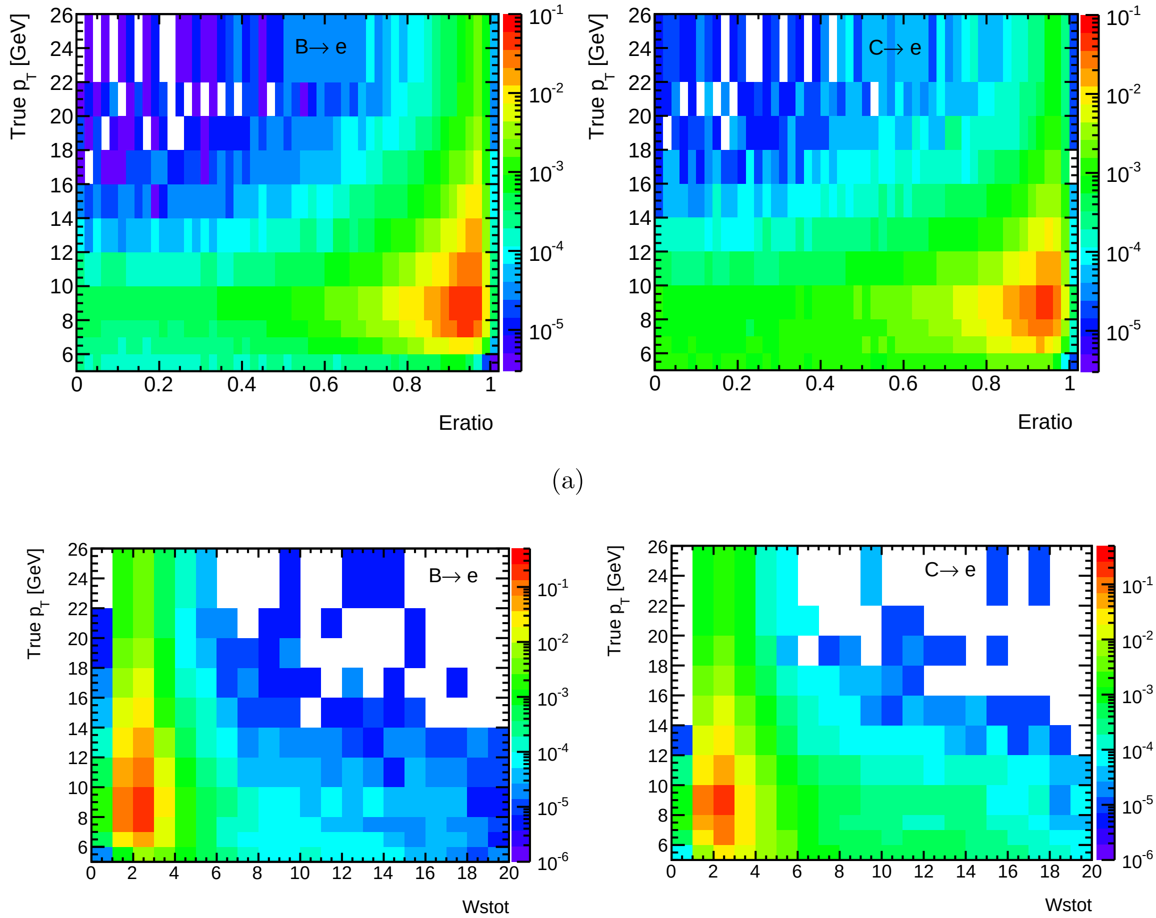

(a)

(b)

Figure 3.16: Shower shape variables E_{ratio} (a) and w_{stot} (b) vs. true electron p_{T} from $B \to e$ (left) and $D \to e$ (right) decays after preselection.

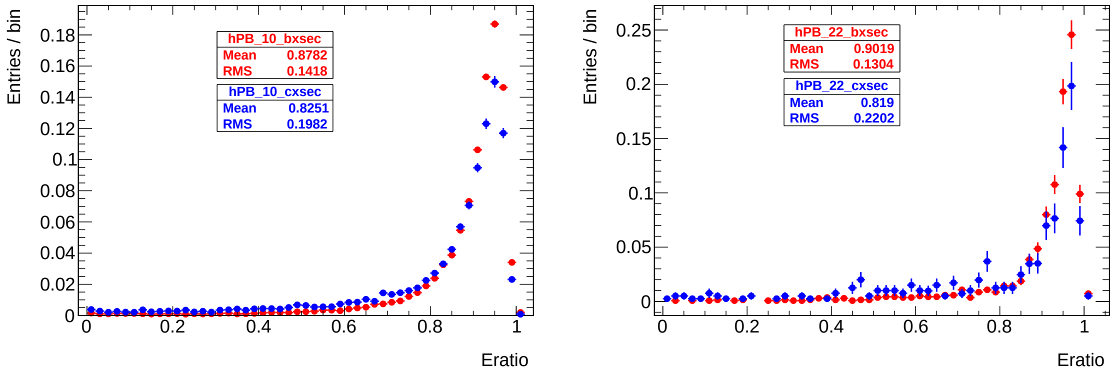

(a)

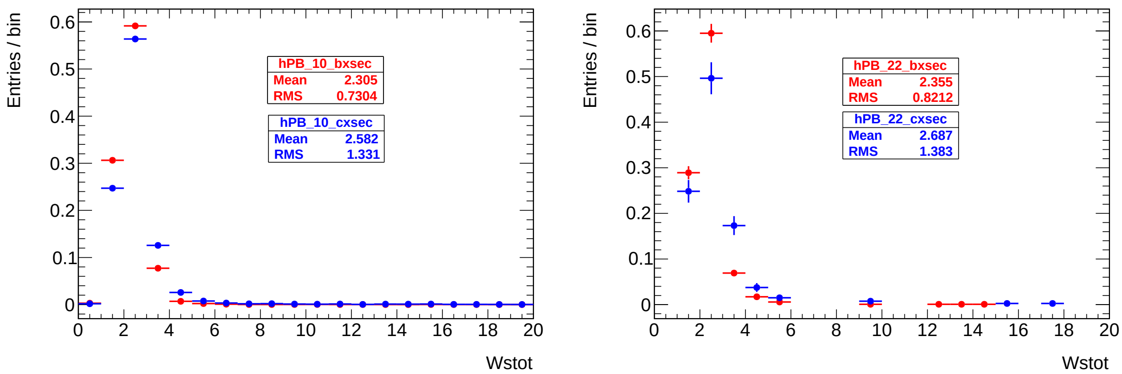

(b)

Figure 3.17: Distribution of shower shape variables E_{ratio} (a) and w_{stot} (b), for electrons from $B \to e$ (red) and $D \to e$ (blue) decays after preselection, in truth E_{T} bins: 10-12 GeV (left) and 22-26 GeV (right).

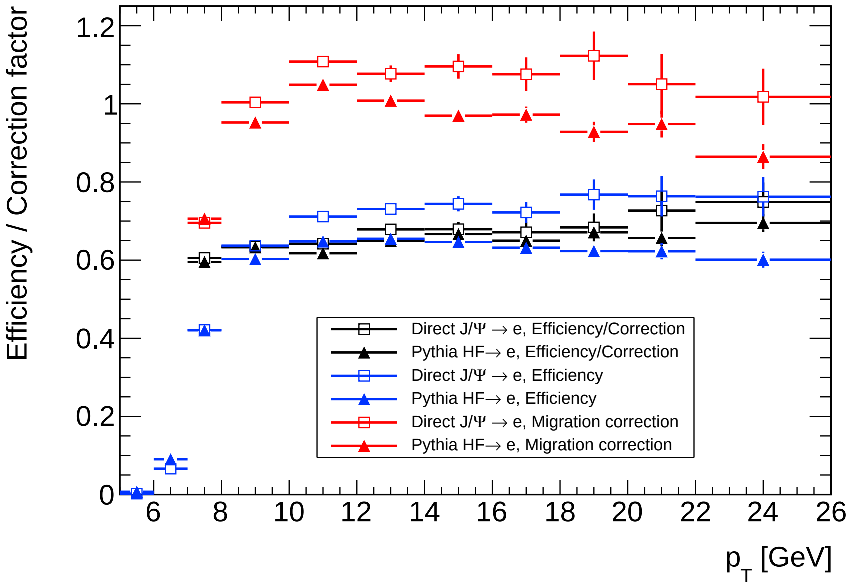

Figure 3.18: Reconstruction and identification efficiencies (blue), migration correction factors (red) and the total correction factor $\epsilon_{\mathrm{reco+ID}}/C_{\mathrm{migration}}$ (black) as a function of electron p_{T} evaluated from `PYTHIA` MC for prompt $J/\psi \to e^+e^-$ (open squares) and combined heavy flavour $(B/D \to e)$ (full triangles). Errors are statistical only.

electrons from D-hadrons more. This implies that there is a stronger migration from low p_{T} to high reconstructed E_{T} for electrons from D-hadrons than from B-hadrons, resulting in a migration correction factor $C^{D\to e}_{\mathrm{migration}} < C^{B\to e}_{\mathrm{migration}} < 1$ in the higher p_{T} bins, as seen in Figure 3.15.

Figure 3.20 shows the distribution of the calorimeter isolation variable EtCone30 – which measures the total E_{T} deposited in the electromagnetic and hadronic calorimeters in a $\Delta R = 0.3$ cone around, but excluding, the calorimeter cluster – for electrons from B and D hadrons versus the true electron p_{T}. It can be noted from the figure that electrons from $D \to e$ tend to be less isolated – have higher values of EtCone30 – than electrons from $B \to e$, especially at low p_{T}.

Additionally, the identification cuts reject less isolated electrons more frequently, as can be seen from the EtCone30 distributions shown in Figure 3.21 for both sources in p_{T} bins $10-12$ GeV and $22-26$ GeV, before and after the identification requirements. Both the mean and the root mean square of the isolation distribution decrease after applying the identification criteria.

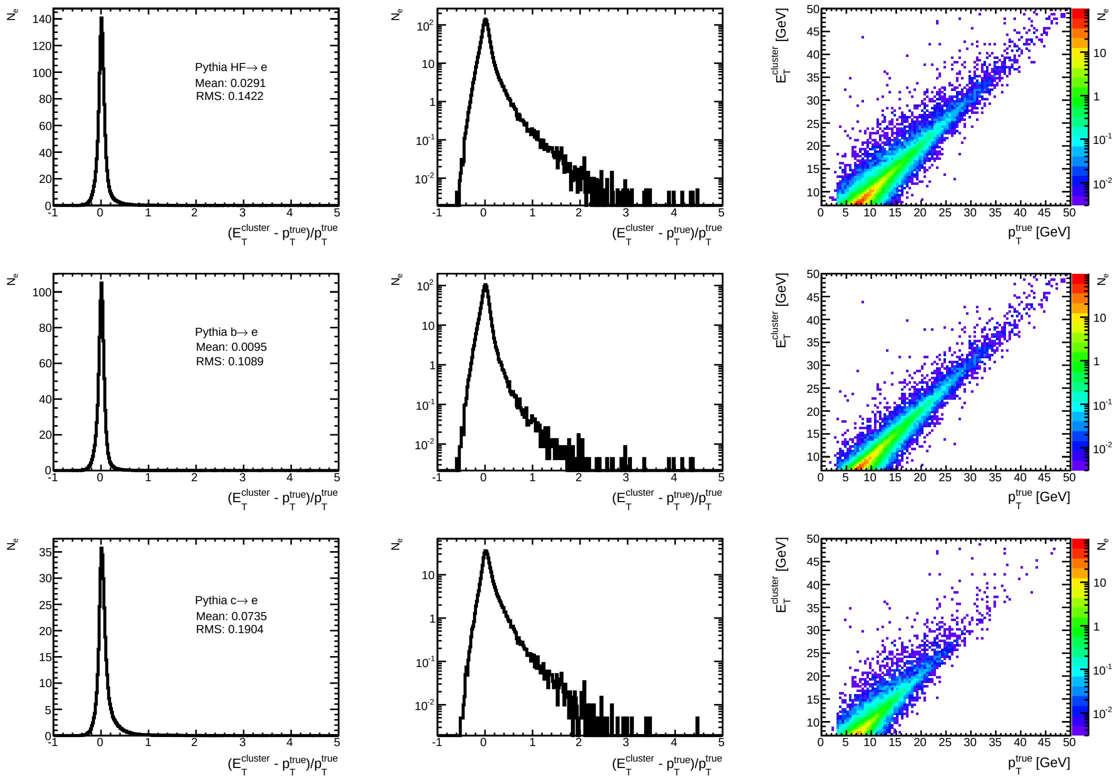

Figure 3.19: Fractional electron transverse energy residuals and true vs. reconstructed transverse energy for all heavy-flavour decays (top row) and separately for B-hadron (middle row) and D-hadron (bottom row) decays.

In summary, the less isolated nature of electrons from D-hadrons explains both their lower identification efficiency and the higher fraction of migration towards higher E_{T}. This results in the ratio $\epsilon_{\mathrm{reco+ID}}/C_{\mathrm{migration}}$ for isolated and non-isolated electrons from heavy-flavour having similar values. The effect of cancellation in this ratio, seen in the comparison of correction factors for B or D-hadrons in Figure 3.15 and for J/ψ in Figure 3.18, is not a design feature, but rather a coincidence. The less isolated signal electrons show lower efficiencies but have more migration – i.e. lower values of $C_{\mathrm{migration}}$ – towards higher E_{T} bins because of the nearby hadronic activity and of the steeply falling p_{T} spectrum.

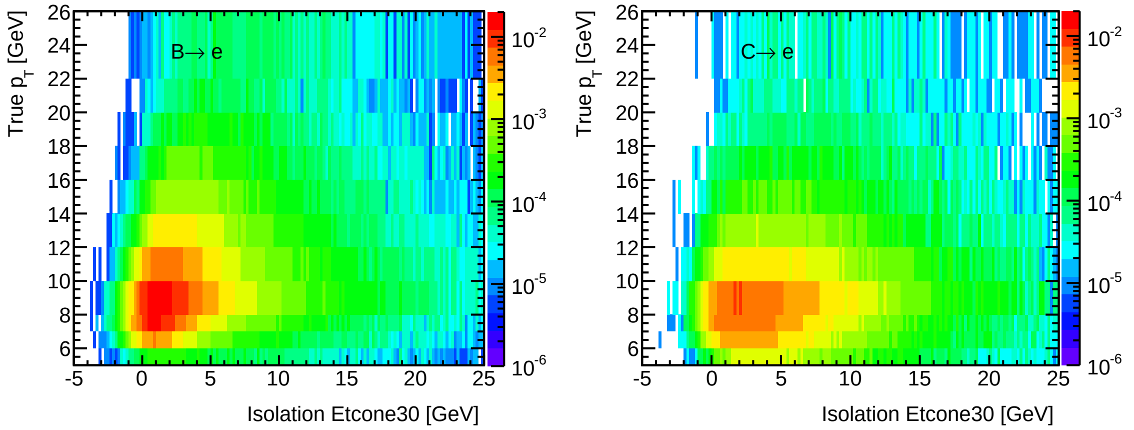

(a)

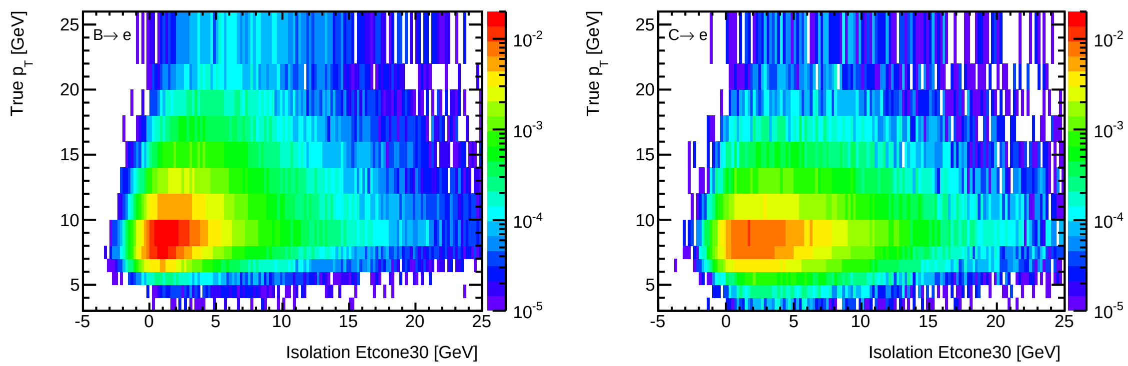

(b)

Figure 3.20: Calorimeter isolation EtCone30 vs. true electron p_{T} for $B \to e$ (left) and $D \to e$ (right) decays after preselection (a) and after identification cuts (b).

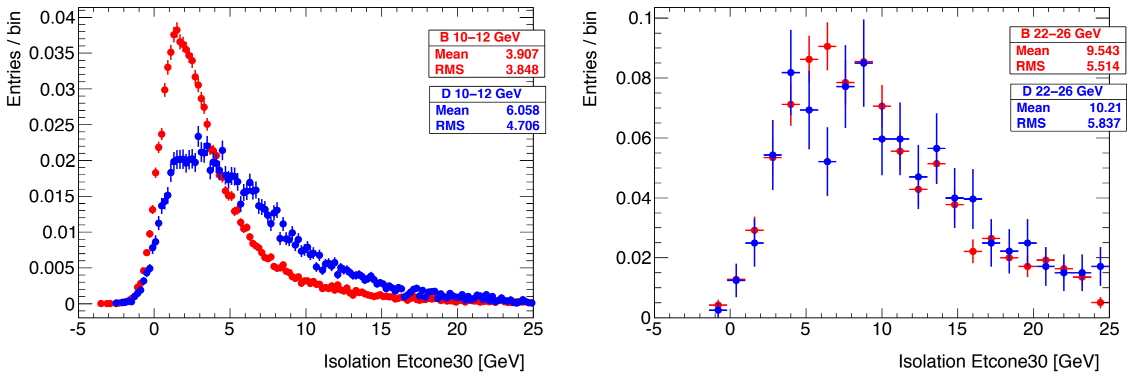

(a)

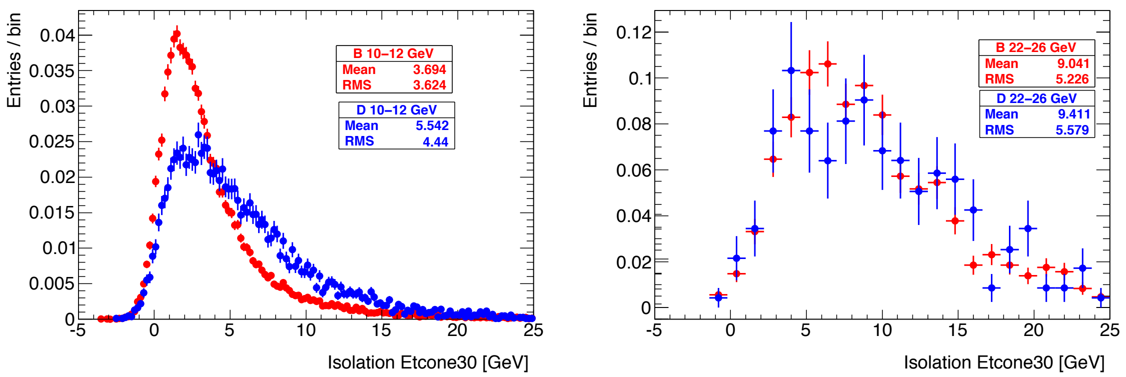

(b)

Figure 3.21: Distribution of the calorimeter isolation EtCone30 for electrons from $B \rightarrow e$ (red) and $D \rightarrow e$ (blue) decays after preselection (a), and after identification (b) in truth E_{T} bins: 10-12 GeV (left) and 22-26 GeV (right).

3.3.2.3 Reconstruction Efficiency Cross-checks with Data

The preselection efficiency cannot be evaluated in an unbiased way using data, as the signal purities before and after preselection are very low. Nevertheless, the efficiencies of individual preselection cuts, which were presented in Table 3.8, are cross-checked on data control samples where possible, as described below:

Vertex-finding efficiency In simulated events, the vertex-finding algorithm is fully efficient for signal events. On data, it is measured for all events with a reconstructed electron that pass the trigger and data quality requirements. The measured efficiency on data is 99.84%, averaged across all electron p_{T} bins, with negligible statistical uncertainty.

Calorimeter fiducial cuts In the electron preselection, kinematic cuts were made to remove electrons reconstructed in parts of the calorimeter with readout or other problems. The precise cuts varied by run period, but amounted to no more than a 7% loss of acceptance. The acceptance of this cut is well modelled by the MC. This was verified using run periods A-C, where the acceptance predicted by MC and that measured on data agreed to within 0.1%.

SCT hit efficiency For the estimation of the silicon hit efficiency from data, the efficiency of reconstructing four silicon hits is approximated by the efficiency of measuring five hits given that one has already been found. The values measured range between 99.8 and 100% and good agreement between data and simulated events is seen, with a maximum discrepancy of less than 0.1%.

TRT hit efficiency The efficiency of requiring ten TRT hits was measured on all events with an electron candidate having at least four silicon hits. The TRT hit efficiency for signal electrons in the MC simulation is about 2% lower than the estimated efficiency for all candidates in the lowest E_{T} bin, the difference decreasing to approximately 0.2% in the final bin. Taking into account all candidates, data/MC agreement is very good, within 0.2%. The value of the efficiency for this cut is found to be between 97 and 99% for signal electrons.

f_1 cut efficiency The final preselection cut, on f_1, is evaluated using a conversion-enhanced sample. Conversions are selected by rejecting electron candidates with a pixel B-layer hit without requiring additional silicon and TRT hits. The measured efficiency is still biased significantly by hadron fakes, which have a lower efficiency, between 92 and 95%. As such, the observed discrepancies between data and MC, of less than 1% do not warrant the inclusion of an additional systematic uncertainty on the efficiency of this cut for signal electrons, for which the efficiency measured in MC is $\sim 99.5\%$.

3.3.2.4 Data-derived Identification Efficiency

The efficiency of the electron identification cuts in the simulation is compared with a measurement made on data using a tag-and-probe (T&P) technique. The identification efficiency $\epsilon_{\mathrm{ID}}^{\mathrm{T\&P}}$ is determined from the fraction of probe signal electrons that also pass the identification criteria,

$$\epsilon_{\mathrm{ID}}^{\mathrm{T\&P}} = \frac{N_{\mathrm{probe\ \&\ identified}}^{Q\to e}}{N_{\mathrm{probe}}^{Q\to e}}. \tag{3.5}$$

The probe candidates, which are required to pass only the preselection cuts of Table 3.2, are taken from a sample of events enriched in heavy-quark pairs where both heavy hadrons decay semi-leptonically. To select such events, the tag electron candidate is subject to more stringent identification cuts than those described in the previous section, including requirements on f_{TR} and n_{BL}. Additionally the T&P candidate pair must have opposite charge and, in order to select only the non-isolated electrons, an invariant mass below the Z mass window and outside of the J/ψ mass region. The remaining isolated-electron contribution outside the region of the Z and J/ψ mass resonances, for example from low-mass Drell-Yan, is very low and does not affect the efficiency calculation [141].

The only difference between the probe electron selection and the preselection cuts defined in Table 3.2 is that the minimum E_{T} of the probe is set at 3 GeV instead of 7 GeV. While this is below the range of interest for the final cross-section measurement, a comparison of the data-derived and MC expected efficiencies is still worthwhile in this high statistics region. This low E_{T} cut can be used since the trigger bias is removed by the tag selection.

The signal purity remains low after the T&P selection, being 9 % for preselected probe candidates and 31% for probe candidates passing also the identification criteria. To extract the signal component of the probe sample before and after the identification cuts, the signal extraction procedure of Section 3.2.1 is applied twice, in order to obtain $N_{\mathrm{probe}}^{Q\to e}$ and $N_{\mathrm{probe\ \&\ identified}}^{Q\to e}$ from

$$
\begin{aligned}
N_{\text{probe}}^{\text{candidates}} &= N_{\text{probe}}^{Q\to e} + N_{\text{probe}}^{h\to e} + N_{\text{probe}}^{\gamma\to e} \\
N_{\text{probe \& identified}}^{\text{candidates}} &= N_{\text{probe \& identified}}^{Q\to e} + N_{\text{probe \& identified}}^{h\to e} + N_{\text{probe \& identified}}^{\gamma\to e}.
\end{aligned}
\tag{3.6}
$$

The Tiles Method used for the T&P extraction differs slightly from that described in Section 3.2.1 since, apart from f_{TR} and n_{BL}, the variable f_1 is used to discriminate the background instead of E/p. The binning of the signal extraction is also modified from the baseline extraction as a consequence of the low statistics, using 5 bins in E_{T} instead of 9 in a slightly enlarged range $3 < E_{\text{T}} < 26$ GeV. Figure 3.22(a) shows the extracted efficiency measured as a function of E_{T} compared to the MC prediction.

The systematic uncertainties for the identification efficiency arise from the use of the Tiles Method to perform the signal extraction before and after identification cuts. Hence the systematic uncertainties are treated in a similar way to those described in Section 3.2.2 for the main signal extraction for the data-MC discrepancy of the templates and the energy scale uncertainty, but must be computed for both extractions. The bias of the method is evaluated using pseudo-experiments. The resulting uncertainties are presented in Table 3.9. Both statistical and systematic errors are shown in the T&P result of Figure 3.22(a).

Source	Uncertainty on T&P efficiency (%)
MC-data discrepancies in $Q \to e$ and $\gamma \to e$ templates:	
-n_{BL} distribution	4.4
-f_{TR} distribution	2.2
-f_1 distribution	2.8
Method bias	3.8
Energy scale uncertainty	2.8
Total Uncertainty	7.4

Table 3.9: Overall systematic errors from the T&P analysis.

The final cross-section determination uses the efficiency derived from simulations, since it is not possible to bin finely enough in E_{T} to provide the required information in a data-driven way. Figure 3.22(b) shows the ratio of the measured efficiency from the T&P procedure to the true efficiency calculated from the MC. This ratio is always compatible with 1 within the systematic uncertainty of the measurement, and it can be concluded that the data-derived and MC efficiencies are consistent. Using the results, a constant is fitted through the points taking into account only their statistical error, from which a relative uncertainty of 5.4% is assigned to the MC-derived identification efficiency in each E_{T} bin of the final analysis.

This systematic uncertainty should be combined with the 7.4% relative systematic uncertainty of the T&P measurement presented in Table 3.9, which leads to a total of 9.2% uncertainty from the T&P method assigned to the MC identification efficiency across all bins. However, for the final cross-section calculation the systematic uncertainties correlated between the efficiency determination and the signal extraction are properly taken into account and therefore at that stage these errors are quoted independently.

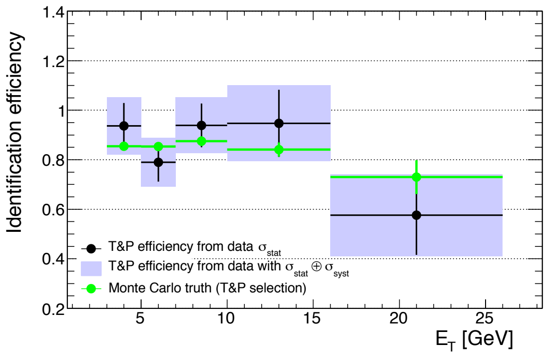

(a)

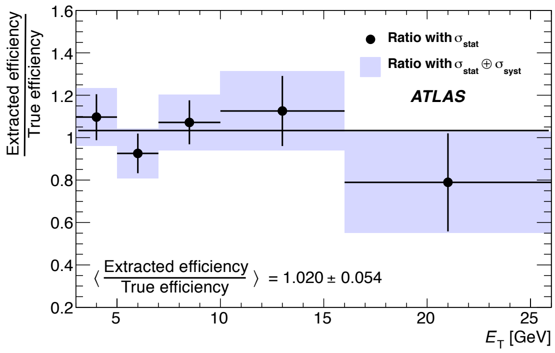

(b)

Figure 3.22: (a) T&P measured electron identification efficiency with statistical and systematic uncertainties as a function of reconstructed E_{T} and (b) ratio of the extracted electron identification efficiency using the T&P method to the true identification efficiency from the simulation, with statistical and statistical plus systematic uncertainties.

3.3.2.5 Summary of Efficiencies and Migration Corrections

The full bin-by-bin correction factor is defined as

$$C_{\mathrm{total}} = \epsilon_{\mathrm{reco+ID}}/C_{\mathrm{migration}}. \tag{3.7}$$

The values of the reconstruction and identification efficiency, the migration correction and the combined correction factor are shown in Table 3.10 and displayed in Figure 3.23. The systematic uncertainty in each bin is estimated using the difference observed when using MC samples simulated with a 10% increase in the amount of material in the ID, with a further uncertainty on ϵ_{ID} coming from the T&P efficiency measurement described in the previous section.

For the material uncertainty, the efficiency difference between the MC samples is scaled by a factor of 0.65 (following [149]), as 5% is a more reasonable estimate for the increment of ID material than 10%, but no simulated sample with a smaller amount of extra material was available for analysis. From Table 3.10 it is evident that the extra material significantly affects the offline energy reconstruction, and has a somewhat smaller effect on the selection efficiency away from the p_{T} threshold at 7 GeV.

Overall, the absolute uncertainty on $\epsilon_{(\mathrm{reco+ID})_i}\ /C_{\mathrm{migration}_i}$ is found to be 7-10%, depending on the electron p_{T}.

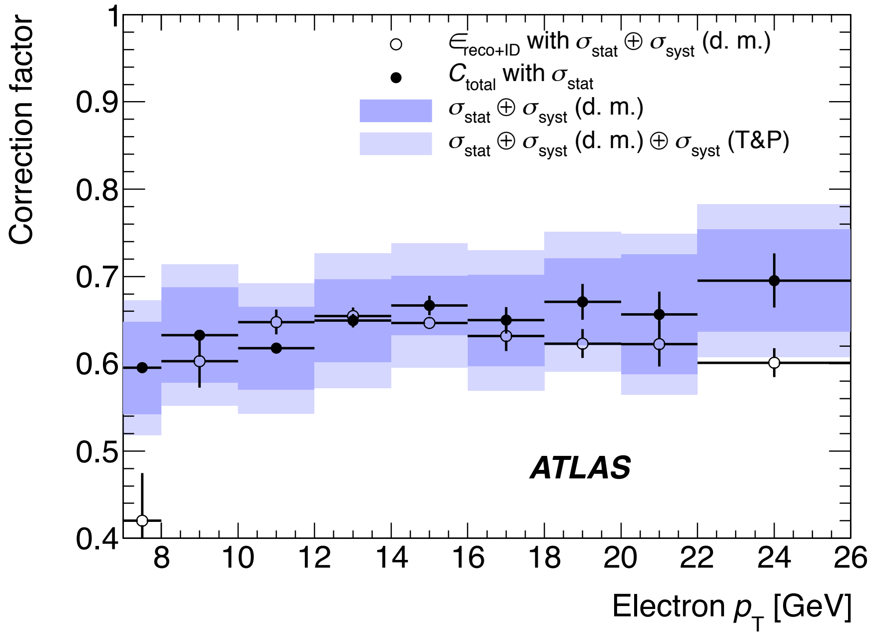

Figure 3.23: Reconstruction and identification efficiency from simulation before and after considering migration effects. The uncertainty shown in the dark shaded region is obtained using samples simulated with extra passive material (d.m.) in the ID and also include the MC statistical error. The light-blue shaded region incorporates as well the uncertainty from the T&P efficiency scale factor of Section 3.3.2.4.

p_{T} bin (GeV)	7-8	8-10	10-12	12-14	14-16	16-18	18-20	20-22	22-26
ϵ_{reco}	46.9	66.9	73.7	75.3	75.9	76.0	76.5	78.3	77.5
$\pm\sigma_{\mathrm{stat}}$	± 0.1	± 0.1	± 0.2	± 0.3	± 0.4	± 0.5	± 0.7	± 0.9	± 0.9
ϵ_{ID}	89.7	90.1	88.0	87.0	85.1	83.1	81.4	80.0	77.6
$\pm\sigma_{\mathrm{stat}}$	± 0.1	± 0.1	± 0.2	± 0.2	± 0.4	± 0.5	± 0.7	± 1.0	± 1.0
$\epsilon_{\mathrm{reco+ID}}$	42.0	60.3	64.8	65.5	64.7	63.2	62.3	62.3	60.1
$\pm\sigma_{\mathrm{stat}}$	±0.1	±0.1	±0.2	±0.3	±0.4	±0.6	±0.8	±1.0	±1.0
$\pm\sigma_{\mathrm{syst}}^{dm}$	±5.4	±3.0	±1.4	±0.9	±0.4	±1.6	±1.5	±2.4	±1.3
$C_{\mathrm{migration}}$	70.6	95.2	104.9	100.8	97.0	97.2	92.86	94.8	86.5
$\pm\sigma_{\mathrm{stat}}$	±0.4	±0.5	±0.8	±1.1	±1.5	±1.5	±2.6	±3.4	±3.6
$\pm\sigma_{\mathrm{syst}}^{dm}$	±3.3	±3.9	±6.5	±6.5	±4.5	±5.6	±4.5	±6.5	±9.0
C_{total}	59.5	63.3	61.8	64.9	66.7	65.0	67.1	65.7	69.5
$\pm\sigma_{\mathrm{stat}}$	±0.4	±0.3	±0.5	±0.8	±1.1	±1.5	±2.1	±2.6	±3.1
$\pm\sigma_{\mathrm{syst}}^{dm}$	±5.3	±5.4	±4.7	±4.7	±3.2	±5.0	±4.5	±6.4	±5.0
$\pm\sigma_{\mathrm{syst}}^{T\&P}$	±5.6	±6.0	±5.8	±6.1	±6.3	±6.1	±6.3	±6.2	±6.5
Total uncertainty	±7.7	±8.1	±7.5	±7.7	±7.1	±8.0	±8.0	±9.2	±8.8

Table 3.10: Summary of efficiencies and migration corrections (in percent) derived from MC, together with their statistical and systematic uncertainties, in bins of the true electron p_{T}. C_{total} is defined in Equation 3.7. Systematic uncertainties arising from the imperfect modeling of the material before the EM calorimeter are denoted $\sigma_{\mathrm{syst}}^{dm}$. The uncertainties from the T&P ($\sigma_{\mathrm{syst}}^{T\&P}$) efficiency scale factor measurement and the resulting total uncertainty on C_{total} are provided in the last two rows.

3.3.3 Unfolding to the True Electron $\mathbf{p_T}$

The measured electron spectrum in E_{T} is unfolded into to a spectrum as a function of true electron p_{T} with a bin-by-bin evaluation of Equation 3.4. The full bin-by-bin correction factor used for the unfolding is defined in Equation 3.7, where the efficiency and migration correction values are taken from the evaluation with `PYTHIA` MC summarised in Table 3.10.

3.3.3.1 Comparison of Unfolding Methods

The possible bias of the baseline bin-by-bin method was tested using independent MC samples as input to the unfolding procedure. Two other methods were also tested, Singular Value Decomposition (SVD) [150] and a Bayesian unfolding method [151].

A comparison of the different unfolding methods was performed using the RooUnfold package [152]. The SVD and Bayesian unfolding methods require square response matrices, with the same range and bins in true and measured p_{T}, so the data must be corrected for the migration from outside the measured range, especially from true $p_{\mathrm{T}} < 7$ GeV, before executing the unfolding procedure. This issue does not affect the bin-by-bin unfolding if the migration correction factor is suitably defined as

$$C^{i}_{\mathrm{migration}} = \frac{N_e\left(p_{\mathrm{T}_i}^{\mathrm{true}};\, E_{\mathrm{T}}^{\mathrm{reco}} > 7\ \mathrm{GeV}\right)}{N_e\left(E_{\mathrm{T}_i}^{\mathrm{reco}};\, \mathrm{any}\ p_{\mathrm{T}}^{\mathrm{true}}\right)}, \tag{3.8}$$

where the numerator corresponds to the number of heavy-flavour electrons in the simulation with true p_{T} in bin i and within the acceptance η region that are matched to a reconstructed electron in the acceptance region with $E_{\mathrm{T}} > 7$ GeV, and the denominator is the number of reconstructed electrons with measured cluster E_{T} in bin i and within the acceptance η region matched to any heavy-flavour true electron, without requirements in true p_{T}. In this case the migration from true $p_{\mathrm{T}} < 7$ GeV is correctly taken into account.

The extent of the migration is illustrated in Figure 3.24, where projections on the two axes of the correlation graphs of Figure 3.19 are shown for electrons from B and D hadrons separately and combined. In the first measured bin, with $7 < E_{\mathrm{T}} < 8$ GeV, a large fraction of electrons have a true $p_{\mathrm{T}} < 7$ GeV and there is a net influx to this bin, which corresponds to a $C_{\mathrm{migration}} < 1.0$, whereas, for example, in the measured bin with $10 < E_{\mathrm{T}} < 12$ GeV there are less reconstructed signal electrons than there are true electrons in this bin, and $C_{\mathrm{migration}} > 1.0$.

For the SVD and Bayesian unfolding methods, an MC based correction must be applied to the input data before unfolding to take into account electrons that migrate from low p_{T} into the measurement range. This correction factor is calculated as the fraction of electrons in each reconstructed E_{T} bin that is matched to a true electron with $p_{\mathrm{T}}^{\mathrm{true}} > 7$ GeV, i.e.

$$f_i = \frac{N_e\left(E_{\mathrm{T}_i}^{\mathrm{reco}};\, p_{\mathrm{T}}^{\mathrm{true}} > 7\ \mathrm{GeV}\right)}{N_e\left(E_{\mathrm{T}_i}^{\mathrm{reco}};\, \mathrm{any}\ p_{\mathrm{T}}^{\mathrm{true}}\right)}. \tag{3.9}$$

The corrected data distribution is then given as input to the unfolding code. The response matrix is built using the `PYTHIA` MC sample and considering only true electrons with $p_{\mathrm{T}} > 7$ GeV for the efficiency normalisation and in the true match for the denominator of $C^{i}_{\mathrm{migration}}$. With this modified definition of the migration correction factor, the MC corrected data distribution can be used as input also to the bin-by-bin method, obtaining the same result as with Equation 3.8. The results for the different unfolding methods are shown in Table 3.11. There is good agreement

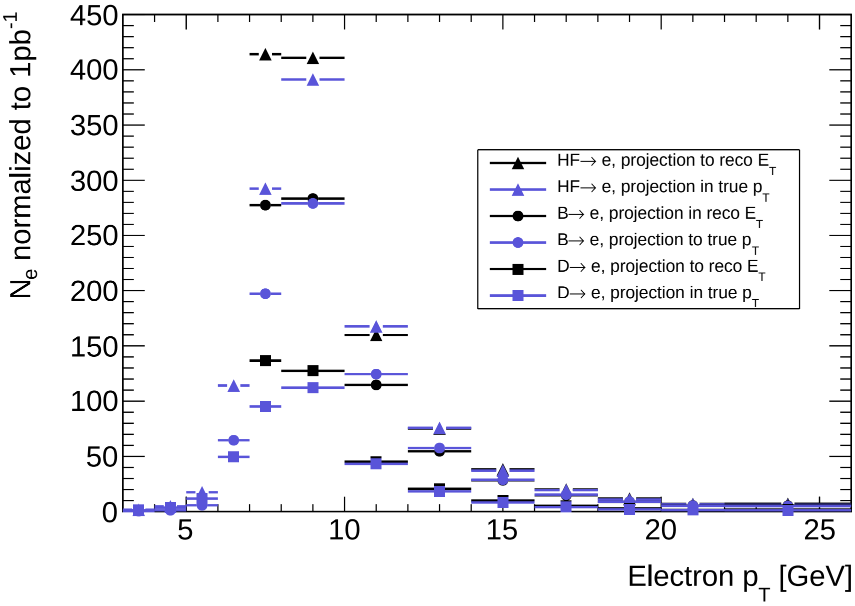

Figure 3.24: Cluster E_{T} (black) and true p_{T} (blue) distributions of identified electrons from `PYTHIA` MC from D and B hadron decays (squares and circles, respectively), and for the combined sample of heavy flavor decays (triangles). The histograms are rebinned projections of the 2-dimensional histograms of Figure 3.19. The blue symbols correspond approximately to the numerator in Equation 3.8 and the black symbols to the denominator.

between the various methods, with the results varying within 2% for the first bin of extracted ATLAS data, for example. Nevertheless, when comparing the outcome using MC simulated input E_{T} distributions to the true MC p_{T} distribution – i.e. the top three blocks of Table 3.11 – both the bin-by-bin method and the SVD method with regularization parameter $k = 2$ perform the best. Based on these studies, and because of the simplicity of its implementation, a bin-by-bin unfolding has been chosen to calculate the inclusive electron cross-section.

Unfolding method	E_{T} bin (GeV)								
	7-8	8-10	10-12	12-14	14-16	16-18	18-20	20-22	22-26
	Input: `PYTHIA`								
Truth	695.7±1.8	649.1±1.7	258.9±1.1	115.9±0.7	57.4±0.5	30.7±0.4	17.6±0.3	10.6±0.2	10.1±0.2
Bin-by-bin	695.7±6.1	649.1±5.1	258.9±3.2	115.9±2.1	57.4±1.4	30.7±1.1	17.6±0.8	10.6±0.6	10.1±0.6
w. toy MC	695.7±4.3	649.1±3.7	258.9±1.9	115.9±1.5	57.4±1.1	30.7±0.8	17.6±0.6	10.6±0.5	10.1±0.4
Bayesian (n=4)	711.5±5.3	650.8±4.3	239.0±2.6	113.8±1.9	59.5±1.3	31.6±1.0	18.5±0.6	11.0±0.5	14.7±0.6
Bayesian (n=1)	704.1±3.1	648.4±2.1	248.9±1.2	113.7±1.0	58.2±0.8	31.7±0.5	18.7±0.4	11.7±0.3	13.1±0.4
SVD (k=4)	714.4±3.6	642.9±3.1	247.3±1.5	112.3±0.9	57.7±0.6	32.3±0.4	19.4±0.3	12.2±0.2	12.1±0.3
SVD (k=2)	695.7±3.2	648.4±2.7	258.5±1.2	115.9±0.6	57.5±0.4	30.9±0.2	17.7±0.2	10.7±0.1	10.3±0.1
	Input: `POWHEG+PYTHIA`								
Truth	309.3±1.4	296.8±1.4	121.2±0.9	57.4±0.6	28.1±0.4	16.3±0.3	9.0±0.2	6.0±0.2	6.0±0.2
Bin-by-bin	307.1±3.1	294.7±2.7	123.3±1.8	57.2±1.2	28.6±0.8	16.9±0.7	8.9±0.5	5.9±0.4	5.6±0.4
w. toy MC	307.1±2.4	294.7±2.1	123.3±1.1	57.2±1.0	28.6±0.7	16.9±0.6	8.9±0.4	5.9±0.3	5.6±0.3
Bayesian (n=4)	311.6±3.0	295.5±2.5	115.0±1.6	56.4±1.2	29.7±0.8	17.5±0.7	9.5±0.4	6.0±0.3	8.1±0.4
Bayesian (n=1)	313.3±1.7	294.5±1.3	117.7±0.7	55.6±0.6	29.2±0.5	16.7±0.3	9.7±0.2	6.3±0.2	7.2±0.3
SVD (k=4)	312.0±2.0	293.2±1.9	118.1±0.9	55.7±0.6	29.5±0.4	17.0±0.2	10.4±0.2	6.6±0.2	6.6±0.2
SVD (k=2)	312.2±1.9	296.6±1.6	120.8±0.7	55.3±0.4	27.9±0.2	15.3±0.2	8.9±0.1	5.4±0.1	5.2±0.1
	Input: `POWHEG+HERWIG`								
Truth	186.3±0.9	173.3±0.9	70.7±0.6	32.3±0.4	16.7±0.3	9.1±0.2	5.1±0.2	3.0±0.1	3.2±0.1
Bin-by-bin	181.8±1.9	172.9±1.6	71.2±1.1	32.8±0.7	16.7±0.5	9.3±0.4	5.2±0.3	3.2±0.2	3.2±0.2
w. toy MC	181.8±1.5	172.9±1.3	71.2±0.7	32.8±0.6	16.7±0.4	9.3±0.3	5.2±0.2	3.2±0.2	3.2±0.2
Bayesian (n=4)	184.9±1.9	173.4±1.6	66.1±1.0	32.4±0.7	17.3±0.5	9.6±0.4	5.5±0.2	3.3±0.2	4.6±0.2
Bayesian (n=1)	185.0±1.1	172.7±0.8	68.1±0.4	32.0±0.4	16.8±0.3	9.4±0.2	5.5±0.1	3.5±0.1	4.1±0.2
SVD (k=4)	185.3±1.3	171.7±1.2	68.2±0.5	32.0±0.4	16.9±0.2	9.7±0.1	5.9±0.1	3.7±0.1	3.7±0.1
SVD (k=2)	183.9±1.2	173.8±1.0	70.4±0.4	32.0±0.2	16.1±0.2	8.8±0.1	5.1±0.1	3.1±0.0	3.0±0.0
	Input: `PYTHIA` distorted material								
Truth	693.2±3.5	655.7±3.4	259.3±2.2	115.9±1.4	58.8±1.0	30.3±0.7	17.7±0.6	11.1±0.4	10.5±0.4
Bin-by-bin	598.6±6.4	569.0±5.7	229.0±3.6	103.1±2.4	54.4±1.7	26.7±1.2	15.8±0.9	9.5±0.7	9.3±0.7
w. toy MC	598.6±5.3	569.0±4.7	229.0±2.4	103.1±2.0	54.4±1.5	26.7±1.1	15.8±0.8	9.5±0.6	9.3±0.5
Bayesian (n=4)	609.7±6.6	571.4±5.6	211.8±3.4	101.1±2.5	57.1±1.8	27.6±1.3	16.4±0.8	9.9±0.7	13.5±0.8
Bayesian (n=1)	608.8±3.8	567.0±2.8	219.9±1.5	101.6±1.3	53.7±1.0	28.4±0.6	16.7±0.5	10.5±0.4	12.0±0.5
SVD (k=4)	612.6±4.5	563.3±4.0	219.8±1.9	101.2±1.2	52.5±0.8	29.3±0.5	17.5±0.4	11.0±0.3	10.9±0.3
SVD (k=2)	604.9±4.0	567.2±3.5	227.6±1.5	102.7±0.8	51.3±0.5	27.7±0.3	15.9±0.2	9.6±0.1	9.3±0.1
	Input: Extracted electron data								
Bin-by-bin	351.2± 15.5	334.3± 12.3	134.0±4.5	60.5±2.6	30.6±1.2	16.1±0.8	9.2±0.5	5.5±0.4	5.2±0.4
w. toy MC	351.2± 15.5	334.3± 11.9	134.0±3.5	60.5±2.5	30.6±1.1	16.1±0.8	9.2±0.4	5.5±0.3	5.2±0.3
Bayesian (n=4)	357.7± 19.1	335.9± 14.0	124.0±4.9	59.4±3.2	31.9±1.3	16.6±1.0	9.6±0.4	5.7±0.3	7.5±0.4
Bayesian (n=1)	357.3± 11.2	332.9±7.0	128.8±2.3	59.3±1.6	30.8±0.8	16.7±0.5	9.7±0.3	6.1±0.2	6.8±0.2
SVD (k=4)	357.2± 11.1	327.3±6.7	129.3±2.5	59.4±1.4	30.5±0.7	16.8±0.4	10.0±0.2	6.4±0.2	6.5±0.2
SVD (k=2)	354.0± 7.3	334.1±6.3	135.0±2.4	61.4±1.1	30.9±0.5	16.8±0.3	9.7±0.2	5.9±0.1	5.7±0.1

Table 3.11: Test of different unfolding methods in bins of electron E_{T} applying correction for migration from true $E_{\mathrm{T}} < 7$ GeV region.

The effect of extra material has already been considered as a systematic error on the efficiency and the bin migration correction evaluation. To account for possible biases due to the signal shape, the predictions of different MC generators for $\epsilon_{\mathrm{reco+ID}}/C_{\mathrm{migration}}$ were compared and discussed in Section 3.3.2.1, and found to agree within statistical errors. Therefore, no additional systematic error is considered in the unfolding.

3.3.4 Fiducial Electron Cross-Section

The results with statistical and systematic uncertainties are shown in Figure 3.25 and compared to the theoretical predictions discussed in Section 2.3.2.3. The systematic uncertainties are summarised in Table 3.12. The total uncertainty on the cross-section measurement is 15−18%. The measured cross-section is in good agreement with both the FONLL and the POWHEG+PYTHIA predictions though the ATLAS data has a slightly more steeply falling spectrum. At this energy range the difference between FONLL and NLO predictions are small as the NLO prediction was calculated using the same non-perturbative fragmentation function parameters as FONLL. PYTHIA describes very well the shape but fails to reproduce the total cross-section predicting about a factor two higher cross-section. It is interesting to note the large difference between the POWHEG predictions with two different parton shower MCs: the POWHEG+HERWIG prediction deviates from the data by a factor of ~ 0.5, while POWHEG+PYTHIA agrees well with the measurement in shape and overall normalisation. In Figure 3.26, the ratio of the theoretical predictions to the measured cross-section are shown. The values of the ratio of the total predicted cross-section to the observed cross-section in the $7 < p_{\mathrm{T}} < 26$ GeV range are 0.95 ± 0.5 for FONLL, 1.00 ± 0.06 for the fixed-order NLO, 1.93 ± 0.11 for PYTHIA, 0.96 ± 0.05 for POWHEG+PYTHIA and 0.55 ± 0.03 for POWHEG+HERWIG, and are shown in the legend.

3.3.4.1 Systematic Uncertainties

All the statistical and systematic uncertainties on $N^{\mathrm{Q}\to\mathrm{e}}$, $\epsilon_{\mathrm{trigger}}$, $C_{\mathrm{migration}}$ and $\epsilon_{\mathrm{reco+ID}}$ discussed in the previous sections are propagated to the inclusive electron cross-section. The uncertainty on the integrated luminosity $\int \mathcal{L}\mathrm{d}t$ is 3.4%.

Two additional sources of systematic uncertainty on $\sigma^{\mathrm{W/Z/}\gamma^*}_{\mathrm{accepted}_i}$ (see Equation 3.4) are considered. The NNLO W and Z production cross-section uncertainty of 5% is taken [149] , although for the low-mass Drell-Yan component the PYTHIA cross-section is used. This approximation has no significant effect on the precision of the final result as the low-mass Drell-Yan correction is always at the sub-percent level. In addition, an experimental systematic uncertainty of 5% is assigned to account for differences of the electron reconstruction and identification efficiencies for isolated electrons between data and MC simulation based on the in-situ efficiency measurements using $W^{\pm}$ and Z events in the 2010 data [34].

Certain sources of systematic uncertainties can be correlated between the extraction of the electron signal and the in-situ efficiency measurement, such as the mismodelling of the discriminating variables f_{TR} and n_{BL} and the energy scale uncertainty. These uncertainties were propagated to the cross-section taking into account possible correlations. The resulting overall uncertainty turned out to be almost identical to the case when all the errors are treated as uncorrelated. A summary of all sources of uncertainties is given in Table 3.12. The relative cross-section uncertainties were averaged over E_{T} using the statistical error on the signal extraction as weight.

Source of uncertainty	Uncertainty value (%)
Statistical error on extracted signal	2.7−4.3
Possible bias of the method	
Electron signal extraction	7.3
Efficiency measurement	3.8
Mismodelling of discriminating variables	
f_{TR} (*)	4.5
n_{BL} (*)	5.6
E/p (electron signal extraction)	3.2
f_1 (efficiency measurement)	2.8
Energy scale (*)	1.5
Efficiency dependence on p_{T} from T&P	5.5
Material uncertainty on $\epsilon_{\mathrm{reco+ID}}/C_{\mathrm{migration}}$	4.8−9.7
MC statistical error on $\epsilon_{\mathrm{reco+ID}}/C_{\mathrm{migration}}$	0.4−3.5
MC statistical error on templates for signal extraction	0.8−2.5
Luminosity	3.4
Trigger efficiency (stat+syst)	< 2
Accepted Drell-Yan cross-section (MC stat+syst)	< 1
Total	15−18

Table 3.12: Summary of systematic errors affecting the inclusive electron cross-section measurement. Sources that are correlated between the signal extraction and the efficiency measurement are marked by (*).

3.3.4.2 Final Result

A fiducial heavy-flavour electron cross-section is obtained by integrating over the p_{T} range of the differential measurement, for electrons of $7 < p_{\mathrm{T}} < 26$ GeV and within $|\eta| < 2.0$, excluding $1.37 < |\eta| < 1.52$, of

$$\sigma^{e}_{\mathrm{HF}} = 0.946 \pm 0.020_{(\mathrm{stat.})} \pm 0.146_{(\mathrm{syst.})} \pm 0.032_{(\mathrm{lumi.})}\ \mu\mathrm{b}. \tag{3.10}$$

To calculate the systematic uncertainty on this fiducial cross-section, contributions from sources uncorrelated among E_{T}-bins (i.e. from sources related to the limited amount of data or MC statistics) were summed in quadrature. The rest of the systematic uncertainties were assumed to be fully correlated and added linearly.

3.3.5 Comparison of inclusive electron and muon cross-section

The inclusive electron and muon cross-sections [12] with their full statistical and systematic uncertainties are compared in Figure 3.27. Except the small 3.4% luminosity uncertainty, all other sources of error are uncorrelated. The systematic errors in the muon measurement are smaller than those for the electrons, since the muon measurement has smaller background components, which results in less uncertainty in the signal extraction, and the systematics of the muon identification efficiency are also reduced.

The two measurements agree within the uncertainties with each other and with the state-of-the art theoretical calculation of `FONLL` and the prediction of `POWHEG+PYTHIA` MC generator. The total integrated cross-section for heavy-flavour muons in the kinematic region shared with the electrons ($|\eta^{\mu}| < 2.0$, excluding $1.37 < |\eta^{\mu}| < 1.52$, and $7 < p^{\mu}_{\mathrm{T}} < 26$ GeV) is

$$\sigma^{\mu}_{\mathrm{HF}} = 0.818 \pm 0.003_{(\mathrm{stat.})} \pm 0.036_{(\mathrm{syst.})} \pm 0.028_{(\mathrm{lumi.})}\ \mu\mathrm{b}, \tag{3.11}$$

which is compatible with the result for electrons from heavy-flavour given in Equation 3.10. The full muon measurement, with $|\eta^{\mu}| < 2.5$ and in the range $4 < p^{\mu}_{\mathrm{T}} < 100$ GeV, is shown in Figure 2.13, in Chapter 2.

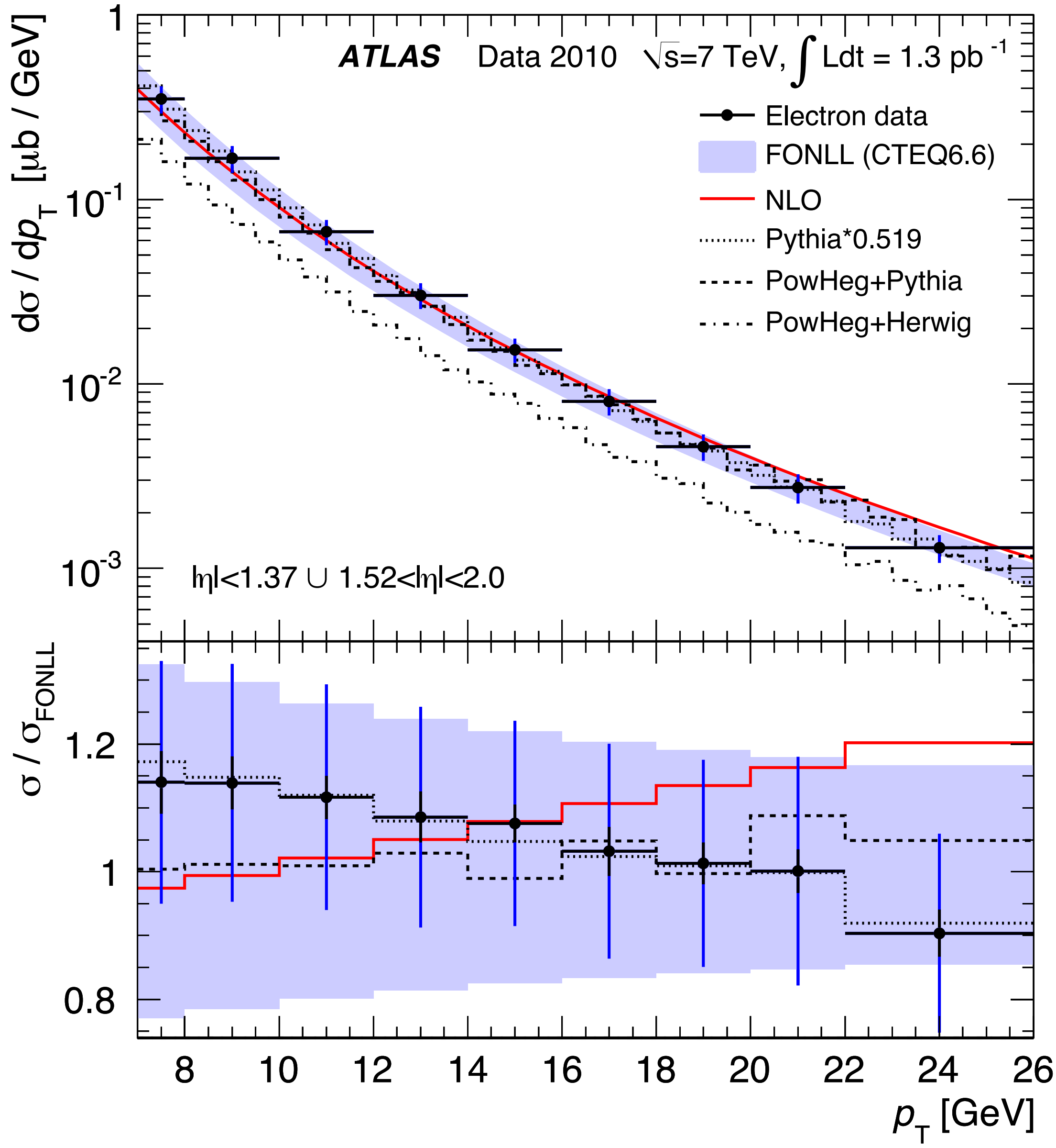

Figure 3.25: Fiducial differential cross-section as a function of the electron p_{T}. The ATLAS measurement with statistical only (black error bars) and statistical plus systematic errors (blue error bars) is compared to the prediction of the FONLL and NLO calculations and of different MC generators: PYTHIA, POWHEG+PYTHIA and POWHEG+HERWIG. The ratios of the measured cross-sections to the FONLL central values are given in the bottom, together with the ratios of the other theoretical predictions to FONLL.

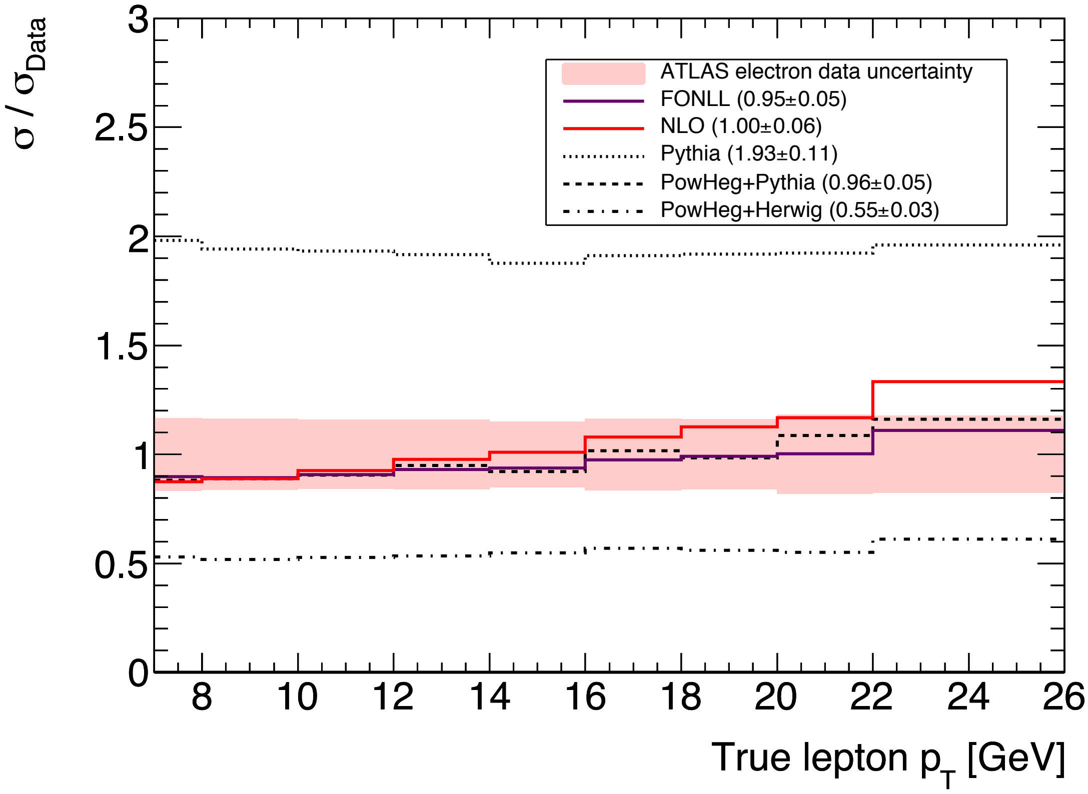

Figure 3.26: The ratio of the different theoretical predictions to the measured electron fiducial differential cross-section as a function of the electron p_{T}. The experimental uncertainty is indicated by the light red band. The normalisation factors from a fit to the cross-section ratios are given in the legend.

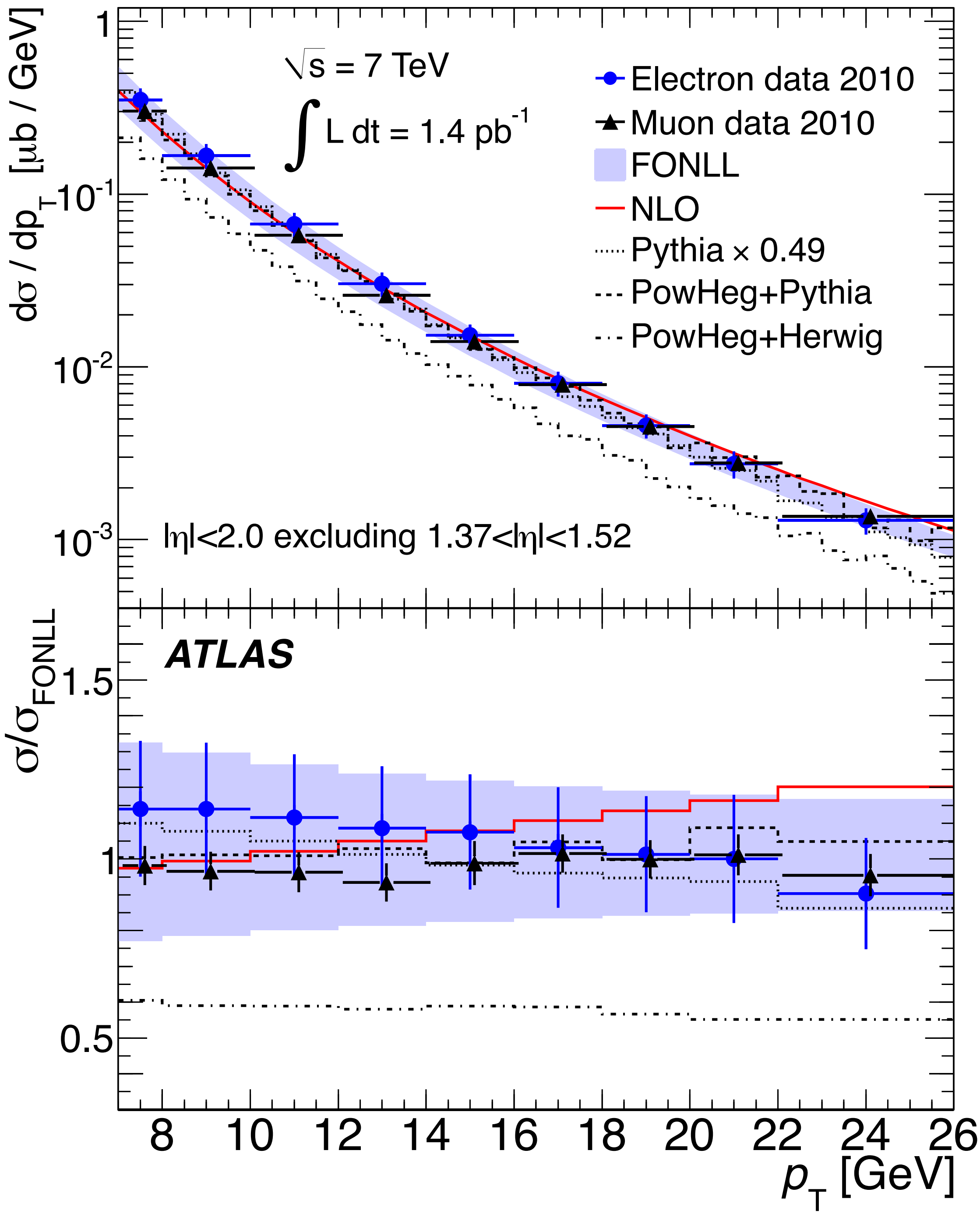

Figure 3.27: Fiducial differential cross-section as a function of the lepton p_{T}. The electron (blue dots) and muon (black triangles) measurements with statistical plus systematic errors are compared to the the `FONLL` (light blue band indicating the theoretical uncertainty) and NLO (red line) predictions and those of different MC generators: `PYTHIA`, `POWHEG+PYTHIA` and `POWHEG+HERWIG`. The ratios of the measured cross-sections to the `FONLL` central values are given in the bottom, together with the ratios of the other theoretical predictions to `FONLL`.

3.4 Conclusions

From 1.28 ± 0.04 pb^{-1} of data collected by ATLAS at $\sqrt{s} = 7$ TeV, a sample of electrons has been selected with custom identification cuts and low threshold trigger requirements in cluster E_{T} range 7-26 GeV and within $|\eta| < 2.0$ (excluding transition regions between the barrel and end-cap EM calorimeters). A maximum likelihood method, the Tiles Method, has been applied to extract the heavy-flavour signal component from the dominant background contributions arising from hadron fakes and electrons from photon conversions, using Transition Radiation particle identification, the presence or not of a hit on the track in the pixel B-layer and the ratio of the measured energy of the EM cluster to the track momentum. The efficiency of the trigger, reconstruction and identification have been measured with the minimal reliance on the MC, to allow a differential cross-section measurement to be obtained from the extracted signal E_{T} distribution.

The measured differential cross-section of electrons arising from heavy-flavour production is found to be in good agreement with the muon measurement in the transverse momentum range $7 < p_{\mathrm{T}} < 26$ GeV and pseudorapidity region $|\eta| < 2.0$ (excluding $1.37 < |\eta| < 1.52$). Integrating over the p_{T} range considered, the total heavy-flavour electron cross-section is found to be

$$\sigma^{e}_{\mathrm{HF}} = 0.946 \pm 0.020_{(\mathrm{stat.})} \pm 0.146_{(\mathrm{syst.})} \pm 0.032_{(\mathrm{lumi.})}\ \mu\mathrm{b}.$$

The theoretical predictions for heavy-flavour production from the `FONLL` computation are in good agreement with the electron and muon measurements. Good agreement is also seen with the predictions of `POWHEG+PYTHIA`, although `POWHEG+HERWIG` predicts a significantly lower cross-section. `PYTHIA` describes the p_{T}-dependence well, but predicts approximately a factor two higher total cross-section.

Chapter 4

Measurement of the Production Rate of Electrons from Bottom Decays

A measurement of the production of B-hadrons at the LHC can provide a test of Quantum Chromodynamics (QCD) in the energy regime of the LHC. This chapter describes a first step towards a B-hadron production measurement using electron final states. The measurement uses $p_{\mathrm{T}}^{\mathrm{rel}}$, the transverse momentum of the electron with respect to a nearby jet, to identify the $B \to e$ signal from the background. Using reconstruction and identification cuts tighter than those used in the previous chapter and a set of MC derived templates for the $p_{\mathrm{T}}^{\mathrm{rel}}$ shapes of the signal and background components, the amount of electrons from B-hadron decays is extracted by means of an extended maximum likelihood fit, performed in bins of the electron cluster E_{T}. The systematic uncertainties are evaluated and the final result is compared with the expected signal from `POWHEG` (NLO) and `PYTHIA` (LO) MC event generators.

This chapter is organised in the following way: the data sample selection is described in Section 4.1, Section 4.2 details the electron candidate selection, and the computation of $p_{\mathrm{T}}^{\mathrm{rel}}$ is delineated in Section 4.3. A detailed characterisation of the extraction and the evaluation of systematic uncertainties are given in Section 4.4, and finally the result is compared with MC predictions in Section 4.5.

4.1 Sample selection

The analysis is performed over the same run and trigger selection of 2010 LHC collisions as for the inclusive electron cross-section measurement described in Chapter 3. In order to carry out the $p_{\mathrm{T}}^{\mathrm{rel}}$ analysis, reconstructed track-jets are required and thus the reconstruction of the data samples differs slightly from the inclusive electron measurement [1]. Aside from the inclusion of track-jets, some data-quality logic changed between the two reconstruction versions. As a result, the luminosity taken in each period has been recalculated and is shown in Table 4.1. The final total integrated luminosity remains very close to the original value of Table 3.1.

L1 Threshold (GeV)	Period	Minimum E_{T} (GeV)	Integrated Luminosity (nb^{-1})
3	ABC	7	12.8 $\pm$ 0.4
6	D	10	102.6 $\pm$ 3.5
11	D	14	176.2 $\pm$ 6.0
15	E	18	984.7 $\pm$ 33.5
Total Integrated Luminosity (nb^{-1})			1276 $\pm$ 43

Table 4.1: Trigger requirement, minimum electron cluster E_{T} and integrated luminosity for the different 2010 ATLAS data-taking periods considered in the B-hadron extraction analysis.

4.2 Electron candidate selection

The candidate selection used as the foundation for the separation of the B-hadron component is modified from that applied in the inclusive electron measurement; using a tighter electron selection, as shown in Table 4.2, in order to increase the signal purity before extraction. The variables that were previously used for the signal and background separation – the number of hits in the B-layer, n_{BL}; the fraction of high-threshold hits in the TRT, f_{TR}; and the ratio of the electron cluster energy to the track momentum, E/p – are now used directly, cutting on these to select the signal. Because of the improved alignment between the calorimeter and the inner detector (ID) in the later version of the reconstruction software, a set of tighter cluster-track matching

[1] The reconstruction software used is a more recent version, so-called *Autumn Reprocessing*, which corresponds to ATHENA version 16.0.2.3+, while the inclusive electrons cross-section measurement used version 15.6.9.8+

cuts can be used. Shower shape and hadronic leakage identification cuts are also applied, which reduces the light hadron background, and a veto on electrons whose track matches a photon conversion vertex suppresses the contribution of these. This selection corresponds to the standard tight electron selection described in Section 1.4. With this tighter selection the signal, defined this time as electrons from B-hadron decays, is the dominant component for E_{T} up to ~ 30 GeV, and the sample purity in this range is estimated from MC to be 40–76%, as shown in Figure 4.1(b).

The expected composition of the electron sample with the selection detailed in Table 4.2 is shown in Figure 4.1(a) for the electrons in the range $7 < E_{\mathrm{T}} < 50$ GeV, where the W/Z component is normalised with the NNLO cross-section [153], the low-mass Drell-Yan component is normalised with the LO cross-section given by the `PYTHIA` generator, and the rest of the contributions – the light hadron, photon conversions, and electron from B and D-hadron decays – are normalised to the data after the subtraction of the $W/Z/\gamma^*$ part. Figure 4.1(b) shows the corresponding fraction of each component for a given cluster E_{T} bin.

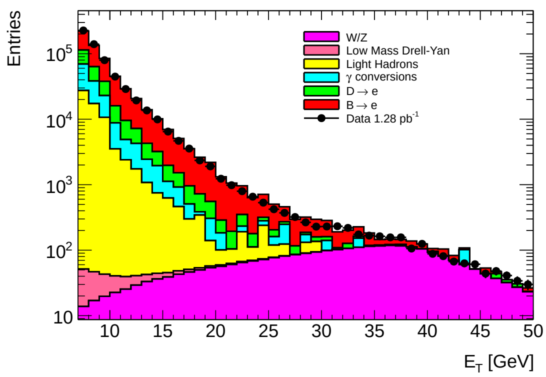

(a)

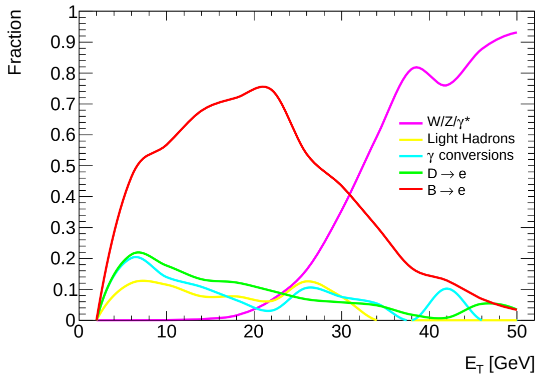

(b)

Figure 4.1: (a) Distribution of cluster E_{T} for the electron candidates passing the tight selection cuts normalised to $\int \mathcal{L}\,\mathrm{dt} = 1.28\mathrm{pb}^{-1}$. (b) The fraction of electron candidates from each source in a given E_{T} bin.

4.3 Computation of $\mathrm{p}_{\mathrm{T}}^{\mathrm{rel}}$

The calculation of the discriminating variable – the transverse momentum of the electron with respect to the axis of a nearby jet, $p_{\mathrm{T}}^{\mathrm{rel}}$ – requires the reconstruction of track-jets. A special tool from the ATLAS B-tagging group [154] is employed to identify the track-jets – collimated bunches of hadrons characterised through the

Type	Description	Name
Acceptance		
Fiducial cuts	$\lvert\eta\rvert < 2.0$ ($1.37 < \lvert\eta\rvert < 1.52$ excluded) $E_{\mathrm{T}} > 7$, 10, 14 or 18 GeV depending on period	- -
Preselection		
Fiducial cuts	Remove candidates with clusters near problematic regions in EM calorimeter Remove candidates with tracks passing through dead B-layer modules	- -
Tracking cuts	At least 10 TRT and 4 silicon hits	-
Strip layer of the EM calorimeter	Fraction of the raw energy deposited in the strip layer (> 0.1)	f_1
Identification (in addition to preselection)		
Hadronic leakage	*Ratio of E_T in the first layer of the hadronic calorimeter to E_T of the EM cluster (used over the range $\lvert\eta\rvert < 0.8$ and $\lvert\eta\rvert > 1.37$)*	R_{had1}
	Ratio of E_T in the hadronic calorimeter to E_T of the EM cluster (used over the range $\lvert\eta\rvert > 0.8$ and $\lvert\eta\rvert < 1.37$)	R_{had}
Middle layer of the EM calorimeter	*Ratio of the energy in 3×7 cells over the energy in 7×7 cells centred at the electron cluster position*	R_η
	Lateral width of the shower	w_2
Strip layer of the EM calorimeter	Total shower width	w_{stot}
	Ratio of the energy difference between the largest and second largest energy deposits in the cluster over the sum of these energies	E_{ratio}
Track quality	*Number of hits in the pixel detector (≥ 1)*	n_{pixel}
	Number of total hits in the pixel and SCT detectors (≥ 7)	n_{Si}
	Transverse impact parameter ($\lvert d_0\rvert$ <1 mm)	d_0
Track–cluster matching	*$\Delta\eta$ between the cluster position in the strip layer and the extrapolated track ($\lvert\Delta\eta\rvert < 0.005$)*	$\Delta\eta_1$
	$\Delta\phi$ between the cluster position in the middle layer and the extrapolated track ($\lvert\Delta\phi\rvert < 0.02$)	$\Delta\phi$
	Ratio of the cluster energy to the track momentum	E/p
TRT	*Ratio of the number of high-threshold hits to the total number of hits in the TRT*	f_{TR}
Conversions	*Number of hits in the b-layer (≥ 1)*	n_{BL}
	Veto electron candidates matched to reconstructed photon conversions	-

Table 4.2: Detail of the acceptance, preselection and *tight* identification cuts used for the basis of the extraction of the B-hadron component of low energy electrons. The variables with descriptions in italics are those for which the cuts where introduced or made tighter with respect to the inclusive electrons identification selection of Table 3.2. The cut values are not explicitly shown in the variable description when these values depend on the E_{T} and η of the electron candidate.

tracks left by charged particles in the ID – with the Anti-k_t algorithm [155] and a ΔR radius of 0.5, for tracks attached to each primary vertex. The procedure is completely independent of calorimeter jets reconstruction.

Additional requirements are imposed on the reconstructed track-jets: a minimum p_{T} of 300 MeV for tracks, at least two tracks to form a track-jet with at least 5 silicon hits; a transverse impact parameter $d_0 < 10$ cm and longitudinal impact parameter $z_0 < 100$ cm with $z_0 \times \sin\theta < 10$ cm; the track-jet $p_{\mathrm{T}} > 2$ GeV, and the reduced track-jet $p_{\mathrm{T}} > 1$ GeV. The reduced track-jet p_{T} is computed only for those track-jets that are matched to an electron candidate that, in turn, passes the cuts of Table 4.2 within $\Delta R \leq 0.5$, by subtracting the electron track p_e^α from the original track-jet (p_{j0}^α), at the 4-momentum level, i.e.

$$p_j^\alpha = p_{j0}^\alpha - p_e^\alpha, \tag{4.1}$$

and then taking the transverse component with respect to the beam axis. The last row in Table 4.3 means that an electron–track-jet pair is kept if the resulting $p_{j\mathrm{T}} > 1$ GeV.

Requirement	Value
Track p_{T}	> 300 MeV
Number of tracks to form a track-jet	≥ 2
n_{Si}	≥ 5
d_0	< 10 cm
z_0	< 100 cm
$z_0 \times \sin\theta$	< 10 cm
Track-jet p_{T}	> 2 GeV
Reduced track-jet p_{T}	> 1 GeV

Table 4.3: Conditions for the construction of a track-jet and further requirements on the track-jet to be considered for the analysis.

Finally, the discriminating variable for this extraction – $p_{\mathrm{T}}^{\mathrm{rel}}$– can be evaluated for a given electron–track-jet combination as

$$p_{\mathrm{T}}^{\mathrm{rel}} = \frac{|\vec{p}_e \times \vec{p}_j|}{|\vec{p}_j|}. \tag{4.2}$$

If an electron is found to be associated with more than one qualifying track-jet passing the requirements of Table 4.3, only the closest match is kept. The comparison of the $p_{\mathrm{T}}^{\mathrm{rel}}$ distributions for all expected components as predicted by MC simulation is shown in Figure 4.2.

In conclusion, the range of study is chosen to be $7 < E_{\mathrm{T}} < 26$ GeV in order to have the minimum contamination from electrons arising from vector bosons, shown in Figure 4.1(b) to be below 20% in this range. In addition, the expected contribution to the observed $p_{\mathrm{T}}^{\mathrm{rel}}$ distribution from electrons coming from Drell-Yan, W and Z bosons is subtracted based on MC simulations before the $B \to e$ signal extraction is performed.

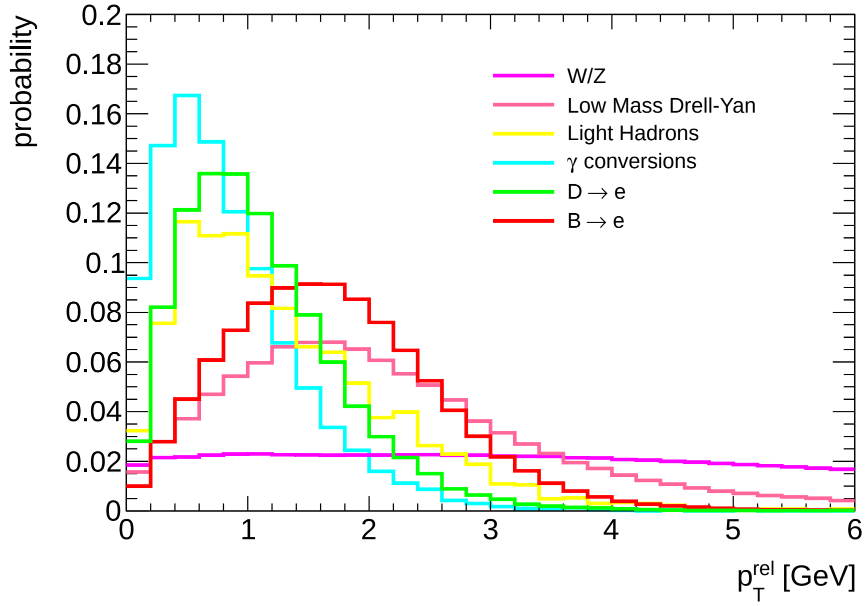

Figure 4.2: Distribution of $p_{\mathrm{T}}^{\mathrm{rel}}$ for electrons from electron conversions, light hadron decays, charm hadron decays, bottom hadron decays and $W/Z/\gamma^{*}$ decays with $E_{\mathrm{T}} >$ 7 GeV, normalised to unit area.

4.4 Extraction

The electron candidates passing the requirements listed in Table 4.2 and matched to a track-jet satisfying the conditions of Table 4.3 are separated in five E_{T} bins and the extraction is performed separately for each bin. The number of selected candidates per E_{T} bin is listed in Table 4.4. A finer binning in E_{T} in line with the inclusive electron cross-section measurement and some binning in η, at least for barrel and end-cap, has been attempted but failed, as the fits did not converge due to lack of statistics.

	E_{T} bin (GeV)				
	7-10	10-14	14-18	18-22	22-26
N_{obs}	4478	9643	5632	6472	2406
$N_{obs} - N_{W/Z/\gamma *}$	4476	9625	5585	6232	2113

Table 4.4: Number of observed electron candidates passing the cuts of Table 4.2, before and after subtracting the expected $W/Z/\gamma *$ contribution.

The subtraction of the expected $W/Z/\gamma^*$ contribution is performed based on MC events simulated with the `PYTHIA` event generator and passed through a detailed detector response simulation using `GEANT4` [81]. The W/Z component is normalised to the NNLO production cross-section [153, 156] and the low-mass Drell-Yann is normalised to the cross-section value predicted by `PYTHIA`. Table 4.4 shows the number of selected electron candidates passing the cuts of Table 4.2 before and after subtraction of the $W/Z/\gamma^*$ contribution.

4.4.1 The maximum likelihood fit

The extraction of the number of electrons from bottom decays is made with a binned extended maximum likelihood fit of three components: the signal and a composite background of conversions and light hadrons including charmed hadrons; on the $p_{\mathrm{T}}^{\mathrm{rel}}$ measurement over four bins: $0 \leq p_{\mathrm{T}}^{\mathrm{rel}} < 1$ GeV, 1 GeV $\leq p_{\mathrm{T}}^{\mathrm{rel}} < 2$ GeV, 2 GeV $\leq p_{\mathrm{T}}^{\mathrm{rel}} < 3$ GeV and $p_{\mathrm{T}}^{\mathrm{rel}} \geq 3$ GeV. This implies that the last $p_{\mathrm{T}}^{\mathrm{rel}}$ bin considered does not stop at 4 GeV, it is in fact an "overflow" bin. The likelihood function to minimise is

$$\begin{aligned} -\ln \mathcal{L}(N_B, N_{BKG}, f_\gamma) = \sum_{i\,(\text{bins})} \Big[& N_{BKG} \cdot \left[p_i^{C+Had}(1-f_\gamma) + p_i^\gamma f_\gamma\right] + N_B\, p_i^B \\ & - n_i^{\text{obs}} \cdot \ln\left(N_{BKG} \cdot \left[p_i^{C+Had}(1-f_\gamma) + p_i^\gamma f_\gamma\right] + N_B\, p_i^B\right)\Big], \end{aligned} \tag{4.3}$$

where N_B is the number of signal electrons from the B-hadron decays, N_{BKG} is the remaining total number of background electrons from charm and light hadrons plus photon conversions, and f_γ is the fraction of the background candidates that corresponds to photon conversions. The first two parameters are completely free-floating in the fit, the last one is constrained with a gaussian function with mean and sigma equal to the value of the fraction of photon conversions in the background in the MC simulations. The p_i^B, p_i^γ and p_i^{C+Had} factors are the probability density functions (pdfs or templates) of the signal, photon conversions and charm plus light hadron decays. These pdfs are obtained from the $p_{\mathrm{T}}^{\mathrm{rel}}$ distribution for each component in the PYTHIA MC simulation.

The number of observed candidates n_i^{obs} in equation 4.3 takes into account the subtraction of the $W/Z/\gamma^*$ contributions mentioned previously. The relative amount of charmed hadrons is fixed with respect to the light hadron rate with the value from PYTHIA MC simulations. The two components are combined into a single component labelled *C+Had* in equation 4.3 since the pdfs are somewhat similar, as can be seen in Figure 4.3(a) for $10 < E_{\mathrm{T}} < 14$ GeV and Figure 4.3(c) for $22 < E_{\mathrm{T}} < 26$ GeV.

In Figures 4.3(b) and 4.3(d) the measured data points – after subtraction of the vector boson expectation – are superimposed with the result of the minimisation, with the total fitted distribution in the yellow line, the signal component in red and the total background in blue. The constituents of the background are also shown as the cyan line for photon conversions and the green line for *C+Had*.

The implementation of the likelihood function made use of the RooFit toolkit [157]. The summary of the results for the whole E_{T} range chosen, with statistical uncertainties returned by MINOS in the minimisation procedure [138], is presented on Table 4.5. In this table, N_B is the fitted number of signal electrons from B decays, N_{BKG} corresponds to the fitted total number of background electrons – grouping photon conversions, light hadrons and D-hadrons – and the fraction of photon conversions in the background is found to be f_γ, where only the statistical asymmetric errors are shown. The χ^2/DOF of the fit with the data is also shown, indicating that for bin $18 < E_{\mathrm{T}} < 22$ GeV the fit result does not perform well. The fitted total number of candidates is also presented as N_{exp}, which corresponds to the sum of the extracted number of signal and background and is expected to be very close to n_{obs}. Finally, the fraction of photon conversions in the background predicted from MC, which is used as a constrain of the fit, is shown as f_γ^{MC}.

Figure 4.4 shows the value of the log-likelihood as a function of the fitted number of electrons from B-hadron decays, for bins $10 < E_{\mathrm{T}} < 14$ GeV and $22 < E_{\mathrm{T}} < 26$ GeV, while leaving the other parameters of the fit, N_{BKG} and f_γ, fixed at the value that minimises the function.

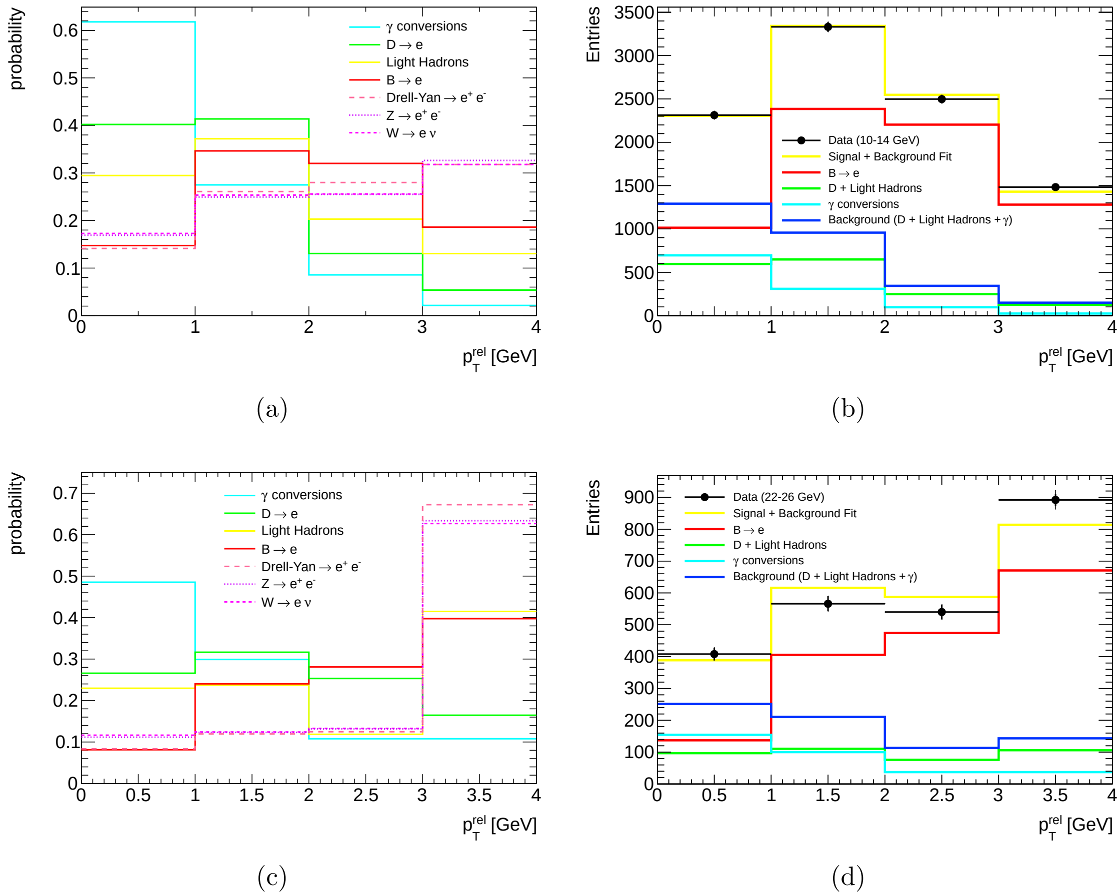

Figure 4.3: For bins $10 < E_{\mathrm{T}} < 14$ GeV (top) and $22 < E_{\mathrm{T}} < 26$ GeV (bottom), the graphs on the left show the templates for the components of the fit (solid lines) and the pdfs of the subtracted W,Z and Drell-Yan components (dashed, dotted and long-dashed, respectively). On the right are the results of the fit overlaid with the data points after $W/Z/\gamma^*$ subtraction.

	E_{T} bin (GeV)				
	7-10	10-14	14-18	18-22	22-26
χ^2/DOF	11.0	2.9	7.0	32.2	0.51
n_{obs}	4476	9625	5585	6232	2113
N_B	2328^{+218}_{-225}	6883^{+245}_{-249}	4181^{+222}_{-241}	4813^{+306}_{-416}	1398^{+181}_{-284}
N_{BKG}	2148^{+226}_{-217}	2742^{+241}_{-235}	1404^{+236}_{-215}	1418^{+414}_{-298}	715^{+284}_{-177}
f_γ	$0.35^{+0.18}_{-0.16}$	$0.41^{+0.13}_{-0.11}$	$0.22^{+0.17}_{-0.14}$	$0.01^{+0.37}_{-0.35}$	$0.46^{+0.38}_{-0.34}$
f_γ^{MC}	0.33	0.30	0.26	0.35	0.41
N_{exp}	4476.0	9625.1	5585.0	6231.0	2113.0

Table 4.5: Summary of the results of the extended maximum likelihood fit of Equation 4.3 in bins of E_{T}.

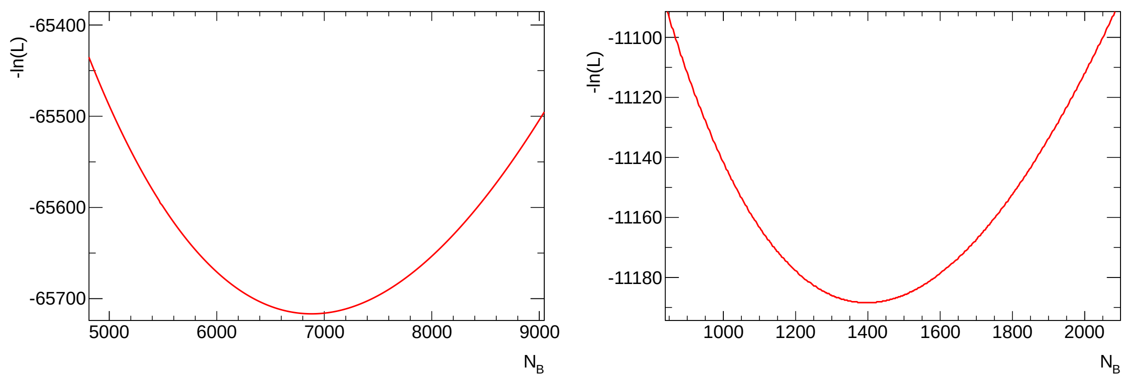

(a) (b)

Figure 4.4: The negative log-likelihood as a function of the fitted number of electrons from B-hadrons, for bins $10 < E_{\mathrm{T}} < 14$ GeV (a) and $22 < E_{\mathrm{T}} < 26$ GeV (b).

4.4.2 Systematic Uncertainties

The assessment of the systematic uncertainties on the extracted number of electrons from bottom decays for the most relevant sources is described in this section. A detailed summary for all E_{T} bins is shown at the end in Table 4.6 in Section 4.4.2.6.

4.4.2.1 Bias of the Method

To evaluate the possible bias on the extraction of electrons from B-hadrons using the extended maximum likelihood fit of equation 4.3, the extraction has been performed over a set of 1000 pseudo-experiments sampled from the MC-derived templates and varying the total number of events generated in each pseudo-experiment with a poisson probability function of mean $\mu_n = n_i^{\mathrm{obs}}$, in a so-called MC closure test. The result of N_B for each pseudo-experiment is subsequently compared to the true amount of signal electrons and the relative residual $\frac{N_B - N_B^{true}}{N_B^{true}}$ is plotted, as in Figure 4.5(a). The resulting distribution is fitted with a gaussian function.

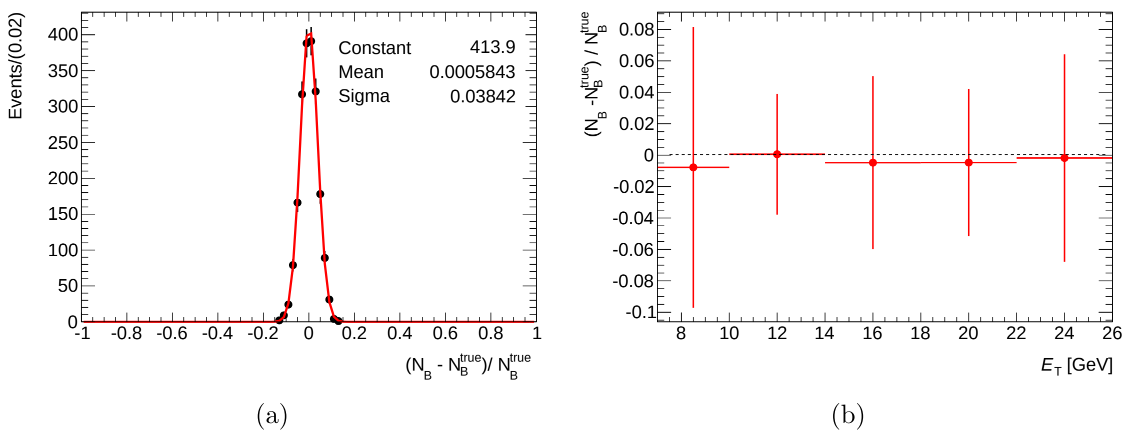

Figure 4.5: (a) Residual distribution for 1000 pseudo-experiments performed on the bin $10 < E_{\mathrm{T}} < 14$ GeV. (b) Relative bias on the extracted number of signal $b \to B \to e$ electron for each electron E_{T} bin as measured by the mean (points) and σ (errors) of the gaussian function fitted to the distribution of the residuals.

The procedure is repeated for every bin of the extraction and a systematic uncertainty is assigned as the standard deviation (σ) of the fitted function if it is significant in comparison with the mean. As shown in Figure 4.5(b), the mean is always very small compared to the standard deviation, thus the latter is taken as the associated systematic uncertainty for each E_{T} bin. The results are included in Table 4.6.

4.4.2.2 Statistical Limitation of MC Templates

Since the MC-derived templates of the $p_{\mathrm{T}}^{\mathrm{rel}}$ distribution for the different components are statistically limited, the error incurred by this constraint is quantified by an alternative set of pseudo-experiments, where the templates are varied and the extraction is made over the measured data distributions. The alterations of the templates are performed as a poisson variation of the number of candidates in each $p_{\mathrm{T}}^{\mathrm{rel}}$ bin, before the distributions are normalised to a probability (unity area), and is made for all 3 components at the same time. This is done recurrently 1000 times and the distribution of extracted number of signal $B \to e$ is fitted with a gaussian function whose mean is cross-checked to be very close to the central value of N_B and its σ is assigned as the uncertainty due to by the finite statistics. An example for the bin with $10 < E_{\mathrm{T}} < 14$ GeV is presented in Figure 4.6 and the results for all bins can be found in Table 4.6.

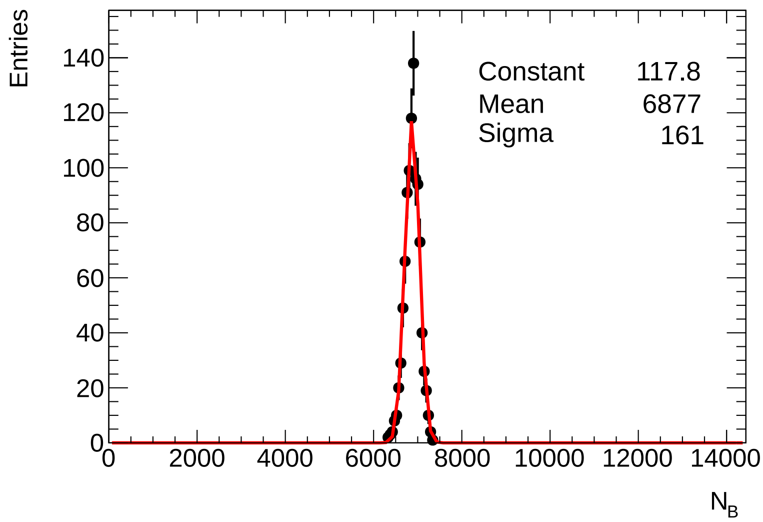

Figure 4.6: The distribution of extracted signal $b \to B \to e$ for the bin $10 < E_{\mathrm{T}} < 14$ GeV, for the pseudo-experiments with modified MC-templates.

4.4.2.3 Electromagnetic Energy Scale and Resolution

The electromagnetic energy scale and resolution uncertainties are determined using the recommendations of the ATLAS electron-γ combined performance group for the 2010 data in ATHENA release 16 [158]. The systematic uncertainty on the electromagnetic energy scale is calculated by scaling the electron cluster E_{T} in the data by to the appropriate amount, determined in dedicated performance studies on $Z \to e^+e^-$ and $J/\psi \to e^+e^-$ events [34] as a function of the cluster E_{T} and η, and then repeating the signal extraction. The difference between the new N_B result and the baseline value is taken as the systematic error due to the energy scale uncertainty.

The energy resolution uncertainty is determined by applying a smearing to the electron cluster E_{T} on the simulation samples. From the smeared distributions a set of modified templates is produced and the extraction is repeated. The difference between the resulting N_B and the central value is taken as the systematic error associated to the uncertainty on the energy resolution. The results are included in Table 4.6.

4.4.2.4 Charm Fraction in Background

The composite background of the model fitted includes photon conversions and electrons from light hadron and charm hadron decays. The last two, being similar in shape, are represented as a single component (C+Had) with the relative amount fixed by the expected fraction $\frac{N_{Had}}{N_C+N_{Had}}$ obtained from MC simulations. The effect of this choice is tested by varying the contribution of charm hadrons when creating the C+Had pdf by $\pm 20\%$ and redoing the minimisation. The difference between the modified and the main result for N_B is taken as the related uncertainty. Since the deviation is always to a smaller amount of N_B when reducing the charm component and a larger contribution when increasing it, an asymmetric systematic error is taken, as shown in Table 4.6.

4.4.2.5 Data-MC Discrepancies for $p_{\mathrm{T}}^{\mathrm{rel}}$ templates

To assess the level of disparity between the pdfs from MC simulations that are used for the main extraction and the real distribution of $p_{\mathrm{T}}^{\mathrm{rel}}$ for the signal and background components, a set of control regions are defined to look at data-derived templates.

$B \to e$ component The control region is defined using a cut on the impact parameter significance: $\frac{d_0}{\sigma_{d_0}} > 7$, where the purity is estimated to be in the range 82–87%. In the B-hadron–enhanced region the MC and data distributions of $p_{\mathrm{T}}^{\mathrm{rel}}$ are compared, producing a ratio distribution. The central MC-based B-hadron pdf is adjusted by the ratio furnished in the previous step. With the new template only for the signal component, the extraction is repeated and the difference of the resulting N_B with the central value is taken as a systematic uncertainty. An example of the ratio distribution, the original pdf and the modified pdf together with the templates from the B-enhanced region for bins $10 < E_{\mathrm{T}} < 14$ GeV and $22 < E_{\mathrm{T}} < 26$ GeV are shown in Figure 4.7.

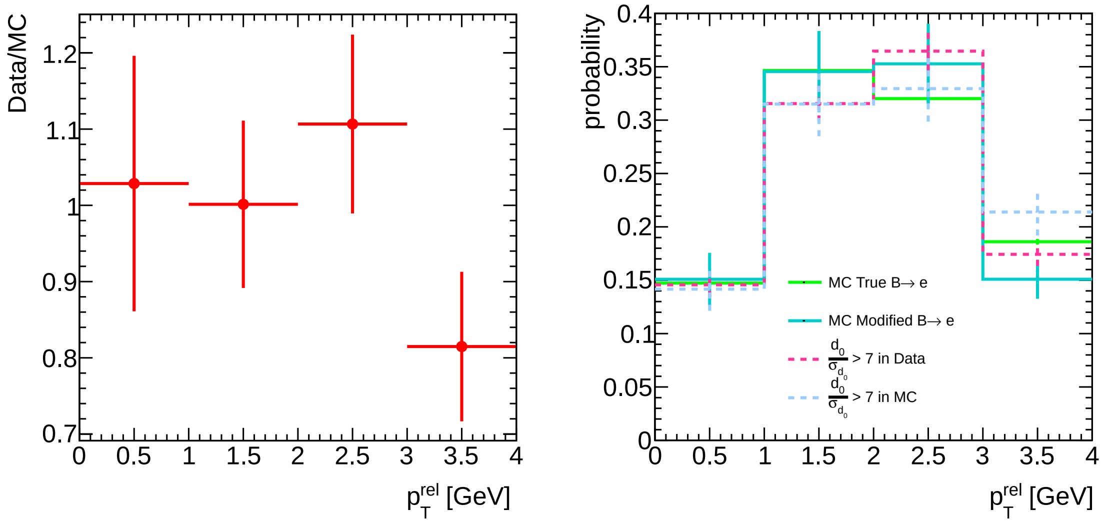

(a)

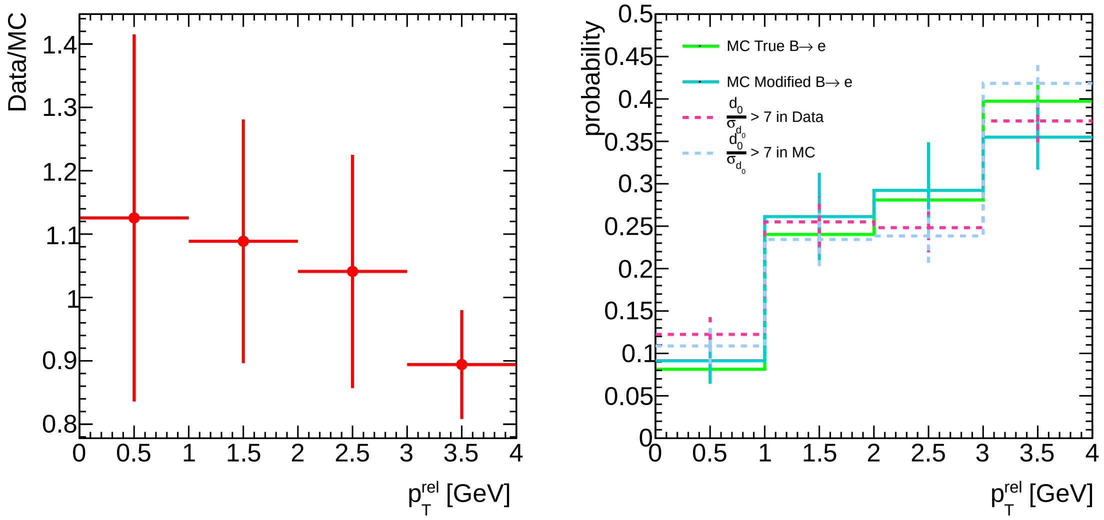

(b)

Figure 4.7: The ratio of data-to-MC template (left) determined from the enhanced B region $\frac{d_0}{\sigma_{d_0}} > 7$, and the $p_{\mathrm{T}}^{\mathrm{rel}}$ templates (right) for the $B \to e$ component before and after the modification in solid green and light-blue lines respectively, as well as the distributions used to produce the ratio in dashed lines, for $10 < E_{\mathrm{T}} < 14$ GeV (a) and $22 < E_{\mathrm{T}} < 26$ GeV (b).

$\gamma \to e$ component The control region for γ conversions is defined by inverting the cut on the number of hits in the pixel B-Layer – demanding that there is no hit at all – and requiring, instead of vetoing, a match of the electron track to a conversion vertex, which gives a photon purity of 98–99%. In this region the MC and data distributions are compared generating a ratio distribution, which is then used to modify the MC-based γ conversions pdf and the fit is carried out once more. The systematic uncertainty is, as before, determined from the difference with the central result of N_B. The ratio, the primary and modified pdfs, and the templates from the γ-enhanced region for bins $10 < E_{\mathrm{T}} < 14$ GeV and $22 < E_{\mathrm{T}} < 26$ GeV are presented in Figure 4.8.

Light and charm hadron component An enhanced light-hadron region is defined using a cut on the fraction of high threshold TRT hits $f_{\mathrm{TR}} < 0.05$ [2] , bringing a purity between 93–98%. In this region the MC and data distributions are compared and a ratio distribution plot is obtained and then used to alter both the charm and the light hadron pdfs. The extraction is performed again with the modified *C+Had* template and the systematic uncertainty is determined from the variation of the resulting N_B with respect to the main result. For bins $10 < E_{\mathrm{T}} < 14$ GeV and $22 < E_{\mathrm{T}} < 26$ GeV, Figure 4.9 displays the ratio distribution, the initial and the modified pdfs and the templates from the hadron-enhanced region.

As a cross-check, the extraction has also been made with all the templates modified by the ratios acquired in the individual control regions defined above and an error is derived from the result. This computation is compared to the sum-in-quadrature of the three uncertainties obtained taking one modification at a time. Hence, the final systematic uncertainty from the discrepancy on the $p_{\mathrm{T}}^{\mathrm{rel}}$ shapes between MC and data shown in Table 4.6 is chosen as the biggest of the two values. Since the effect of using modified templates consistently returns a reduced N_B compared to the central value, the uncertainty associated to the data-MC discrepancy is defined with a negative sign.

[2] In the main selection listed in Table 4.2 the requirement on a *minimum* f_{TR} depends on the η of the electron track, however the threshold is always > 0.05.

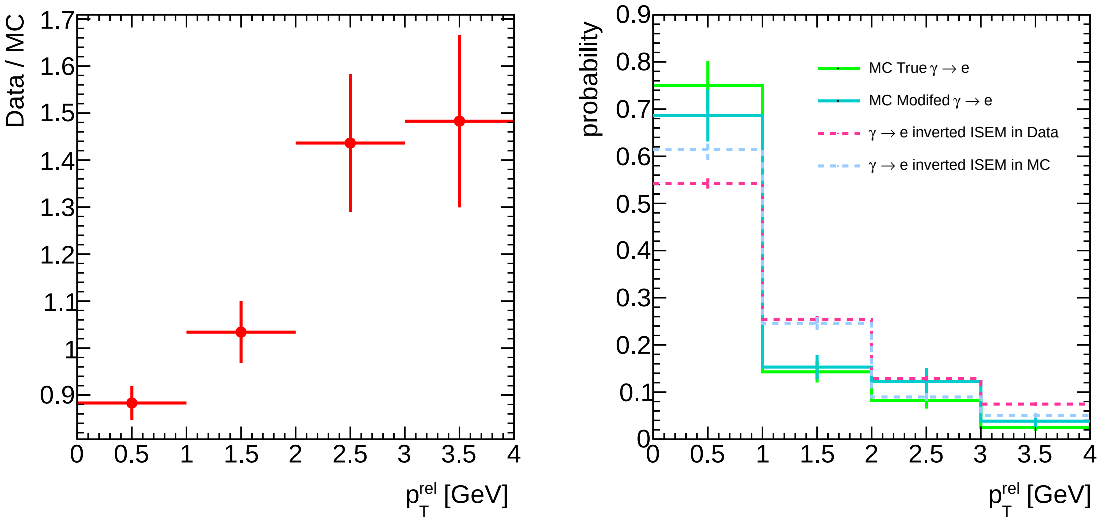

(a)

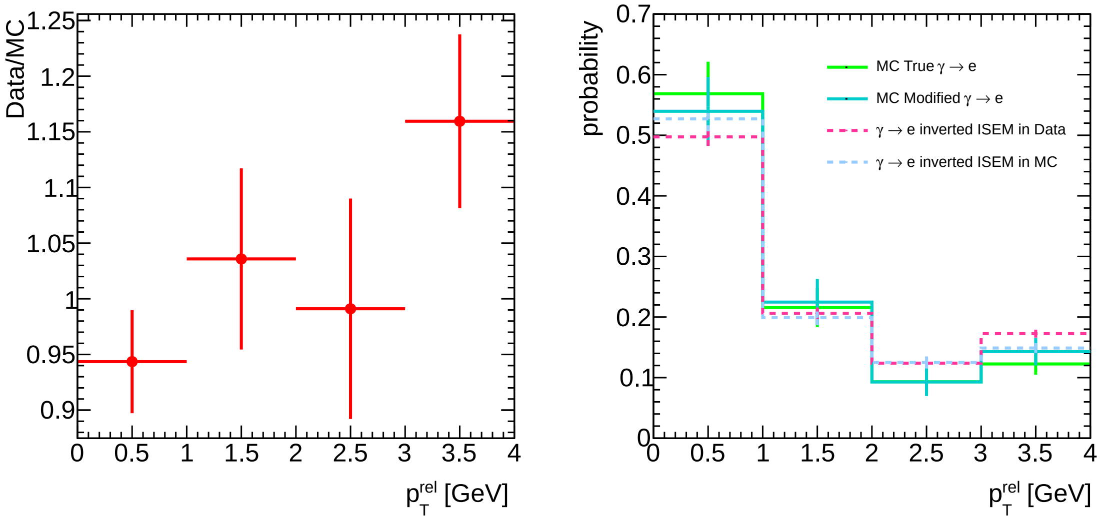

(b)

Figure 4.8: The ratio of data-to-MC template (left) determined from the enhanced conversions region with a conversion vertex and $n_{\mathrm{BL}} = 0$, and the $p_{\mathrm{T}}^{\mathrm{rel}}$ templates (right) for the $\gamma \to e$ component before and after the modification in solid green and light-blue lines respectively, as well as the distributions used to produce the ratio in dashed lines, for $10 < E_{\mathrm{T}} < 14$ GeV (a) and $22 < E_{\mathrm{T}} < 26$ GeV (b).

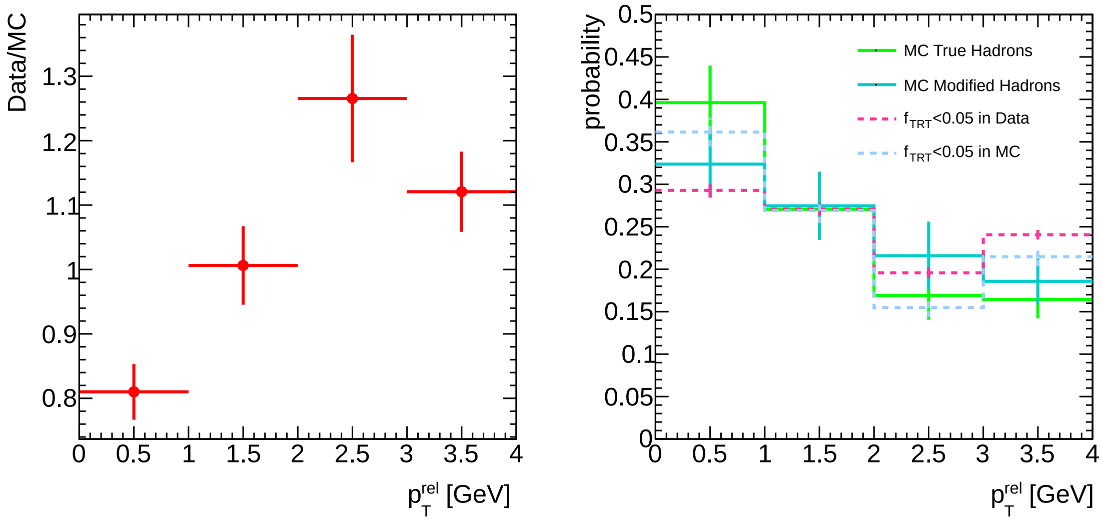

(a)

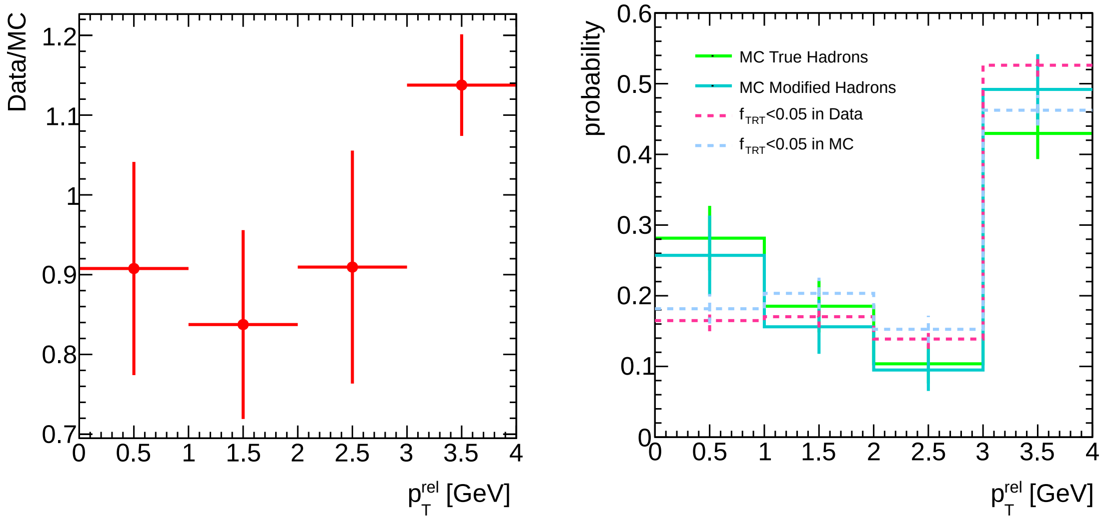

(b)

Figure 4.9: The ratio of data-to-MC template (left) determined from the enhanced light hadron region $f_{\mathrm{TR}} < 0.05$ and the $p_{\mathrm{T}}^{\mathrm{rel}}$ templates (right) for the light hadron component before and after the modification in solid green and light-blue lines respectively, as well as the distributions used to produce the ratio in dashed lines, for $10 < E_{\mathrm{T}} < 14$ GeV (a) and $22 < E_{\mathrm{T}} < 26$ GeV (b).

4.4.2.6 Total Uncertainty

Table 4.6 summarises the statistical and systematical uncertainties on the measurement of N_B in 5 E_T bins. The asymmetry of the statistical error is most important for bins $E_\mathrm{T} > 18$ GeV. The error induced from the discrepancy of the $p_\mathrm{T}^\mathrm{rel}$ distribution between data and MC for all components is the most important and, since the effect studied has always been one of decreasing the signal yield, it is taken only for the negative side.

	E_T bin (GeV)				
Source of error	7-10	10-14	14-18	18-22	22-26
Luminosity	—— 3.4 % ——				
Statistical (low)	-9.7 %	-3.6 %	-5.8 %	-8.6 %	-20.3 %
Statistical (high)	+9.4 %	+3.6 %	+5.3 %	+6.4 %	+13.0 %
Bias of the method	8.9 %	3.8 %	5.5 %	4.7 %	6.6 %
Statistical error on MC templates	3.8 %	2.3 %	4.9 %	8.7 %	10.7 %
Energy scale	1.1 %	3.3 %	3.6 %	2.3 %	2.4 %
Energy resolution	0.2 %	0.5 %	0.5 %	3.2 %	2.3 %
Charm fraction in C+Had (-20%)	-3.3 %	-0.8 %	-1.3 %	-8.4 %	-0.7 %
Charm fraction in C+Had (+20%)	+2.3 %	+0.5 %	+0.9 %	+3.7 %	+1.7 %
Data/MC discrepancies in templates	-19.3 %	-11.5 %	-46.6 %	-65.4 %	-39.1 %
Total Uncertainty (low)	-24.2 %	-13.8 %	-47.8 %	-67.4 %	-46.1 %
Total Uncertainty (high)	+14.2 %	+7.5 %	+10.4 %	+13.4 %	+18.7 %

Table 4.6: Systematic and statistical uncertainties in the measurement of N_B in each cluster E_T bin. For asymmetrical errors the appropriate sign is shown.

4.4.3 Final Result

The final extraction result with statistical and systematic asymmetric errors is shown in Table 4.7. The error on the measured ATLAS luminosity is not included in this table, because the normalisation has not been applied at this stage.

4.5 Comparison to Monte Carlo Predictions

Figure 4.10 shows the extraction results on the number of electrons from B-hadron decays – with the values from Table 4.7 normalised to $1\,\mathrm{nb}^{-1}$ of integrated luminosity and taking into account all the errors listed in Table 4.6 – together with the expected number of electrons in `PYTHIA`, `POWHEG`+`PYTHIA` and `POWHEG`+`HERWIG` MC simulations, as a function of electron cluster E_T.

	E_{T} bin (GeV)				
	7-10	10-14	14-18	18-22	22-26
N_B	2328	6883	4181	4813	1398
$\sigma^{-}_{\mathrm{stat}}$	-225	-249	-241	-416	-284
$\sigma^{+}_{\mathrm{stat}}$	$+218$	$+245$	$+222$	$+306$	$+181$
$\sigma^{-}_{\mathrm{syst}}$	-510	-885	-1981	-3215	-576
$\sigma^{+}_{\mathrm{syst}}$	$+235$	$+389$	$+345$	$+542$	$+183$

Table 4.7: Summary of the extraction results with absolute statistical and systematic errors for the low (-) and high(+) sides.

Similarly to the result from the inclusive electron cross-section measurement, the `PYTHIA` LO prediction for the production of electrons from B-hadron decays is larger than the measurement by a factor of ~ 1.5. The NLO MC prediction from `POWHEG` + `PYTHIA`, which matched the inclusive electron measurement very well, shows reasonable agreement in this case for the higher E_{T} bins; however in the first two E_{T} bins the prediction is slightly smaller compared to the extracted number and lies just outside the error band, with a deviation of less than 3σ. The prediction from `POWHEG` + `HERWIG` is roughly a factor 0.5 too small, resembling the comparison with the inclusive electron cross-section; nevertheless the spectrum shape agrees well with the measured E_{T} distribution.

4.6 Summary and Outlook

A measurement of the E_{T} distribution of electrons from B-hadron decays, using $1.28\,\mathrm{pb}^{-1}$ of pp collisions data recorded by the ATLAS experiment during 2010, has been presented. The dataset chosen is the same as in the inclusive electron cross-section measurement, but with tighter electron identification cuts in order to have a more pure sample and using a more advanced version of the reconstruction software which can reconstruct track-jets. A binned maximum likelihood fit in the relative p_{T} of the electron with respect to the track-jet axis, $p_{\mathrm{T}}^{\mathrm{rel}}$, is performed in order to separate the component of electrons from B-hadron decays from the backgrounds of photon conversions and electrons from charm or light hadron decays.

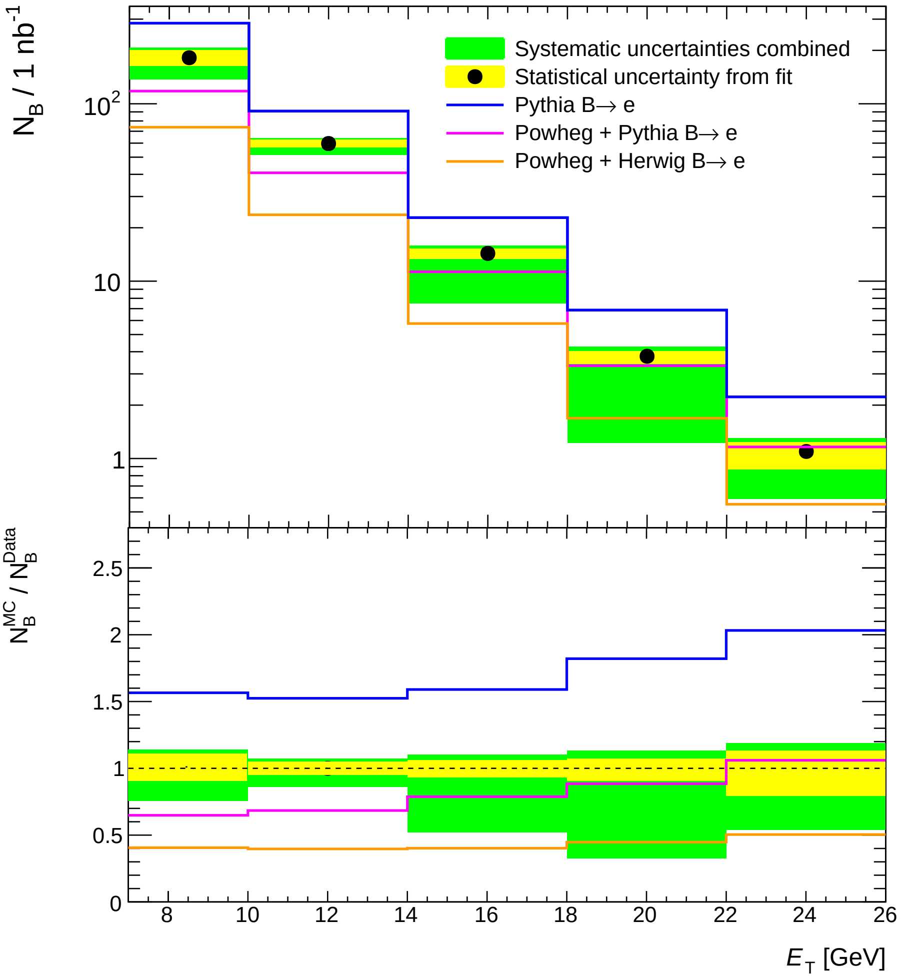

Figure 4.10: The number of signal electrons from B-hadron decays N_B obtained from the fit on $p_{\mathrm{T}}^{\mathrm{rel}}$ as a function of electron E_{T} , scaled to $\int \mathcal{L}\mathrm{dt} = 1\mathrm{nb}^{-1}$ and showing statistical and statistical plus systematic errors. The predictions of the E_{T} distribution for PYTHIA, POWHEG+PYTHIA and POWHEG+HERWIG simulations of $B \to e$ are overlaid as solid curves. On the bottom is the ratio of the MC predictions to the measured N_B in data.

The systematic errors of the measurement were evaluated; the uncertainty on the description of the $p_{\mathrm{T}}^{\mathrm{rel}}$ templates is found to be the most significant. The extracted E_{T} distribution with statistical and systematic errors is compared to the predictions for the production of electrons from B-hadron decays from PYTHIA at LO and POWHEG, interfaced with PYTHIA or HERWIG for the parton showering and hadronisation, at NLO. The PYTHIA prediction is found to be larger than the measurement by a factor of $\sim$ 1.5, in a similar way to the result of the inclusive electron cross-section. The POWHEG+PYTHIA prediction shows the best agreement, although at low E_{T} the measurement is somewhat larger than the expectation. The POWHEG+PYTHIA MC prediction was also the one that agreed best with the inclusive cross-section in Chapter 3. The POWHEG + HERWIG prediction is approximately 0.5 times smaller than the measured $B \to e$ rates; however there is better agreement with the shape of the E_{T} spectrum of data, as evidenced in Figure 4.10.

A possible improvement of this analysis would be to apply a veto on electrons from $W \to e\nu$ and $Z \to ee$ using transverse mass and invariant mass of electron pairs, respectively. This would eliminate the need for the MC-based subtraction before the extraction. Another modification that could bring better results is to use the full MC history in the simulation, as was done in the electron classification of the inclusive electron cross-section measurement, in order to minimise the contribution of signal electrons from B-hadron decays in the charm background template. If this information were included, a study of the signal efficiency would be possible and thus a proper cross-section could be measured.

The lack of convergence in the fits when binning finer in E_{T} and η prevented this type of binning to be used in the extraction. One possibility to overcome this difficulty would be to include more data recorded with HLT electron selections, which could allow to have enough events in every E_{T}-η bin to perform the likelihood fit. An unbinned likelihood fit could be performed if the shape of the templates for signal and background were known as an analytical function or derived as a smooth curve from MC simulations.

The dominant systematic uncertainty originates from the $p_{\mathrm{T}}^{\mathrm{rel}}$ template discrepancies between data and MC, therefore for a more conclusive measurement the definitions of the templates should be improved.

Summary and Conclusions

Two complementary measurements have been presented, using up to 1.28 ± 0.04 pb^{-1} of data collected by the ATLAS experiment at $\sqrt{s} = 7$ TeV with low-threshold electromagnetic triggers, in the cluster E_{T} range 7-26 GeV and within $|\eta| < 2.0$, excluding the transition regions between the barrel and end-cap EM calorimeters, $1.37 < |\eta| < 1.52$.

For the first measurement presented in Chapter 3, a sample of electrons was selected using loose identification cuts. A maximum likelihood method, the Tiles Method, has been applied to extract the heavy-flavour signal component from the dominant background contributions arising from hadron fakes and electrons from photon conversions, using Transition Radiation particle identification, the presence or not of a hit in the B-layer of the pixel detector and the ratio of the measured energy of the EM cluster to the track momentum. The efficiency of the trigger has been measured in data, while the reconstruction and identification efficiencies have been determined from the MC simulations and cross-checked with data estimations. A differential cross-section has been obtained from the extracted signal E_{T} distribution by applying the efficiency and migration corrections with a bin-by-bin unfolding method. The contribution of $W/Z/\gamma^{*}$ has been subtracted with NNLO accuracy before unfolding the p_{T} spectrum. The measured differential cross-section of electrons arising from heavy-flavour production is found to be in accord with a measurement made in the muon channel. The theoretical predictions for heavy-flavour production from the `FONLL` computation are in good agreement with both electron and muon measurements. The measurement also complies with the predictions of NLO MC from `POWHEG` with parton shower and hadronisation managed by `PYTHIA`. However, when `POWHEG` is interfaced with `HERWIG`, a significantly lower cross-section, by about ~ 0.5, is predicted. Leading-order parton-shower MC generated with `PYTHIA` describes the p_{T}-dependence well, but the overall normalisation computed is a factor two higher than the measurement and the NLO calculations. The full muon measurement, which was briefly explained in Section 2.4.2.4, covers the pseudorapidity range $|\eta| < 2.5$ and extends the spectrum over 4 GeV $< p_{\mathrm{T}}^{\mu} <$ 100 GeV thanks to the uniform response of the muon spectrometer to isolated and non-isolated muons, which allows to perform the spectrum unfolding before the subtraction of the vector-boson contribution.

The second measurement, presented in Chapter 4, uses the same dataset as the inclusive electron cross-section measurement, although using a more stringent set of identification cuts and a more advanced version of the reconstruction software, capable of providing track-jets. The distributions of the relative p_{T} of the electron with respect to the track-jet axis ($p_{\mathrm{T}}^{\mathrm{rel}}$) is used in a binned maximum likelihood fit as a means to extract the B-hadron component. The backgrounds considered in this study are photon conversions, electrons from charm decays and from light hadronic jets with leptonic or Dalitz decays among its constituents. A meticulous investigation of systematic errors on the event rate was performed, where the uncertainty on the description of the $p_{\mathrm{T}}^{\mathrm{rel}}$ templates is found to be the dominant one. The measured $B \rightarrow e$ rate as a function of the cluster E_{T} is compared with theoretical predictions, using exclusive MC generators: `PYTHIA` at LO and `POWHEG` at NLO, the latter interfaced with `PYTHIA` or `HERWIG` for the parton showering and hadronisation.

Similarly to the case of the inclusive electron cross-section measurement, the E_{T} distribution predicted by `PYTHIA` is found to be larger than the measurement by a factor of ~ 1.5, with a less steeply falling spectrum than observed in data. Also resembling the results of the inclusive electron cross-section measurement, the prediction from `POWHEG`+`PYTHIA` shows the best agreement with the measurement, although in the first two E_{T} bins the extracted number is slightly higher than expected, with a discrepancy of less than 3σ. The simulation from `POWHEG` + `HERWIG` predicts a distribution roughly a factor 0.5 smaller than data, again in correspondence with the inclusive electron measurement, with the spectrum shape agreeing well with the measured E_{T} distribution.

Bibliography

[1] M. L. Mangano, *The Saga of bottom production in $p\bar{p}$ collisions*, AIP Conf.Proc. **753** (2005) 247–260, arXiv:hep-ph/0411020.

[2] M. Cacciari, S. Frixione, N. Houdeau, et al., *Theoretical predictions for charm and bottom production at the LHC*, arXiv:1205.6344 [hep-ph].

[3] CDF Collaboration, F. Abe et al., *Measurement of the bottom quark production cross-section using semileptonic decay electrons in $p\bar{p}$ collisions at* $\sqrt{s} = 1.8\ TeV$, Phys.Rev.Lett. **71** (1993) 500–504.

[4] CDF Collaboration, F. Abe et al., *Measurement of bottom quark production in 1.8 TeV $p\bar{p}$ collisions using semileptonic decay muons*, Phys. Rev. Lett. **71** (1993) 2396–2400.

[5] D0 Collaboration, S. Abachi et al., *Inclusive μ and B quark production cross-sections in $p\bar{p}$ collisions at* $\sqrt{s} = 1.8\ TeV$, Phys.Rev.Lett. **74** (1995) 3548–3552.

[6] D0 Collaboration, B. Abbott et al., *The $b\bar{b}$ production cross section and angular correlations in $p\bar{p}$ collisions at* $\sqrt{s} = 1.8\ TeV$, Phys.Lett. **B487** (2000) 264–272, arXiv:hep-ex/9905024.

[7] CDF Collaboration, D. Acosta et al., *Measurement of the J/ψ meson and $b-$hadron production cross sections in $p\bar{p}$ collisions at* $\sqrt{s} = 1960\ GeV$, Phys.Rev. **D71** (2005) 032001, arXiv:hep-ex/0412071.

[8] D0 Collaboration, V. Abazov et al., *Measurement of inclusive differential cross sections for υ_{1S} production in $p\bar{p}$ collisions at $\sqrt{s}$ = 1.96-TeV*, Phys.Rev.Lett. **94** (2005) 232001, arXiv:hep-ex/0502030.

[9] M. Cacciari, M. Greco and P. Nason, *The p_{T} spectrum in heavy flavor hadroproduction*, JHEP **9805** (1998) 007, arXiv:hep-ph/9803400.

[10] M. Cacciari and P. Nason, *Is there a significant excess in bottom hadroproduction at the Tevatron?*, Phys.Rev.Lett. **89** (2002) 122003, arXiv:hep-ph/0204025.

[11] M. Cacciari, S. Frixione, M. L. Mangano, P. Nason and G. Ridolfi, *QCD analysis of first b cross-section data at 1.96TeV*, JHEP **0407** (2004) 033, arXiv:hep-ph/0312132.

[12] ATLAS Collaboration, G. Aad et al., *Measurements of the electron and muon inclusive cross-sections in proton-proton collisions at $\sqrt{s} = 7$ TeV with the ATLAS detector*, Physics Letters B **707** (2012) no. 5, 438 – 458, arXiv:1109.0525 [hep-ex].

[13] P. W. Higgs, *Broken Symmetries and the Masses of Gauge Bosons*, Phys. Rev. Lett. **13** (Oct, 1964) 508–509.

[14] F. Englert and R. Brout, *Broken Symmetry and the Mass of Gauge Vector Mesons*, Phys. Rev. Lett. **13** (Aug, 1964) 321–323.

[15] P. W. Higgs, *Broken symmetries, massless particles and gauge fields*, Physics Letters **12** (1964) no. 2, 132 – 133.

[16] ATLAS Collaboration, G. Aad et al., *The ATLAS Experiment at the CERN Large Hadron Collider*, JINST **3** (2008) S08003.

[17] L. Evans (ed.), P. Bryant (ed.), *LHC Machine*, JINST **3** (2008) S08001.

[18] CERN Press Office, *LHC to run at 4 TeV per beam in 2012*, http://press.web.cern.ch/press/PressReleases/Releases2012/PR10.12E.html.

[19] ATLAS Collaboration, G. Aad et al., *Updated Luminosity Determination in pp Collisions at $\sqrt{s}$=7 TeV using the ATLAS Detector*, ATLAS-CONF-2011-011 (2011) . https://atlas.web.cern.ch/Atlas/GROUPS/PHYSICS/CONFNOTES/ATLAS-CONF-2011-011/.

[20] ATLAS Collaboration, G. Aad et al., *Luminosity Determination in pp Collisions at $\sqrt{s} = 7$ TeV using the ATLAS Detector in 2011*, ATLAS-CONF-2011-116 (2011) . https://atlas.web.cern.ch/Atlas/GROUPS/PHYSICS/CONFNOTES/ATLAS-CONF-2011-116/.

[21] ATLAS Collaboration, G. Aad et al., *Particle Identification Performance of the ATLAS Transition Radiation Tracker*, ATLAS-CONF-2011-128 (2011) . https://atlas.web.cern.ch/Atlas/GROUPS/PHYSICS/CONFNOTES/ATLAS-CONF-2011-128/.

[22] ATLAS Collaboration, G. Aad et al., *Expected performance of the ATLAS experiment : detector, trigger and physics*, arXiv:0901.0512.

[23] ATLAS Collaboration, G. Aad et al., *Alignment of the ATLAS Inner Detector Tracking System with 2010 LHC proton-proton collisions at $\sqrt{s} = 7$ TeV*, ATLAS-CONF-2011-012 (2011) . https://atlas.web.cern.ch/Atlas/GROUPS/PHYSICS/CONFNOTES/ATLAS-CONF-2011-012/.

[24] ATLAS Collaboration, G. Aad et al., *Performance of the ATLAS Detector using First Collision Data*, JHEP **1009** (2010) 056, arXiv:1005.5254 [hep-ex].

[25] ATLAS Collaboration, G. Aad et al., *Performance of primary vertex reconstruction in proton-proton collisions at $\sqrt{s} = 7$ TeV in the ATLAS experiment*, ATLAS-CONF-2010-069 (2010) . https://atlas.web.cern.ch/Atlas/GROUPS/PHYSICS/CONFNOTES/ATLAS-CONF-2010-069/.

[26] ATLAS Collaboration, G. Aad et al., *Characterization of Interaction-Point Beam Parameters Using the pp Event-Vertex Distribution Reconstructed in the ATLAS Detector at the LHC*, ATLAS-CONF-2010-027 (2010) . https://atlas.web.cern.ch/Atlas/GROUPS/PHYSICS/CONFNOTES/ATLAS-CONF-2010-027/.

[27] ATLAS Collaboration, G. Aad et al., *Performance of the ATLAS Trigger System in 2010*, Eur.Phys.J. **C72** (2012) 1849, arXiv:1110.1530 [hep-ex].

[28] ATLAS Collaboration, Y. Nakahama, *Designing the ATLAS trigger menu for high luminosities*, ATL-DAQ-PROC-2012-037 (2012) . https://cdsweb.cern.ch/record/1458571.

[29] ATLAS Collaboration, A. Solodkov, *ATLAS status, operation and performance*, ATL-PHYS-PROC-2010-147 (2010) . https://cdsweb.cern.ch/record/1316166/.

[30] ATLAS Collaboration, S. Ask et al., *The ATLAS central level-1 trigger logic and TTC system*, JINST **3** (2008) P08002.

[31] ATLAS Collaboration, R. Achenbach et al., *The ATLAS level-1 calorimeter trigger*, JINST **3** (2008) P03001.

[32] C. Eck, J. Knobloch, L. Robertson, et al., *LHC computing Grid: Technical Design Report. Version 1.06.* Technical Design Report LCG. CERN, Geneva, 2005.

[33] ATLAS Collaboration, *Atlas Computing: technical design report.* CERN, Geneva, 2005.

[34] ATLAS Collaboration, G. Aad et al., *Electron performance measurements with the ATLAS detector using the 2010 LHC proton-proton collision data*, Eur.Phys.J. **C72** (2012) 1909, `arXiv:1110.3174 [hep-ex]`.

[35] ATLAS Collaboration, G. Aad et al., *Performance of the electron and photon trigger in p-p Collisions at $\sqrt{s} = 7$ TeV collisions with the ATLAS Detector at the LHC*, ATLAS-CONF-2011-114 (2011) . `https://atlas.web.cern.ch/Atlas/GROUPS/PHYSICS/CONFNOTES/ATLAS-CONF-2011-114/`.

[36] ATLAS Collaboration, G. Aad et al., *Expected electron performance in the ATLAS experiment*, ATL-PHYS-PUB-2011-006 . `https://cdsweb.cern.ch/record/1345327`.

[37] ATLAS Collaboration, G. Aad et al., *Observation of inclusive electrons in the ATLAS experiment at $\sqrt{s} = 7$ TeV.*, ATLAS-CONF-2010-073 (2010) . `https://atlas.web.cern.ch/Atlas/GROUPS/PHYSICS/CONFNOTES/ATLAS-CONF-2010-073/`.

[38] *Response uniformity of the ATLAS liquid argon electromagnetic calorimeter*, Nuclear Instruments and Methods in Physics Research Section A: Accelerators, Spectrometers, Detectors and Associated Equipment **582** (2007) no. 2, 429 – 455, `arXiv:0709.1094 [physics.ins-det]`. `http://www.sciencedirect.com/science/article/pii/S0168900207018591`.

[39] J. Gaiser, *Charmonium Spectroscopy from Radiative Decays of the J/ψ and ψ'.* PhD thesis, Stanford University, 1982. SLAC-0255.

[40] M. Oreglia, *A Study of the Reactions $\psi' \to \gamma\gamma\psi$.* PhD thesis, Stanford University, 1980. SLAC-0236.

[41] T. Skwarnicki, *A study of the radiative cascade transitions between the Υ' and Υ resonances.* PhD thesis, Cracow Institute of Nuclear Physics, 1986. DESY-F31-86-02.

[42] ATLAS Collaboration, *Observation of a new particle in the search for the Standard Model Higgs boson with the ATLAS detector at the LHC*, Phys.Lett. **B716** (2012) 1–29, `arXiv:1207.7214 [hep-ex]`.

[43] CMS Collaboration, S. Chatrchyan et al., *Observation of a new boson at a mass of 125 GeV with the CMS experiment at the LHC*, Phys.Lett. **B716** (2012) 30–61, `arXiv:1207.7235 [hep-ex]`.

[44] Particle Data Group Collaboration, J. Beringer et al., *Review of Particle Physics (RPP)*, Phys. Rev. **D86** (2012) 010001.

[45] D. H. Perkins, *Introduction to high-energy physics; 4th ed.* Cambridge Univ. Press, Cambridge, 2000.

[46] B. Cleveland, T. Daily, J. Davis, Raymond, et al., *Measurement of the solar electron neutrino flux with the Homestake chlorine detector*, Astrophys.J. **496** (1998) 505–526.

[47] Super-Kamiokande Collaboration, S. Fukuda et al., *Determination of solar neutrino oscillation parameters using 1496 days of Super-Kamiokande I data*, Phys.Lett. **B539** (2002) 179–187, `arXiv:hep-ex/0205075`.

[48] Kamiokande Collaboration, Y. Fukuda et al., *Solar neutrino data covering solar cycle 22*, Phys.Rev.Lett. **77** (1996) 1683–1686.

[49] SNO Collaboration, Q. Ahmad et al., *Direct evidence for neutrino flavor transformation from neutral current interactions in the Sudbury Neutrino Observatory*, Phys.Rev.Lett. **89** (2002) 011301, `arXiv:nucl-ex/0204008`.

[50] SNO Collaboration, Q. Ahmad et al., *Measurement of the rate of $\nu_e + d \to p + p + e^-$ interactions produced by B-8 solar neutrinos at the Sudbury Neutrino Observatory*, Phys.Rev.Lett. **87** (2001) 071301, `arXiv:nucl-ex/0106015`.

[51] GALLEX Collaboration, W. Hampel et al., *GALLEX solar neutrino observations: Results for GALLEX IV*, Phys.Lett. **B447** (1999) 127–133.

[52] GNO Collaboration, M. Altmann et al., *Complete results for five years of GNO solar neutrino observations*, Phys.Lett. **B616** (2005) 174–190, arXiv:hep-ex/0504037.

[53] Super-Kamiokande Collaboration, Y. Fukuda et al., *Evidence for oscillation of atmospheric neutrinos*, Phys.Rev.Lett. **81** (1998) 1562–1567, arXiv:hep-ex/9807003.

[54] Super-Kamiokande Collaboration, Y. Ashie et al., *Evidence for an oscillatory signature in atmospheric neutrino oscillation*, Phys.Rev.Lett. **93** (2004) 101801, arXiv:hep-ex/0404034.

[55] KamLAND Collaboration, K. Eguchi et al., *First results from KamLAND: Evidence for reactor anti-neutrino disappearance*, Phys.Rev.Lett. **90** (2003) 021802, arXiv:hep-ex/0212021.

[56] KamLAND Collaboration, T. Araki et al., *Measurement of neutrino oscillation with KamLAND: Evidence of spectral distortion*, Phys.Rev.Lett. **94** (2005) 081801, arXiv:hep-ex/0406035.

[57] RENO Collaboration, J. Ahn et al., *Observation of Reactor Electron Antineutrino Disappearance in the RENO Experiment*, Phys.Rev.Lett. **108** (2012) 191802, arXiv:1204.0626 [hep-ex].

[58] DAYA-BAY Collaboration, F. An et al., *Observation of electron-antineutrino disappearance at Daya Bay*, Phys.Rev.Lett. **108** (2012) 171803, arXiv:1203.1669 [hep-ex].

[59] K2K Collaboration, M. Ahn et al., *Measurement of Neutrino Oscillation by the K2K Experiment*, Phys.Rev. **D74** (2006) 072003, arXiv:hep-ex/0606032.

[60] MINOS Collaboration, P. Adamson et al., *Improved search for muon-neutrino to electron-neutrino oscillations in MINOS*, Phys.Rev.Lett. **107** (2011) 181802, arXiv:1108.0015 [hep-ex].

[61] T2K Collaboration, K. Abe et al., *Indication of Electron Neutrino Appearance from an Accelerator-produced Off-axis Muon Neutrino Beam*, Phys.Rev.Lett. **107** (2011) 041801, arXiv:1106.2822 [hep-ex].

[62] S. Glashow, *Partial Symmetries of Weak Interactions*, Nucl.Phys. **22** (1961) 579–588.

[63] A. Salam, *Weak and electromagnetic interactions*, in *Proc. of the 8th Nobel Symposium on 'Elementary Particle Theory, Relativistic Groups and Analyticity', Stockholm, Sweden, 1968*, N. Svartholm, ed., pp. 367–377. 1969.

[64] S. Weinberg, *A Model of Leptons*, Phys.Rev.Lett. **19** (1967) 1264–1266.

[65] UA1 Collaboration, G. Arnison et al., *Experimental Observation of Isolated Large Transverse Energy Electrons with Associated Missing Energy at* $\sqrt{s} = 540\ GeV$, Phys.Lett. **B122** (1983) 103–116.

[66] UA1 Collaboration, G. Arnison et al., *Experimental Observation of Lepton Pairs of Invariant Mass Around* 95 GeV/c^2 *at the CERN SPS Collider*, Phys.Lett. **B126** (1983) 398–410.

[67] UA1 Collaboration, G. Arnison et al., *Further Evidence for Charged Intermediate Vector Bosons at the SPS Collider*, Phys.Lett. **B129** (1983) 273.

[68] UA2 Collaboration, M. Banner et al., *Observation of Single Isolated Electrons of High Transverse Momentum in Events with Missing Transverse Energy at the CERN anti-p p Collider*, Phys.Lett. **B122** (1983) 476–485.

[69] UA2 Collaboration, P. Bagnaia et al., *Evidence for* $Z^0 \rightarrow e^+e^-$ *at the CERN anti-p p Collider*, Phys.Lett. **B129** (1983) 130–140.

[70] A. Pich, *The Standard Model of Electroweak Interactions*, `arXiv:1201.0537 [hep-ph]`.

[71] M. H. Seymour, *Quantum chromodynamics*, `arXiv:hep-ph/0505192`.

[72] R. K. Ellis, W. J. Stirling, and B. R. Webber, *QCD and Collider Physics*. Cambridge monographs on particle physics, nuclear physics, and cosmology. Cambridge Univ. Press, Cambridge, 1996.

[73] B. Kniehl, G. Kramer, I. Schienbein, and H. Spiesberger, *Inclusive B-Meson Production at the LHC in the GM-VFN Scheme*, Phys.Rev. **D84** (2011) 094026, `arXiv:1109.2472 [hep-ph]`.

[74] B. Kniehl, G. Kramer, I. Schienbein, and H. Spiesberger, *Inclusive Charmed-Meson Production at the CERN LHC*, Eur.Phys.J. **C72** (2012) 2082, `arXiv:1202.0439 [hep-ph]`.

[75] S. Alioli, P. Nason, C. Oleari and E. Re, *A general framework for implementing NLO calculations in shower Monte Carlo programs: the POWHEG BOX*, JHEP **1006** (2010) 043, `arXiv:1002.2581 [hep-ph]`.

[76] S. Frixione, P. Nason and G. Ridolfi, *A Positive-weight next-to-leading-order Monte Carlo for heavy flavour hadroproduction*, JHEP **0709** (2007) 126, `arXiv:0707.3088 [hep-ph]`.

[77] T. Sjostrand, S. Mrenna and P. Skands, *PYTHIA 6.4 Physics and Manual*, JHEP **0605** (2006) 026, `arXiv:hep-ph/0603175`.

[78] G. Corcella, I.G. Knowles, G. Marchesini, S. Moretti, K. Odagiri, P. Richardson, M.H. Seymour and B.R. Webber, *HERWIG 6: An Event generator for hadron emission reactions with interfering gluons (including supersymmetric processes)*, JHEP **0101** (2001) 010, `arXiv:hep-ph/0011363`.

[79] S. Frixione, B.R. Webber, *Matching NLO QCD computations and parton shower simulations*, JHEP **0206** (2002) 029, `arXiv:hep-ph/0204244`.

[80] S. Frixione, P. Nason, and B. R. Webber, *Matching NLO QCD and parton showers in heavy flavor production*, JHEP **0308** (2003) 007, `arXiv:hep-ph/0305252`.

[81] GEANT4 Collaboration, S. Agnostinelli and others, *Geant4 — a simulation toolkit*, Nucl. Instrum. Meth. **A506** (2003) 250–303.

[82] P. Nason, S. Dawson, and R. K. Ellis, *The Total Cross-Section for the Production of Heavy Quarks in Hadronic Collisions*, Nucl.Phys. **B303** (1988) 607.

[83] P. Nason, S. Dawson, and R. K. Ellis, *The One Particle Inclusive Differential Cross-Section for Heavy Quark Production in Hadronic Collisions*, Nucl.Phys. **B327** (1989) 49–92. Erratum-ibid. B335 (1990) 260.

[84] M. Cacciari and M. Greco, *Large p_T hadroproduction of heavy quarks*, Nucl.Phys. **B421** (1994) 530–544, `arXiv:hep-ph/9311260`.

[85] M. Cacciari, P. Nason and C. Oleari, *A Study of heavy flavored meson fragmentation functions in e^+e^- annihilation*, JHEP **0604** (2006) 006, `arXiv:hep-ph/0510032`.

[86] V. Kartvelishvili, A. Likhoded, and V. Petrov, *On the Fragmentation Functions of Heavy Quarks Into Hadrons*, Phys.Lett. **B78** (1978) 615.

[87] M. Cacciari and P. Nason, *Charm cross-sections for the Tevatron Run II*, JHEP **0309** (2003) 006, `arXiv:hep-ph/0306212`.

[88] P. Nadolsky and others, *Implications of CTEQ global analysis for collider observables*, Phys.Rev. **D78** (2008) 013004, `arXiv:0802.0007 [hep-ph]`.

[89] A.D. Martin, W.J. Stirling, R.S. Thorne and G. Watt, *Parton distributions for the LHC*, Eur.Phys.J. **C63** (2009) 189–285, `arXiv:0901.0002 [hep-ph]`.

[90] H1 and ZEUS Collaborations, F.D. Aaron and others, *Combined Measurement and QCD Analysis of the Inclusive $e^{\pm}$ p Scattering Cross Sections at HERA*, JHEP **1001** (2010) 109, `arXiv:0911.0884 [hep-ex]`.

[91] H.L. Lai and others, *Uncertainty induced by QCD coupling in the CTEQ global analysis of parton distributions*, Phys.Rev. **D82** (2010) 054021, `arXiv:1004.4624 [hep-ph]`.

[92] T. Gleisberg, S. Hoeche, F. Krauss, et al., *Event generation with SHERPA 1.1*, JHEP **0902** (2009) 007, `arXiv:0811.4622 [hep-ph]`.

[93] T. Sjostrand and P. Z. Skands, *Transverse-momentum-ordered showers and interleaved multiple interactions*, Eur.Phys.J. **C39** (2005) 129–154, `arXiv:0408302 [hep-ph]`.

[94] S. Schumann, *Monte Carlo generator for the LHC*, 2012. `http://www.bw-grid.de/projekte/2012/05/11/monte-carlo-generator-for-the-lhc/`.

[95] M. L. Mangano, *Two lectures on heavy quark production in hadronic collisions*, `arXiv:hep-ph/9711337`.

[96] S. P. Baranov and M. Smizanska, *Semihard b quark production at high-energies versus data and other approaches*, Phys. Rev. **D62** (2000) 014012.

[97] S. Frixione, M. Smizanska, et al., *Heavy flavor production and fragmentation*, J.Phys. **G27** (2001) 1111–1157.

[98] M. Smizanska, *PythiaB interface to Pythia6 dedicated to simulation of beauty events*, 2005. `http://atlas-sw.cern.ch/cgi-bin/viewcvs-atlas.cgi/offline/Generators/PythiaB/doc/PythiaB.pdf`.

[99] M. L. Mangano, P. Nason, and G. Ridolfi, *Heavy quark correlations in hadron collisions at next-to-leading order*, Nucl.Phys. **B373** (1992) 295–345.

[100] J. Alwall, A. Ballestrero, P. Bartalini, et al., *A Standard format for Les Houches event files*, Comput.Phys.Commun. **176** (2007) 300–304, `arXiv:hep-ph/0609017`.

[101] P. Nason, *A New Method for Combining NLO QCD with Shower Monte Carlo Algorithms*, JHEP **0411** (2004) 040, `arXiv:hep-ph/0409146`.

[102] S. Frixione, P. Nason, C. Oleari, *Matching NLO QCD computations with Parton Shower simulations: the POWHEG method*, JHEP **0711** (2007) 070, `arXiv:0709.2092 [hep-ph]`.

[103] David J. Lange, *The EvtGen particle decay simulation package*, Nucl. Instrum. Meth. **A462** (2001) 152–155.

[104] W. J. Stirling, *Cross section plots: Standard Model cross sections as a function of collider energy*, 2012. `http://www.hep.phy.cam.ac.uk/~wjs/plots/plots.html`.

[105] F. Bsser, L. Camilleri, L. D. Lella, et al., *Observation of high transverse momentum electrons at the CERN ISR*, Physics Letters B **53** (1974) no. 2, 212 – 216.

[106] J. J. Aubert, U. Becker, P. J. Biggs, et al., *Experimental Observation of a Heavy Particle J*, Phys. Rev. Lett. **33** (Dec, 1974) 1404–1406.

[107] J. E. Augustin, A. M. Boyarski, M. Breidenbach, et al., *Discovery of a Narrow Resonance in e^+e^- Annihilation*, Phys. Rev. Lett. **33** (Dec, 1974) 1406–1408.

[108] UA1 Collaboration, C. Albajar et al., *Beauty Production at the CERN Proton - anti-Proton Collider. 1.*, Phys.Lett. **B186** (1987) 237–246.

[109] UA1 Collaboration, C. Albajar et al., *Search for B0 anti-B0 Oscillations at the CERN Proton - anti-Proton Collider. 2.*, Phys.Lett. **B186** (1987) 247.

[110] O. Botner, L. Eek, T. Ekelof, et al., *Production of Prompt Electrons in the Charm p_T region at $\sqrt{s}$ = 630GeV*, Phys.Lett. **B236** (1990) 488.

[111] UA1 Collaboration, C. Albajar et al., *Measurement of the Bottom Quark Production Cross-Section in Proton - anti-Proton Collisions at $\sqrt{s}$ = 0.63 TeV*, Phys.Lett. **B213** (1988) 405.

[112] UA1 Collaboration, C. Albajar et al., *Beauty production at the CERN p anti-p collider*, Phys.Lett. **B256** (1991) 121–128.

[113] M. Cacciari, *Rise and fall of the bottom quark production excess*, `arXiv:hep-ph/0407187`.

[114] CDF Collaboration, F. Abe et al., *Evidence for top quark production in $\bar{p}p$ collisions at $\sqrt{s} = 1.8$ TeV*, Phys.Rev.Lett. **73** (1994) 225–231, `arXiv:hep-ex/9405005`.

[115] CDF Collaboration, F. Abe et al., *Observation of top quark production in $\bar{p}p$ collisions*, Phys.Rev.Lett. **74** (1995) 2626–2631, `arXiv:hep-ex/9503002`.

[116] D0 Collaboration, S. Abachi et al., *Observation of the top quark*, Phys.Rev.Lett. **74** (1995) 2632–2637, `arXiv:hep-ex/9503003`.

[117] E. L. Berger, J.-w. Qiu, and Y.-l. Wang, *Transverse momentum distribution of Υ production in hadronic collisions*, Phys.Rev. **D71** (2005) 034007, `arXiv:hep-ph/0404158`.

[118] E. L. Berger, J.-W. Qiu, and Y. Wang, *Υ transverse momentum at hadron colliders*, Int.J.Mod.Phys. **A20** (2005) 3753–3755, `arXiv:hep-ph/0411026`.

[119] CMS Collaboration, V. Khachatryan et al., *Inclusive b-hadron production cross section with muons in pp collisions at $\sqrt{s} = 7$ TeV*, JHEP **1103** (2011) 090, `arXiv:1101.3512 [hep-ex]`.

[120] CMS Collaboration, V. Khachatryan et al., *Prompt and non-prompt J/ψ production in pp collisions at $\sqrt{s} = 7$* TeV, Eur.Phys.J. **C71** (2011) 1575, `arXiv:1011.4193 [hep-ex]`.

[121] CMS Collaboration, S. Chatrchyan et al., *J/ψ and $\psi(2S)$ production in pp collisions at $\sqrt{s} = 7$* TeV, JHEP **1202** (2012) 011, `arXiv:1111.1557 [hep-ex]`.

[122] CMS Collaboration, S. Chatrchyan et al., *Measurement of the Strange B Meson Production Cross Section with $J/\psi\ \phi$ Decays in pp Collisions at* $\sqrt{s} = 7$ TeV, Phys.Rev. **D84** (2011) 052008, arXiv:1106.4048 [hep-ex].

[123] CMS Collaboration, S. Chatrchyan et al., *Measurement of the B^0 production cross section in pp Collisions at* $\sqrt{s} = 7$ TeV, Phys.Rev.Lett. **106** (2011) 252001, arXiv:1104.2892 [hep-ex].

[124] CMS Collaboration, V. Khachatryan et al., *Measurement of the B^+ Production Cross Section in pp Collisions at $\sqrt{s} = 7$ TeV*, Phys.Rev.Lett. **106** (2011) 112001, arXiv:1101.0131 [hep-ex].

[125] CMS Collaboration, V. Khachatryan et al., *Measurement of the Inclusive Υ production cross section in pp collisions at* $\sqrt{s} = 7$ TeV, Phys.Rev. **D83** (2011) 112004, arXiv:1012.5545 [hep-ex].

[126] CMS Collaboration, S. Chatrchyan et al., *Measurement of the cross section for production of $b\bar{b}X$, decaying to muons in pp collisions at* $\sqrt{s} = 7$ TeV, JHEP **1206** (2012) 110, arXiv:1203.3458 [hep-ex].

[127] ALICE Collaboration, B. Abelev et al., *Measurement of electrons from semileptonic heavy-flavour hadron decays in pp collisions at $\sqrt{s} = 7$ TeV*, arXiv:1205.5423 [hep-ex].

[128] ALICE Collaboration, B. Abelev et al., *Heavy flavour decay muon production at forward rapidity in proton–proton collisions at $\sqrt{s} = 7$ TeV*, Phys.Lett. **B708** (2012) 265–275, arXiv:1201.3791 [hep-ex].

[129] LHCb Collaboration, R. Aaij et al., *Measurement of $\sigma(pp \to b\bar{b}X)$ at $\sqrt{s} = 7$ TeV in the forward region*, Phys.Lett. **B694** (2010) 209–216, arXiv:1009.2731 [hep-ex].

[130] LHCb Collaboration, R. Aaij et al., *Measurement of J/ψ production in pp collisions at $\sqrt{s}$=7 TeV*, Eur.Phys.J. **C71** (2011) 1645, arXiv:1103.0423 [hep-ex].

[131] LHCb Collaboration, R. Aaij et al., *Measurement of the $B^\pm$ production cross-section in pp collisions at $\sqrt{s}$=7 TeV*, JHEP **1204** (2012) 093, arXiv:1202.4812 [hep-ex].

[132] ATLAS Collaboration, G. Aad et al., *Measurement of the differential cross-sections of inclusive, prompt and non-prompt J/ψ production in proton-proton collisions at $\sqrt{s} = 7$ TeV*, Nucl.Phys. **B850** (2011) 387–444, arXiv:1104.3038 [hep-ex].

[133] ATLAS Collaboration, G. Aad et al., *Measurement of the $\Upsilon(1S)$ Production Cross-Section in pp Collisions at $\sqrt{s} = 7$ TeV in ATLAS*, Phys.Lett. **B705** (2011) 9–27, arXiv:1106.5325 [hep-ex].

[134] G. T. Bodwin, E. Braaten, and G. P. Lepage, *Rigorous QCD analysis of inclusive annihilation and production of heavy quarkonium*, Phys.Rev. **D51** (1995) 1125–1171, arXiv:hep-ph/9407339 [hep-ph].

[135] T. Sjostrand, S. Mrenna, and P. Z. Skands, *A Brief Introduction to PYTHIA 8.1*, Comput.Phys.Commun. **178** (2008) 852–867, arXiv:0710.3820 [hep-ph].

[136] ATLAS Collaboration, G. Aad et al., *Measurement of the b-hadron production cross section using decays to $D^*\mu^- X$ final states in pp collisions at $\sqrt{s} = 7$ TeV with the ATLAS detector*, Nucl.Phys. **B864** (2012) 341–381, arXiv:1206.3122 [hep-ex].

[137] ATLAS Collaboration, G. Aad et al., *Electron and photon reconstruction and identification in ATLAS: expected performance at high energy and results at 900 GeV*, ATLAS-CONF-2010-005 (2010) . https://atlas.web.cern.ch/Atlas/GROUPS/PHYSICS/CONFNOTES/ATLAS-CONF-2010-005/.

[138] F. James, *MINUIT - Function Minimization and Error Analysis*, http://wwwinfo.cern.ch/asdoc/minuithtml3/minmain.html. CERN Program Library Entry D506 (unpublished).

[139] ATLAS Collaboration, G. Aad et al., *Study of the Material Budget in the ATLAS Inner Detector with K_s^0 decays in collision data at $\sqrt{s} = 900$ GeV*, ATLAS-CONF-2010-019 (2010) . http://atlas.web.cern.ch/Atlas/GROUPS/PHYSICS/CONFNOTES/ATLAS-CONF-2010-019/.

[140] *Energy scale recommendations for release 15*, https://twiki.cern.ch/twiki/bin/view/AtlasProtected/EnergyScaleResolutionRecommendations#2010_data_Release_15. Restricted to ATLAS members.

[141] M. Backes, P. Bell, S. Bordoni, W. Fedorko, M. Flowerdew, D. Froidevaux, S. Gadomski, C. Mora Herrera, G. Pasztor, M. Ridel, T. Vu Anh, and X. Wu, *Measurement of the inclusive electron cross-section from the decays of heavy flavour hadrons in pp collisions at* $\sqrt{s}$=7 *TeV*, ATL-PHYS-INT-2012-056 (2012) . https://cdsweb.cern.ch/record/1460430.

[142] B. Efron and R. J. Tibshirani, *An Introduction to the Bootstrap*. Chapman & Hall, New York, NY, 1993.

[143] ATLAS Collaboration, G. Aad et al., *Performance of the Minimum Bias Trigger in p-p Collisions at* $\sqrt{s} = 900$ *GeV*, ATLAS-CONF-2010-025 (2010) . http://atlas.web.cern.ch/Atlas/GROUPS/PHYSICS/CONFNOTES/ATLAS-CONF-2010-025/.

[144] J. Butterworth, J. R. Forshaw, and M. Seymour, *Multiparton interactions in photoproduction at HERA*, Z.Phys. **C72** (1996) 637–646, arXiv:hep-ph/9601371.

[145] S. Jadach, J. H. Kuhn, and Z. Was, *TAUOLA: A Library of Monte Carlo programs to simulate decays of polarized tau leptons*, Comput.Phys.Commun. **64** (1990) 275–299.

[146] S. Jadach, Z. Was, R. Decker, et al., *The tau decay library TAUOLA: Version 2.4*, Comput.Phys.Commun. **76** (1993) 361–380.

[147] P. Golonka and Z. Was, *PHOTOS Monte Carlo: A Precision tool for QED corrections in* Z *and* W *decays*, Eur.Phys.J. **C45** (2006) 97–107, arXiv:hep-ph/0506026.

[148] *Standard Model W/Z WG recommendations on pile-up reweighting*, https://twiki.cern.ch/twiki/bin/view/AtlasProtected/WZElectroweakCommonTopics.

[149] ATLAS Collaboration, G. Aad et al., *Measurement of the* $W \to l\nu$ *production cross-section and observation of* $Z \to ll$ *production in proton-proton collisions at* $\sqrt{s}$=7 *TeV with the ATLAS detector*, ATLAS-CONF-2010-051 (2010) . https://atlas.web.cern.ch/Atlas/GROUPS/PHYSICS/CONFNOTES/ATLAS-CONF-2010-051/.

[150] A. Hocker, V. Kartvelishvili, *SVD Approach to Data Unfolding*, Nucl. Instrum. Meth. **A372** (1996) 469–481, arXiv:hep-ph/9509307.

[151] G. D'Agostini, *A multidimensional unfolding method based on Bayes' theorem*, Nucl. Instrum. Meth. **A362** (1995) 487–498.

[152] T. Adye, R. Claridge, K. Tackmann and F. Wilson, *RooUnfold: ROOT Unfolding Framework*, `http://hepunx.rl.ac.uk/~adye/software/unfold/RooUnfold.html`.

[153] ATLAS Collaboration, G. Aad et al., *Measurement of the inclusive W± and Z/γ∗ cross sections in the e and μ decay channels in pp collisions at $\sqrt{s} = 7$ TeV with the ATLAS detector*, Phys.Rev. **D85** (2012) 072004, `arXiv:1109.5141 [hep-ex]`.

[154] ATLAS Collaboration, B. Butler and A. Schwartzman, *Track-Jet Reconstruction and Performance*, ATL-PHYS-INT-2010-040 (2010) . Restricted to ATLAS members.

[155] M. Cacciari, G. P. Salam, and G. Soyez, *The Anti-k(t) jet clustering algorithm*, JHEP **0804** (2008) 063, `arXiv:0802.1189 [hep-ph]`.

[156] C. Anastasiou and L. J. Dixon, K. Melnikov, and F. Petriello, *High-precision QCD at hadron colliders: Electroweak gauge boson rapidity distributions at next-to-next-to leading order*, Phys. Rev. **D69** (2004) 094008, `arXiv:hep-ph/0312266`.

[157] L. Moneta, K. Cranmer, G. Schott, et al., *The RooStats project*, in *Proceedings of the 13th International Workshop on Advanced Computing and Analysis Techniques in Physics Research. February 22-27, 2010, Jaipur, India.*, p. 57. 2010. `arXiv:1009.1003 [physics.data-an]`. `http://adsabs.harvard.edu/abs/2010acat.confE..57M`.

[158] *Energy scale recommendations for release 16*, `https://twiki.cern.ch/twiki/bin/view/AtlasProtected/EnergyScaleResolutionRecommendations#2010_data_Release_16`. Restricted to ATLAS members.

Appendix A

Electron classification from Primary Hadron

The candidate classification used in the efficiency assessment for the inclusive electrons analysis used a private algorithm in order to categorise the electrons according to the primary hadron in the decay chain from which it is produced. At the same time, a requirement on the last hadron of the decay chain is set in order to label this electron as coming from heavy-flavour or from light hadron decays. In order to perform this classification, the full Monte Carlo parton shower record is needed, therefore special *D3PD* samples are created where the full history is kept. The algorithm works as follows:

1. For each truth electron found, the direct *parent* is checked. The parent `pdgID` code is checked, if it corresponds to a tau lepton, a non-final-state electron or a heavy-flavour (charmed or bottom) hadron then the electron is kept for the next step. The `pdgID` code of the first hadron found going backwarkds in the electron history is saved for the analysis.

2. An recursive function, which checks on the *parents* of the hadron, is called iteratively for each hadron found in the electron Monte Carlo history, going backwards. When the parent found is no longer a hadron, i.e. `pdgID` < 111, the last found hadron, which is the primary hadron originated in the simulated collision, is kept and its pdgID code saved.

3. According to the flavour of the primary hadron, the electron is categorised as either coming from a B-hadron if the *greatest* digit in the third or the fourth position from the right in the `pdgID` code –idenfied as n_{q2} and n_{q1}, respectively,

in the PDG particle numbering scheme [44]– is equal to 5, the code for b-quark; or coming from a charmed hadron if the *greatest* digit in the third or fourth position from the right in the`pdgID` code is equal to 4, the code for c-quark.

4. Two methods were explored to match the truth electron to a reconstructed electron. The first one uses the pairing done by the *Monte Carlo Truth Classifier* –a tool which matches the particle's reconstructed track in the simulation to the truth object. In the second method, for every reconstructed electron a match is searched with $\Delta R < 0.2$ between the electron track and the truth electron *among those already classified from heavy-flavour*, and if more than one is found, the closest one is kept. For the final evaluation of the efficiencies, the first method was used.

Appendix B

Breakdown of Efficiencies

The effect of the individual cuts on the signal efficiency in true p_{T} bins, based on `PYTHIA` MC simulation is shown in Table B.1 and in Figure 3.9. To compare with the data-derived efficiencies in Section 3.3.2.4, the single cut efficiencies with respect to the previous cut are given in reconstructed E_{T} bins in Table B.2 and in Figure 3.10 for the default truth classification used for the efficiency determination from MC, described in Appendix A, and in Figure B.1 for the MCTruthClassifier classification used for the template generation. As expected, the results agree to better than 0.1%.

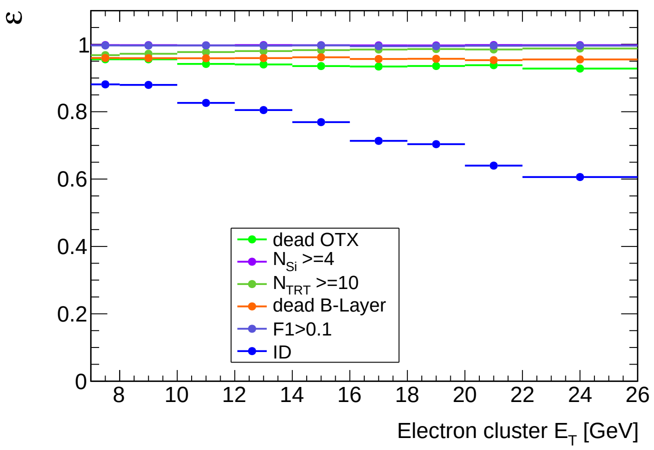

Figure B.1: Efficiencies of selection cuts with respect to the previous cut with MCTruthClassifier truth matching in reconstructed E_{T} bins.

Single cut efficiencies wrt to previous cut											
True p_{T} bin (GeV)	5-6	6-7	7-8	8-10	10-12	12-14	14-16	16-18	18-20	20-22	22-26
Vertexing	99.99 ± 0.00	99.99 ± 0.00	99.99 ± 0.00	99.99 ± 0.00	100.00 ± 0.00	100.00 ± 0.00	99.99 ± 0.01	100.00 ± 0.00	99.93 ± 0.04	100.00 ± 0.00	100.00 ± 0.00
η (and electron author cut)	74.57 ± 0.06	80.41 ± 0.08	83.25 ± 0.10	85.14 ± 0.09	86.87 ± 0.14	87.56 ± 0.21	88.49 ± 0.28	88.52 ± 0.39	89.19 ± 0.50	89.67 ± 0.63	90.26 ± 0.62
$E_{\mathrm{T}} > 7$ GeV	2.37 ± 0.02	15.61 ± 0.08	63.10 ± 0.13	89.00 ± 0.09	97.22 ± 0.07	99.04 ± 0.06	99.40 ± 0.07	99.59 ± 0.08	99.50 ± 0.12	99.81 ± 0.09	99.55 ± 0.15
dead OTX	96.06 ± 0.21	96.57 ± 0.10	96.30 ± 0.07	95.38 ± 0.06	93.60 ± 0.11	92.63 ± 0.18	91.99 ± 0.26	92.23 ± 0.35	91.97 ± 0.46	92.15 ± 0.59	91.66 ± 0.61
N_{Si}	99.14 ± 0.10	99.81 ± 0.02	99.91 ± 0.01	99.88 ± 0.01	99.86 ± 0.02	99.87 ± 0.02	99.85 ± 0.04	99.84 ± 0.05	99.76 ± 0.08	99.89 ± 0.08	99.79 ± 0.11
N_{TRT}	97.07 ± 0.18	97.40 ± 0.09	97.19 ± 0.06	97.01 ± 0.05	97.49 ± 0.07	97.95 ± 0.10	98.32 ± 0.13	98.44 ± 0.17	98.82 ± 0.19	98.88 ± 0.24	98.74 ± 0.26
dead B-Layer	96.40 ± 0.20	96.02 ± 0.11	95.72 ± 0.07	95.88 ± 0.06	96.00 ± 0.09	96.20 ± 0.13	95.96 ± 0.19	95.48 ± 0.28	95.75 ± 0.36	96.49 ± 0.42	95.96 ± 0.46
$f_1 > 0.1$	99.53 ± 0.08	99.66 ± 0.03	99.69 ± 0.02	99.67 ± 0.02	99.69 ± 0.03	99.60 ± 0.04	99.62 ± 0.06	99.65 ± 0.08	99.40 ± 0.14	99.63 ± 0.14	99.54 ± 0.16
ID (isEM)	45.60 ± 0.55	79.99 ± 0.23	89.69 ± 0.11	90.06 ± 0.10	87.95 ± 0.16	86.96 ± 0.24	85.13 ± 0.36	83.10 ± 0.52	81.42 ± 0.72	79.50 ± 0.95	77.56 ± 1.00
Total	0.71 ± 0.01	9.02 ± 0.05	42.03 ± 0.13	60.27 ± 0.13	64.78 ± 0.20	65.47 ± 0.30	64.65 ± 0.42	63.19 ± 0.58	62.31 ± 0.77	62.26 ± 1.00	60.12 ± 1.03

Cutflow											
True p_{T} bin (GeV)	5-6	6-7	7-8	8-10	10-12	12-14	14-16	16-18	18-20	20-22	22-26
Vertexing	99.99 ± 0.00	99.99 ± 0.00	99.99 ± 0.00	99.99 ± 0.00	100.00 ± 0.00	100.00 ± 0.00	99.99 ± 0.01	100.00 ± 0.00	99.93 ± 0.04	100.00 ± 0.00	100.00 ± 0.00
η (and electron author cut) η	74.56 ± 0.06	80.40 ± 0.08	83.25 ± 0.10	85.13 ± 0.09	86.87 ± 0.14	87.56 ± 0.21	88.49 ± 0.28	88.52 ± 0.39	89.12 ± 0.50	89.67 ± 0.63	90.26 ± 0.62
$E_{\mathrm{T}} > 7$ GeV	1.76 ± 0.02	12.55 ± 0.06	52.52 ± 0.13	75.77 ± 0.11	84.45 ± 0.15	86.71 ± 0.21	87.96 ± 0.29	88.16 ± 0.39	88.68 ± 0.51	89.50 ± 0.63	89.85 ± 0.64
dead OTX	1.70 ± 0.02	12.12 ± 0.06	50.58 ± 0.13	72.27 ± 0.12	79.05 ± 0.17	80.32 ± 0.25	80.91 ± 0.35	81.31 ± 0.47	81.56 ± 0.62	82.47 ± 0.78	82.36 ± 0.80
N_{Si}	1.68 ± 0.02	12.10 ± 0.06	50.54 ± 0.13	72.18 ± 0.12	78.94 ± 0.17	80.22 ± 0.25	80.79 ± 0.35	81.18 ± 0.47	81.36 ± 0.62	82.38 ± 0.79	82.18 ± 0.80
N_{TRT}	1.63 ± 0.02	11.78 ± 0.06	49.12 ± 0.13	70.03 ± 0.12	76.96 ± 0.18	78.57 ± 0.26	79.43 ± 0.36	79.91 ± 0.49	80.40 ± 0.63	81.46 ± 0.80	81.15 ± 0.82
dead B-Layer	1.57 ± 0.02	11.31 ± 0.06	47.01 ± 0.13	67.14 ± 0.12	73.88 ± 0.18	75.59 ± 0.27	76.22 ± 0.38	76.30 ± 0.51	76.99 ± 0.67	78.60 ± 0.85	77.87 ± 0.87
$f_1 > 0.1$	1.57 ± 0.02	11.28 ± 0.06	46.87 ± 0.13	66.92 ± 0.12	73.66 ± 0.18	75.29 ± 0.27	75.94 ± 0.38	76.03 ± 0.52	76.53 ± 0.68	78.31 ± 0.85	77.51 ± 0.88
ID (isEM)	0.71 ± 0.01	9.02 ± 0.05	42.03 ± 0.13	60.27 ± 0.13	64.78 ± 0.20	65.47 ± 0.30	64.65 ± 0.42	63.19 ± 0.58	62.31 ± 0.77	62.26 ± 1.00	60.12 ± 1.03

Table B.1: Efficiencies of event, acceptance, preselection and identification cuts in true p_{T} bins with respect to the previous cut (upper table) and presented as a cutflow (lower table). The graphics corresponding to this result are in figures 3.9.

Default truth classification									
Reco E_T bin (GeV)	7-8	8-10	10-12	12-14	14-16	16-18	18-20	20-22	22-26
dead OTX	95.56 ± 0.06	95.55 ± 0.06	94.17 ± 0.11	94.04 ± 0.16	93.59 ± 0.22	93.44 ± 0.30	93.55 ± 0.38	93.76 ± 0.47	92.82 ± 0.48
$N_{Si} >= 4$	99.79 ± 0.01	99.78 ± 0.01	99.72 ± 0.02	99.79 ± 0.03	99.76 ± 0.05	99.71 ± 0.07	99.69 ± 0.09	99.81 ± 0.09	99.78 ± 0.09
$N_{TRT} >= 10$	96.80 ± 0.05	97.20 ± 0.05	97.73 ± 0.07	98.00 ± 0.09	98.26 ± 0.12	98.47 ± 0.15	98.62 ± 0.19	98.50 ± 0.24	98.78 ± 0.21
dead B-Layer	95.94 ± 0.06	95.90 ± 0.06	95.88 ± 0.09	95.92 ± 0.13	96.17 ± 0.18	95.68 ± 0.25	95.75 ± 0.32	95.33 ± 0.42	95.53 ± 0.40
$f_1 > 0.1$	99.67 ± 0.02	99.65 ± 0.02	99.67 ± 0.03	99.61 ± 0.04	99.68 ± 0.05	99.45 ± 0.09	99.46 ± 0.12	99.55 ± 0.14	99.61 ± 0.12
ID (isEM)	88.20 ± 0.10	88.06 ± 0.10	82.74 ± 0.18	80.65 ± 0.28	77.13 ± 0.41	71.50 ± 0.58	70.53 ± 0.76	63.96 ± 0.99	60.62 ± 0.97

MCTruthClassifier classification									
Reco E_T bin (GeV)	7-8	8-10	10-12	12-14	14-16	16-18	18-20	20-22	22-26
dead OTX	95.56 ± 0.06	95.56 ± 0.06	94.19 ± 0.11	94.03 ± 0.16	93.55 ± 0.23	93.42 ± 0.30	93.57 ± 0.38	93.81 ± 0.47	92.81 ± 0.48
$N_{Si} >= 4$	99.79 ± 0.01	99.78 ± 0.01	99.72 ± 0.03	99.80 ± 0.03	99.76 ± 0.05	99.70 ± 0.07	99.69 ± 0.09	99.81 ± 0.09	99.77 ± 0.09
$N_{TRT} >= 10$	96.80 ± 0.05	97.20 ± 0.05	97.71 ± 0.07	98.01 ± 0.09	98.29 ± 0.12	98.47 ± 0.15	98.60 ± 0.19	98.48 ± 0.24	98.77 ± 0.21
dead B-Layer	95.95 ± 0.06	95.90 ± 0.06	95.87 ± 0.09	95.92 ± 0.14	96.16 ± 0.18	95.66 ± 0.26	95.71 ± 0.33	95.31 ± 0.43	95.52 ± 0.40
$f_1 > 0.1$	99.67 ± 0.02	99.65 ± 0.02	99.66 ± 0.03	99.60 ± 0.04	99.68 ± 0.05	99.45 ± 0.10	99.45 ± 0.12	99.58 ± 0.13	99.61 ± 0.12
ID(isEM)	88.12 ± 0.10	87.96 ± 0.10	82.62 ± 0.19	80.49 ± 0.28	76.91 ± 0.41	71.34 ± 0.58	70.36 ± 0.76	63.99 ± 0.99	60.60 ± 0.98

Table B.2: Efficiencies of preselection and identification cuts with respect to the previous cut in reconstructed E_T bins with default (upper table) and MCTruthClassifier (lower table) truth matching.

Appendix C

Composition of Heavy-Flavour MC Samples

Composition of the heavy-flavour signal electrons in the MC samples.

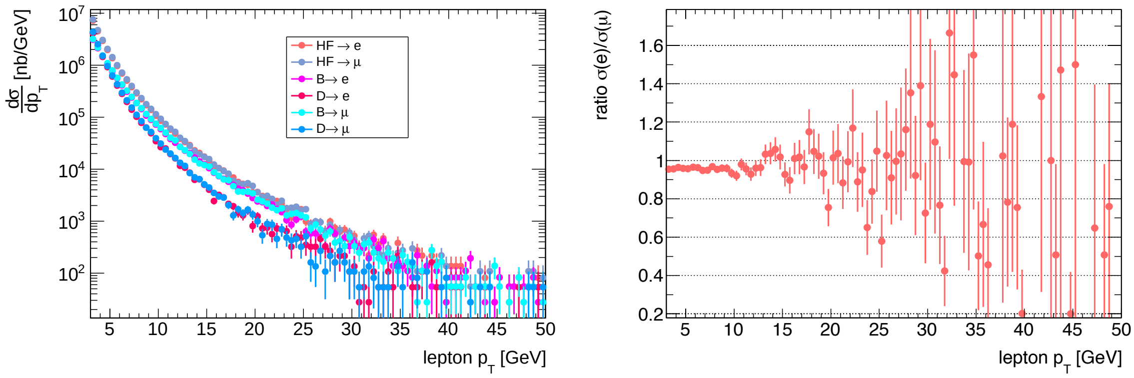

(a) (b)

Figure C.1: (a) Inclusive electron and muon spectra from heavy flavour decays predicted by POWHEG+PYTHIA. (b) Ratio of inclusive electron and muon rates from heavy flavour decay.

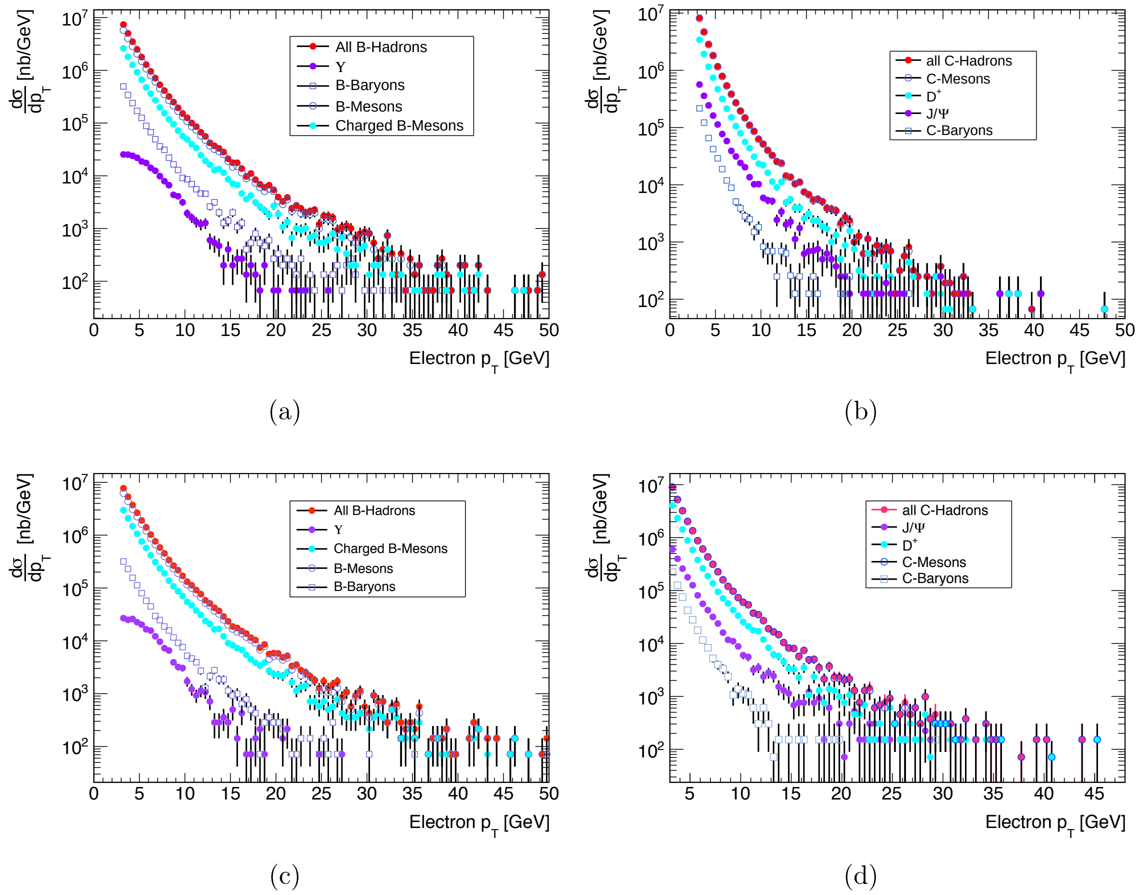

Figure C.2: Composition of electron spectra from (left) B and (right) D-hadron decays as predicted by (top) `PYTHIA` and (bottom) `PYTHIA + EVTGEN`.

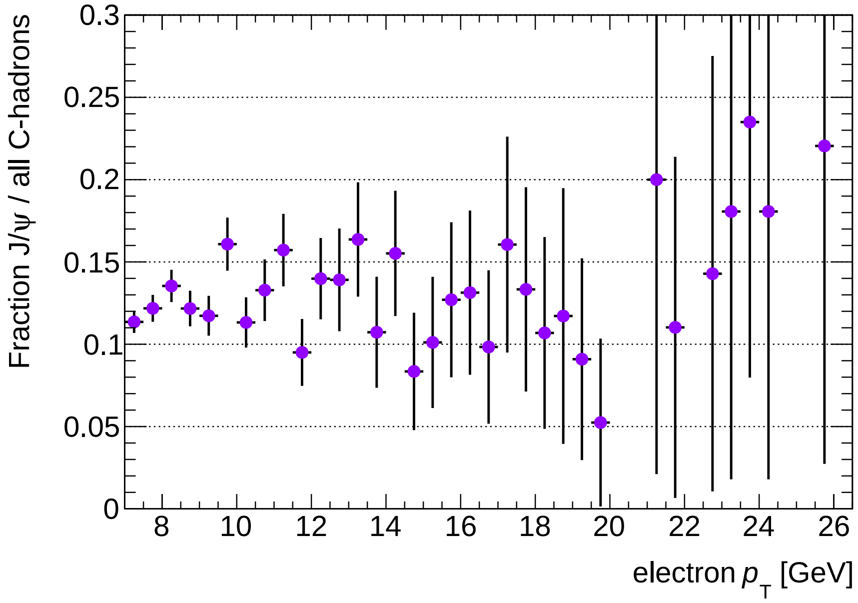

(a)

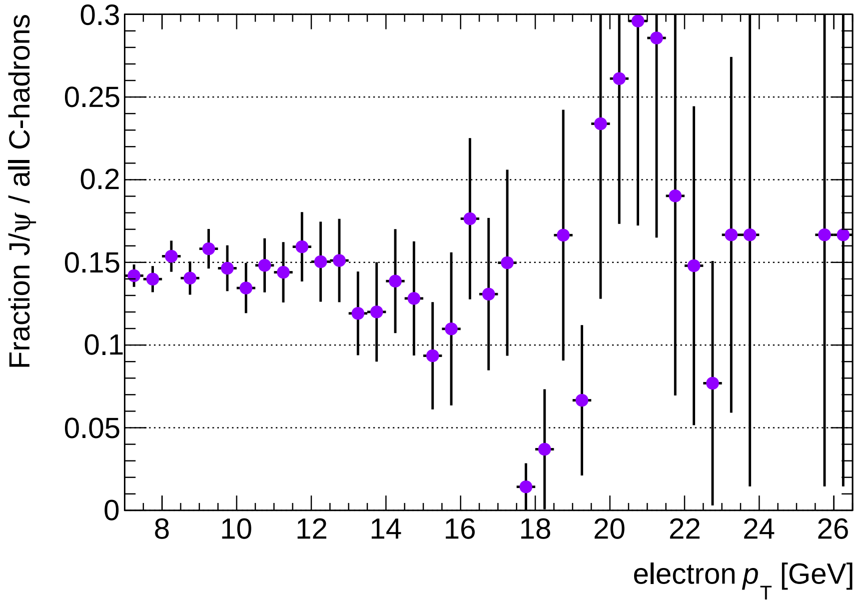

(b)

Figure C.3: Fraction of prompt J/ψ hadrons with respect to all D hadrons in PYTHIA (a) and in POWHEG+PYTHIA (b).

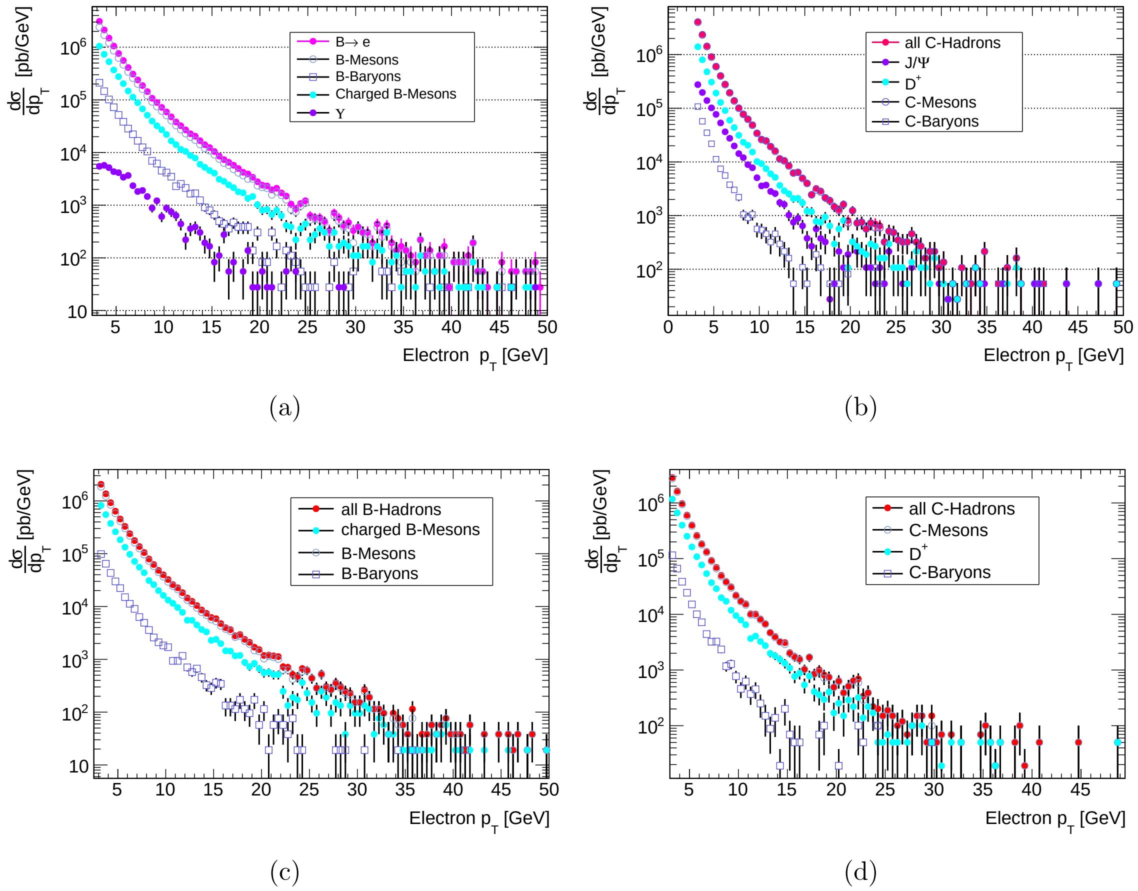

Figure C.4: Composition of electron spectra from (left) B and (right) D-hadron decays as predicted by (top) `POWHEG+PYTHIA` and (bottom) `POWHEG+HERWIG`.

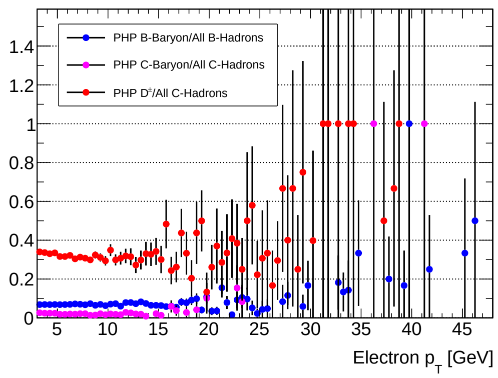

(a)

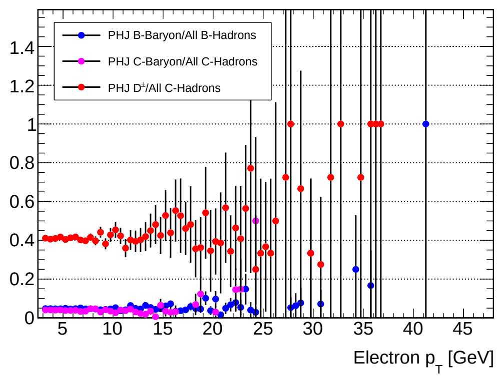

(b)

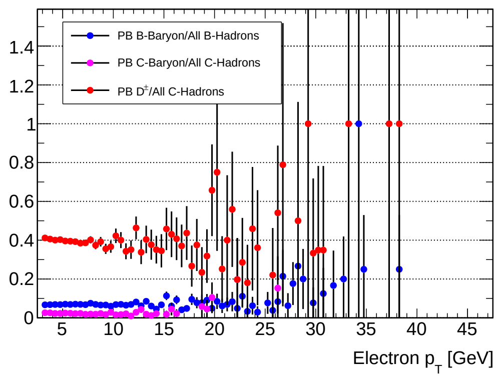

(c)

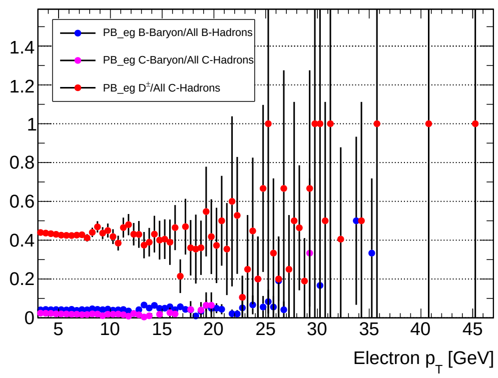

(d)

Figure C.5: Fraction of electrons from baryon decays as predicted by (a) `POWHEG+PYTHIA`, (b)`POWHEG+HERWIG`, (c) `PYTHIA` and (d) `PYTHIA+EVTGEN`. The fraction of electrons from $D^{\pm}$ decays to all D hadron decays is also shown.